MODELING AND ANALYSES OF THE THERMOHYDROLOGICAL-MECHANICAL BEHAVIOR OF BENTONITE BUFFER AND CLAY HOST ROCK IN THE HE-E TEST

Prepared for

U.S. Nuclear Regulatory Commission
Contract NRC–HQ–12–C–02–0089

Prepared by

Chandrika Manepally[1]
Stuart Stothoff[1]
Goodluck Ofoegbu[1]
Biswajit Dasgupta[1]

and

Randall Fedors[2]

[1]Center for Nuclear Waste Regulatory Analyses
San Antonio, Texas

[2]U.S. Nuclear Regulatory Commission
Washington, DC

November 2016

CONTENTS

CONTENTS (Continued)

CONTENTS (Continued)

Section Page

APPENDIX A

FIGURES

FIGURES (Continued)

FIGURES (Continued)

FIGURES (Continued)

FIGURES (Continued)

FIGURES (Continued)

TABLES

EXECUTIVE SUMMARY

This report describes numerical modeling performed as part of participation by the U.S. Nuclear Regulatory Commission (NRC) and the Center for Nuclear Waste Regulatory Analyses (CNWRA®) in the **De**velopment of **Co**upled Models and Their **Val**idation Against **Ex**periments (DECOVALEX) 2015 project. Several groups, including NRC/CNWRA, participated in the DECOVALEX-2015 Task B1 modeling exercise, which has an overall objective of understanding the thermal-hydrological-mechanical (THM) processes relevant to the performance of a nuclear waste disposal design that includes a bentonite buffer in an argillaceous host rock.

NRC participates in the DECOVALEX program to develop staff capabilities with respect to understanding complex physical behavior related to natural and engineered barriers that may affect performance of a geologic repository for nuclear waste. These capabilities include (i) technical expertise in evaluating implications for barrier performance given uncertain, variable, and incomplete data, and (ii) computational resources for appropriately simulating key features of a repository system to evaluate its anticipated performance. By pooling experimental and computational resources to address challenging problems, the DECOVALEX program offers a variety of insights and resources beyond the scope of a single radioactive waste disposal program. Participating in the DECOVALEX program also provides an opportunity for NRC and CNWRA staffs to leverage international experience and gain peer relations with staff from international organizations involved in coupled processes in argillaceous buffers and host rocks.

Background

The NRC/CNWRA team elected to participate in Task B1 because (i) the modeling exercises addressed its technical needs and (ii) the buffer-related tasks covered a wide range of applicability for processes and models and are therefore relevant to the current status of the U.S. radioactive waste repository program, for which the geologic media, repository conditions and design are currently unknown. Task B1 participants progressed through three separate modeling subtasks during the DECOVALEX-2015 cycle: (i) THM responses to a heater test in a water-saturated argillaceous host rock (the HE-D heater test) at the Mont Terri Underground Research Laboratory (URL), (ii) THM responses to heating and water imbibition in a laboratory column test filled with a buffer material (the column test), and (iii) THM responses to heaters placed in an unsaturated buffer in a 1:2 scale microtunnel in the same host rock (the HE-E heater test). The subtasks were performed during successive years in the three-year DECOVALEX cycle. The first two subtasks were performed in 2013 and 2014, with prior reports capturing progress after each subtask. The current report provides a snapshot of staff progress after completing the simulation tasks for the HE-E heater test.

The HE-E test provided an excellent culmination to Task B1, with insights and modeling approaches gained from the first two subtasks used to address the additional complexities manifested in the third subtask. The Task B1 leader supplied sensor data from the heaters, buffer, and host rock, and requested that the task participants provide model results at selected times and locations to allow comparison between models. Prior subtasks considered the constitutive properties for the buffer media and intact host rock. The HE-E heater test subtask considered a geometry representative of repository conditions for the proposed Swiss design, and included additional engineered components not considered in previous subtasks.

The HE-E experiment considers the THM responses to two 4-m [13-ft]-long heaters in a 1.3-m [4.3 ft]-diameter microtunnel bored into the Opalinus Clay host rock. The experiment consisted

of two adjacent test sections filled with a buffer material, with a plug on each end and a third plug isolating the test sections. Each section includes a heater along the axis of the microtunnel, which rests on a bentonite block pedestal. One test section is backfilled with a granular bentonite buffer medium that the Swiss National Cooperative for the Disposal of Radioactive Waste (Nagra) is considering for use as repository backfill material. The other test section is filled with a sand–bentonite mixture that the German organization Gesellschaft für Anlagen-und Reaktorsicherheit (GRS) is considering for use as backfill material.

The NRC/CNWRA team selected a pair of codes, xFlo and Fast Lagrangian Analysis of Continua (FLAC), to perform the HE-E heater test modeling. NRC and CNWRA developed the thermohydrological (TH) xFlo code in the mid-2000s with the intention of eventually replacing the existing coupled-process MULTIFLO simulator (Painter, 2006). MULTIFLO (Painter and Seth, 2003) consists of the METRA code (a TH simulator) and the GEM code (a reactive transport simulator) that can be run in stand-alone mode or coupled using the MULTIFLO driver program. xFlo currently implements most of the METRA functionality. xFlo considers mass balance of two phases (liquid and gas) and two components (water and air), as well as energy balance. FLAC is a commercially available THM code that calculates the geomechanical responses of solid and porous media to pressure and temperature changes, but did not consider coupled THM processes at the level of detail that the team considered necessary for HE-E modeling.

The NRC/CNWRA team planned to couple the xFlo and FLAC codes for Task B1 during the first two subtasks. Coupling consists of using saturation, pressure, and temperature outputs from xFlo to update the geomechanical state of the system modeled in FLAC, and using output from FLAC to update porosity values used by xFlo. The DECOVALEX-2015 modeling work was the first extended use of the xFlo code, and an extended shakedown period was necessary prior to developing the software coupling process. This shakedown period extended through the previous subtasks. During the past year, the NRC/CNWRA team successfully implemented one-way coupling from xFlo to FLAC, so that the importance of one-way feedbacks can be assessed. Two-way coupling between xFlo and FLAC, using FLAC output to update xFlo parameters, has been identified as a potential topic of future work.

HE-E Model Results Provided to DECOVALEX

The Task B1 leader was responsible for selecting the modeling tasks for the task participants and providing the data for model comparisons. The Task B1 leader selected a cross section perpendicular to the microtunnel axis passing through the center of the Nagra heater section for comparisons between the observations and simulations prepared by the various teams. The NRC/CNWRA team had focused on simulating responses in this buffer material for the column test experiment.

Although the HE-E test is fully three-dimensional (3-D), the team was able to develop a two-dimensional (2-D) model that captures the key processes at the selected cross section by taking advantage of geometric symmetries. This decision allowed the team to develop a model with a grid resolution suited to resolving the sharp capillary pressure and saturation gradients that appear adjacent to the interface between contrasting material properties (e.g., in the buffer and host rock at the microtunnel wall). The model was sufficiently fast that ~120 xFlo simulations were performed to explore sensitivities. Selected xFlo simulation outputs were used to drive FLAC. A fully 3-D model was also developed by replicating the 2-D model as slices along the microtunnel axis, but this model proved to be too slow for practical use.

Model parameters were largely obtained from previous modeling work. For engineered media not previously included in a model, model parameters were based on manufacturer's specification sheets where available. Features such as gaps and cracks were included using additional parameterizations to assess sensitivity to the features. Boundary conditions and initial conditions were based on measured values.

The Task B1 leader requested that outputs from three separate simulations be provided for cross-comparisons between task participants. One transient simulation was to use the uncalibrated parameter set to simulate the actual test period. The other two simulations were to be run using the final calibration parameter set with both runs terminated when the buffer completely resaturated. One of the two simulations was to assume that the heaters were shut down at a specified time; the other was to assume that the current heater strategy continued indefinitely (i.e., heater power adjusted to maintain constant temperature at a sensor location on the surface of the heater liner).

The NRC/CNWRA team considered the uncalibrated parameter set to be the initial parameter values for each key engineered component, although numerous simulations were performed to identify key components and refine their geometry in the model. The initial parameter set assumed that the host rock was intact [i.e., no excavation damaged zone (EDZ) existed]. The calibrated parameter set included a representation for the EDZ and adjusted the contact between the bentonite block and the heater liner, but otherwise the parameter set was essentially unchanged from the initial values.

Each of the simulations provided to the Task B1 leader were run to 100 years. In all of the simulations, saturation, temperature, and pressure profiles were essentially radial from the liner to the far field, except for some distortions in and near the bentonite pedestal and an underlying steel cable channel. All three simulations reached an equilibrium final state, with the buffer drying out for the simulation with the initial parameter set and completely resaturating for the two simulations with the final parameter set. The Task B1 leader defined resaturation as occurring when all the nodes in the buffer have a liquid saturation of at least 99 percent. Resaturation occurred approximately twice as fast when the heater remained on, because water is less viscous when heated. Because the simulated behavior of the excavation damaged zone EDZ determines whether rewetting occurs in the simulations, and because the EDZ is expected to heal upon rewetting, prediction of the time to rewetting is highly uncertain.

The FLAC simulations focused on the mechanical response of the buffer material, assuming that the host rock remained saturated. For these simulations, changes in calculated buffer porosity occurred in concentric rings, with compression causing reduced porosity and expansion causing increased porosity. The largest change in buffer porosity occurred in narrow compression bands near the heater, with porosity locally decreasing by as much as 0.08. Some compression also occurred near the host rock, with porosity locally decreasing by less than 0.025. Most of the buffer interior showed mild expansion, with porosity locally increasing by less than 0.025, and expansion occurred adjacent to the side and bottom of the liner. FLAC calculated similar expansion and compression patterns and similar magnitudes of porosity change after equilibrium was reached regardless of whether the buffer dried or resaturated.

Confirmation and Auxiliary Analyses

The NRC/CNWRA team performed a series of post-mortem auxiliary analyses after completing the Task B1 modeling, to better understand the model limitations and to consider potential implications for buffer performance.

An important confirmatory analysis considered heat loss using a detailed 3-D COMSOL model of the full HE-E test geometry and materials. The COMSOL software is useful for confirmatory simulations with complex geometry but relatively simple governing equations and material properties. This analysis confirms that axial heat loss would be expected to occur in the heater components and buffer, but this should have only a mild effect on the simulation results for the 2-D cross section because of its central location in the heater.

Output from a series of confirmatory analyses was used to evaluate the experimental data in greater detail to better understand measured buffer and near-field behavior with potential performance implications. These analyses were conducted where unusual or unexpected data and mismatches between the model calculations and the sensor data were observed. In particular, the analyses considered implications of (i) unexpected temperature profiles inside the microtunnel, (ii) unexpected reverse pore pressure responses during power outages, and (iii) relative displacements at the microtunnel wall that indicated large tunnel expansion during heating.

The 3-D model was adapted to investigate anomalous temperature profiles within the microtunnel, with apparent temperature jumps at the heater liner and host rock wall. Adding a thin thermally resistant layer between the heater liner and tunnel wall explains these temperature jumps, implying that the buffer may have poor contact with the heater liner and particularly with the host rock.

Pore pressure responses measured several meters into the host rock during HE-E heater power failures show rapid transients starting within hours of the failure at some locations, but not at others. Such rapid thermally induced responses are unusual in most porous media, because thermally induced pore pressure responses normally propagate with the temperature front, which takes much longer to reach the sensor location. Even more unusual, some of the rapid responses showed increased pore pressure before the cooling front reached the sensor.

A number of lines of investigation were taken to understand this unusual behavior. Reverse pressure responses have been described frequently in a clay aquitard adjacent to a pumped aquifer when the pumps are turned on or off, and these responses have been shown to be due to deformation of the aquitard by the varying stresses carried by the solid skeleton (effective stress). Rapid pore pressure responses to construction stresses were observed at several locations in the Mont Terri URL. Re-examining the HE-D heater test data showed that similar rapid reverse pressure events were repeatedly recorded by many of the HE-D sensors following power outages. These data, combined with observed pore pressure distributions around mined openings that are oriented with the principal stresses, suggest that in the host rock pore pressures respond so slowly to pore pressure gradients that measured pore pressure distributions are largely passive indicators of stress and thermal changes, at least on the time scales of the HE-E test. By implication, xFlo will need to be coupled with FLAC to properly represent pore pressures in the Opalinus Clay.

Relative deformation data were provided by the Task B1 leader, but no specific comparison was requested. Examining the relative deformation data shows that heating increased the radius of the microtunnel by ~17 mm [0.67 in], consistent with an induced ring of compression further in the host rock that would raise pore pressures. The large and uniform radial deformation implies that the host rock is likely to develop circumferential tension and radial compression, implying that approximately radial cracks or crack systems would pull apart. The relative deformation data show a sudden expansion of up to 4 mm [0.16 in] in 2 to 3 hours, which may be due to

formation of a radial tension crack, or perhaps parting between the host rock and the poured concrete in a plug.

The near-field pore pressure data suggest that an unsaturated zone persists up to two tunnel radii into the host rock throughout the HE-E test. This unsaturated zone is consistent with a radially dominated unsaturated fracture system pneumatically connected with the microtunnel, in conjunction with a poor hydraulic connection between the host rock and the buffer.

Lessons Learned

The comparison between observations and model results suggested that the TH constitutive relationships used in previous subtasks were appropriate for the third subtask. However, additional analysis of the modeling work indicates that the models should have also accounted for various gaps and cracks that the data indicate were present in the field test. The data suggest that (i) gaps developed between the buffer and both the heater and the host rock that delay rewetting, (ii) the excavation damaged zone develops extended radial crack systems during heating, and (iii) the hydraulic response of the host rock during the test interval is primarily driven by the mechanical response to heating.

Static gaps and cracks can be modeled with the current software, but two-way coupling between xFlo and FLAC would be necessary to account for the feedback between mechanical and TH responses and the models would need to account for the dynamic change in aperture. The time to buffer rewetting appears to be highly dependent on the nature of cracks in the EDZ, at least for the Opalinus Clay, and how fractures mechanically respond to heating and rewetting is not well-understood. The HE-E test was too short to provide information on the long-term evolution of crack properties.

Thermal and pore pressure data both suggest that the buffer is in poor contact with the host rock, whereas the TH modeling assumes a good contact exists. The FLAC model was not specifically constructed to examine whether or not gaps formed, but calculated deformation patterns soon after the buffer and near field reached a thermal equilibrium hint that the buffer may pull away from the sides of the liner. Further work to understand the formation of gaps between the buffer and surrounding media would be useful for understanding buffer performance with respect to rewetting and implications for radionuclide transport.

Experience with the xFlo code suggests that the xFlo version 1.0β implementation is fundamentally sound, but there are changes to the computational structure and user interface that would improve its ease of use, calculation robustness, links to other models such as FLAC, and flexibility for addressing assessment calculations. Preliminary modifications to a copy of xFlo were made to (i) test alternatives for the user interface and (ii) test alternatives for moving duplicated routines into a generic interface and thereby substantially simplify the logic in the computational modules. Such modifications offer additional flexibility with respect to code maintenance, code expansion, computational flexibility, and user interactions. To ensure traceability, the current version of xFlo (Stothoff and Painter, 2016) without these test modifications was used for all simulations for DECOVALEX.

NRC and CNWRA staff recommend that potential future modeling tasks using xFlo–FLAC include (i) investigating the near-field THM behavior for cases with high waste package temperatures (~200 °C) [392 °F] and (ii) evaluating the potential for gas generation and migration to support activities related to corrosion and performance assessment.

ACKNOWLEDGMENTS

This report was prepared to document work performed by the Center for Nuclear Waste Regulatory Analyses (CNWRA®) for the U.S. Nuclear Regulatory Commission (NRC) under Contract No. NRC–HQ–12–C–02–0089. The activities reported here were performed on behalf of the NRC Office of Nuclear Material Safety and Safeguards, Division of Spent Fuel Management. The report is an independent product of CNWRA and does not necessarily reflect the views or regulatory position of NRC. The NRC staff views expressed herein are preliminary and do not constitute a final judgment or determination of the matters addressed or of the acceptability of any licensing action that may be under consideration at NRC.

This work was performed in conjunction with the DECOVALEX-2015 collaborative project, Task B1 (see www.decovalex.org). The HE-E and Column Test experiments have received funding from the European Atomic Energy Community's Seventh Framework Programme (FP7/2007-2011) under grant agreement no. 249681. The authors would like to thank C. Dinwiddie for her technical review and G. Wittmeyer for his programmatic review. The authors also appreciate M. Hickinbotham and A. Ramos for providing word processing support in preparation of this document.

QUALITY OF DATA, ANALYSES, AND CODE DEVELOPMENT

DATA: All CNWRA-generated data contained in this report meet quality assurance requirements described in the Geosciences and Engineering Division Quality Assurance Manual. Data for the HE-E and HE-D tests was provided by the DECOVALEX Task B1 leader[1] and was collected under the quality assurance protocols of external programs.

ANALYSES AND CODES: The computer software FLAC™ (Itasca Consulting Group, 2011), *xFlo* Version 1.1β (Stothoff and Painter, 2016), and COMSOL Multiphysics® were used in the analyses contained in this report. *xFlo* (Version 1.1β) is controlled under Technical Operating Procedure (TOP)–018, Development and Control of Scientific and Engineering Software. COMSOL Multiphysics, FLAC and MATLAB are commercial software also controlled under TOP–018. Documentation for the calculations and model input values can be found in Scientific Notebooks 1103E (Ofoegbu and Dasgupta, 2015), 1611E (Manepally, 2015), and 1177 (Stothoff, 2015).

References:

Manepally, C. "ISFR Task Order 9-Decovalex-Related Activities." Scientific Notebook No. 1611. San Antonio, Texas: Center for Nuclear Waste Regulatory Analyses. 2015.

Ofoegbu, G.I. and B. Dasgupta. "Development of Constitutive Relations for Unsaturated Soil and Thermal-Hydrological-Mechanical Coupling." Scientific Notebook No. 1103E. San Antonio, Texas: Center for Nuclear Waste Regulatory Analyses. 2015.

Stothoff, S. and S. Painter. "xFlo Version 1.1β User's Manual: DECOVALEX–2015 Version." San Antonio, Texas: Center for Nuclear Waste Regulatory Analyses. ML16167A315, U.S. Nuclear Regulatory Commission. 2016.

[1]Email correspondence (dated 2/11/2015) from Benoit Garitte (Task B1 leader) to NRC and CNWRA providing the link to the FTP HE-E Test data.

Stothoff, S. "xFlo Development and Analyses." Scientific Notebook No. 1177. San Antonio, Texas: Center for Nuclear Waste Regulatory Analyses. 2015.

Itasca Consulting Group. "FLAC V 7.0, Fast Lagrangian Analysis of Continua, User's Guide." Minneapolis, Minnesota: Itasca Consulting Group. 2011.

CONVERSION FACTORS

Length, area, pressure and temperature conversions have been included in the text. The conversions for other parameters are provided in this table.

Name	SI Unit	Conversion
Density	1 g/cc 1 kg/m^3	= 0.036 lb_m/in^3 = 0.06243 lb_m/ft^3
Heat transfer rate	1 W	= 3.4123 Btu/hr
Length	1 cm 1 m	= 0.394 in = 3.28 ft
Permeability	1 m^2	= 1.01 × 10^{12} darcies
Area	1 m^2	= 10. 8 ft^2
Power	1 W	= 3.412 Btu/hr
Pressure and Stress*	1 N/m^2 (1 Pa) 1 MPa	= 0.000145 psi = 145 psi
Specific heat	1 kJ/kg·K	= 0.2389 $Btu/lb_m·°F$
Thermal conductivity	1 W/m·K	= 0.57782 Btu/hr·ft·°F
Temperature	1 °F	= 1.8 × T °C + 32
Viscosity (dynamic)†	1 N·s/m^2	= 5.8016 × 10^{-6} $lb_f·hr/ft^2$
Mass	1 g	= 0.002 lb_m
Physical Constants		
Gravitational Acceleration (Sea Level)		g = 9.807 m/s^2 = 32.174 ft/s^2

*The SI name for the quantity pressure is Pascal (Pa) having units N/m^2 or $kg/m·s^2$
†Also expressed in equivalent units of kg/s·m

1 INTRODUCTION

The **De**velopment of **Co**upled Models and Their **Val**idation Against **Ex**periments (DECOVALEX) project is an international collaboration of modeling teams focused since 1992 on modeling thermal-hydrological-mechanical-chemical processes associated with the deep geologic disposal of high-level radioactive waste and spent nuclear fuel[1]. The project aims to improve the reliability of modeling tools and performance predictions through comparisons with data from laboratory and large-scale field experiments. An important component of the project is the evolution and improvement of modeling tools through comparisons of different approaches, both within each team and among modeling teams.

The current and sixth phase of DECOVALEX, called DECOVALEX-2015, was initiated in April 2012 and will conclude in December 2015. This phase involved modeling teams from 10 international organizations participating in five tasks for modeling laboratory or field experiments. Leaders assigned to each DECOVALEX task have several responsibilities including (i) defining the scope and schedule of the modeling steps, (ii) providing laboratory and field data to participants, and (iii) analyzing modeling results from task participants for comparison. The U.S. Nuclear Regulatory Commission (NRC)/Center for Nuclear Waste Regulatory Analyses (CNWRA®) team participated in Task B1[2], which is designed to improve understanding of the thermal-hydrological-mechanical (THM) processes in a bentonite buffer and argillaceous host rock at the Mont Terri Underground Research Laboratory (URL), Switzerland. Task B1 is based on three tests:

1. HE-D heating test at Mont Terri (rock only)

2. Laboratory column test for granular bentonite (used as a buffer for the HE-E test)

3. HE-E heating experiment at Mont Terri (integrating buffer materials and host rock)

The modeling of the HE-D test and laboratory column test for granular bentonite were summarized in previous milestones (Ofoegbu et al., 2015a; Stothoff et al., 2015a).

This report provides a summary of the progress of the NRC/CNWRA team in modeling swelling clays used for buffer materials for the HE-E Test, which is the final task for DECOVALEX-2015. The report summarizes work related to (i) HE-E test modeling as defined by Task B1 leader (Chapters 2 through 6) and (ii) supplemental analyses of site data to improve conceptual and numerical models of key processes (Chapter 7).

1.1 Description of the HE-E Experiment

The HE-E test is a 1:2 scale *in-situ* experiment that is part of the Performance of Engineered Barrier Systems (PEBS) project, funded by the seventh framework project of the European Commission (Gaus et al., 2014a,b; Teodori and Gaus, 2011). The PEBS project aims at understanding processes that influence (i) behavior of the engineered barrier systems (EBS) and (ii) conceptual and parameter uncertainties. The HE-E test focuses on the THM processes in the EBS during the very-early post closure period under temperatures of 140 °C [284 °F] at

[1]http://decovalex.org/index.html

[2]http://decovalex.org/task-b1.html

the heater that could be expected for some repository designs. Some of the THM processes, such as heating and non-uniform resaturation of the buffer, could significantly affect its effective hydraulic conductivity and swelling capabilities and affect its barrier capabilities. This test also aims to (i) provide data to validate existing THM models and (ii) evaluate the need for upscaling thermal conductivity of the partially saturated buffer materials (granular bentonite and sand–bentonite mixture) from laboratory to field scale. The laboratory column test (Villar et al., 2012, 2014), described in a CNWRA report by Stothoff et al. (2015a), evaluated the thermal conductivity of the buffer materials used in the HE-E test.

The HE-E experiment is located in the microtunnel in the Mont Terri URL in Switzerland (Figure 1-1). The Mont Terri URL is located at a depth of 250 to 320 m [820 to 1,050 ft] below the ground surface. The microtunnel, approximately central to the URL, is 50 m [164 ft] long with a diameter of 1.3 m [4.3 ft]. The HE-E test section has a length of 10 m [32.8 ft] and was characterized extensively for the Ventilation Experiment (Mayor et al., 2007). This test section is isolated from the rest of the microtunnel using concrete plugs (shown as Plug 1 and Plug 3 in Figure 1-2) that contain thermal insulation and vapor barriers. The construction of the HE-E test was initiated during December 2010 and completed during June 2011. The HE-E experiment consists of two symmetrical sections, each 4 m [13 ft] long, which are separated by a plug (Plug 2 in Figure 1-2).

Each section has a heater representing emplaced waste on compacted MX-80 bentonite blocks. Heaters were designed to be operated either by power or temperature control and they function independently for the two sections. The first section, called the Gesellschaft für Anlagen- und Reaktorsicherheit (GRS) section, is filled with sand–bentonite mixture that is being considered as an alternative EBS material in Germany. The second section, called the Nationale Genossenschaft für die Lagerung radioaktiver Abfälle (Nagra) section, is filled with granular bentonite, which Nagra has proposed to use for a repository in Switzerland. This layout allows comparison of THM behavior of the two buffer materials when subjected to identical heating conditions. The bentonite blocks used in this experiment are also being considered in Nagra's repository design. Heating began during June 2011 and the heat load was increased gradually (discussed in detail in Section 2.1.4) until a maximum temperature of 140 °C [284 °F] was observed at the heater during June 2012. The heater temperature has been held constant and the test is ongoing. A detailed description of the buffer materials, bentonite block and Opalinus Clay is presented in Section 2.2.

Monitoring sensors were emplaced at various locations during the HE-E test. By section, sensors include:

1. Heater: Each heater section has thermocouples located on three radial planes. At each radial plane, four thermocouples are placed on the inner part of the 8 mm [0.3 in]-thick heater liner, enabling monitoring of the heater surface temperature along the perimeter of the heater (Figure 1-3). Additional thermocouples contact the outer (four thermocouples) and middle (two thermocouples) cylinders of the heater at each radial plane.

2. EBS (Buffer material and bentonite blocks) and interface with the Opalinus Clay: Temperature and relative humidity was measured extensively at these locations to ensure accurate spatial characterization of thermohydrological (TH) behavior. There were 36 sensors in the buffer, 24 in the bentonite blocks and 18 at the EBS/Opalinus Clay interface. The sensor locations are shown in Figure 1-4.

3. Near-field Opalinus Clay {<2 m [6.6 ft] from the microtunnel}: This zone was monitored extensively because it was influenced by the construction of the tunnel Ventilation Experiment (Mayor et al., 2007). There were 34 piezometers to measure pore pressure), 20 capacitive sensors to measure temperature and relative humidity, 8 extensometers to measure relative displacement and 17 psychrometers to measure relative humidity (Figure 1-5).

4. Far-field Opalinus Clay: This zone, extending from 2 to 6 m [6.6 to 19.7 ft] from the microtunnel, was considered less disturbed by changes in TH conditions in the microtunnel. In addition to two existing boreholes that were used in the Ventilation Experiment, two additional boreholes were installed to monitor hydraulic pressure using piezometers (Figure 1-6).

A network of (i) geoelectric sensors to monitor changes in saturation in the Opalinus Clay and (ii) seismic monitors in the sand–bentonite mixture and Opalinus Clay to monitor changes in the material properties in response to construction and heating were installed. These results were not analyzed as a part of the DECOVALEX task.

1.2 Description of the Numerical Modeling Approach

The primary THM model is implemented in a two-dimensional (2-D) coordinate system perpendicular to the axis of the microtunnel at the center of the Nagra section (granular bentonite buffer) of the HE-E Test. The model includes three test phases:

1. Prior to emplacement: The various microtunnel conditions before, during, and after the Ventilation Experiment are approximated with 15 years of steady boundary conditions

2. Prior-to-heating phase: The plug, buffer, and heater installation period is modeled as installed instantaneously 75 days prior to start of heating

3. Heating phase: Heating is based on three-day averages of the measured heat load in a spreadsheet provided by the Task B1 leader, extended into the future based on the simulation scenario.

The Task B1 leader requested that model results be provided for three scenarios:

1. Predictive modeling: using the same parameters used for column tests and HE-D tests

2. Interpretative modeling: with calibrated parameters assuming that the heater temperatures are maintained indefinitely

3. Interpretative modeling with shutdown: with calibrated parameters assuming that the heater was shut down on June 1, 2019

All the models were simulated for 100 years after start of heating to capture the time when the buffer was saturated. The buffer is considered to be saturated when all the nodes in the buffer have a liquid saturation of at least 99 percent.

Two different simulators were used to represent the coupled THM processes. TH processes were modeled using xFlo. Three simulations were performed (one for each phase described above), with the final state from one simulation used as the initial condition to the next.

Geomechanical processes were modeled using FLAC. The xFlo model represented the EBS components and the Opalinus Clay. The FLAC model assumed that unsaturated elastic–plastic deformation could occur in the buffer and bentonite blocks, while only elastic deformation would occur in the Opalinus Clay (because it is saturated except for a thin zone adjacent to the microtunnel) in the geomechanical analysis.

xFlo−FLAC Coupling

The coupling in xFlo-FLAC is achieved by passing xFlo output (e.g., temperature, liquid pressure, saturation) to the FLAC model. Typically, approximately 100 points in time were preselected for outputs to capture anticipated gradual changes in temperature, pressure, and saturation. These time steps were preselected to ensure that the approximately logarithmic evolution of TH processes in the buffer and host rock were represented appropriately in the FLAC model. A set of batch files processed the xFlo output files at these preselected time steps into FLAC input after the xFlo simulation completed. This procedure does not feed FLAC outputs, such as changes to porosity, back to xFlo. Approaches are being considered for automatic information transfer between xFlo and FLAC, as discussed further in Chapter 7.

1.3 Auxiliary Analyses

In addition to the DECOVALEX task, staff performed a series of auxiliary analyses using auxiliary models. These supplemental analyses, discussed in Chapters 4 and 5, were used to provide confidence in the primary model, to clarify aspects of the HE-E test setting, and to explore aspects of the test comparison more fully. These supplemental tasks, focused on THM processes in Opalinus Clay, include analyses of:

- Initial pore pressure distributions in the Opalinus Clay around the microtunnel prior to heating based on observations elsewhere in the Mont Terri underground laboratory and from the earlier Ventilation Experiment in the microtunnel

- Influence of power failures on THM processes in Opalinus Clay, using the HE-E data and revisited data from the HE-D test

- Extensometer data in Opalinus Clay

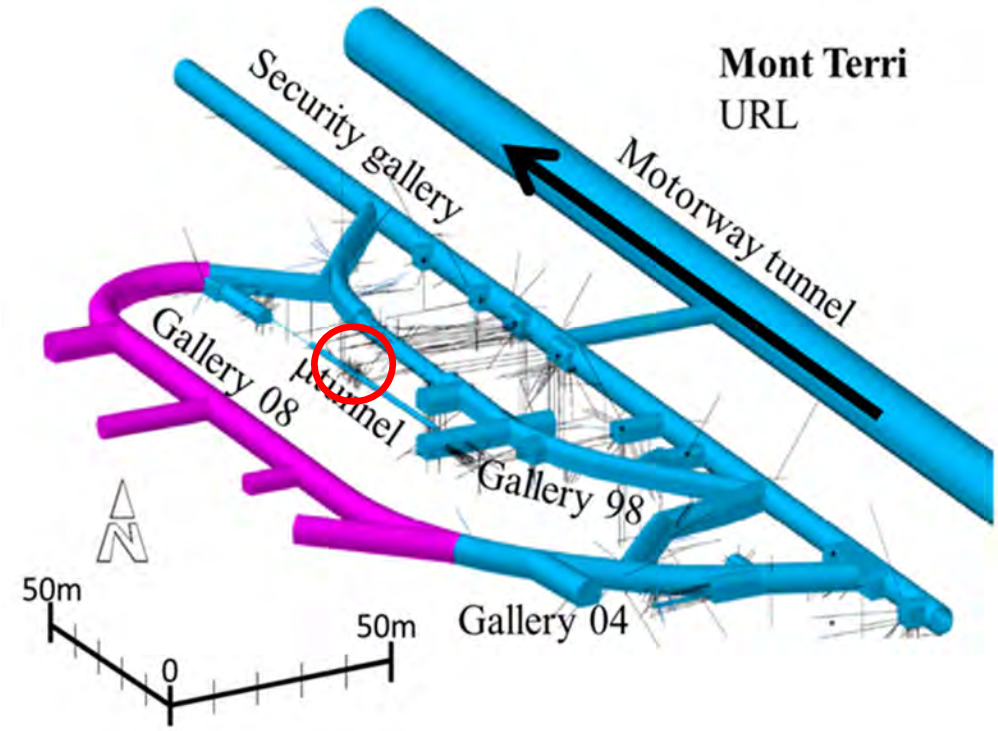

Figure 1-1. Location of the HE-E Test in the Microtunnel (µtunnel) is Encircled on a Diagram of the Mont Terri Underground Research Laboratory (Gaus et al., 2014a) [1 m = 3.3 ft]

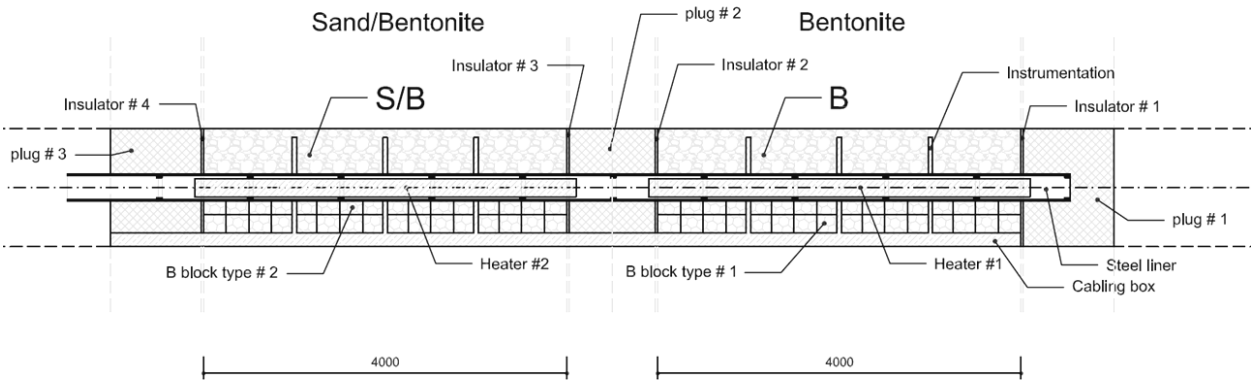

Figure 1-2. Schematic of the HE-E Microtunnel Test Section Showing Granular Bentonite (Nagra) and Sand–Bentonite (GRS) Subsections and Plugs Used to Isolate the Heaters (Gaus et al., 2014a). [1 mm = 0.039 in]

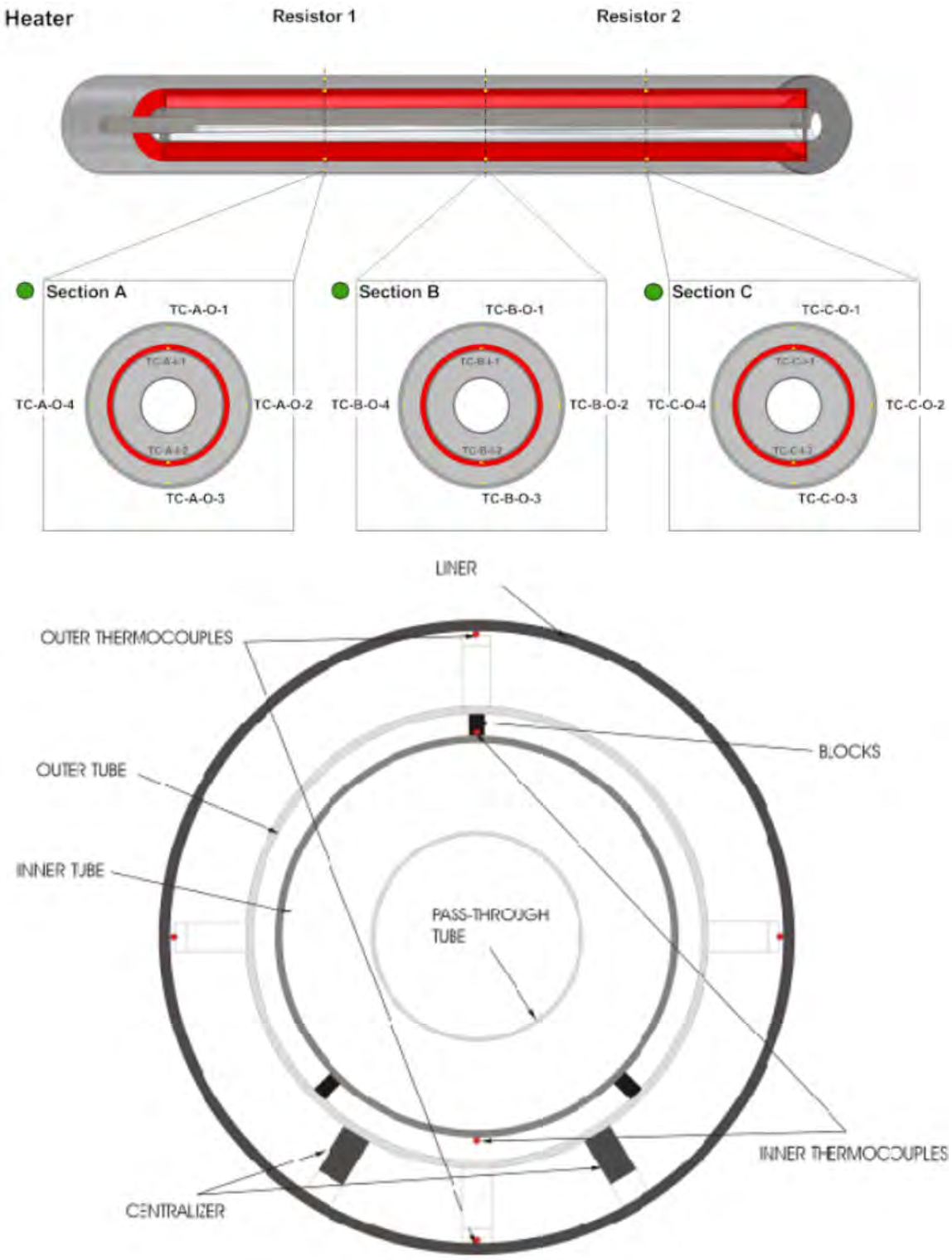

Figure 1-3. Heater Schematic Illustrates Thermocouple Monitoring Locations (Gaus et al., 2014a)

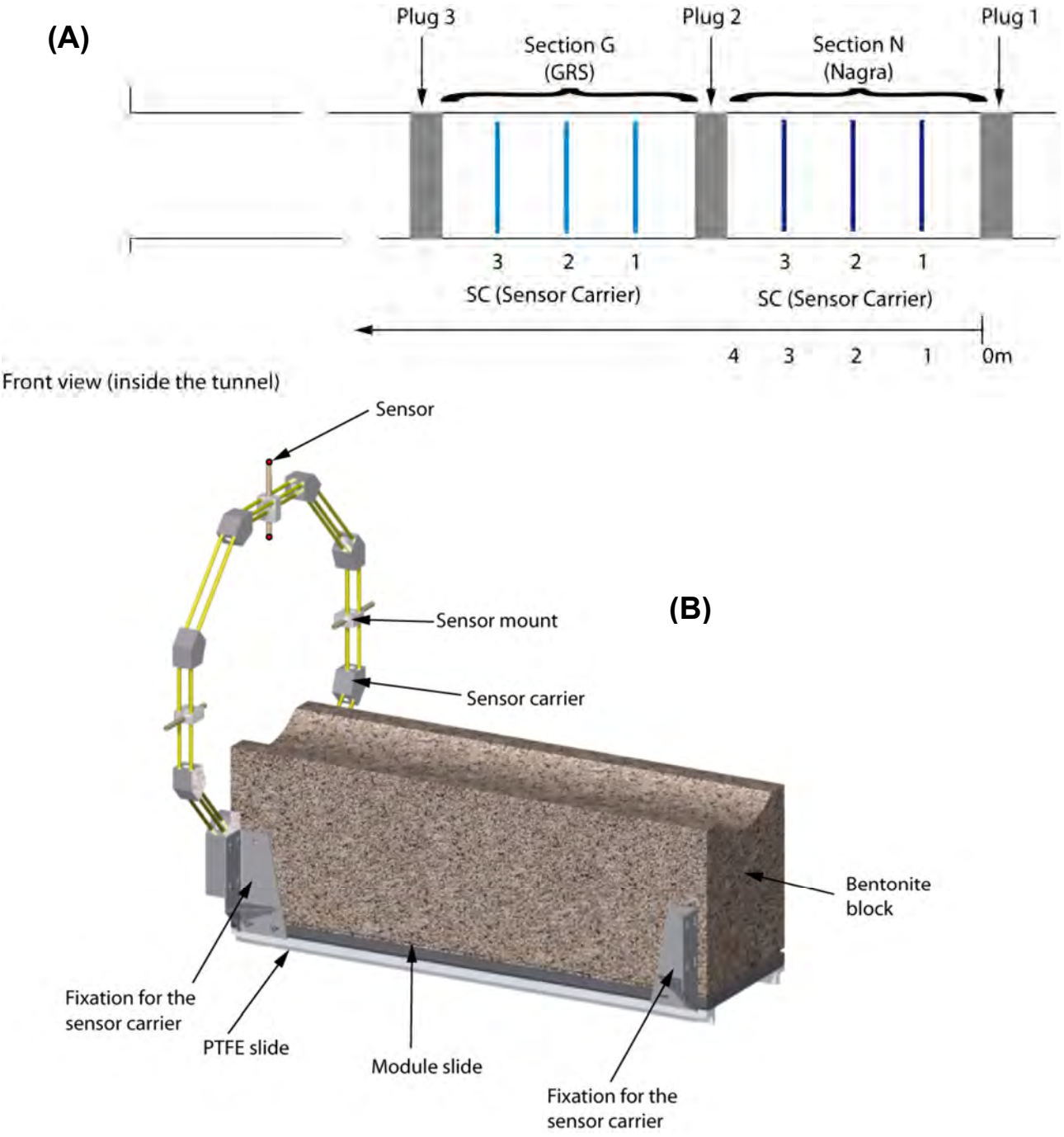

Figure 1-4. Instrumentation in the Engineered Barrier System for the HE-E Test: (A) Locations of the Sensor Carriers (Details in B) Along the Test Section; (B) Prefabricated Modules Used to Mount the Sensor Carriers.

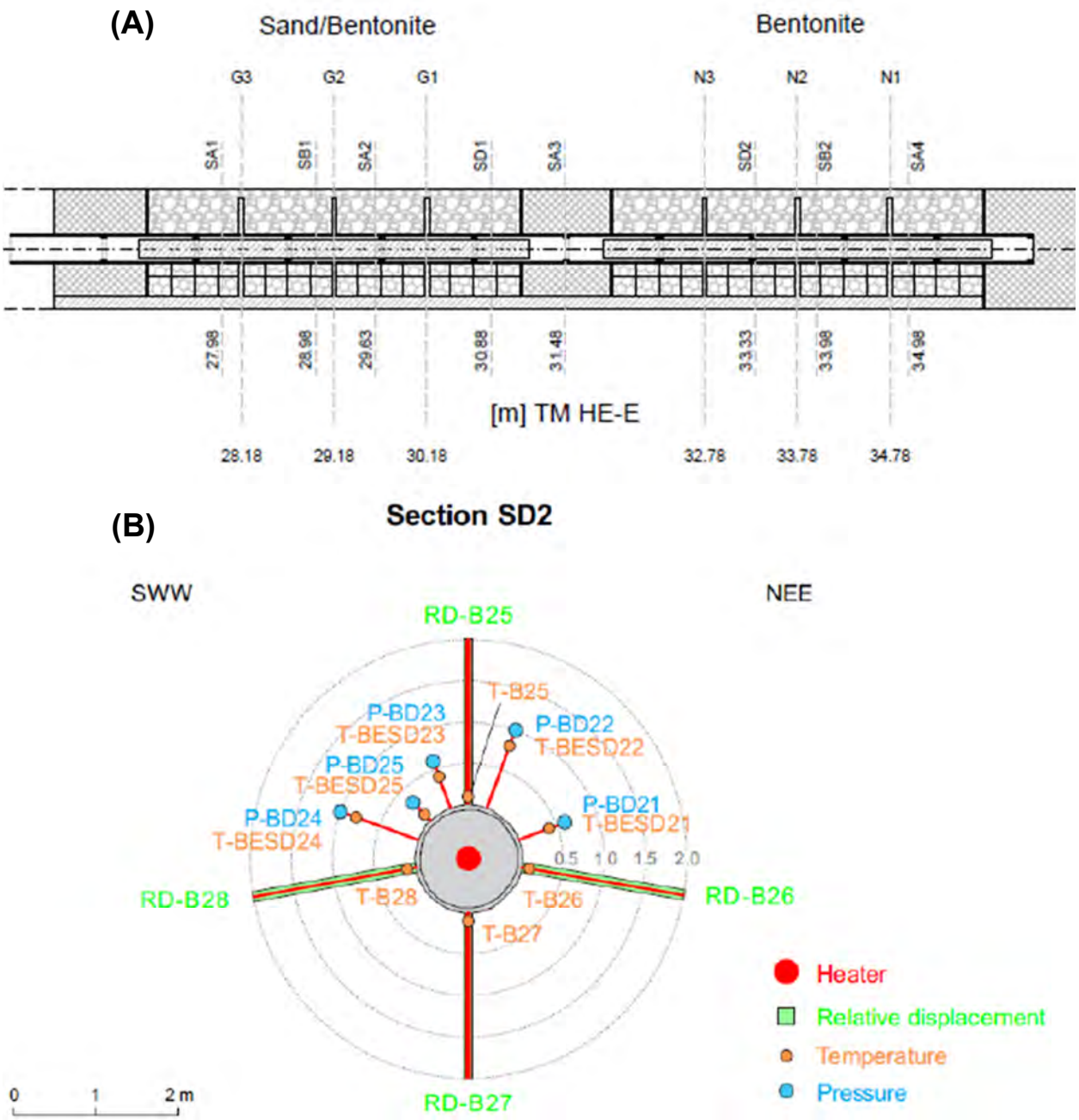

Figure 1-5. (A) Locations Along the Microtunnel for Monitoring Cross Sections in the Near-Field Opalinus Clay. Cross Sections SA4, SB2, and SD2 are in the Granular Bentonite (Nagra) Section. Cross Sections SD1, SA2, SB1 and SA1 are in the Sand–Bentonite (GRS) Section. (B) Instrumentation for Cross Section SD2 (Gaus et al., 2014a) [1 m = 3.3 ft]

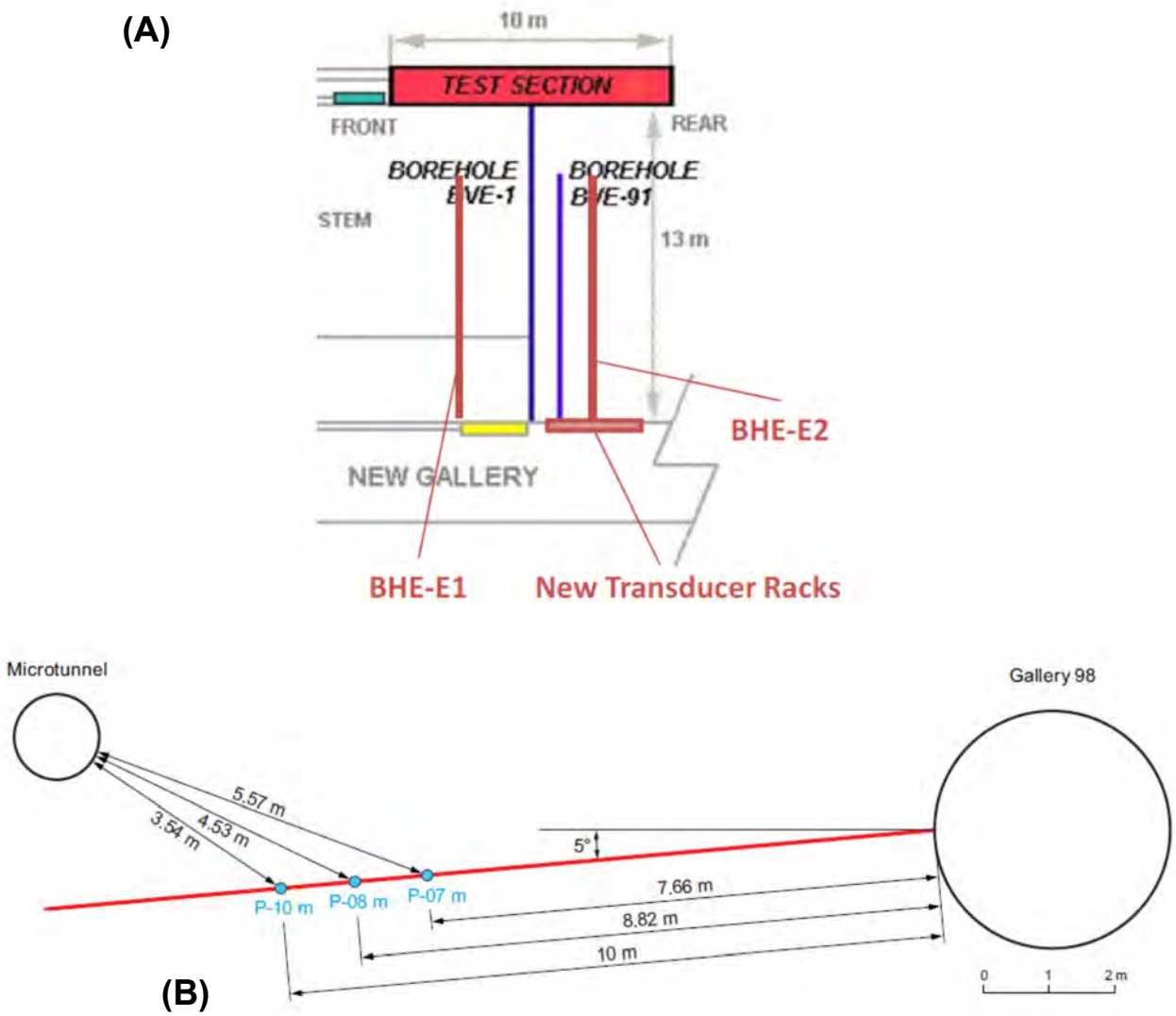

Figure 1-6. (A) Plan View of the Boreholes BVE-1, BVE-91, BHE-E1 and BHE-E2 Used to Monitor Pore Pressure in the Far-Field Opalinus Clay; (B) BVE-91 Borehole Schematic Illustrates the Locations of Pore Pressure Monitoring Sensors (Gaus et al., 2014a) [1 m = 3.3 ft]

2 HE-E COMPONENTS AND MATERIALS

Task B1 of the **De**velopment of **Co**upled Models and Their **Val**idation Against **Ex**periments (DECOVALEX)-2015 project considered thermal-hydrological-mechanical (THM) responses of bentonite-based buffer materials and the near field to heating, primarily focusing on the buffer responses and the interaction of the engineered barrier systems with the Opalinus Clay (host rock). This chapter describes the set of components at a high level, describing key aspects and uncertainties. The actual properties used for modeling are described in Chapter 3.

This chapter provides a detailed description of the components of the HE-E test (i) Opalinus Clay; (ii) Buffer–granular bentonite, sand–bentonite mixtures and compacted bentonite blocks; (iii) heaters and accessory materials; and (iv) the cable channel.

The HE-E test, a 1:2 scale test based on the Nationale Genossenschaft für die Lagerung radioaktiver Abfälle (Nagra) design, was intended to provide the THM response of the buffer and Opalinus Clay (host rock) when subject to temperatures under 140 °C [284°F].
The geometry of the test allows reasonable interpretations in a cross section perpendicular to the microtunnel axis at the center of each heater, as long as the model represents the far-field geometry adequately. The actual experiment has a number of different components that affect interpretations away from the central cross section, because these components have significantly different properties.

As described previously in Section 1.1, the HE-E test contains two types of buffer separated by a plug (Figure 2-1). In Figure 2-1, the rearmost section is to the northwest, farthest from MI Niche. From back to front, the HE-E test section consists of (i) Plug 1, (ii) the Nagra (granular bentonite) section, (iii) Plug 2, (iv) the Gesellschaft für Anlagen- und Reaktorsicherheit (GRS) (sand/bentonite) section, (v) Plug 3, and (vi) the microtunnel section connected to MI Niche. Host rock surrounds the microtunnel.

2.1 Host Rock

The host rock material consists of the shaly facies of the Opalinus Clay along the entire HE-E test. The bedding plane dips from left to right in Figure 2-2, along the axis of the microtunnel. Bath et al. (2003, Table 6.1) calculate a dip angle of 42° in the reconnaissance tunnel at a location corresponding to the HE-E test, but Teodori and Gaus (2011) report a dip angle of 25° at the HE-E test. The shallower dips at the HE-E test may be due to local rotation of the shaly facies near the Main Fault, which passes through the microtunnel. The anisotropy ratio is not well established, but earlier work at the Mont Terri site suggested that both thermal and hydraulic conductivities are approximately twice as large in the bedding plane than perpendicular to the bedding plane.

Excavating the host rock creates an excavation damaged zone (EDZ). The effective depth to where the EDZ extends and its effects on the thermal and hydraulic conductivities are not well established, but the host rock may be affected to some extent tens to hundreds of centimeters into the rock. For example, Martin et al. (2004) estimated that the EDZ extends approximately one radius from the tunnel wall around the 3.6-m [11.8 ft]-diameter ED-B test tunnel at Mont Terri, which is the section of Gallery 98 parallel to the HE-E test northwest of Niche HE. Nussbaum et al., (2005) estimated that the EDZ after the Ventilation Test was 5 cm [2 in]. Some of the rock along the microtunnel wall spalled prior to the HE-E test, so the rock face is not smooth through the entire test section. The host rock is entirely saturated except for a zone

around the microtunnel. Based on pore pressures, at the start of the HE-E test the unsaturated zone likely extends less than a meter [<3.3 ft] into the host rock.

2.2 Buffer Materials

Three types of buffer materials are installed: (i) granular bentonite (Nagra section), (ii) a sand–bentonite mixture (GRS section), and (iii) compacted bentonite blocks (both sections, used only as a pedestal for the heater). The U.S. Nuclear Regulatory Commission (NRC)/Center for Nuclear Waste Regulatory Analyses (CNWRA®) DECOVALEX modeling effort focused on modeling the granular bentonite, which consists of dried granular bentonite ground to a size distribution similar to fine sand. Detailed measurements are available for the granular bentonite and sand–bentonite mixture, but less information is available for the bentonite blocks.

An auger system with a flexible spiral was designed and built for the emplacement of both buffer materials in the microtunnel (Teodori and Gaus, 2011). Using concrete and wooden tubes, the emplacement procedure was tested offsite to (i) ensure complete filling of the crown area and (ii) evaluate potential for segregation of fines and coarse particles, and (iii) estimate spatial variation in bulk density for the granular bentonite. Observations at the offsite test include:

- Some degree of grain segregation occurred by grain size, particularly at the outer and bottom areas.
- A small amount of fine grains at low density was found at the bottom part of the liner and the corresponding bentonite block foundation.
- Target dry densities were not attained at locations where significant grain segregation had occurred. Hence, the granular bentonite material was emplaced in five discrete layers rather than in a single step to achieve the target dry density of 1.45 g/cm^3.
- Sensor carriers (shown in Figure 1-4) were displaced (3–10 mm [0.1–0.4 in]) because of the granular bentonite overburden. Accordingly, sensor carriers for the HE-E test used horizontal stabilization to avoid displacement.

The granular bentonite to be emplaced in this experiment is the same as that used for the Engineering Studies and Demonstration of repository designs (ESDRED) project, mixture type E (sodium bentonite MX-80 from Wyoming) (Figure 2-3A).

The sand–bentonite mixture (Figure 2-3B), incorporated in the three-dimensional (3-D) model, was composed of 65 percent quartz sand and 35 percent sodium bentonite GELCLAY WH2 (granular material of the same composition as MX-80) (Teodori and Gaus, 2011). The thermal properties of the sand–bentonite mixture differ somewhat from the granular bentonite, somewhat affecting the power balance between the two heaters and the heat fluxes in the near field, but this is likely to be of secondary importance when interpreting the granular bentonite measurements.

The dimensions of the compacted bentonite blocks (shown in Figure 2-4) were determined so that (i) the axis of the liner was coincident with the axis of the microtunnel and (ii) the width of the cable channel below the blocks was sufficient to accommodate the instrumentation cables. The upper and lower blocks were joined together by moistening the contact surface between the blocks. The top of the blocks was machined to precisely match the heater liner outer radius.

During the early stages of construction of the Nagra section, some of the bentonite blocks were cracked or locally failed, and several pieces had spalled off before the buffer was emplaced (Figure 2-5). This event was attributed to the liner weight and transfer of water vapor from the high relative humidity (70 percent) tunnel air to the low initial water content (10 percent) blocks during a week of exposure to the tunnel air. Testing of the damaged blocks indicated that they had higher water contents, thus implying that the blocks absorbed water leading to local swelling and deformation. Construction continued with the original blocks and minor changes to the design of Plug 2 to support the liner. The sand–bentonite mixture was emplaced quickly after installing the bentonite blocks in the GRS section to prevent any exposure and potential damage to the blocks.

Interpreting the granular bentonite behavior during the HE-E test requires that the bentonite blocks are also well characterized, because the blocks significantly influence the thermal and moisture redistribution. Little information is available on pneumatic behavior of the compacted bentonite blocks used for the pedestal, although pneumatic redistribution in the compacted bentonite blocks is probably more restricted than in the open pore structures of the buffer materials (at least until rewetting occurs)..

2.3 Plug Materials

Three plugs are used to isolate the heater sections. All three plugs feature at least two layers of cement bricks joined using cement mortar, a rockwool thermal barrier, and a vapor barrier placed adjacent to the rockwool (Figures 2-6 and 2-7). The vapor barriers were made of two layers of aluminum foils, with a glass fiber mesh between the layers. The two end plugs also feature a poured concrete core. The heater liner penetrates Plugs 2 and 3, but is isolated from the plugs by a layer of rockwool. The vapor barrier is on both sides of the rockwool in Plug 2, and is on one side of the rockwool (the opposite side from the heater) in Plugs 1 and 3.

The documentation available for the DECOVALEX modeling specifies dimensions for the plug components but does not specify constitutive properties for the cement or cement bricks, leading to considerable uncertainty. Initial water content is also uncertain.

Rockwool and vapor barrier properties were estimated based on manufacturer's specification sheets. The vapor barrier simply blocks vapor and liquid transport, so its effects can be included simply by providing a layer that is impermeable to mass transfer. The rockwool layers may reduce heat transfer between the sections to some extent, but the other components of the plug are likely to be fairly efficient at promoting radial heat transfer relative to the buffer. The presence of a rockwool layer around the portion of the heater liner that extends through the plug may be most important because it allows air pressure to equilibrate between the heater sections and MI Niche.

Some modeling discretion is necessary when considering the hydraulic properties for rockwool. The rockwool achieves high thermal resistance in that it is mostly air. Water entering the rockwool, such as during rewetting from the host rock, would strongly alter the rockwool's thermal properties. The hydraulic properties of the rockwool strongly contrast with the host rock, thus rewetting may cause some convergence difficulty in simulations.

2.4 Heater and Accessory Materials

The heater structure consists of concentric sealed stainless steel cylinders, isolated by spacers, inside a stainless steel liner (Figures 1-3 and 2-8). The central cylinder is used to support two

heating elements that are coiled around it with the help of metal brackets. The outer cylinder seals and protects the ensemble (Figure 2-8C). The inner tube contains cables that pass through the heaters. The actual heating element is a layer of wire wrapped around one of the internal heater layers (Figure 2-8A). The design of the heater is intended to promote radiative heat transfer between the concentric layers as the dominant heat transfer mechanism, and conductive heat loss from the heater liner to the buffer and surrounding materials. The heaters were installed using a cable pulley system after construction of plugs, emplacement of buffer and bentonite blocks and installation of the liner was completed.

The heater liner consists of two sections, one for the Nagra section and one for the GRS section, isolated by a Teflon™ coupling inside Plug 2. The thermal properties of stainless steel and Teflon are readily available, and the dimensions are specified in the HE-E documentation.

Stainless steel has a much larger thermal conductivity than the buffer materials, and stainless steel had a large influence on the column test results. Accordingly, explicitly representing thermal redistribution in the steel components may significantly affect the simulation results.

The heating strategy was to achieve the maximum temperature at the liner gradually. The following steps were implemented independently for the Nagra and GRS sections:

1. Power-controlled heating {150–200 W} was applied for a few days to calibrate the temperature-control algorithm

2. Temperature-controlled heating was applied to linearly increase liner surface temperature (i) to 80–90 °C [176–194 °F] by approximately 3 months after the start of heating and (ii) to 140 °C [284 °F] by approximately 1 year after the start of heating

3. Temperature-controlled heating to maintain 140 °C [284 °F] at the heater liner.

2.5 Cable Channel

A U-shaped steel channel with UPE 300 cross section was used to create a railway above a poured concrete floor in the microtunnel (shown in Figure 2-7C). The steel channel was subsequently converted into a cable channel (also referred to as a cable box in some reference documents). The cable channel should not be confused with the inner tube for the heater (see Section 2.4), which also carries cables but was not modeled. The bentonite blocks were placed on a lid resting on the cable channel. Two ports were cut on each side of the cable channel within each test section to allow cables into the test sections. The cable channel was of particular interest, because of (i) the dominant effect of stainless steel on thermal conduction in the column test, and (ii) the cable ports, which would allow air pressure to equilibrate between the different test sections and MI Niche.

The steel channel dimensions are described in the HE-E documentation, and the thermal properties are readily available. Some uncertainty remains regarding the size of the cable ports, and it is unclear how to represent the interior of the channel. The lid is described as steel in the HE-E documentation, but the Task B1 leader described it as a Teflon plate. Lid thickness is not specified.

The top elevation of the concrete floor is available from the HE-E documentation, but not the properties.

2.6 Discussion

One of the goals of the NRC/CNWRA DECOVALEX modeling team is to understand how the buffers interact with the host rock and other engineered components. This is relevant to repository performance, because these interactions significantly impact the THM response of the buffer, resaturation rate and ultimately the barrier capability of the buffer. The teams associated with the HE-E experiment and prior studies investigated the properties of the host rock, granular bentonite, and sand–bentonite mixtures in detail, thus this information is fairly well determined with some remaining uncertainties regarding the influence of moisture content, density, and temperature. Properties of some manufactured components (i.e., dry rockwool, steel, Teflon) are also known, although the experiment does not prevent rockwool from becoming wetted, which would very substantially change its insulation properties.

The responses in the central portions of the heater sections are likely to be dominated by the buffer and host rock. Some residual uncertainties in the hydrothermal properties remain, especially with respect to the EDZ near the microtunnel and to bedding-plane anisotropy in the host rock. The EDZ is unlikely to substantially affect thermal transfer, which is dominated by conduction through the matrix, but may allow preferential liquid and gas transport through opened microfractures. Because of the different stress states at the top and side of the microtunnel walls, EDZ microfractures may preferentially open radially in some locations and circumferentially in others, implying that the EDZ may not have the same properties around the entire microtunnel circumference. The least resistance to cracking presumably occurs aligned with bedding planes, which may affect EDZ properties, as well. Host-rock anisotropy will make heat and mass transport occur preferentially in the bedding planes, which implies that heat and mass transfer will be larger on the sides of the microtunnel than on the top and bottom.

Some uncertainty remains regarding thermal contact between the heater liner and the surrounding buffer and bentonite pedestal. The bentonite pedestal was machined to precisely contact the liner, but exhibited swelling and spalling after partially equilibrating with the microtunnel humidity prior to backfilling and plugging. Accordingly, complete contact may not occur between the liner and block. It is difficult to assure complete contact between the buffer and the underside of the liner during backfilling, leading to a thermal resistance. The degree of contact worsens if the buffer contracts because of moisture loss during heating. The best contact is presumably maintained on the top of the liner, with the weight of the overlying buffer keeping the buffer pressed to the liner, but even in this case the grain contact with the liner is likely to be poorer than the contact between grains in the bulk media, which may impart some thermal resistance.

The influence of the plugs on overall hydrothermal response during the HE-E test is uncertain, because the concrete and concrete block properties are not described in the available documentation. Depending on the density and moisture content of these components, the blocks may have properties roughly comparable to the buffers or may be much more thermally and hydraulically conductive. In the latter case, the plugs represent preferential conduits for heat loss to the host rock, which may substantially reduce radial heat flow in the nearby buffer.

The bentonite-block pedestal and underlying cable channel both have somewhat uncertain properties, and temperature measurements suggest that the blocks are substantially cooler than the buffer at the same radius. Less information is available for the bentonite blocks than for the buffer materials. The pedestal is likely somewhat more thermally conductive than the buffers, as is the cable channel, so this combination will tend to alter the thermal response in the nearby buffer. The bentonite blocks also have larger initial moisture content than the buffers, and thus

act as a local moisture source. The thermal connection of the bentonite block to the cable channel strongly depends on the lid, but the lid thickness is not provided and it is uncertain whether the lid is steel or Teflon, which have distinctly different thermal conductivities.

The concrete floor has the same uncertain range of properties as the poured concrete in Plugs 1 and 3. Because the floor is relatively thin, assuming that the concrete floor has the same properties as the intact host rock should not strongly affect model results, as long as the concrete does not actually form a substantial barrier to radial flow.

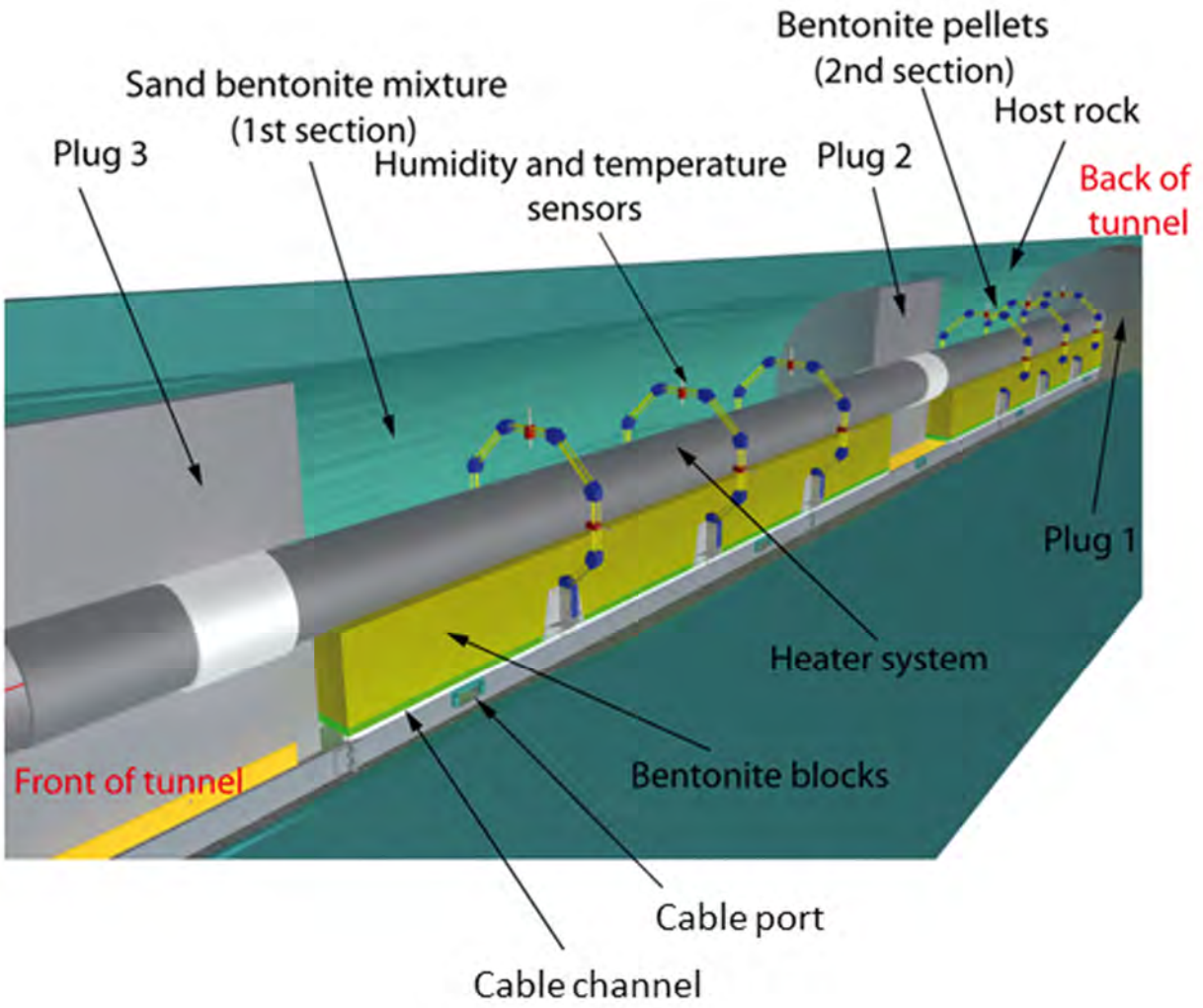

Figure 2-1. Schematic of the HE-E Experiment (Modified From Teodori and Gaus, 2011, Their Figure 2.3)

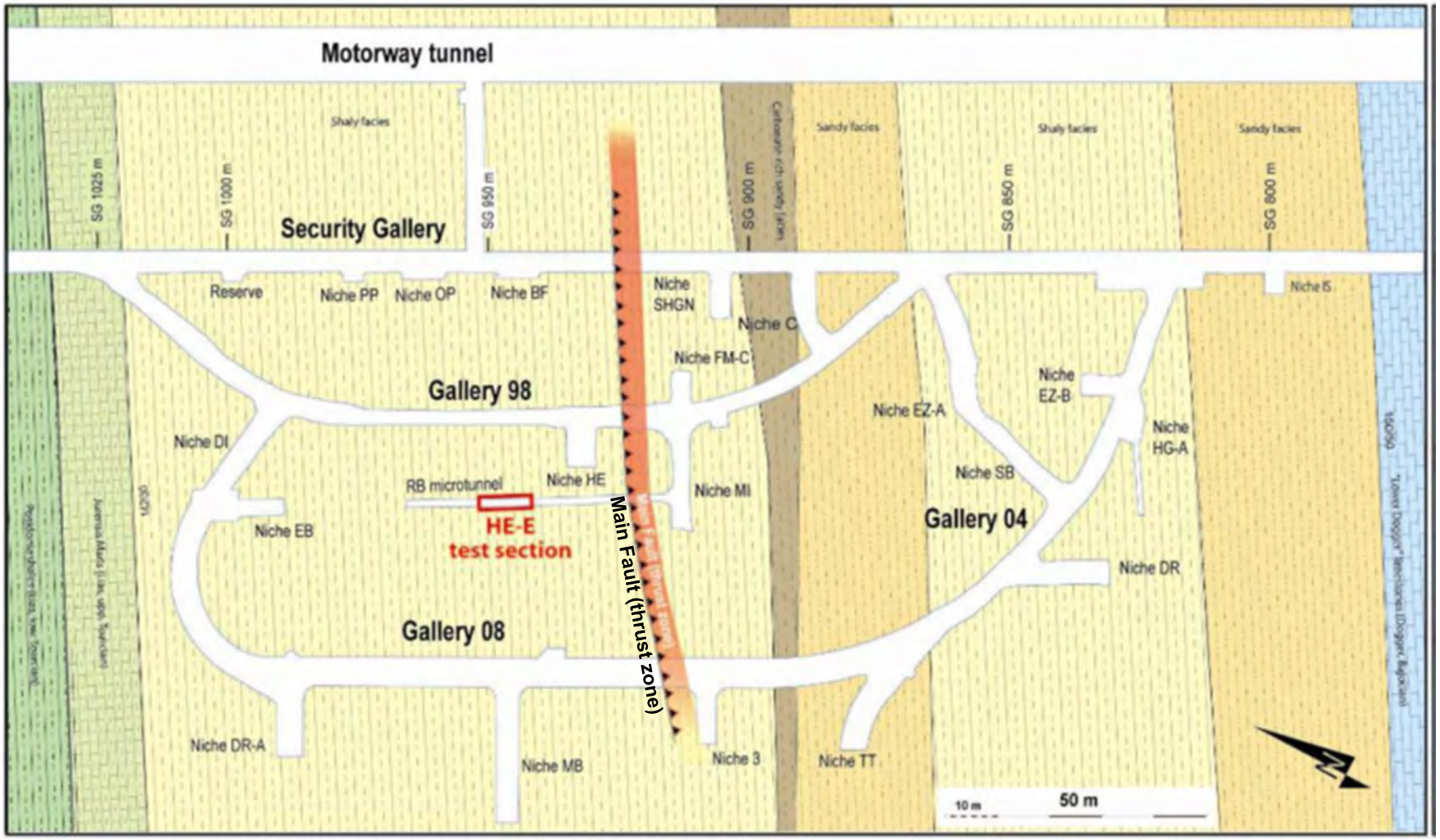

Figure 2-2. Location of the HE-E Test Section (Red). Figure Reproduced From Marschall et al. (2004, their Figure 2.1). [1 m = 3.3 ft]

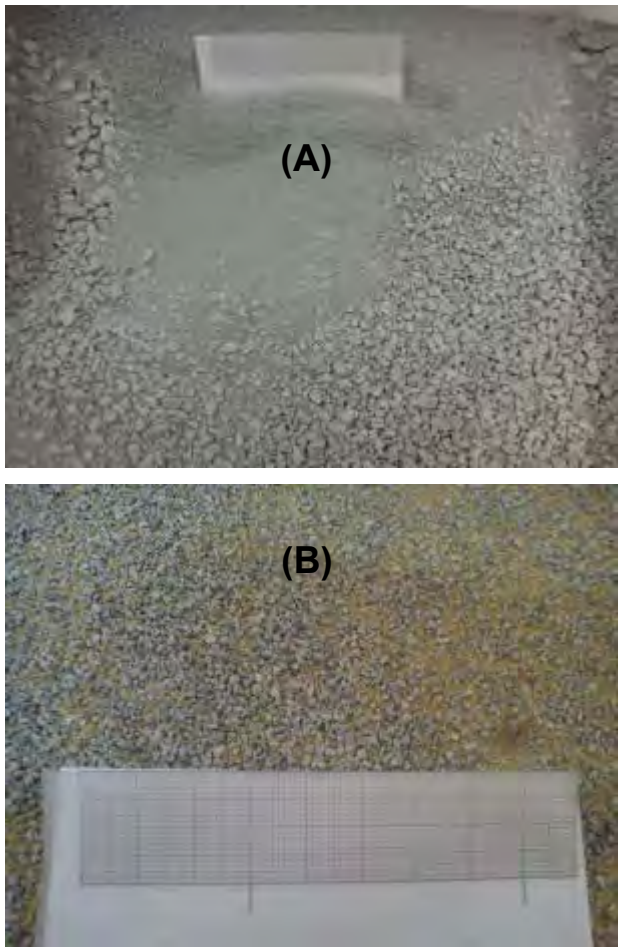

Figure 2-3. Photographs of the (A) Granular Bentonite and (B) Sand–Bentonite Mixture Used in the HE-E Experiment (Villar et al., 2012)

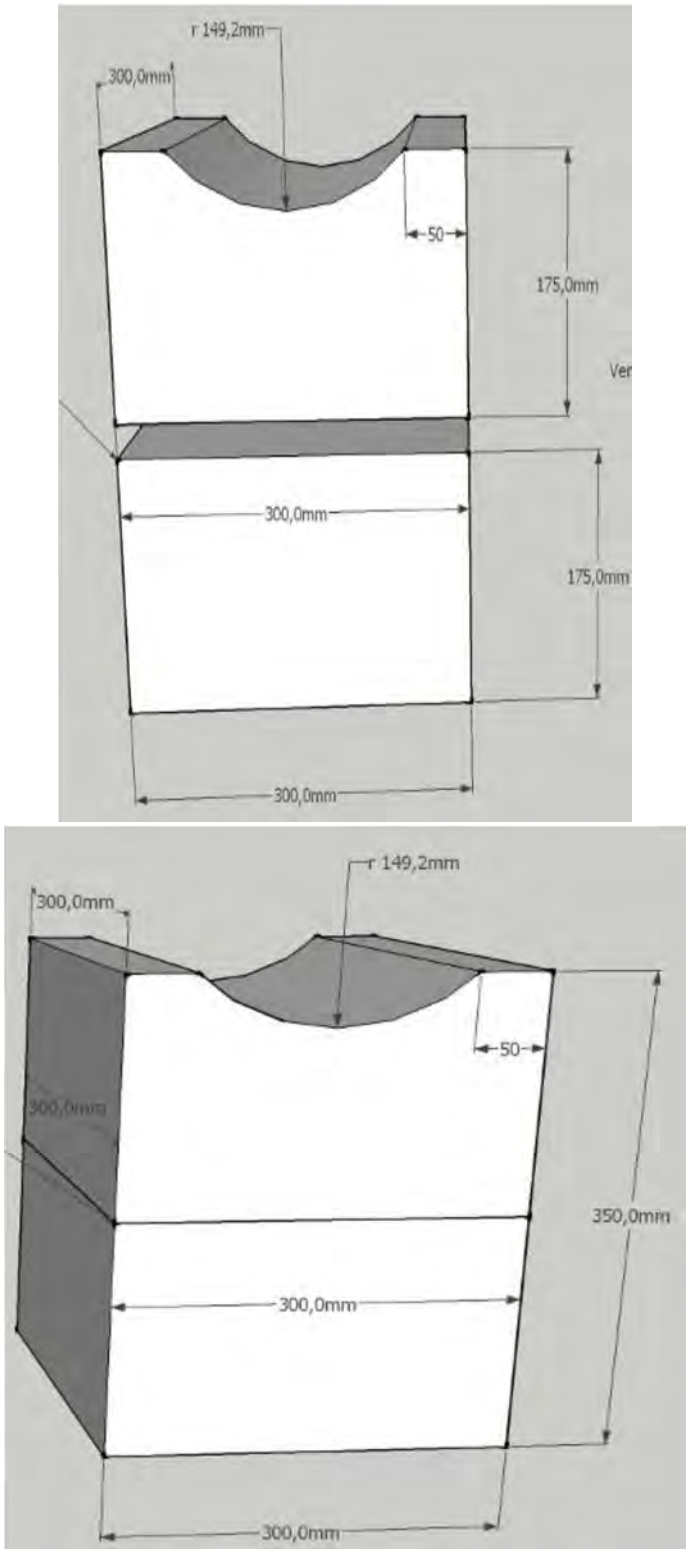

Figure 2-4. Details of the Bentonite Blocks Used in the HE-E Experiment (Teodori and Gaus, 2011) [1 mm = 0.039 in]

Figure 2-5. Damage to Some of the Bentonite Blocks During the Initial Stages of Construction of the Nagra Section (Teodori and Gaus, 2011)

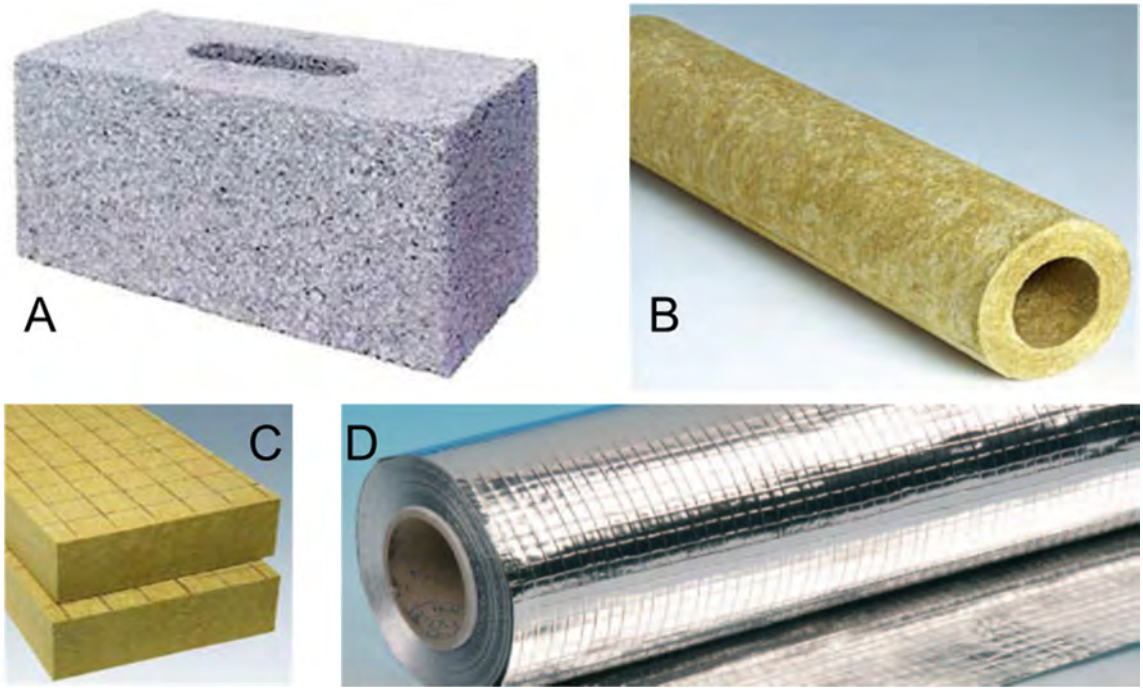

Figure 2-6. Components of Plugs for the HE-E Test: (A) Cement Brick, (B) Rockwool in Cylinder Form, (C) Rockwool in Panel Form, and (D) Vapor Barrier (Teodori and Gaus, 2011)

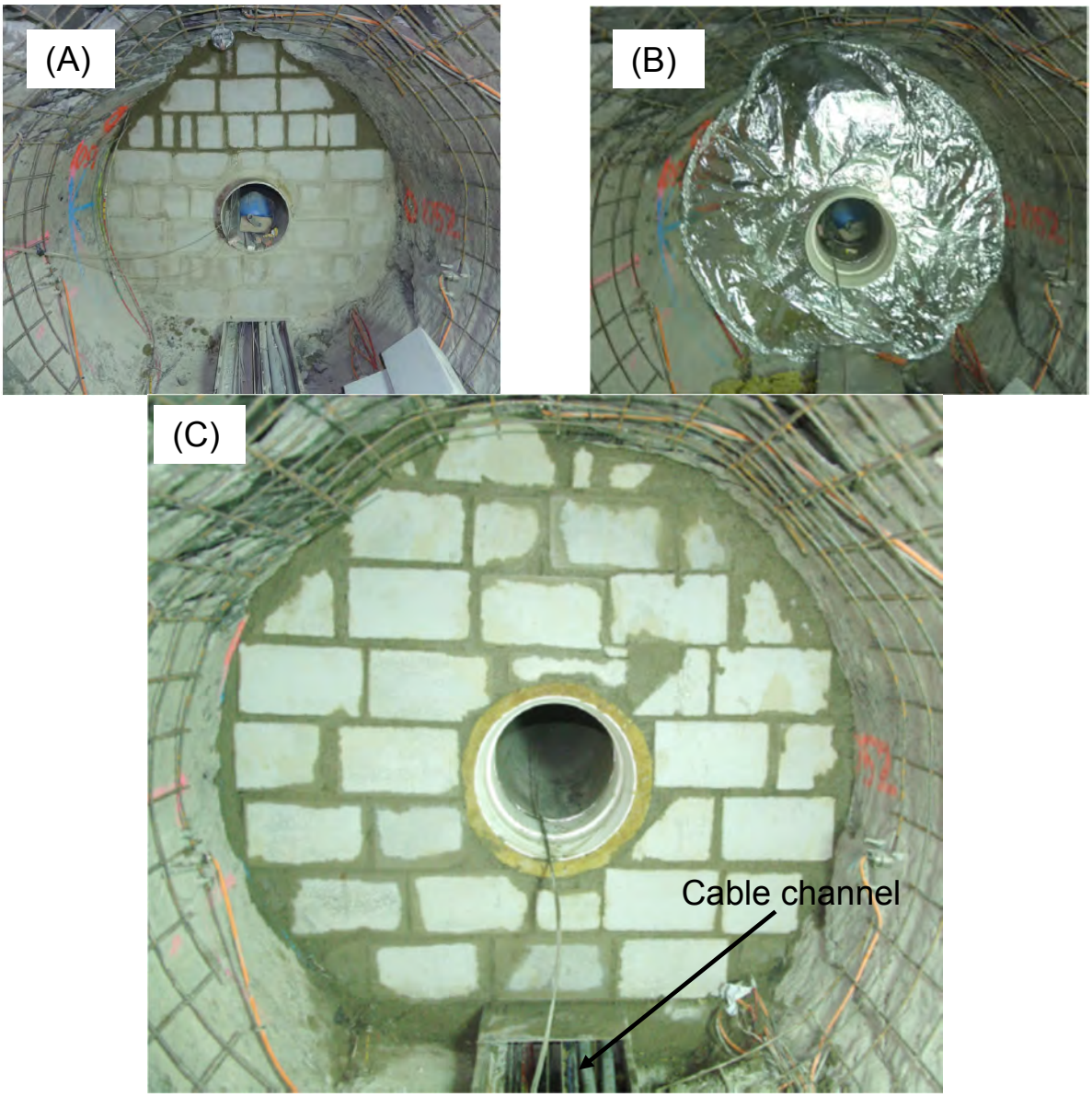

Figure 2-7. Photographs Illustrating Stages in Construction of Plug 2: (A) Construction of the First Wall; (B) Construction of the Isolation System and Vapor Barrier; (C) Construction of the Second Wall (Teodori and Gaus, 2011)

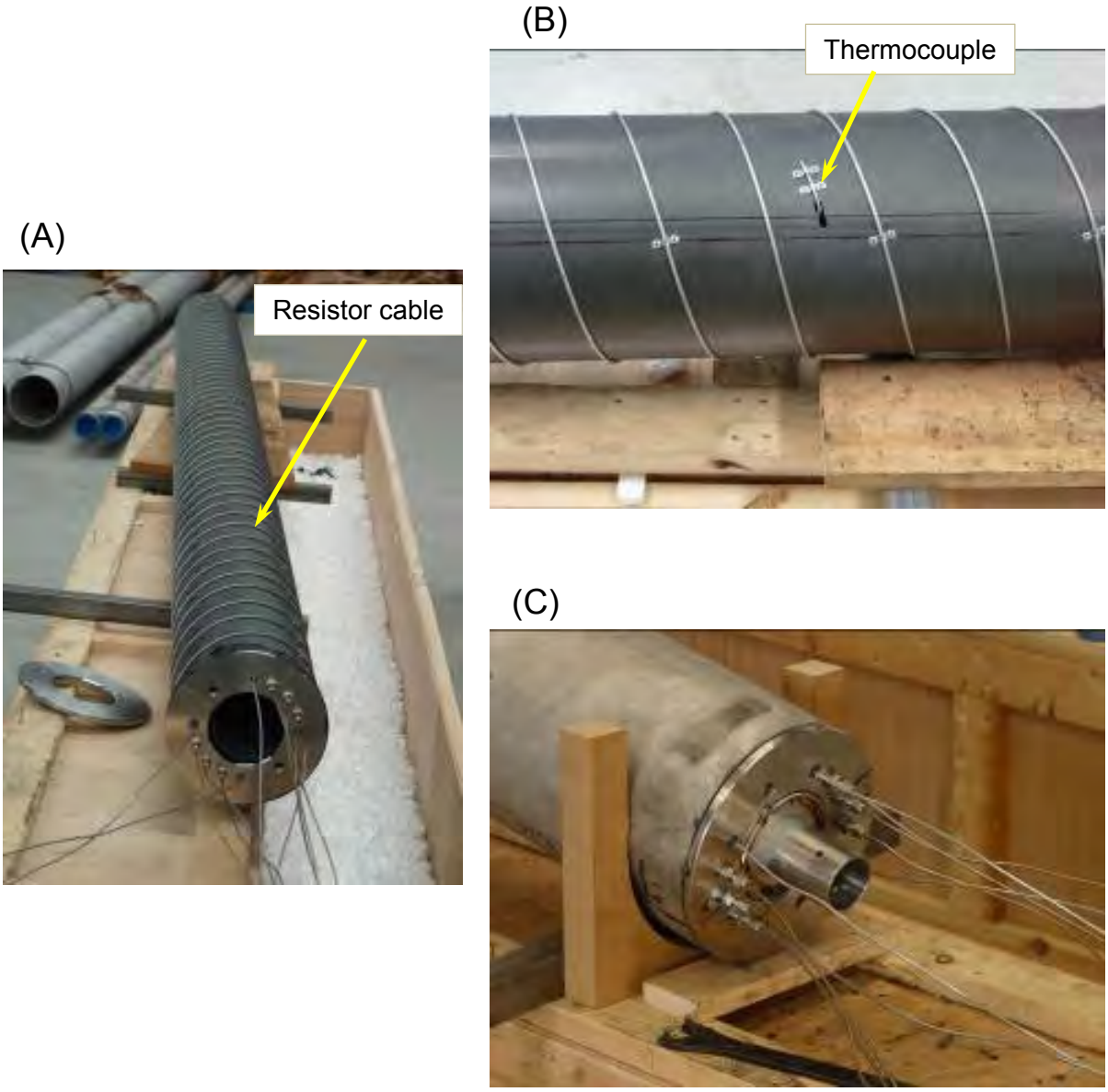

Figure 2-8. Photographs of the Components of the Heater System Used in the HE-E Experiment: (A) Central Heater Tube With Spiral-Wrapped Resistor Cables; (B) Internal Thermocouple on the Central Heater Tube; (C) Central Heater Tube Being Inserted Into the Outer Cylinder (Teodori and Gaus, 2011)

3 INPUT PARAMETERS FOR THE HE-E TEST

3.1 Thermal-Hydrologic Analysis (xFlo) Model

The xFlo model (Painter, 2006) is an integrated finite volume model developed by the U.S. Nuclear Regulatory Commission (NRC) and the Center for Nuclear Waste Regulatory Analyses (CNWRA®) that uses a computational framework similar to the well-known TOUGH (i.e., Transport of Unsaturated Groundwater and Heat) model family (Pruess et al., 2012). The xFlo model was developed in the mid-2000s with the intention of it eventually replacing the existing coupled-process MULTIFLO simulator (Painter, 2006). MULTIFLO (Painter and Seth, 2003) consists of two codes (METRA and GEM) that can be run as stand-alone thermohydrology and reactive transport codes or coupled using the MULTIFLO driver program. xFlo currently implements most of the METRA functionality. xFlo considers mass balance of two phases (liquid and gas) and two components (water and air), as well as energy balance. Equilibrium and saturation constraint equations are employed to reduce the equation set to three fully coupled equations for (i) total mass, (ii) gas mass, and (iii) energy.

xFlo models water and air mass balances that are fully coupled with an energy balance, and air and water are assumed present in both the liquid and gas phases. Porosity, permeability, and the vapor diffusion coefficient were each set to zero in solid components (e.g., steel) to eliminate mass transport, with the result that thermal conduction is the only process considered.

3.1.1 Input Parameters

The input parameters for bulk Opalinus Clay and granular bentonite were based on previous work related to the HE-D test (Ofoegbu et al., 2015a) and laboratory column test (Stothoff et al., 2015a) respectively. The input parameters used in xFlo for the engineered barrier systems (EBS) and Opalinus Clay are provided in Table 3-1. Anisotropy was imposed by scaling the separation distance between grid cells according to the square root of the anisotropy ratio. This procedure scales permeability, thermal conductivity, and diffusion coefficients by the same ratio. The calibrated simulation uses an anisotropy ratio of two (preferential diffusion in the horizontal direction). Note that the bedding dips in the axial direction, so the physical anisotropy perpendicular and parallel to the bedding plane slightly differs from the anisotropy in the perpendicular cross section.

3.1.1.1 Thermal Conductivity

The values of thermal conductivity were based on available laboratory and literature data. The effective thermal conductivity (k_{eff}) is calculated as function of the wet and dry thermal conductivities (k_{wet} and k_{dry}) and liquid saturation (S_l) using the function (Stothoff et al., 2015b)

$$k_{eff} = k_{dry} + (k_{wet} - k_{dry})S_l^p \quad \text{Eq. 3-1}$$

where p is an interpolation parameter, where $p \approx 0.9 + 1.5\phi$ and ϕ is porosity. The values of p for the materials are listed in Table 3-1. The relationship between saturation and thermal conductivity used in the numerical model for granular bentonite and Opalinus Clay is shown in Figure 3-1. Figure 3-2 shows the relationship between moisture content (estimated from saturation) and thermal conductivity for bentonite blocks used in xFlo. The uncalibrated thermal conductivity model was retained in the calibrated parameter set.

Granular Bentonite: The thermal conductivity of the bentonite medium was measured by Villar et al. (2012) as 0.12 W/m·K under as-received conditions (saturation of 0.22). Preliminary tests by Wieczorek et al. (2011) measured thermal conductivity values in the range of 0.34 to 0.45 W/m·K for the granular bentonite at a higher density range of 1.6 to 1.7 g/cc compared to the density of 1.5 g/cc used in the column test, with an as-delivered thermal conductivity of 0.45 W/m·K.

Bentonite Blocks and Opalinus Clay: The wet and dry thermal conductivity values of bentonite blocks and the Opalinus Clay properties were based on information in Wieczorek et al. (2011) and Gaus et al., (2014a) and were fit using a relationship by Stothoff et al. (2015b, Equation 1).

The measured temperatures in the bentonite blocks were consistently approximately 10 °C [18 °F] cooler than the temperatures in the granular bentonite, and there is a steeper drop in temperature adjacent to the liner, possibly due to deteriorated contact between the bentonite blocks and the liner. The thermal contact area was adjusted over a range to explore this hypothesis. For the calibrated run, reducing the thermal contact area between the liner and blocks to 20 percent of the physical area provided better agreement between measured and modeled temperatures, but the temperature profiles still are not in good agreement. Some other unaccounted for factor is likely affecting the temperature profiles.

3.1.1.2 Water Retention and Relative Permeability

Granular Bentonite: The moisture retention properties are based on measured values (Rizzi et al., 2012) (Figure 3-3). The measured data with saturations more than 1 could be attributed to not accounting for the change in porosity in the calculations. The van Genuchten model (1980) is used assuming that the temperature is unchanged from the reference temperature at which the retention relationship was determined. The retention relationship describing capillary pressure is assumed to be derived at a reference temperature of 20 °C [68 °F]; capillary pressure is scaled by the ratio of temperature-dependent surface tension to surface tension at the reference temperature. Capillary pressure is subsequently adjusted based on the ratio of surface tensions under actual and reference temperatures. Analyses of the Column Test model (Manepally et al., 2015) indicated that vapor transport in bentonite was sensitive to this temperature-dependent adjustment under the moisture and temperature conditions of the experiment. In xFlo, relative permeability in the liquid phase is related to saturation by combining van Genuchten's relation with Mualem's (1976) model (Painter, 2006).

The moisture retention parameters for the bentonite blocks and Opalinus Clay were based on information in HE-E final report (Gaus et al., 2014a).

3.1.1.3 Permeability

The permeability values were based on values available in the literature for all the materials (Gaus et al., 2014a). The host rock was assumed to be homogeneous but anisotropic, except for locally increased permeability in the excavation damage zone (EDZ) near the microtunnel wall. The permeability in the EDZ is assumed to decrease exponentially in the radial direction. Accounting for the EDZ, the host rock permeability is multiplied by a scale factor K_m in the form

$$K_m = 1 + (\lambda - 1)\exp[-\beta(r - R_T)] \qquad \text{Eq. 3-2}$$

where β is a decay factor, λ is a permeability multiplier, r is radial distance, and R_T is the microtunnel radius. The calibrated simulation uses $\beta = 1/R_T$ and $\lambda = 5$.

3.1.1.4 Gas Permeability

The pore size distribution for the granular bentonite buffer medium is quite different at the initial low water content than when fully saturated. The grain size distribution of the granules is similar to fine sand. The medium is multimodal at low water content, with one mode consisting of the pore space around the granules and others for the pores within the granules, and the water is sequestered inside the small pores inside the granules. As the water content increases, the granules preferentially take in the additional water and become larger, shrinking the pores outside the granules. At full saturation, the granules merge into a single mass and the original pores outside the granules become negligibly small as the bentonite platelets in the granules reorient during wetting.

Because the large pores are much larger under dry conditions, the permeability under unsaturated conditions is much larger than the permeability under saturated conditions. This rearrangement of pore space has profound implications for gas movement, which occurs in the unsaturated (largest) pores. The Klinkenberg functional model provides a way to adjust the gas permeability independent of the liquid permeability to approximately account for the change in pore size distribution. This use is not a common practice, instead is simply a convenience unrelated to the physical system of gas slippage in low permeability media for which the Klinkenberg model was developed (Stothoff et al., 2015a; Rutqvist et al., 2013). A Klinkenberg parameter ten orders of magnitude larger than atmospheric pressure will increase gas conductivity by ten orders of magnitude.

The Klinkenberg functional model assumes that the pore size distribution is fixed. Additional work is needed to derive a functional model that accounts for the changing pore size distribution with water content, and the new functional model would supersede this usage of the Klinkenberg model.

3.1.1.5 Water Properties

Water properties are described by the National Institute of Standards and Technology Steam Table (e.g., http://webbook.nist.gov/chemistry/fluid/). The gas phase is governed by the ideal gas law. Dissolved air is in equilibrium with the gas phase through Henry's Law. Water vapor is in equilibrium with the liquid phase, considering temperature- and capillary-pressure-dependent vapor pressure lowering using the Kelvin equation.

3.1.1.6 Additional Inputs to the 3-D Model

As described in Section 3.1.1.3, the three-dimensional (3-D) model included the sand–bentonite (GRS) section and Plugs 1 and 3. The additional inputs for the 3-D model are listed in Table 3-2.

Rockwool and vapor barrier properties were estimated based on the manufacturer's specification sheets. The vapor barrier, which blocks vapor and liquid transport, was represented in the xFlo model as a material that is impermeable to mass transfer, but allows heat transfer.

3.1.2 Boundary and Initial Conditions

The initial pressure and temperature were set to 1.7 MPa [247 psi] and 15.5 °C [60 °C], respectively, and these were retained for the far-field boundary condition for both the

two-dimensional (2-D) and 3-D models. These values are generally consistent with (i) measured values and (ii) assumptions made for models described in Gaus et al. (2014a). The heater was represented in one of two ways during different simulations: (i) a transient heat flux uniformly applied to the liner interior and (ii) a transient temperature uniformly applied to the liner. The transient heater conditions were derived from data provided by the Task B1 leader.

3.1.3 Sources and Sinks

Gallery 98 (see Figure 2-2) is included in the 2-D model by linking three grid cells to the ambient pressure and temperature. The cable channel below the bentonite block pedestal (see Figures 2-1 and 2-7) contains ports egressing to the buffer; the air cell adjacent to the port included in the 2-D model is linked to ambient pressure and temperature, allowing air to exit in the axial direction within the cable channel. In addition, a thermal sink is incorporated in the EBS by connecting the steel in the channel to the ambient temperature, conceptually at a distance of 10 m [33 ft].

3.2 Mechanical Analysis (FLAC) Model

Mechanical analysis was performed with FLAC using the temperature, liquid saturation, and gas pressure output from the thermal-hydrologic (TH) xFlo model as input to calculate the mechanical response in terms of deformation (porosity change) and stress change. Mechanical behavior of the granular bentonite, sand–bentonite mix, and bentonite blocks was represented using the MCUS (modified CAM-clay model for unsaturated soils) constitutive model (Ofoegbu et al., 2013). In the MCUS model, suction contribution to soil stress is evaluated using the Bishop principle of effective stress, with the Bishop parameter evaluated using the water retention curve that was used for the xFlo model (discussed in Section 3.1.1.2). The model incorporates the effects of suction and compaction on mechanical properties, and uses stress-strain relationships based on conventional elasto-plasticity. Mechanical behavior of a material in the MCUS model is controlled by three functions derived from the moisture retention curve: suction pressure (suction contribution to effective pressure) versus suction, bulk modulus versus suction, and preconsolidation pressure versus suction. The suction pressure versus suction and bulk modulus versus suction functions for the granular bentonite, sand–bentonite mixture, and bentonite blocks are described in Figures 3-4 and 3-5. The preconsolidation pressure function is not shown because the mechanical state remained elastic throughout the modeling period so the yield strength (controlled by the preconsolidation pressure) had no direct effect on the mechanical response. Mechanical behavior of the host rock, Opalinus Clay, was modeled as linear-elastic.

Swelling and shrinkage (therefore, swelling pressure) of the granular bentonite, sand–bentonite mixture, and bentonite blocks are incorporated in the mechanical model using the procedure described in Ofoegbu et al. (2013). The granular bentonite and bentonite blocks were assigned unit swelling (or shrinkage) potential (α_{CW}) determined based on analysis of the column test and vary with moisture content (Figure 3-6). The sand–bentonite mixture was assigned unit swelling potential based on laboratory data described in Ofoegbu et al. (2013, Figure 12).

3.2.1 Geometrical Model

The model domain (Figure 3-7) consists of a vertical slice through the heated tunnel and surrounding rock, terminated on a circular boundary concentric with the tunnel and at a distance of 200 m [656 ft] from the tunnel axis. A vertical symmetry plane normal to the tunnel axis was used to cut the model to half size as shown in Figure 3-7. The model is in the granular

bentonite section as shown in the geometrical model with material details plot (Figure 3-8). The sand–bentonite section was not modeled. As shown in Figure 3-8, the materials represented in the model are granular bentonite (main buffer material), bentonite blocks (support buffer material), cable box with hollow interior, concrete invert, and host rock and EDZ. The host rock and EDZ were represented as the same material in the mechanical model but as different materials in the TH model. Representing the EDZ in the mechanical model is not necessary because structural stability of the opening is not challenged under the test conditions. In contrast, the relatively large permeability of the fracture system in the EDZ may strongly impact the hydraulic response, which affects the thermal response, and was represented in the xFlo simulations (Section 3.1.1.3). The heater was not included explicitly in the mechanical model but was represented in terms of temperature histories received from the TH model. However, a steel liner was included in the model to represent the mechanical boundary between the heater and buffer materials.

3.2.2 Boundary and Initial Conditions and Calculation Sequence

Boundary conditions consist of zero displacement normal to the boundary, explicitly at the circular boundary surface and by implication on the line of symmetry (vertical line at left model boundary in Figure 3-7).

The mechanical model consists of three stages. In the first stage, the entire model domain (Figure 3-7) consists of the host rock. The model was subjected to an initial stress of 6.5 MPa [940 psi] vertical, 2.2 MPa [320 psi] horizontal and in-plane, and 4.3 MPa [620 psi] horizontal and out-of-plane (along tunnel axis). The model was brought to static equilibrium with the initial stress and boundary conditions. In the second stage, the tunnel-section zones were deactivated to simulate tunnel excavation and static equilibrium was re-established for this condition. The third stage consisted first of re-activation of the tunnel-section zones with material properties consistent with the material types described in Figure 3-8 and initial stress of 0.1 MPa [14.5 psi] in the three principal directions. The small initial stress of 0.1 MPa [14.5 psi] was applied to avoid numerical problems that could result from initiating the buffer in a stress-free state. However, an all-round stress of 0.1 MPa [14.5 psi] is too small to contribute to the calculated buffer response. Then temperature, liquid-saturation, and air pressure (pore-water pressure in host rock zones) corresponding to the start of heating in the TH model were read in to define the initial TH state for mechanical analysis. Subsequently, the TH variables were read in again at several time steps (as described in Section 1.2) and the corresponding changes in mechanical state were calculated.

3.2.3 Input Parameters

The input parameters for mechanical analysis are described in Table 3-3. These parameters are described in detail in Ofoegbu et al. (2015b).

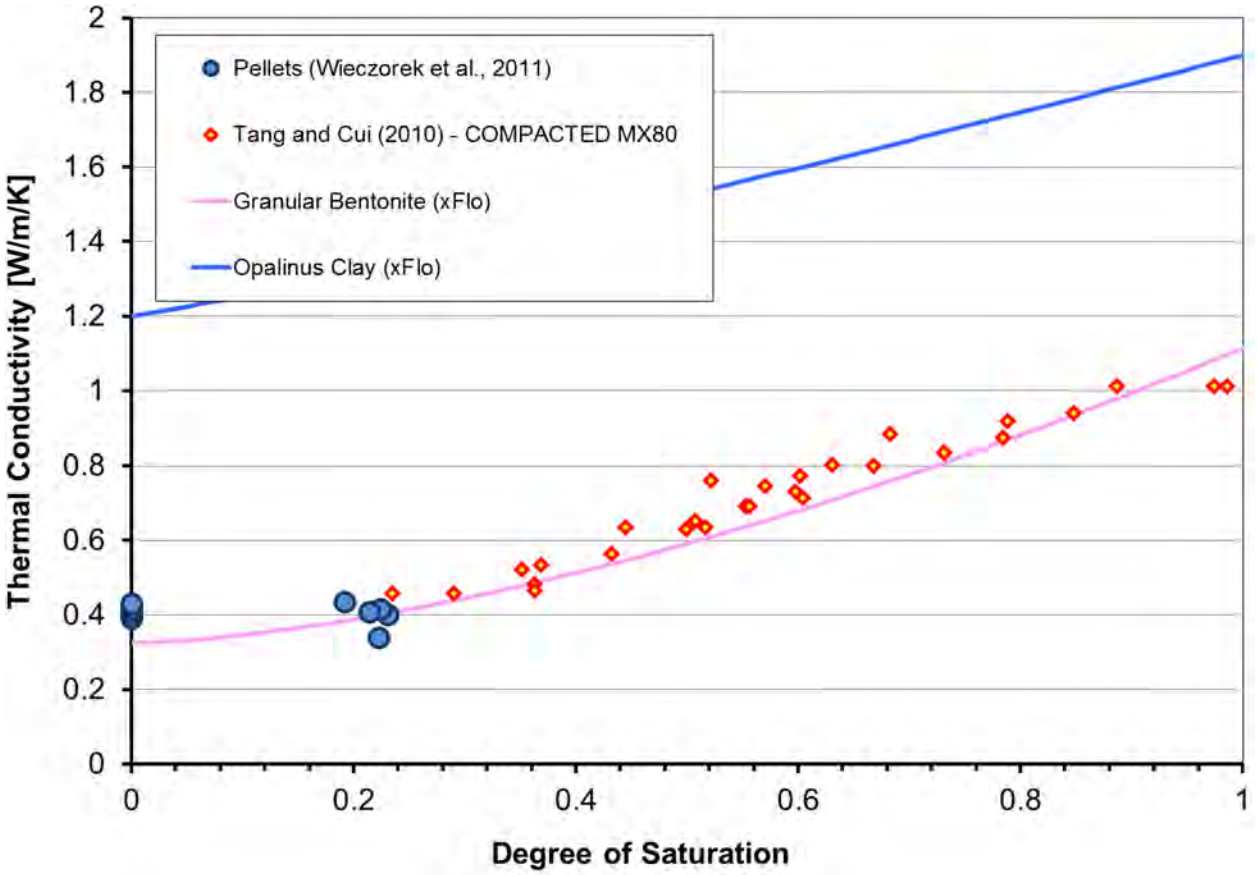

Figure 3-1. Thermal Conductivity–Saturation Relationship Used in xFlo for Granular Bentonite and Opalinus Clay. Experimental Data for Granular Bentonite are Also Included.

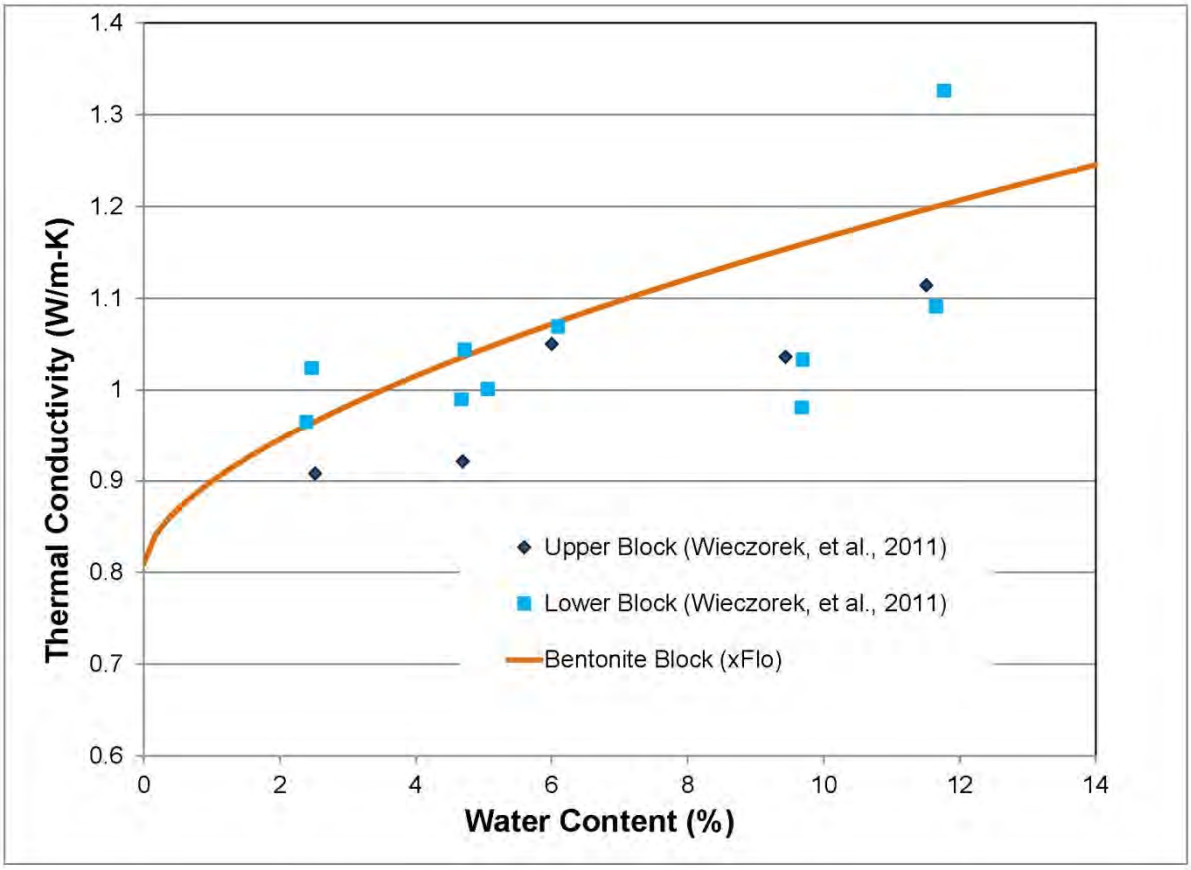

Figure 3-2. Thermal Conductivity–Water Content Relationship Used in xFlo for Bentonite Block. Experimental Data for Bentonite Block are Also Shown.

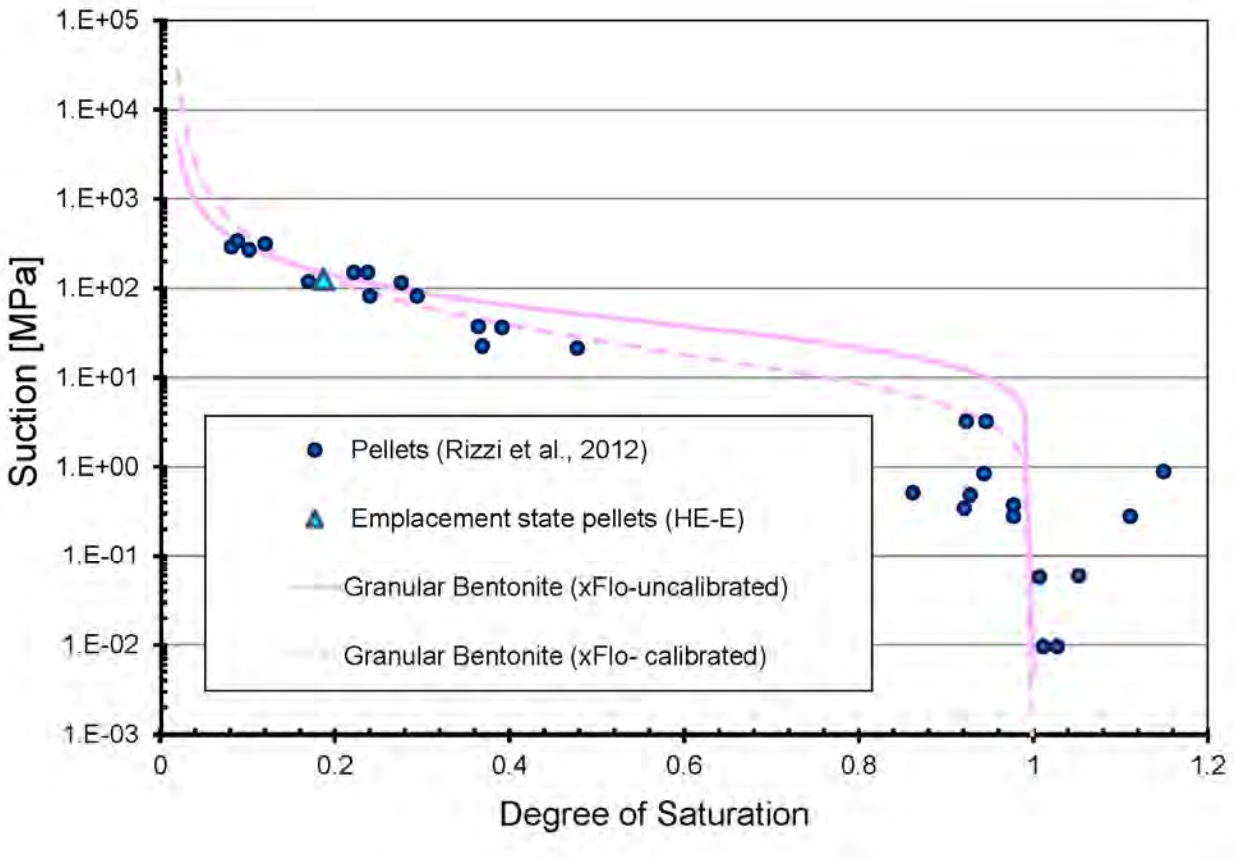

Figure 3-3. Moisture Retention Relationship Used in xFlo for Granular Bentonite. Experimental Data for Granular Bentonite are Also Shown. [1MPa = 145 psi]

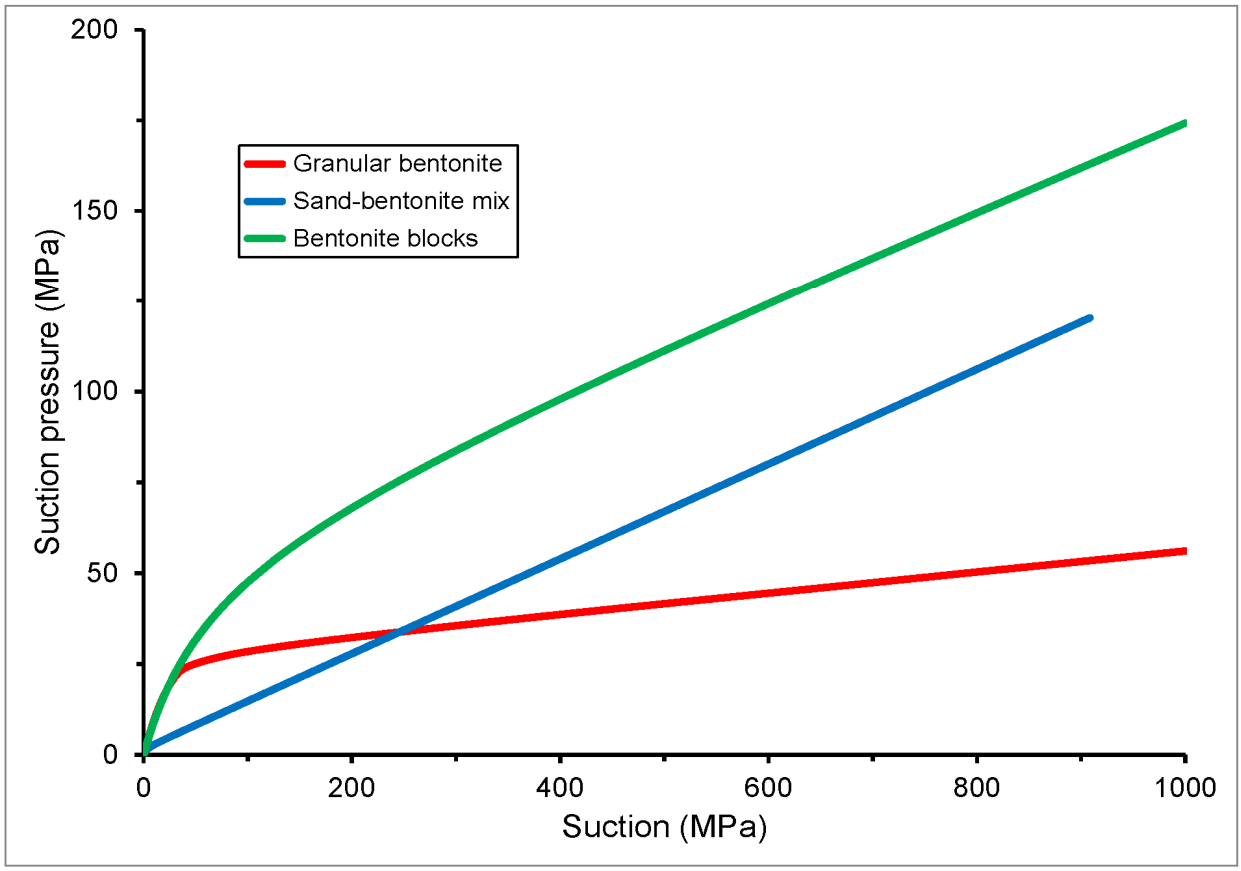

Figure 3-4. Suction Pressure Versus Suction Relationships for Granular Bentonite, Sand–Bentonite, and Bentonite Blocks (Source: Ofoegbu et al., 2015) [1MPa = 145 psi]

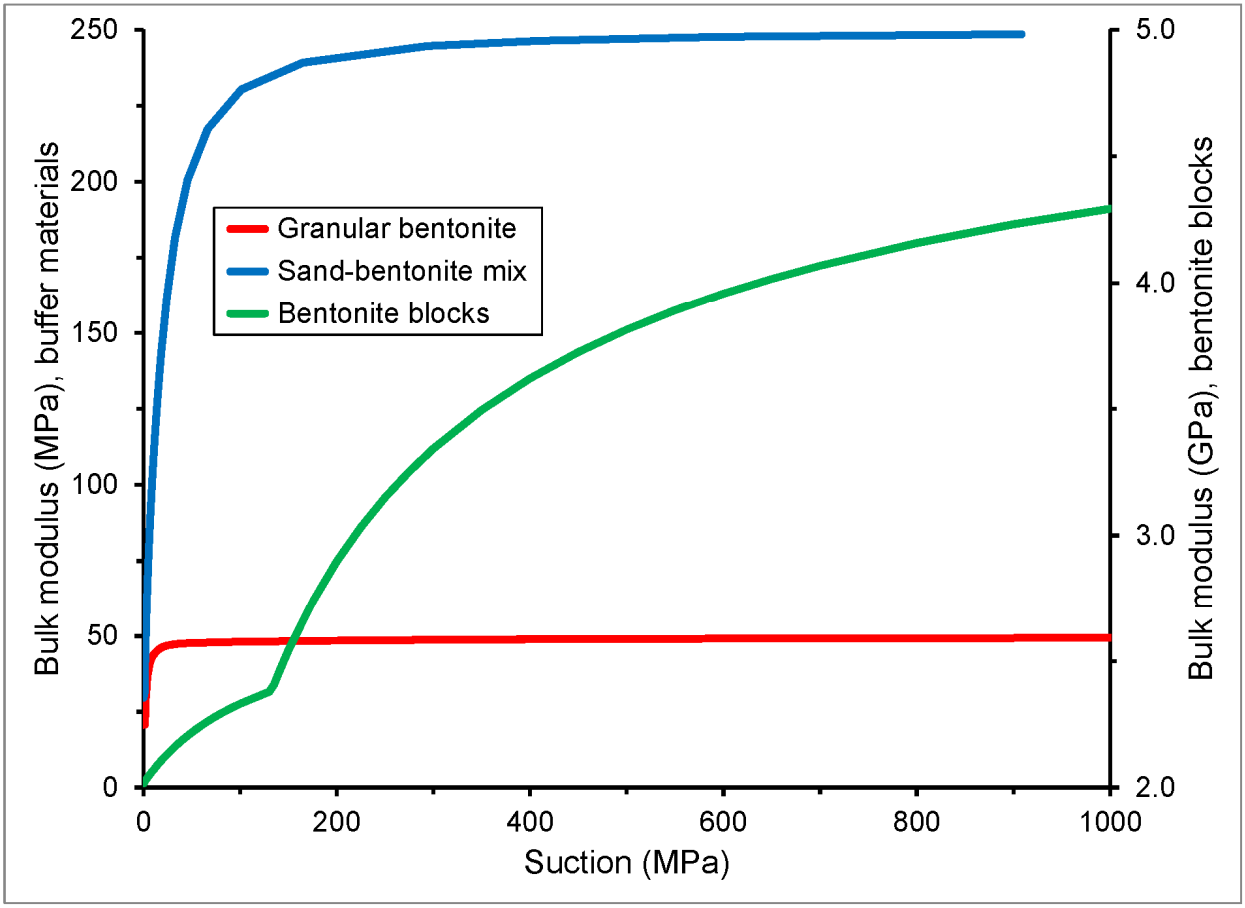

Figure 3-5. Bulk Modulus Versus Suction Relationships for Granular Bentonite (Left Axis), Sand–Bentonite (Left Axis), and Bentonite Blocks (Right Axis) (Source: Ofoegbu et al., 2015) [1MPa = 145 psi; 1GPa = 145037.7psi]

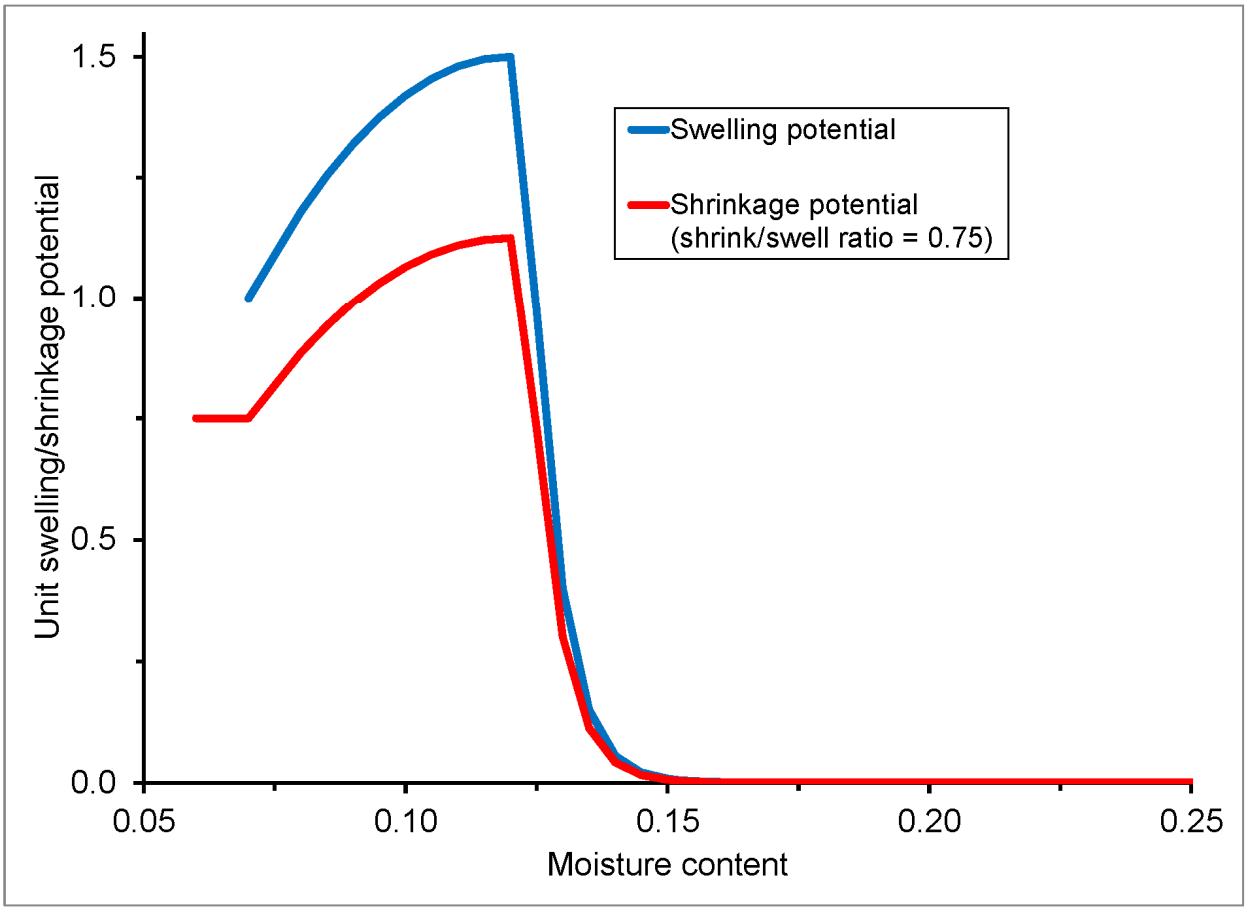

Figure 3-6. Unit Swelling/Shrinkage Potential (α_{CW}) Versus Gravimetric Moisture Content Relationships for the Granular Bentonite and Bentonite Blocks (Source: Ofoegbu et al., 2015)

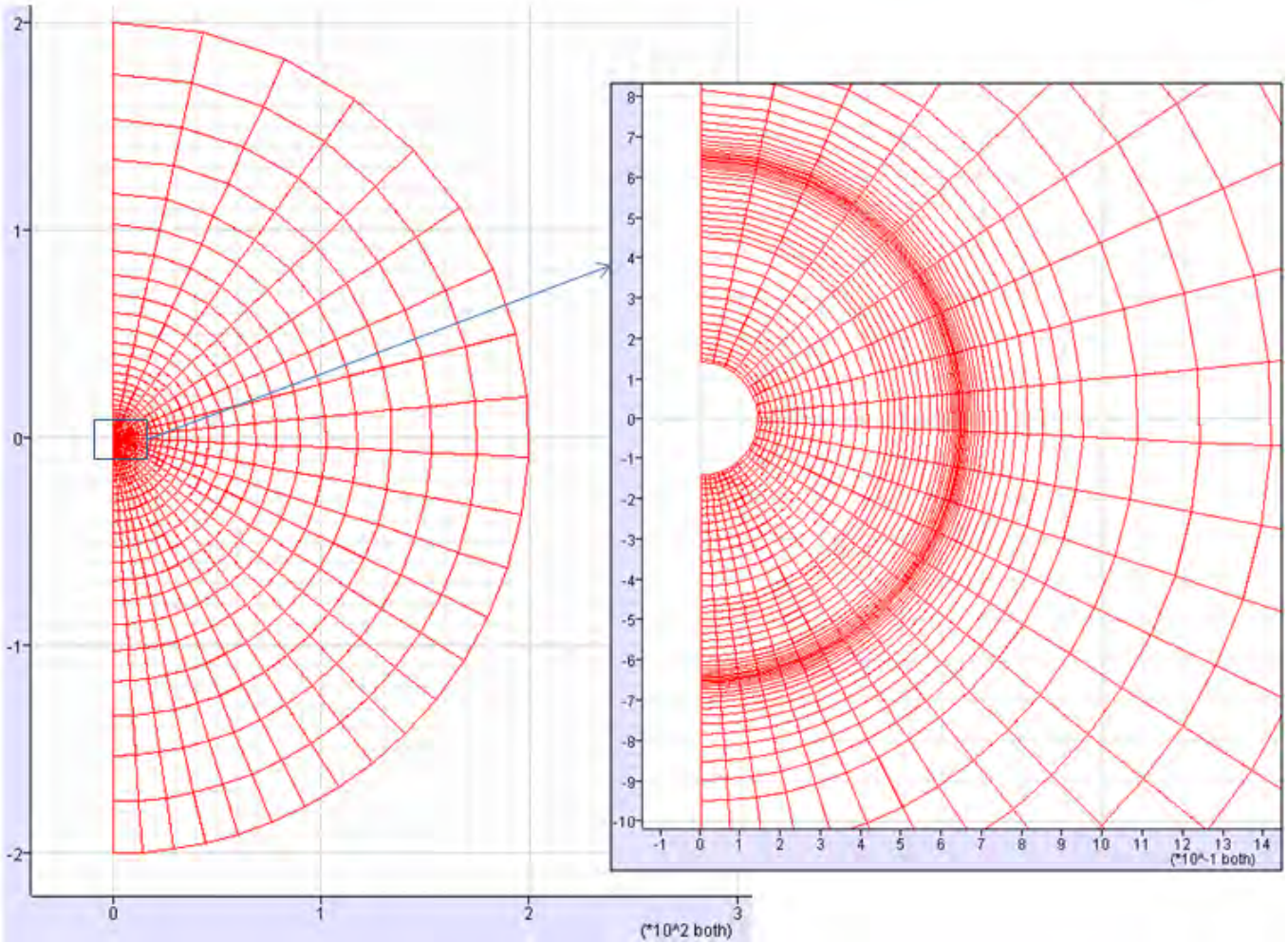

Figure 3-7. Model Geometry Showing the Finite-Difference Mesh for the Model Domain Used for the FLAC Mechanical Analysis (Same as Was Used for the xFlo TH Analysis). "*10^2 both" Means "Multiply Every Axis Value by 100" [1 m = 3.3 ft]

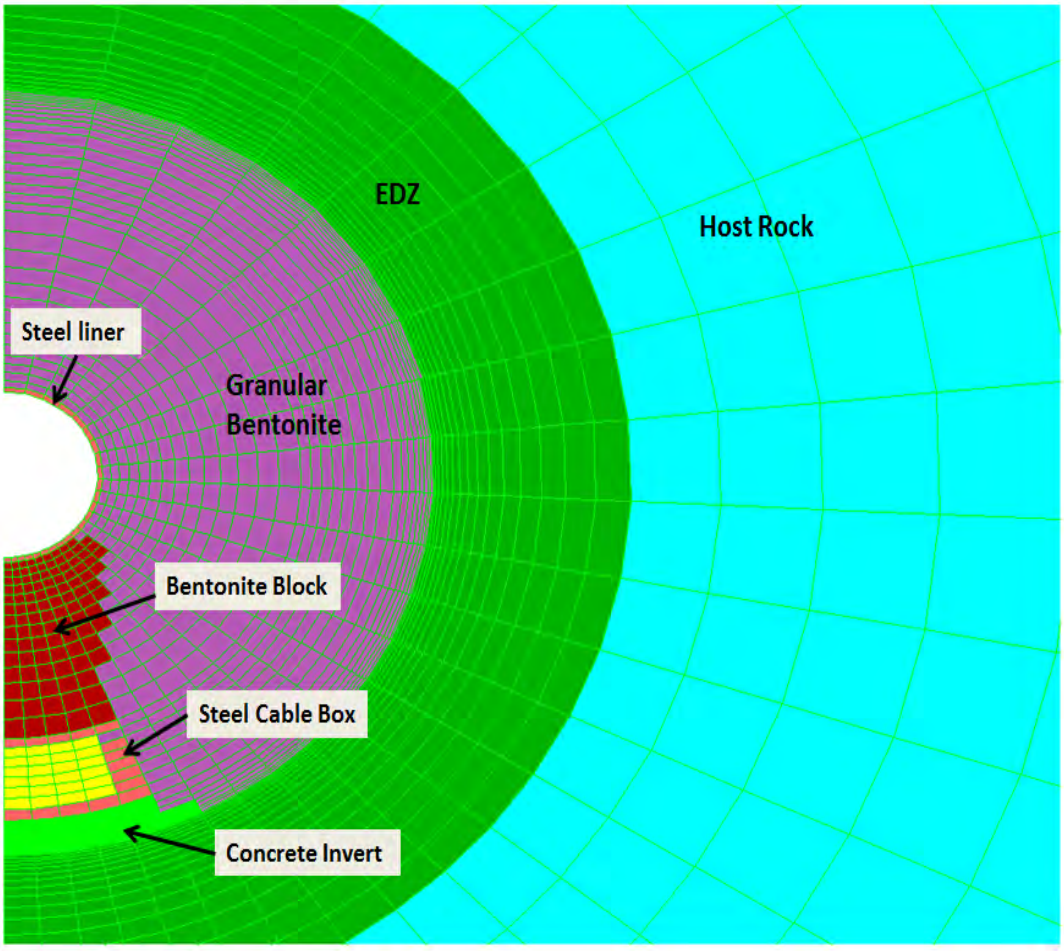

Figure 3-8. Model Geometry Showing Material Details Within the Tunnel and Immediate Vicinity of the Tunnel (Tunnel Diameter is 1.3 m) [1 m = 3.3 ft]

Table 3-1. Input Properties for the 2-D and 3-D xFlo Models							
Description	**Opalinus Clay (EDZ properties are superimposed) (OPA properties were not calibrated)**	**Uncalibrated Bentonite Block Properties**	**Calibrated Bentonite Block Properties**	**Uncalibrated Granular Bentonite**	**Calibrated Granular Bentonite**	**Air in the Channel**	**Liner and Channel Steel**
Moisture Retention and Relative Permeability Relationship	VG	VG	VG	VG	VG	VG	
van Genuchten Alpha (1/Pa)	9.09E-08	4.55E-08	4.55E-08	3.50E-08	1.00E-07	2.80E-04	
van Genuchten *m* (or Lambda)	0.3	0.3	0.3	0.512	0.4	0.6	
Residual Saturation	0.007	0.01	0.01	0.015	0.015	0	
Permeability (m^2)	2.50E-20	7.74E-21	7.74E-21	7.74E-21	7.74E-21	1.00E-12	0
Porosity	0.137	0.33	0.33	0.444	0.444	0.95	0
Dry thermal conductivity (W/m·K)	1.2	0.81	0.81	0.325	0.325	0.04	54
Wet thermal conductivity (W/m·K)	1.9	1.3	1.3	1.114	1.114	0.04	
Exponent p (See Section 3.1.2.1 - Equation 3-1)	1.1055	0.6	0.6	1.566	1.566	0.5	0.5
Specific Heat of rock grain (J/kg·K)	1097	1058	1058	640	640	0	461
Density of rock grain (kg/m^3)	2700	2700	2700	1530	1530	0	7850
Diffusion Coefficient of gas in liquid (m^2/s)	2.13E-09	2.13E-09	2.13E-09	2.13E-09	2.13E-09	0	
Klinkenberg parameter at Sl = 0 (Pa)	5E+06	0	1E+08	1E+12	1E+12	0	
Klinkenberg parameter at Sl = 1 (Pa)	5E+04	0	1E+06	1E+06	1E+06	0	
Gas Tortuosity	2	1	1	2	2	0	

Table 3-2. Additional Input Properties for the 3-D xFlo Model					
Description	**Concrete in Plugs 1 and 3**	**Sand–Bentonite Mixture**	**Rockwool Around the Liner**	**Rockwool in Plug**	**Cement Blocks in Plugs 1, 2, and 3**
Moisture Retention and Relative Permeability Relationship	VG	VG	VG	Not applicable	VG
van Genuchten Alpha (1/Pa)	6.67E-08	5.00E-06	1.00E-04		6.67E-07
van Genuchten *m* (or Lambda)	0.5	0.24	0.5		0.5
Residual Saturation	0.01	0	0.01		0.01
Permeability (m^2)	1.00E-20	1.20E-17	1.00E-14	0	1.00E-20
Porosity	0.15	0.467	0.94	0	0.25
Dry thermal conductivity (W/m·K)	0.5	0.35	0.038	0.038	0.5
Wet thermal conductivity (W/m·K)	1.4	1.3	0.58		1.4
Exponent p (See Section 3.1.2.1 - Equation 3-1)	0.5	0.5	0.5	0.5	0.5
Specific Heat of rock grain (J/kg·K)	1000	826	730	1000	1000
Density of rock grain (kg/m^3)	2650	2700	2650	70	2650
Diffusion Coefficient of gas in liquid (m^2/s)	2.13E-09	2.13E-09	2.13E-09		2.13E-09
Klinkenberg parameter at Saturation = 0 (Pa)	1E+07	1E+07	0		1E+07
Klinkenberg parameter at Saturation = 1 (Pa)	1E+07	1E+07	0		1E+07
Gas Tortuosity	1E+07	1	1		1E+07

Table 3-3. Input Parameters for Mechanical Model Based on Using MCUS Model for Granular and Block Bentonites and Linear Elasticity for All Other Materials (See Figure 3-8 for Materials)			
Host Rock, EDZ, Steel Liner, Cable Box, and Concrete Invert (All Linear-Elastic)			
Parameter	**Values**	**Units**	
Density	2313	kg/m^3	
Young's modulus, *E*	7000	MPa	
Poisson's ratio, ν	0.27		
Material Parameters for MCUS Model			
Parameter, Symbol, and Units	**Value for Granular Bentonite**	**Value for Block Bentonite**	
Density (kg/m^3)	1000	1000	
Poisson's ratio, ν	0.3	0.3	
Maximum bulk modulus, K_∞ (MPa)	50	5000	
Reference pressure, p_{ref} (MPa)	0.1	0.1	
Saturated-state preconsolidation pressure, P_{c0} (MPa)	3	60	
Slope of critical state line, M	1.2	1.2	
Fitting parameter for Bishop versus effective saturation, a_{bs}	1	1	
Fitting parameters for effective saturation versus suction			
S_T (MPa)	40	10	
S_{eT}	0.6	0.92	
S_{ea} (a)	85	90	
S_{eb} (b)	1.75	1.25	
S_{ec} (c)	0.05	4.0	
Relative density of mineral particles, G_s	2.74	2.74	
Fitting parameters for slope of virgin compression line, λ_s (with pressure in MPa)			
λ_{s0}	0.23	0.05	
λ_{sa} (a)	100	10^4	
λ_{sb} (b)	20	10^3	
Fitting parameters for slope of recompression (unload-reload) line, κ_r (with pressure in MPa)			
$\kappa_{r\text{max}}$	0.05	0.04	
κ_{ra} (a)	5000	9000	
κ_{rb} (b)	25	95	
Fitting parameters for reference specific volume versus suction			
v_{refOMax}	2.0	1.6	
v_{refOa} (a)	175.0	300.0	
v_{refOb} (b)	3.7	5.0	
Fitting parameters for tensile strength versus suction			
T_{s0}	0	0	

Table 3-3. Input Parameters for Mechanical Model Based on Using MCUS Model for Granular and Block Bentonites and Linear Elasticity for All Other Materials (See Figure 3-8 for Materials)		
T_{sa} (a)f	10	10
Maximum tensile strength, $T_{s\infty}$ (MPa)	0.01	5.0
Fitting parameters for unit swelling potential (α_{CW}) versus moisture content (θ_l)		
α_{CW0}	1.0	1.0
α_{CWmax}	1.5	1.5
α_{CWmin}	0.001	0.001
α_{CWb}	200	200
θ_{l0}	0.07	0.07
θ_{lm}	0.12	0.12
Shrinkage limit	0.06	0.06
Ratio (unit shrinkage potential)/(unit swelling potential)	0.75	0.75

4 xFLO MODEL CALIBRATION PROCESS

As a final modeling product for **De**velopment of **Co**upled Models and Their **Val**idation Against **Ex**periments (DECOVALEX)-2015 Task B1, the Task B1 leader requested that task participants provide results from three simulations: (i) the experiment period using uncalibrated properties; (ii) the experiment period extended until rewetting occurs, using calibrated properties and assuming that the heater remains throughout; and (iii) the experiment period extended until rewetting occurs, using calibrated properties, and assuming that the heater shuts off on June 1, 2019.

The Task B1 leader provided measurements to the Task B1 participants including (i) input power to both heaters; (ii) temperature and relative humidity in the buffers; (iii) temperature, relative humidity, and pore pressure in the host rock; and (iv) displacement measurements from boreholes in the host rock[1]. From this data, the task leader selected a subset of the temperature, relative humidity, and pressure sensors to provide the model comparison locations. Almost all of the selected sensors are located approximately on a cross section perpendicular to the microtunnel axis midway between Plug 1 and Plug 2, at or near the center of the Nagra section, except for far-field pressure sensors located in a borehole adjacent to the central plug. Section 4.1 describes thermal-hydrologic (TH) sensor data provided to the Task B1 participants. The Task B1 leader did not include displacements in the inter-model comparisons.

A primary goal of the staff participation in the DECOVALEX program is to understand the buffer behavior under intensive heating and during rewetting, as mediated by the near field of the host rock. As with the column test, however, accurately modeling the buffer behavior requires that mass and energy exchanges with the external environment are appropriately represented. For the purposes of model comparisons under Task B1, the team strategy was to keep the analyses as simple as possible while capturing key buffer responses. As the modeling work progressed, it became clear that appropriately representing the near field also may strongly affect buffer responses.

Given the Task B1 goals, the modeling work focused on reproducing processes in the cross section perpendicular to the axis of the tunnel at the center of the Nagra section (the N2 cross section). This cross section corresponds to the sensor locations provided by the task leader. At this location along the axial direction, axial moisture and energy transport in the buffer and the near field should be a relatively small fraction of the overall mass and energy balance equations because the large ratio of heater length to tunnel radius implies that radial temperature and moisture gradients are much stronger than the axial gradients. Simulations of a cross section are attractive for exploring parameter sensitivities, because two-dimensional (2-D) simulations are much more computationally tractable than fully three-dimensional (3-D) simulations, allowing more efficient exploration of uncertainties and parameters. However, it is important to understand the limitations of 2-D models relative to 3-D models.

Modeling of the HE-E test occurred in several stages. A scoping analysis (Section 4.2) using COMSOL suggested that a 2-D cross section model would over-estimate temperatures in the buffer, but calculate the correct near-field temperature gradients. This analysis also suggested that a 3-D spherical model would correctly estimate far-field temperatures, but misrepresent the

[1]Email correspondence (dated 2/11/2015) from Benoit Garitte (Task B1 leader) to NRC and CNWRA providing the link to the FTP HE-E Test data.

near-field behavior. Based on this analysis, a hybrid grid approach was developed for xFlo simulations that transitioned from cylindrical shells to spherical shells at the radius where the interfacial area matched (i.e., half the heater length). A one-dimensional (1-D) version of the hybrid grid model suggested that xFlo calculates excessive water transfer from the host rock to the buffer unless the radial grid increment at the transition is small (i.e., several millimeters) due to the contrasting capillary properties.

With this information as guidance, a series of 2-D hybrid-grid cross section models were built. Nearly 120 simulations were run with various combinations of input parameters and boundary conditions (Section 4.3). Assuming that the buffer and host rock were already relatively well characterized, initial simulations developed representations for system components other than the buffer and host rock (primarily the bentonite block pedestal and cable channel). Most of this effort was devoted to refining the model geometry, parameter zones, and boundary conditions.

The initial sequence of simulations culminated in the uncalibrated inputs and resulting simulation provided to the Task B1 lead. Once the basic model components were established, a further series of simulations explored different representations of the host rock and excavation damaged zone (EDZ) around the tunnel, as well as the influence of Gallery 98 on pore pressure. A set of properties with slightly different parameter values for the bentonite block, host rock, and EDZ was used as the calibrated input set for the calibrated simulations requested by the Task B1 lead. Section 4.4 discusses the rationale for the property set selections.

4.1 TH Sensor Data

Some of the sensor data provided by the Task B1 lead is related to the HE-E test buffer materials and other data is obtained from within the host rock. All of the sensors inside the microtunnel were installed for the HE-E test; many of the sensors in the host rock were inherited from the Ventilation Experiment (VE) test.

4.1.1 Discussion of TH Buffer Data

The Task B1 leader provided spreadsheets with several data streams from sensors in the buffers, bentonite pedestals, heater, and host rock. These data streams included temperature, relative humidity, pore pressure, applied power to the heaters, and relative displacement. The Task B1 leader is comparing the model performance from each of the teams by directly comparing data streams from selected sensors. Moisture content and saturation can only be indirectly estimated from this data based on constitutive relationships with uncertain parameters.

Figures 4-1 and 4-2 illustrate the time history of daily average (i) power (top panel), (ii) temperature (middle panel), and (iii) relative humidity (bottom panel) for sensors in the N2 cross section. The N2 cross section is at the center of the Nagra heater test section. Using daily average values reduces sensor noise at the cost of reducing sensitivity during rapid changes. Time zero is June 30, 2011, the first day with sustained nonzero power. For comparison, Figure 4-3 illustrates the same responses in the G2 cross section (the center of the GRS heater section). Note that the simulations did not consider the GRS section. The corresponding plots for all cross sections are included in Appendix A for reference. Figures 4-4 and 4-5 provide the measured heater and liner temperatures for all Nagra and GRS cross sections, respectively. Figures 4-6 and 4-7 show the same temperatures represented as the difference between the sensor value and the corresponding value from the top sensor in the middle cross section for each heater. In these figures, the dotted and dashed-dotted lines are from the sensors that are closest to the outer plugs and the central plug.

The background color in Figures 4-1 through 4-7 indicates the general different heater regimes, with pale yellow, peach, and salmon representing initial step-wise power increases, steadily increasing power, and temperature-controlled power, respectively. Vertical blue and red lines cutting across panels indicate the start and stop of a power outage. The vertical gray line cutting across panels at day 458 marks a sudden decrease in relative displacement marked by all extensometers, ranging from 0.5 to 4 mm [0.02 to 0.15 in] in a few hours, which is discussed further in Section 6.4.

The sensors are color coded by radius from the microtunnel axis and are also distinguished by line type. Hot colors indicate sensors in the microtunnel and the cool colors indicate sensors in the host rock immediately outside the microtunnel. Solid lines in Figure 4-1 indicate sensors placed vertically above the axis (i.e., 12 o'clock) and dashed lines indicate sensors at the 3 and 9 o'clock positions. Solid lines in Figure 4-2 indicate sensors on one side of the bentonite block pedestal and dashed lines indicate mirrored sensors on the other side. The sensors are nominally at consistent distances from the heater axis but small emplacement irregularities exist. Note that additional temperature readings are available from the heater, heater liner, and host rock under the microtunnel.

The top sensors are usually the hottest sensors in the buffer, liner, and heater (especially in the Nagra cross sections). In the heater and liner, the bottom sensors are almost always the coolest. In contrast, the host rock is usually the coolest above the microtunnel; sensors from deeper in the rock show that the host rock is warmest below the microtunnel. Maximum liner temperature is ~18 and ~15 °C [32 and 27 °F] warmer than minimum measured temperature in the Nagra and GRS cross sections, respectively, even though the input power is uniformly distributed for each heater. Maximum temperature is at the top of the middle cross section (N2 and G2) and minimum temperature is at the bottom of the outer cross section (N1 and G3) one meter [3 ft] away. The heater temperature drops ~13 and ~10 °C [23 and 18 °F] over the same distance. No sensors are located at the outer ends of the heater and liner, an additional one meter [3 ft] further from the middle cross section.

The temperature responses are closely dependent on heater power, with the strongest responses near the heater. Although not visible at this resolution, response times show an increasing lag with distance from the heater. The occasional power outages show a distinct dip and recovery for every sensor.

The relative humidity responses also depend on heater power. The host rock relative humidity climbs with temperature. Responses inside the microtunnel are more complex, varying according to material and accumulated history. Relative humidity drops during an outage in the bentonite blocks (Figure 4-2), increases during an outage in the sand–bentonite buffer (Figure 4-3), and has a mixed response in the granular bentonite (Figure 4-1). The bentonite block responses in the G2 and N2 cross sections are very similar.

The temperature and relative humidity data from Figures 4-1 through 4-3 provide some insight into the functional dependences between moisture content, relative humidity, and temperature for the different materials when plotted as trajectories in temperature/relative humidity space (Figures 4-8 and 4-9). The trajectory for each sensor pair is indicated by a curve with (i) four markers for the transitions between the three heater regimes shown by background colors in Figures 4-1 through 4-3, (ii) successively heavier coloring to mark each successive heater regime, and (iii) dots placed every 10 days. Large dot separations indicate rapid rates of change and small separations indicate slow rates. Markers are filled with yellow, orange, red, and black to indicate the successive transitions between regimes.

The bentonite block temperature/relative humidity trajectories are similar in the N2 and G2 cross sections (Figures 4-9 and 4-10, bottom subfigure), and other cross sections follow similar trajectories until reaching a cooler transition point during the last heater regime (Appendix A, Figures A-13 through A-18). The first (shortest) heater regime produces a slight increase in relative humidity with a substantial warming. The second heater regime produces declining relative humidity as warming progresses further. The final (longest) heater regime produces a substantial decline in relative humidity with slightly warming temperatures. The final regime is marked by distinct power outages, each resulting in a cooling spike with a slight decline in relative humidity. The cooling spikes are approximately parallel to the trend in the first heater regime and the return warming trajectory after heater resumption almost overlaps the initial cooling trajectory. The cooling spikes occur rapidly; hence only one or two dots are present on the spikes.

The bentonite block temperature/relative humidity trajectories are consistent with minimal moisture redistribution during initial warming and during outages. Relative humidity is somewhat temperature-dependent given moisture content. Relative humidity is almost identical for a given temperature during the cooling and warming phases of each outage spike, indicating minimal change in moisture content during the outage event. The similar gradient of relative humidity with respect to temperature during the initial heater regime and the outage spikes implies that little redistribution is occurring during the initial heater regime, as well. Each spike is offset successively lower in relative humidity, indicating that moisture content dropped between the initial phase to the first outage, and dropped further to the final outage.

The bentonite block temperature/relative humidity trajectories show moisture loss during the phases with temperatures above 50 °C [122 °F]. Up to the start of the third heater phase (equilibrium temperature held at the liner), all sensors follow essentially the same trajectory of declining relative humidity with increasing temperature, just offset in time based on how near the sensor is to the liner. Once the equilibrium temperature phase begins, relative humidity continues to drop while the temperature mildly increases. The small temperature rise during the equilibrium regime is consistent with (i) expansion of the temperature front in the host rock and (ii) reduction in thermal conductivity inside the blocks due to moisture loss. Little or no change occurs in the long period after the last outage (successive 10-day dots are essentially on top of each other), indicating that an approximate equilibrium has been reached. In particular, there are no changes that would indicate rewetting has begun.

The general patterns for the temperature/relative humidity trajectories in the granular bentonite buffer are fairly similar to the bentonite block trajectories. Trajectories for the middle sensors cluster more tightly than the inner sensors. The two sensor sets follow slightly different trajectories, especially during the initial phase experiencing multiple step changes in power. Material packing is more variable for the granular buffer than for the bentonite blocks because of the emplacement method, which may explain some of the difference in trajectories. The trajectories from the beginning to the end of the equilibrium regime are offset from one another, but they have essentially the same shape, except for responses during power outages.

The temperature/relative humidity trajectories of the innermost sensors show relatively large changes in temperature and relative humidity during the power outages. It is notable that the rewarming phase of each outage had a larger relative humidity for a given temperature, especially for the innermost sensors, indicating that the buffer had locally rewetted during the outage. The outages occurred after the innermost sensors had achieved stable conditions (the smaller initial spike at 427 days is nested inside the larger second spike starting at 571 days), and the same state was restored after the perturbations. In contrast, the outer buffer

sensors are still very slowly warming and decreasing in humidity at the end of the data sequence.

The general patterns for the sand–bentonite buffer temperature/relative humidity trajectories are fairly similar to the granular bentonite trajectories. The sand–bentonite trajectories are better clustered than the granular bentonite trajectories, and the sensor states change relatively little during the equilibrium regime. The temperature change is comparable or slightly smaller during outages, but the relative humidity change is larger. The larger relative humidity change suggests that the magnitude of moisture transport is larger for the sand–bentonite buffer. The overall response times are consistent with moisture profiles in the sand–bentonite buffer remaining in equilibrium with power inputs and resulting temperature profiles that vary smoothly on time scales seen during the second heater regime.

The host rock temperature/relative humidity trajectories are fairly similar among the N1, N2, and N3 sensors, and are fairly similar among the G1, G2, and G3 sensors. The host rock tends to reach a relative humidity of 100 percent between 35 and ~50 °C [95 and 122 °F] for the Nagra cross sections, and between 23 and 32 °C [73.4 and 89.6 °F] for the GRS cross sections. The host rock sensors showed slightly reduced initial relative humidity in the Nagra cross-sections (0.55 to 0.65 versus 0.58 to 0.68). Note that the sensors can only resolve relative humidity to within a few percent near saturation, thus a relative humidity reading of 100 percent (implying fully saturated rock) may actually be slightly lower (implying a partially saturated rock). However, the rock has such small pores that it remains essentially saturated even when the relative humidity is well below 100 percent.

The G1 cross section exhibited rapid relative humidity responses to power changes in two of the three host rock sensors, including drops in relative humidity (i) at the initial power-on time and (ii) during two outages. At the initial power-on time, the drop in host rock relative humidity for one sensor was synchronous with a drop in buffer relative humidity at the outer sensors and increase at the inner sensors (note that the same buffer behavior is found at the power-on time for all six cross sections). During the outages, the drop in host rock relative humidity at the other sensor was synchronous with increases in all buffer sensors. The same rock sensor recorded a drop in relative humidity followed 3 months later by a persistent increase in relative humidity at one inner buffer sensor. Although responses observed in a single sensor may be attributable to sensor malfunction, synchronous and repeated responses in multiple sensors are less likely to be due to sensor malfunctions.

The different responses of the host rock, combined with the different responses in the two buffers, are consistent with moisture exchanges between the host rock and buffer causing the saturation condition rather than rewetting from the host rock. The increase in host rock relative humidity is consistent with condensation of vapor mobilized from the buffer. The sand–bentonite buffer appears to have achieved approximate equilibrium profiles for moisture and temperature soon after the start of the equilibrium regime, whereas the granular bentonite has almost achieved equilibrium by the end of the available data and the bentonite blocks are still very slowly drying. An equilibrium condition implies that rewetting would require either that the heater temperature lowers or the host rock state changes to promote inflow.

4.1.2 Discussion of Pore Pressure Data

Pore pressure data are available only from the host rock. The pore pressure data were obtained from boreholes (see layout in Figure 1-6), with packers used to ensure good hydraulic contact with the low-permeability rock and to provide isolation. Two boreholes from Gallery 98

drilled for the VE test (BVE-91 and BVE-1) dip 6.4° and are oriented to pass under the microtunnel, and two boreholes from Gallery 98 drilled for the HE-E test (BE-1 and BE-2) rise 6.2° and are oriented to hit the microtunnel axis. BE-2 is in line with the N2 cross section, BE-1 is in line with the G2 cross section, BVE-1 is under Plug 2, and BVE-91 is between the N2 section and Plug 2. Each borehole has four pore pressure sensors separated with packers.

An additional set of pore pressure sensors were installed from the microtunnel, with sensors emplaced for the VE test augmented by newer sensors for the HE-E test. These sensors are generally within ~2 m [6.6 ft] of the microtunnel wall.

The pore pressure history for the Gallery 98 and microtunnel borehole sensors are shown in Figures 4-10 and 4-11. In general, the pore pressures increase with distance from the microtunnel, but the pore pressure distributions vary with angle about the microtunnel axis or with location along the axis. For example, the range of radii overlaps for sensors in boreholes BVE-91 and BVE-1 but the pore pressures are quite different in the overlap zone.

The furthest sensor from the microtunnel in both BE-1 and BE-2 consistently maintains pore pressures that are less than measured in closer sensors from the same borehole. The anomalous sensor may be affected by Gallery 98 or may have some installation discrepancy with respect to packer pressure.

The pore pressures in the microtunnel boreholes show a consistent pattern of near-atmospheric pore pressures within 1 to 2 m [3.3 to 6.6 ft] of the microtunnel wall, but pore pressure increases further out appear to be quite dependent on orientation around the microtunnel axis in each cross section. Anisotropy and heterogeneity are the likely cause of the inconsistent response patterns.

Some confirmation of the consistency between borehole and microtunnel sensors is obtained by comparing the P-B1-11m sensor in the BVE-1 borehole to the nearby P-B39 microtunnel sensor, which is approximately 0.7 m [2.3 ft] closer to the microtunnel. These sensors have similar traces (compare Figures 4-10 and 4-11). The P-B39 sensor responds considerably later but ultimately achieves similar pore pressures.

The Task B1 lead did not provide pore pressure data for cross section SA4, near cross section N1 between N1 and Plug 1. Annual monitoring reports (Grava et al., 2012; Gräfe and Rösli, 2013, 2014) show that all sensors in the SA4 cross section stayed near atmospheric except for sensor P-B7, which rose to 850 kPa [123 psi] before beginning a slow descent. All sensors are within 1.5 m [4.9 ft] of the microtunnel wall except for P-B7, which is >2 m [6.6 ft] from the microtunnel wall.

The hydrological conditions in the fringe above a water table provides an analogy that facilitates an explanation of hydrological conditions in the host rock around the microtunnel. In well-drained fine porous media, atmospheric pore pressures are found in the saturated zone along a front called the water table. The water table marks the boundary between above- and below-atmospheric pressures in the saturated zone. Below-atmospheric pressures may occur in an extended saturated capillary fringe where water will not enter the borehole without applying suction. Pore pressure gradients are unaffected by the water table because the medium remains saturated, but can be strongly influenced at the transition between saturated and unsaturated.

The 2-m [6.6-ft] fringe of near-atmospheric pore pressures found around the microtunnel, even after extended heating, suggests that (i) the sensors are failing to record tensions in a saturated capillary fringe; (ii) a water table condition is being maintained by unsaturated conditions, perhaps in a fracture network; or (iii) some other process is maintaining consistent atmospheric pressures up to 2 m [6.6 ft] into the rock even though every cross section has multiple relative humidity sensors located approximately 6 cm [2.4 in] into the rock that do not detect unsaturated conditions. If the sensors are accurately recording pore pressure, the implication is that liquid water fluxes are negligible within the fringe exhibiting near-atmospheric pressures unless the local permeability is orders of magnitude larger than the intact rock outside the fringe.

4.2 Model Gridding

Relatively simple models accurately represent the relevant processes in certain idealized configurations. The HE-E test captures some aspects of a repository configuration with waste packages placed end-to-end in long lines. In assessing performance of a repository configuration, a performance assessment model considering the buffer might represent the entire system as radially symmetric perpendicular to the axis, which is reasonable when (i) the host rock is isotropic, (ii) a single medium fills the void between waste package and host rock, and (iii) there is a single long line of waste packages. In this configuration, a 1-D model in cylindrical coordinates (a cross section model with full circumferential symmetry) captures the key behavior. With multiple parallel drifts, a 2-D model perpendicular to the drifts would capture the key behavior. The emplacement geometry with a long line of waste packages implies that axial gradients are likely to be very small relative to gradients in the plane perpendicular to the drift, so little is lost when modeling in 1-D and 2-D instead of 3-D.

The HE-E test deviates from the idealized configuration in several key aspects: (i) the host rock is bedded and dipping relative to the microtunnel axis, (ii) the annular space between the heater and the host rock contains several different materials with quite different properties, (iii) measured perturbations to the environment occur at radial distances that are comparable to the heater length, and (iv) relatively steep axial gradients exist at the ends of the experimental sections.

Several grid options were considered to best represent the TH response in the near field, including (i) fully 3-D, (ii) cylindrical 2-D along the axis of the tunnel, (iii) planar 2-D in a cross section perpendicular to the tunnel, and (iv) 1-D models. Although excellent grid resolution can be achieved, the 1-D models were considered too simplistic to represent key geometric features. The fully 3-D approach was considered, but the grid resolution likely required for computational accuracy was considered too computationally demanding for performing numerous simulations.

The two 2-D approaches are better at capturing different effects. A 2-D model along the axis of the tunnel, which assumes circumferential symmetry at each axial position and radius, is better suited to exploring end effects near the plugs and in the far field but cannot address anisotropy in the host or the bentonite blocks and cable channel in the microtunnel. A 2-D model perpendicular to the microtunnel axis can address host anisotropy, bentonite blocks and the cable channel, but cannot consider end effects.

Given the elongated geometry within each heater section, it is reasonable to expect that mass and energy transport in the buffer occurs predominantly within the 2-D cross section perpendicular to the microtunnel axis, perhaps affected by anisotropy along the dip direction in the host rock. If anisotropy and the effect of bedding dip are small, it is computationally

attractive to use a 2-D grid that is aligned with a cross section perpendicular to the tunnel axis in a location that experiences minimal mass and energy transport in the axial direction. In this case, the effects of neglecting the third dimension can be assessed using limited auxiliary analyses with a fully 3-D model.

Model dimensionality was assessed with a set of transient COMSOL thermal simulations. A reference 3-D model reproduced the geometry of the two 4-m [13.1-ft]-long, 0.3-m [0.9-ft]-diameter heaters separated by a plug, with a far field held at the ambient temperature at a radius of 50 m [164 ft]. Each heater was assigned a total power of 700 W for 3 years. The host rock and buffer were assigned thermal conductivity values of 1.8 and 0.4 W/m·K, respectively. An equivalent COMSOL model was created in a 2-D plane with the same heater and far-field radius, thermal properties, and power per unit heater surface area. A second equivalent COMSOL model was created with a pair of concentric spheres representing the heater and microtunnel. Each sphere preserves the corresponding surface area. Again the same heater power, far-field radius, and thermal properties were used.

The temperature profiles after 3 years are illustrated in Figure 4-12, where they are shown for all three simulations in the radial direction from the microtunnel axis at the center of one of the heaters. The 2-D planar model is hotter than the fully 3-D model because the far field is misrepresented, but has the same temperature gradient as the 3-D model in the near field ($r < L/2$, where r is the radial distance and L is the heater length). The profile from one of the pair of 3-D spheres is much too hot in the near field, suggesting that the near field is misrepresented, but matches well in the far field ($r > L/2$). These simulations suggest that a hybrid approach transitioning from cylindrical to spherical coordinates may capture both the near field and far field reasonably well.

A 1-D model was developed to test the hybrid approach using the built-in *pdepe* function in Matlab. The model calculates area and volume in cylindrical coordinates for $r < L/2$ and in spherical coordinates for $r > L/2$, but otherwise uses the same parameters as the COMSOL models. The model results shown in Figure 4-12 match well within the buffer zone, but are slightly colder several meters into the host rock. In this region, the 3-D model accounts for both heaters, but the hybrid model only considers one heater. In the buffer, which is the primary area of interest, the hybrid model is far superior to the purely 2-D planar model.

The comparison between a fully 3-D model and the 1-D hybrid model suggests that the temperature dynamics should be well captured for the heating process using the hybrid gridding approach.

Gas and liquid redistribution is also governed by diffusive processes in porous media, especially in a low-permeability medium where gravity is unimportant as a driving force. The strong disequilibrium conditions generated by the initial dry buffer adjacent to the buffer and subsequent redistribution driven by heating imply that mass redistribution in the buffer and near field is likely to be essentially in the plane perpendicular to the axis, similar to thermal redistribution. Because exchange with the buffer in the HE-E test sections are likely to be larger than any other section of the microtunnel, especially behind Plug 1, the test section is likely to behave like a finite-length source/sink zone so that porewater movement in the far field is also likely to be dominated by spherically radial flows. Accordingly, the same hybrid 2-D gridding approach should be reasonable for mass transport.

This model comparison and rationale were used for grid development for all subsequent modeling. Gridding is described in Sections 4.3 and 5.2.1. Two other aspects of the xFlo finite

volume implementation also were considered in developing grids. The current implementation (i) is more accurate when fluxes are approximately perpendicular to cell faces, and (ii) does not explicitly consider anisotropy. Accordingly, the grids should be aligned as closely as possible with dominant flux directions. The restriction on anisotropy can be somewhat overcome when the principal directions of anisotropic properties are aligned with the grid by artificially adjusting distances between cells and their faces, as discussed in Section 4.3.

The unstructured xFlo grid allows specialized boundary conditions that can approximately represent axial fluxes in a 2-D model, although usually the axial fluxes would be more accurately represented in a fully 3-D model. Any grid cell can be provided with a link to a boundary condition cell, and an arbitrary number of links can be attached to any grid cell. The only geometric factors in calculating fluxes are the cross-sectional area for the link and the separation distance between cells. With appropriate selection of material properties in the boundary cell, mass and energy transfers can be selected or precluded for a link to the cell, permitting a variety of boundary conditions. Using a link to a boundary condition allows the "strength" of the boundary condition to be tuned, especially useful when the boundary condition represents a small flux. Such links were used to represent axial flow in the cable channel and the EDZ, as well as permitting an attenuated representation of the Gallery 98 atmospheric pressure condition.

4.3 Calibration Process for the 2-D Model

The goal for a model of the HE-E test is to accurately simulate the time history of each temperature and relative humidity sensor at the cross section perpendicular to the axis of the heater at the center of the Nagra section. These sensors are located in three media: (i) the granular bentonite buffer, at the 3, 9, and 12 o'clock positions relative to the axis; (ii) the solid bentonite block pedestal below the heater; and (iii) the host rock. The bentonite block pedestal occupied a relatively small fraction of the annular space, but temperature and relative humidity responses in the pedestal differed substantially from the granular bentonite.

The hybrid 2-D cross section modeling approach was used to model the HE-E test. For simplicity, the model took advantage of symmetry, with a vertical boundary placed at the axis of the tunnel. The xFlo grid is topologically rectangular, consistent with FLAC conventions, with spatial coordinates defined with radius and angle about the origin. The origin is placed at the axis of the heater, but the inner boundary was placed at the heater liner. The model used a hybrid grid, with cylindrical shells used near the heater and spherical shells used further from the heater. Calculations with xFlo do not use cell coordinates, just cell volumes, interfacial areas, and distance from the cell centroid to the interface. Therefore, cells for the spherical shells are introduced by adjusting cell volumes, interfacial areas, and distances to the centroid. The area of a cylinder with radius r is $2\pi rL$, where L is the cylinder (e.g., heater) length. The area of a sphere is $4\pi r^2$. The cylinder and sphere areas are equal when $2r = L$, thus the grid transitioned from cylindrical shells to spherical shells at $r = L/2$. In general, r was smoothly discretized between breakpoints representing interfaces between material properties, and increased logarithmically in the far field. The shells were partitioned into elements in the circumferential direction, with finer resolution at the bottom to better represent the bentonite blocks and cable channel. Circumferential partitioning of the spherical shells used arcs, resulting in elements shaped like lunes (e.g., the crescent shape between two longitudes on a globe).

The 2-D simulations focused on understanding the TH behavior of granular bentonite buffer undergoing heating and moisture exchange with the near-field host rock. For these simulations,

(i) the buffer and heater properties were assumed to be known based on manufacturer's specifications and prior modeling work, (ii) the host rock was assumed to be isotropic in all properties with values determined from the literature, and (iii) EDZ was assumed to have isotropic properties within a fixed radius. With the assumption that these properties were relatively well established, the simulations focused on representing engineered components with more uncertain properties.

As the simulations progressed, a set of physics-based heuristic criteria was developed to assess how well the simulation results matched the measurements.

- A good calculated match to thermal measurements (i) is 4 °C [7.2 °F] warmer at the top of the heater liner than at bottom after the first year, (ii) reproduces the measured radial temperature profiles in both the granular bentonite and bentonite pedestal, and (iii) reproduces the measured temperatures in the host rock. Simulations were able to match the temperature profiles in the granular bentonite and host rock reasonably well, but had difficulty with the solid bentonite blocks. It was difficult to achieve the measured radial temperature profiles in both the buffer and pedestal simultaneously, and it was difficult to achieve a temperature difference less than 8 °C [14.4 °F] from the top to bottom of the heater. Although measured temperature profiles vary significantly from profile to profile, the temperature drop across the heater liner is similar in all of the profiles and the block is consistently cooler than the buffer. Accordingly, consistent discrepancies between calculated and measured thermal responses may be a symptom that some important system feature is not included in the model.

- A good match to relative humidity measurements shows response times and gradients similar to measured values. Instrument limitations limit accuracy when relative humidity is near 100 percent, thus measured relative humidity values greater than 95 percent are considered questionable. Simulations matched the relative humidity profiles in the granular bentonite reasonably well. The unsaturated zone usually appears to penetrate too deeply into the rock, although there may be residual error in sensor measurements when the relative humidity is near 100 percent. Relative humidity changes in the bentonite that are calculated by xFlo are typically substantially slower than measured, but the late-time profiles typically match reasonably well.

- Most pore pressure measurements are offset from the plane of the N2 cross section and do not show a clear pattern with radial distance from the microtunnel. Pore pressures in Borehole BE-2, which is in the plane, were still responding to the initial emplacement transient at the start of heating and therefore do not provide an initial condition. Staff considers the offset measurements somewhat problematic for model comparisons because they are not in the plane of the cross section and may be subject to gradients in the axial direction. Measurements several meters into the host rock may be far enough into the model far-field spherical domain to be considered representative. The heuristic criterion suggests that a reasonable match between calculated and measured values might be within the range of values measured at different boreholes.

Initial simulation results exhibited calculated heater and buffer temperatures that were too large, which made the mass balance calculations suspect. Accordingly, staff initially focused on adjusting the thermal balance. Because of the different thermal responses in the different bentonite media and the presence of the thermally conductive cable channel below the bentonite pedestal, staff suspected that thermal fluxes in the bentonite blocks were significantly larger than thermal fluxes in the granular bentonite buffer and significant axial heat loss was

occurring in the steel channel. After a series of trial and error simulations, reasonable thermal responses were achieved when (i) the steel cable channel was included at the bottom of the bentonite pedestal, allowing an enhanced thermal pathway to the host rock and (ii) an axial 1-D connection in the channel was included to allow heat loss to an ambient temperature sink (nominally at the ambient zone outside Plug 3 in the microtunnel).

Initial simulation results also exhibited large gas pressures in the microtunnel, well above the far-field background pore pressures, even though measured pore pressures had a much smaller response. Staff thought that gas pressures might rise substantially in a well-sealed repository scenario, but a large pressure increase appeared to be inconsistent with the measurements. Gas pressure must equalize rapidly throughout each buffer zone because of the large buffer gas permeability, at least until the buffer resaturates, so small connections to the ambient air pressure in the microtunnel outside Plug 3 are likely to keep air pressure within the buffers near atmospheric. Ultimately two types of pressure relief locations were identified: (i) cable access ports in the cable channel, and (ii) a 3-cm [1.2 in] rockwool wrap around the heater liner where the heater passes through Plugs 2 and 3. The cable ports were identified after dozens of simulations. The rockwool wrap was identified while developing a full 3-D model, after completing most of the 2-D simulations. Other Task B1 participants did not appear to consider gas pressure, likely because most participants used the Richards assumption (instantaneous gas equilibration) and therefore gas migration was not an issue.

The 2-D cross section simulations include a gap in the steel cable channel to allow air to pass from the granular bentonite to the interior of the channel. Staff considered a variety of techniques to link the port to the ambient conditions in the microtunnel, because the simulation time step tended to be strongly limited by convergence limitations in the air within the channel. Ultimately a single axial 1-D link was imposed to the ambient conditions in the microtunnel. The properties for this link are poorly known, because (i) the interior of the cable channel is not described and (ii) the adjacent sand–bentonite section also has cable ports. Simulations suggested that making the link too strong dried out the buffer. Accordingly, the cable channel link was treated as a calibration parameter, adjusting the link until gas pressure changes were limited without overly drying the buffer. Note that putting a gap in the channel wall is somewhat unsatisfactory from a thermal balance perspective, because this strongly limits vertical heat fluxes in a 2-D model. A revised model might connect the axial link directly to the bentonite cell without explicitly representing the cable port.

Properly representing the thermal fluxes through the pedestal is necessary before drawing firm conclusions regarding the calibration of the granular bentonite properties. Accordingly, staff focused substantial effort on properly representing the pedestal and channel.

Inputs representing different engineered components were varied for this set of simulations to better match temperature, moisture, and pore pressure profiles in the buffer and near field. Adjustments to the simulation inputs were made primarily to (i) better represent the bentonite block pedestal and embedded steel cable channel geometry, (ii) account for a limited amount of loss of air, vapor, and sensible heat to MI Niche using selected axial boundary conditions, and (iii) better resolve sharp gradients at material boundaries. Although numerous simulations were used to develop the resulting input set, the buffer and host rock properties were not modified. For the purposes of the Task B1 lead, the “uncalibrated” model has initial material properties but component geometry, boundary conditions, and gridding are refined relative to the initial input deck.

After adjusting parameters for engineered components through trial and error, the resulting simulation outputs generally agreed with measurements but differed in some details. In particular, measured temperature and relative humidity gradients within the buffer and pedestal only approximately matched the corresponding calculated gradients. Measured temperatures for the heater liner are within ~4 °C [7.2 °F] at each cross section, usually warmest on top and coolest on the bottom (one cross section has warmest temperatures on one side). The measured temperatures drop with axial distance from the heater center. Measured radial temperature gradients are substantially shallower in the granular bentonite than in the bentonite blocks, so that the outermost temperature sensors in the bentonite blocks {where r is 34 cm [13.4 in]} are approximately 10 °C [18 °F] cooler than the granular bentonite at the same radius. The host rock is warmer below the microtunnel than above the microtunnel, suggesting downward thermal fluxes are larger than upward fluxes in the microtunnel. The uncalibrated property set does not completely capture the different temperature gradients in the two bentonite media. Further, the measured relative humidity values in the bentonite blocks suggest much faster drying than the simulations calculate.

The next set of simulations considered anisotropic properties for the host rock, assumed due to bedding anisotropy, and considered various representations for the EDZ. For the simulations, anisotropy is assumed to be aligned with horizontal bedding planes (the bedding dip in the direction of the microtunnel axis is neglected).

The xFlo algorithms currently allow heterogeneous material properties, but do not consider anisotropy. Anisotropy can be implemented as a scaling factor for conductivities when the grid is aligned with the principal directions of the anisotropy. Another way to implement an anisotropic conductivity is to scale distances in the principal directions by the inverse square root of the anisotropic scaling factor when calculating gradients. For example, if conductivity in the horizontal direction is nine times larger than in the vertical direction, distances in the horizontal direction are effectively three times smaller than in the vertical direction.

To explore anisotropy, the preprocessing routines defining the input grid geometry used scaled coordinates to calculate distances in the grid cells. This scaling procedure was only applied in the host rock. The preprocessing routines calculated cell volumes with the undistorted coordinates. This approach means that the thermal conductivity, permeability, and diffusion coefficients all have the same anisotropy ratio. To apply different anisotropy ratios for each coefficient, xFlo would require modification to supply a separate scaling factor for each coefficient in each link.

A simple representation of the EDZ permeability was used to explore the effect of the EDZ on moisture redistribution. The preprocessing routines represented the EDZ by applying a scaling factor to the host-rock permeability in cells near the microtunnel. This scaling factor was assumed to remain unchanged throughout the simulation (i.e., rewetting and deformation did not influence the EDZ). The EDZ scaling factor was assumed to decrease exponentially with distance from the tunnel wall. This approach has two parameters to explore: (i) a permeability scaling factor at the tunnel wall, and (ii) a decay coefficient with distance. Note that this scaling is layered on top of the host-rock anisotropy, and may not completely capture the radial and circumferential anisotropy and heterogeneity implied by crack patterns and permeability tests uncovered by studies at other locations in the Mont Terri URL. These investigations suggested that permeability enhancement depends on host rock stresses under ambient conditions, and some quadrants may have permeabilities that are orders of magnitude larger than in other quadrants.

EDZ permeability distributions presumably would respond if thermal stresses deform the host rock significantly. Limited relative displacement data provided by the Task B1 team leader suggest that thermal stresses caused the microtunnel to enlarge and become more circular (see Section 6.4), consistent with a more uniform stress field around the microtunnel circumference. If so, the EDZ permeability also would be more symmetric after heating.

Simulation results suggested that observations at sensor locations may be compatible with a range of properties, and the observations could be compatible with both long-term rewetting and long-term drying depending on the particular combination of input properties describing anisotropy and the EDZ.

4.4 Rationale for Property Sets

Staff had completed more than 100 simulations by the time the task lead defined the final modeling product—an uncalibrated property set and a calibrated property set. The input set for the simulations gradually evolved from the start of the modeling exercise to the end of the simulation phase, but the process was not organized to yield a specific calibrated property set distinct from an initial uncalibrated property set. To satisfy the spirit of the task, staff revisited its approach during the modeling process to identify representative input sets.

At the onset of modeling, staff considered the buffer properties to be relatively well characterized because of experience with the column test. Staff also considered the properties for the bentonite-block pedestal and host rock far field to be relatively well characterized but somewhat more uncertain than the buffer. Staff considered the hydraulic effects of the EDZ to be relatively uncertain because unexamined fractures present might strongly affect near-field flow patterns. Staff considered engineered components, such as the cable channel, to have a potentially significant but relatively uncertain influence on temperatures and gas pressures in the buffer.

By the end of modeling, staff had not modified the buffer properties and had concluded that there was little basis to modify the bentonite block properties. Initial simulations were much too hot, but simply including the cable channel with representative geometry and material properties from the literature into the model brought the simulation results in line with measured values. Once the cable channel was included, the remaining simulations examined tweaks to bentonite block properties, edge effects between the liner and the underlying bentonite block, host rock anisotropy, and EDZ effects.

In the spirit of the Task B1 comparison, the uncalibrated property set consists of the initial buffer, bentonite block, and host rock properties with the cable channel included in the model with its final configuration, assuming that the lid was made from steel. The cable channel properties remained the same for all subsequent simulations. The uncalibrated property set imposed a horizontal-to-vertical anisotropy ratio of 2 for permeability, thermal conductivity, and diffusion coefficients. Note that the uncalibrated property set assumes that the EDZ is not present, thus it provides insight into what might occur if the EDZ heals rapidly.

Selecting a calibrated property set was more difficult because none of the simulations perfectly matched the observations. Various combinations of host rock anisotropy and estimated EDZ properties provided results that appeared to match the observations nearly as well while significantly differing where no observations were available. In some of the simulations, long-term rewetting would progress fairly rapidly, while other simulations suggested that the

observed host rock rewetting was local and transient and that ultimately a dryout zone would expand into the host rock.

The final calibrated parameter set provides the best overall match to the relative humidity, temperature, and pore pressure observations among all simulations. The least-squares deviation between the calculated and measured parameters was calculated for each simulation across all simulation output times and measurement locations. To provide a fair comparison between different parameters, each calculated deviation was normalized by dividing by the smallest value among all simulations. This procedure leaves a value of unity for the smallest deviation. The set of three normalized values for each simulation were averaged, and the average was ranked from smallest to largest. The best overall simulation ranked 20, 22, and 20 when temperature, relative humidity, and pressure were considered individually. The same simulation ranked second when just temperature and relative humidity were averaged. Increasing the EDZ permeability only minimally affected rankings, and altering the EDZ decay depth also had little effect. Increasing the anisotropy ratio improved relative humidity matches at the cost of deteriorating temperature matches.

The final property set also imposes a horizontal-to-vertical anisotropy ratio of 2 for permeability, thermal conductivity, and diffusion coefficients, and includes a permeability multiplier that exponentially decays from the tunnel wall. The area of contact between the liner and underlying bentonite block is reduced by a factor of five to mimic a zone of poor contact.

Relative humidity in the host rock and buffer is the primary means for discriminating between the different models, but the available data are fairly sparse. Most sensors in the host rock registered 100 percent relative humidity long before the end of the available dataset, but may be accurate to within only a few percent near this level. Relative humidity sensors in the buffers generally remained essentially steady once the peak temperature was reached, showing no sign that the buffer was receiving incoming water from the host rock. None of the simulations were consistent with both sets of sensors; preventing rewetting in the buffer requires that the host rock retain a dryout zone, and allowing rewetting in the host rock results in the buffer rewetting.

In the spirit of the Task B1 comparison, the calibrated property set describes a mildly anisotropic host rock with an EDZ that is sufficiently permeable near the microtunnel to allow rewetting. The bentonite block properties are adjusted at the heater liner to allow only 20 percent of the block to contact the liner.

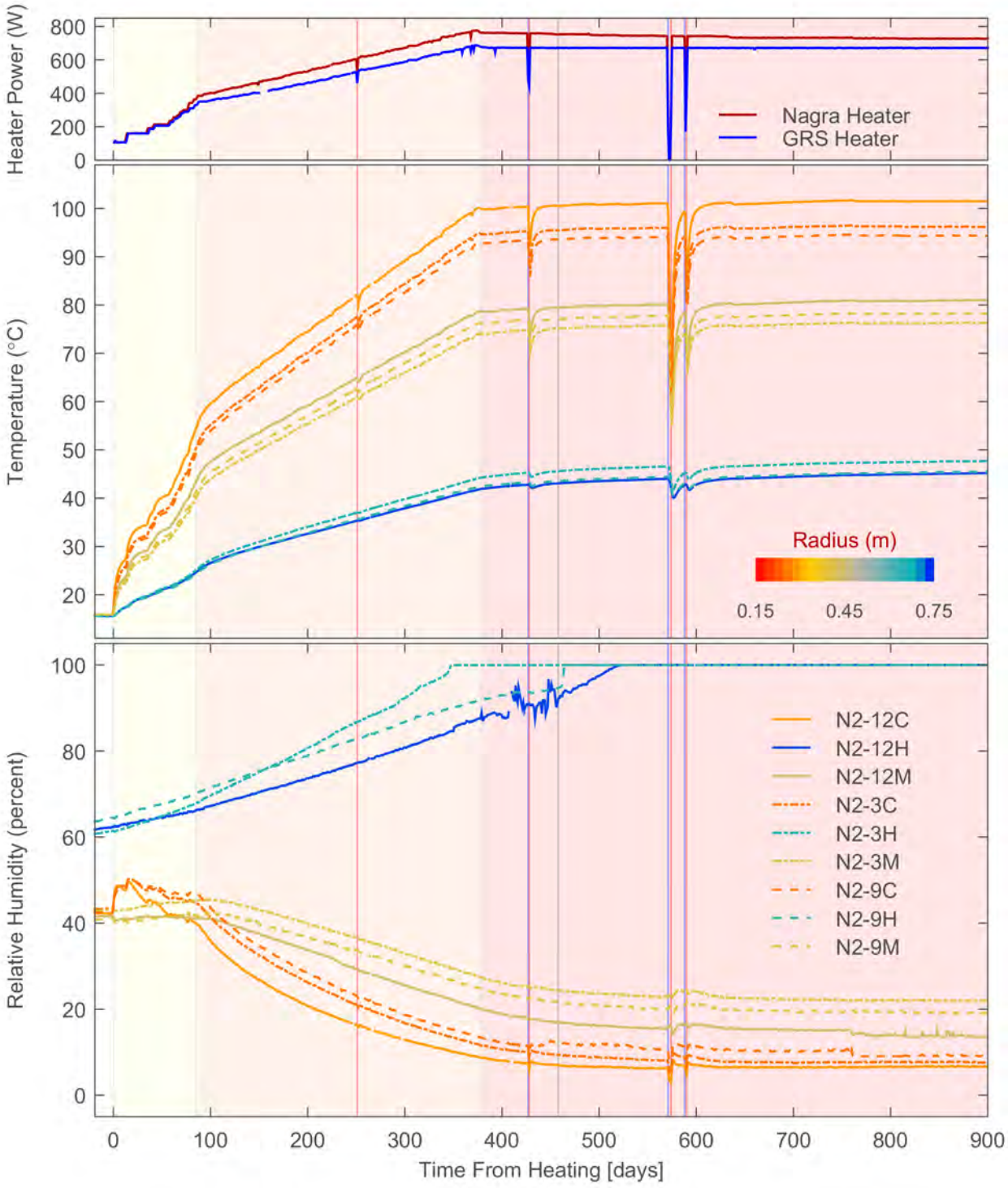

Figure 4-1. Daily Average Measured Heater Power (Top), Temperature (Middle), and Relative Humidity (Bottom) in the Granular Bentonite Buffer and Host Rock at the N2 Cross Section. [°F = (1.8 × T °C + 32), 1 m = 3.3 ft]

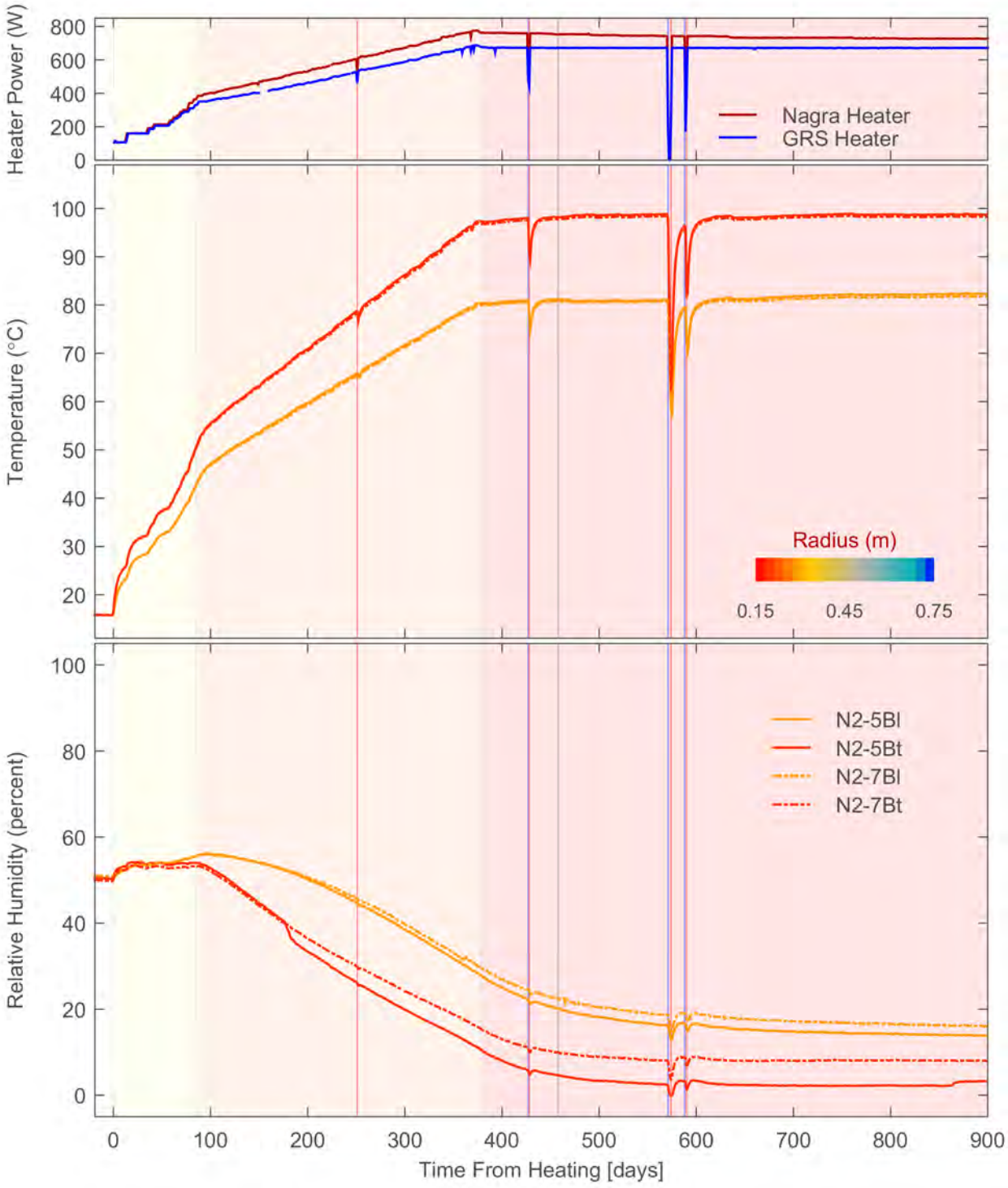

Figure 4-2. Daily Average Measured Heater Power (Top), Temperature (Middle), and Relative Humidity (Bottom) in the Bentonite Block Pedestal at the N2 Cross Section. [°F = (1.8 × T °C + 32), 1 m = 3.3 ft]

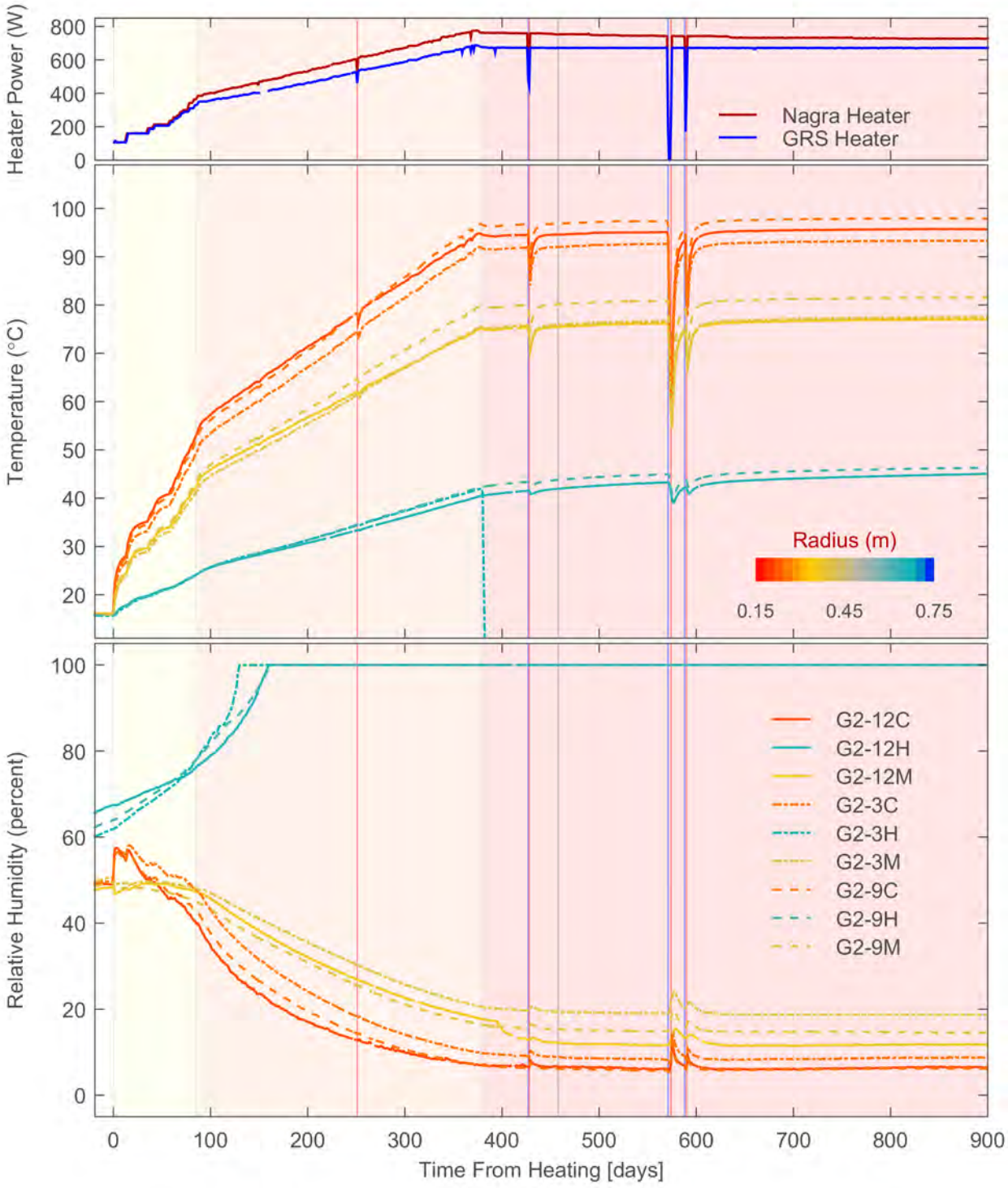

Figure 4-3. Daily Average Measured Heater Power (Top), Temperature (Middle), and Relative Humidity (Bottom) in the Sand–Bentonite Buffer and Host Rock at the G2 Cross Section. [°F = (1.8 × T °C + 32), 1 m = 3.3 ft]

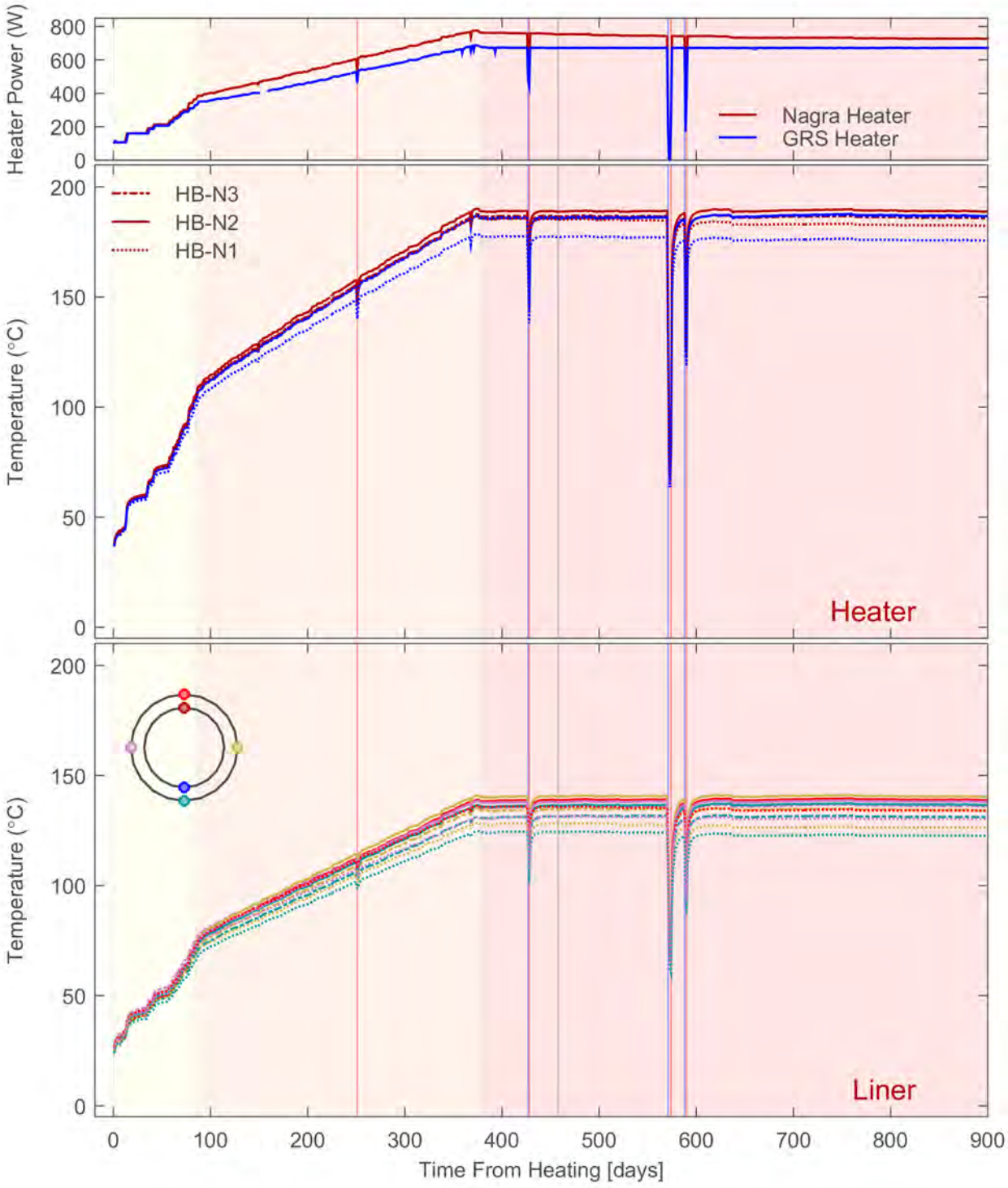

Figure 4-4. Daily Average Measured Heater Power (Top) and Temperatures in the Heater (Middle) and Liner (Bottom) for the Granular Bentonite Buffer Cross Sections. [°F = (1.8 × T °C + 32)]

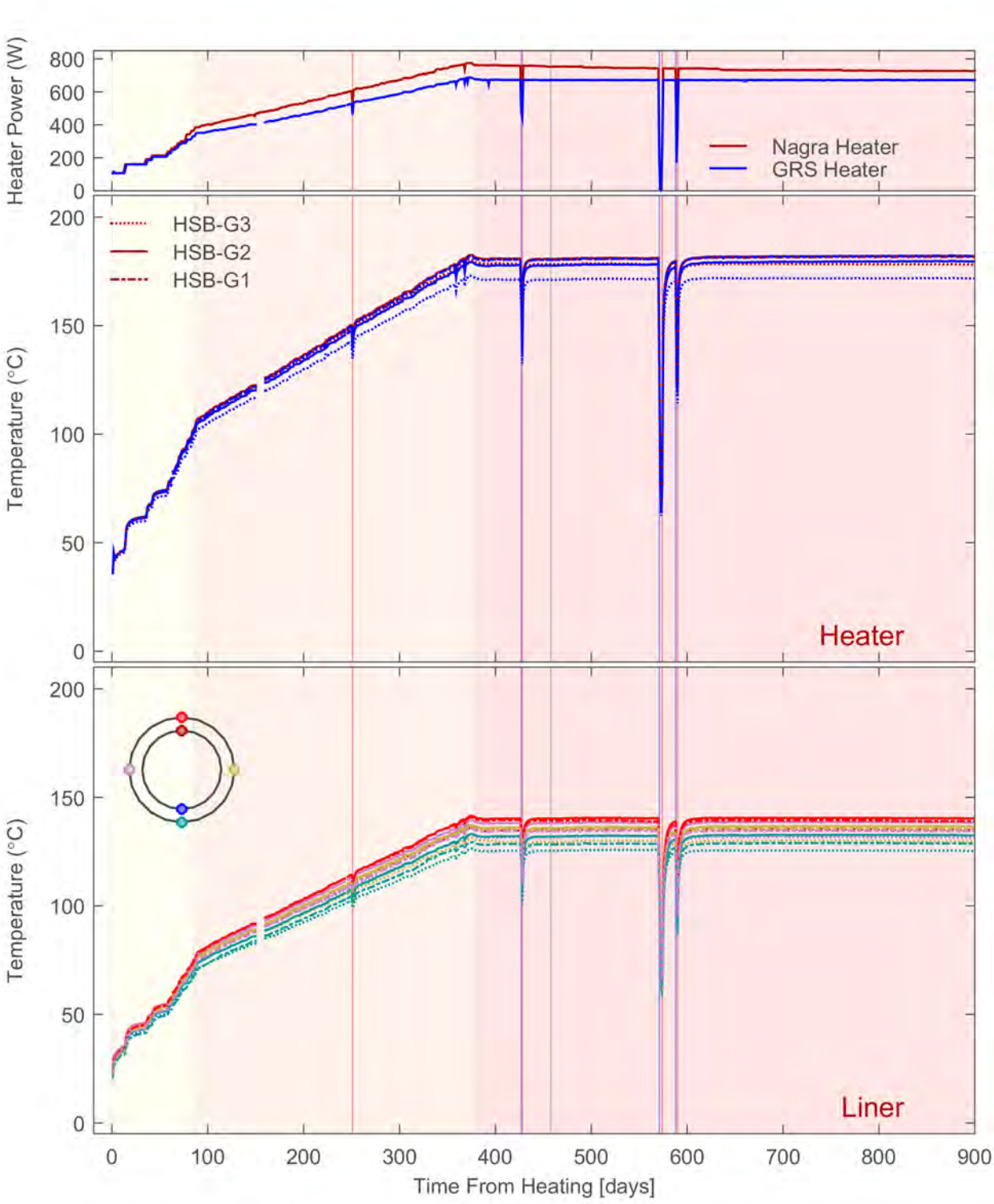

Figure 4-5. Daily Average Measured Heater Power (Top) and Temperatures in the Heater (Middle) and Liner (Bottom) for the Sand–Bentonite Buffer Cross Sections. [°F = (1.8 × T °C + 32)]

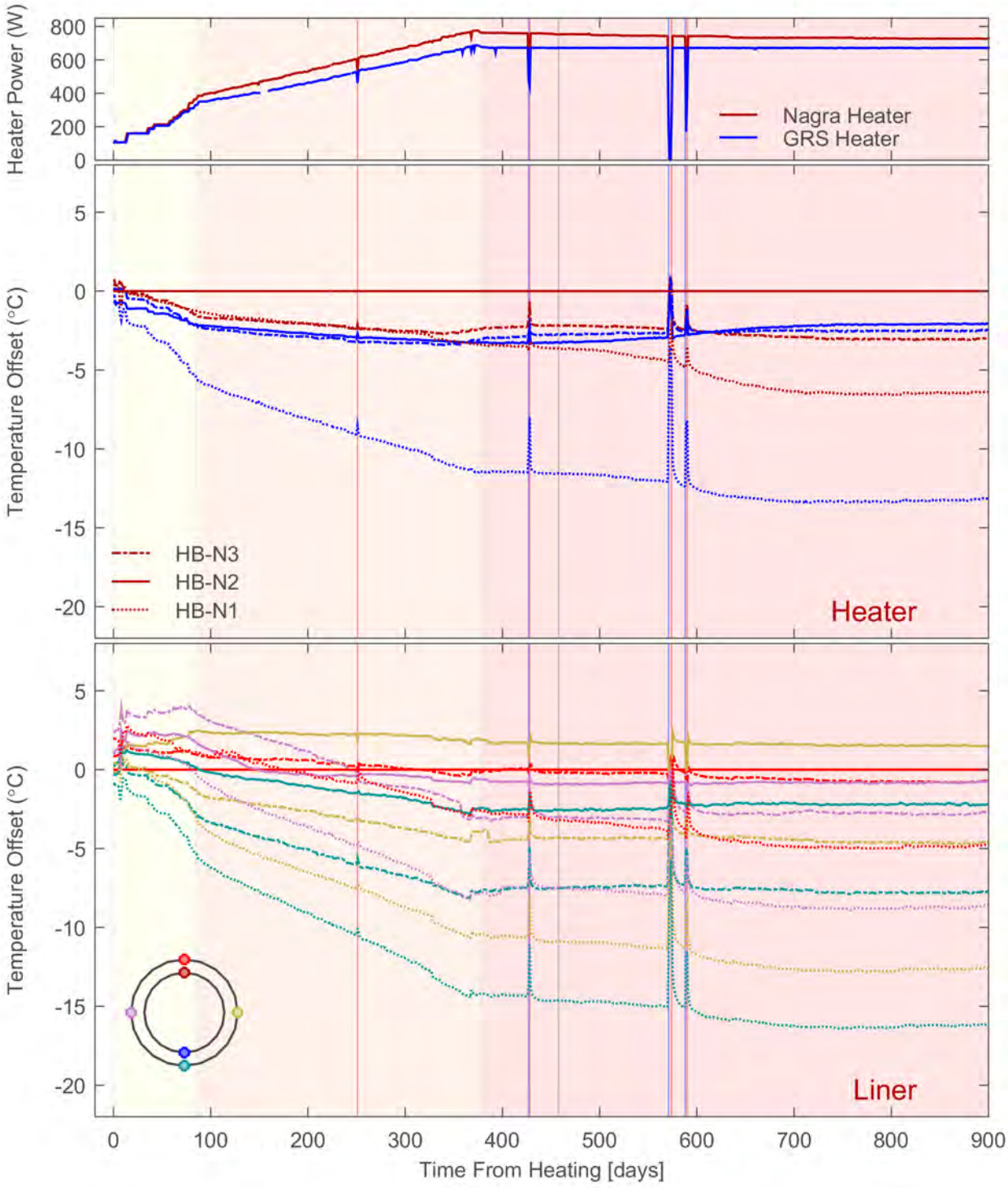

Figure 4-6. Daily Average Measured Heater Power (Top) and Temperature Offsets in the Heater (Middle) and Liner (Bottom) for the Granular Bentonite Buffer Cross Sections. Temperature Offsets are With Respect to the Top Sensor in the N2 Cross Section. [(ΔT)°F = (1.8) (ΔT)°C where (ΔT = Temperature Offset)]

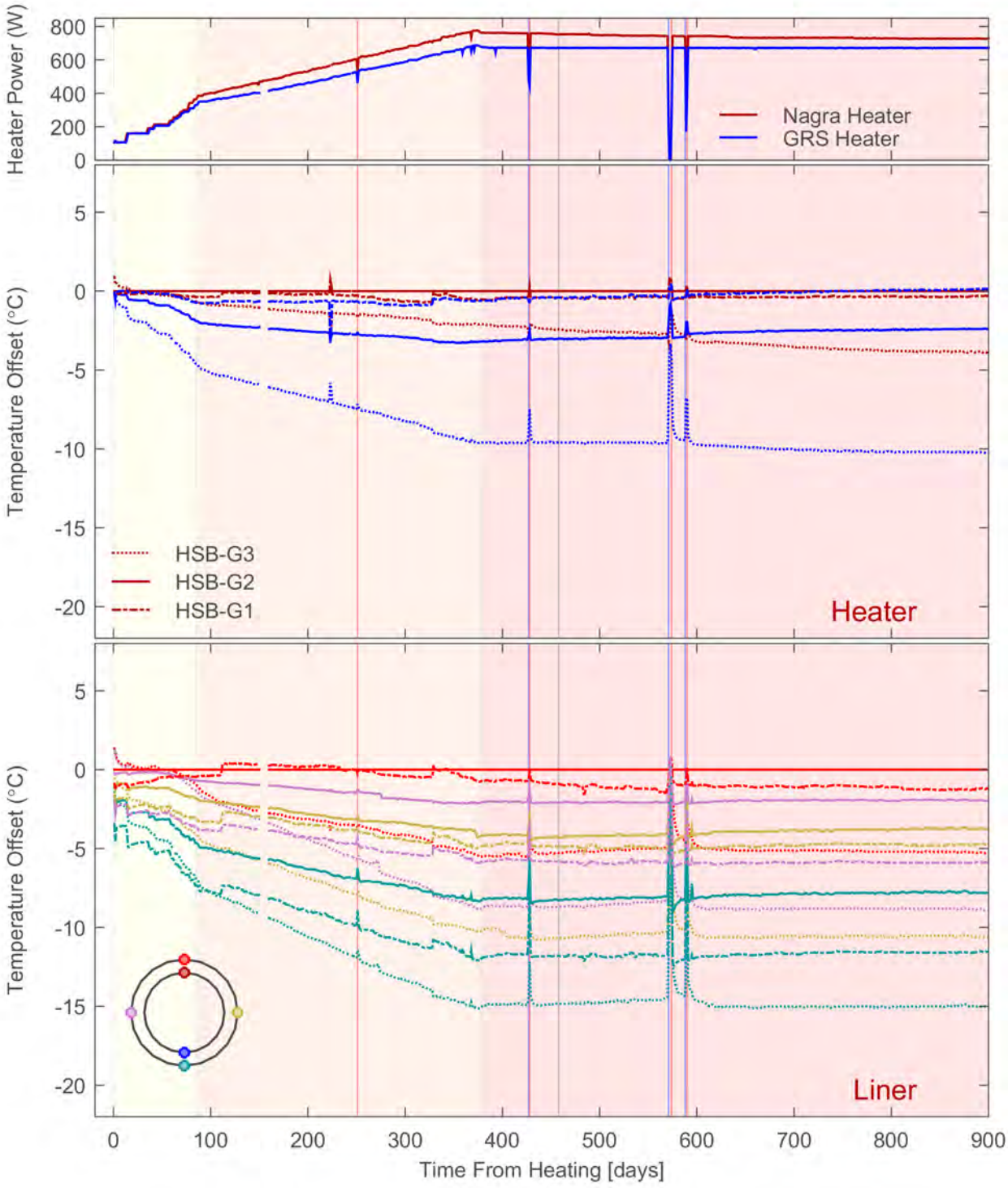

Figure 4-7. Daily Average Measured Heater Power (Top) and Temperature Offsets in the Heater (Middle) and Liner (Bottom) for the Sand–Bentonite Buffer Cross Sections. Temperature Offsets are With Respect to the Top Sensor in the G2 Cross Section. [(ΔT)°F = (1.8) (ΔT)°C Where (ΔT = Temperature Offset)]

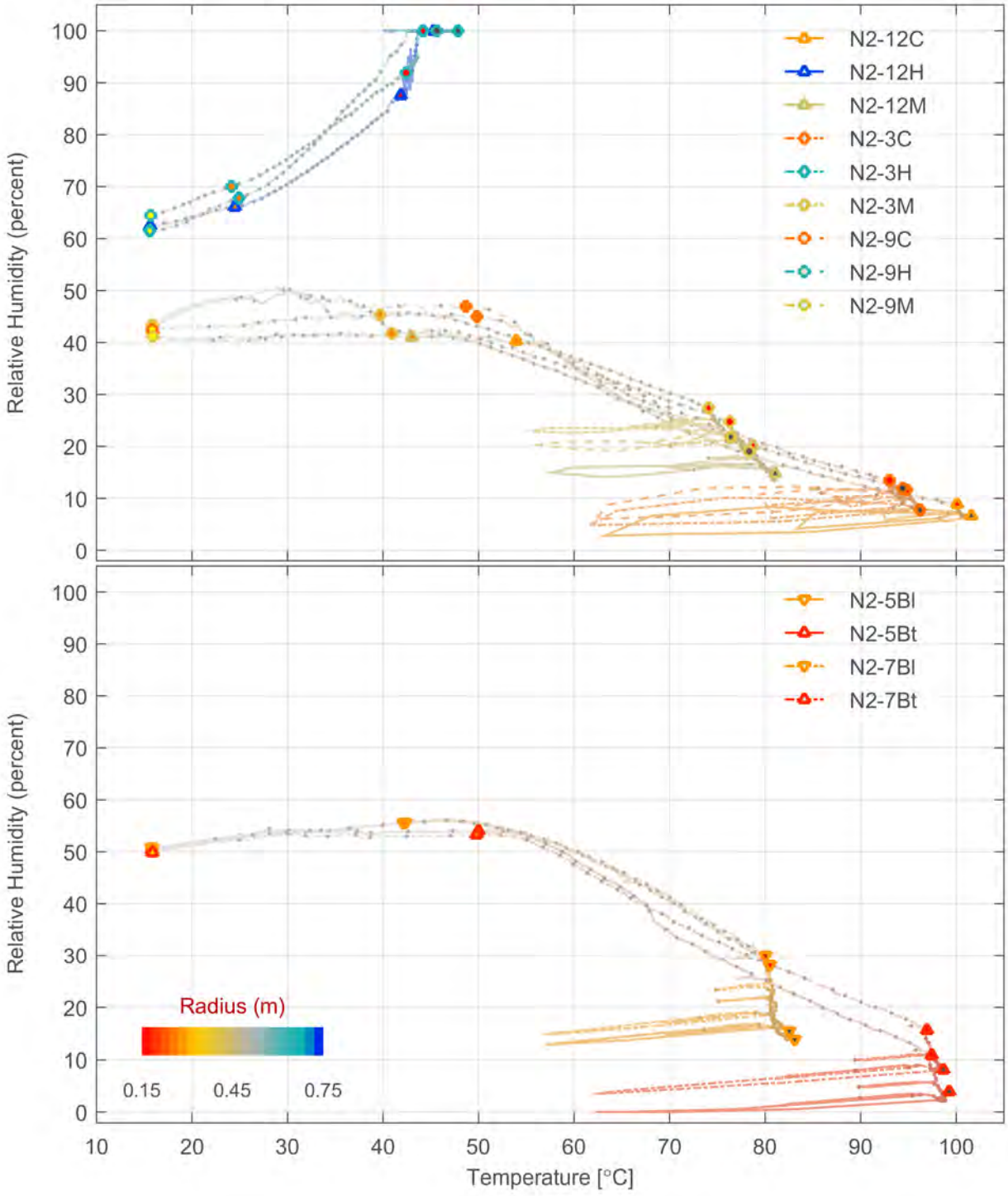

Figure 4-8. Joint Response of Daily Average Measured Temperature and Relative Humidity in the Granular Bentonite Buffer and Host Rock (Top) and in the Bentonite Block Pedestal (Bottom) at the N2 Cross Section. Dots are Spaced 10 Days Apart. [°F = (1.8 × T °C + 32), 1 m = 3.3 ft]

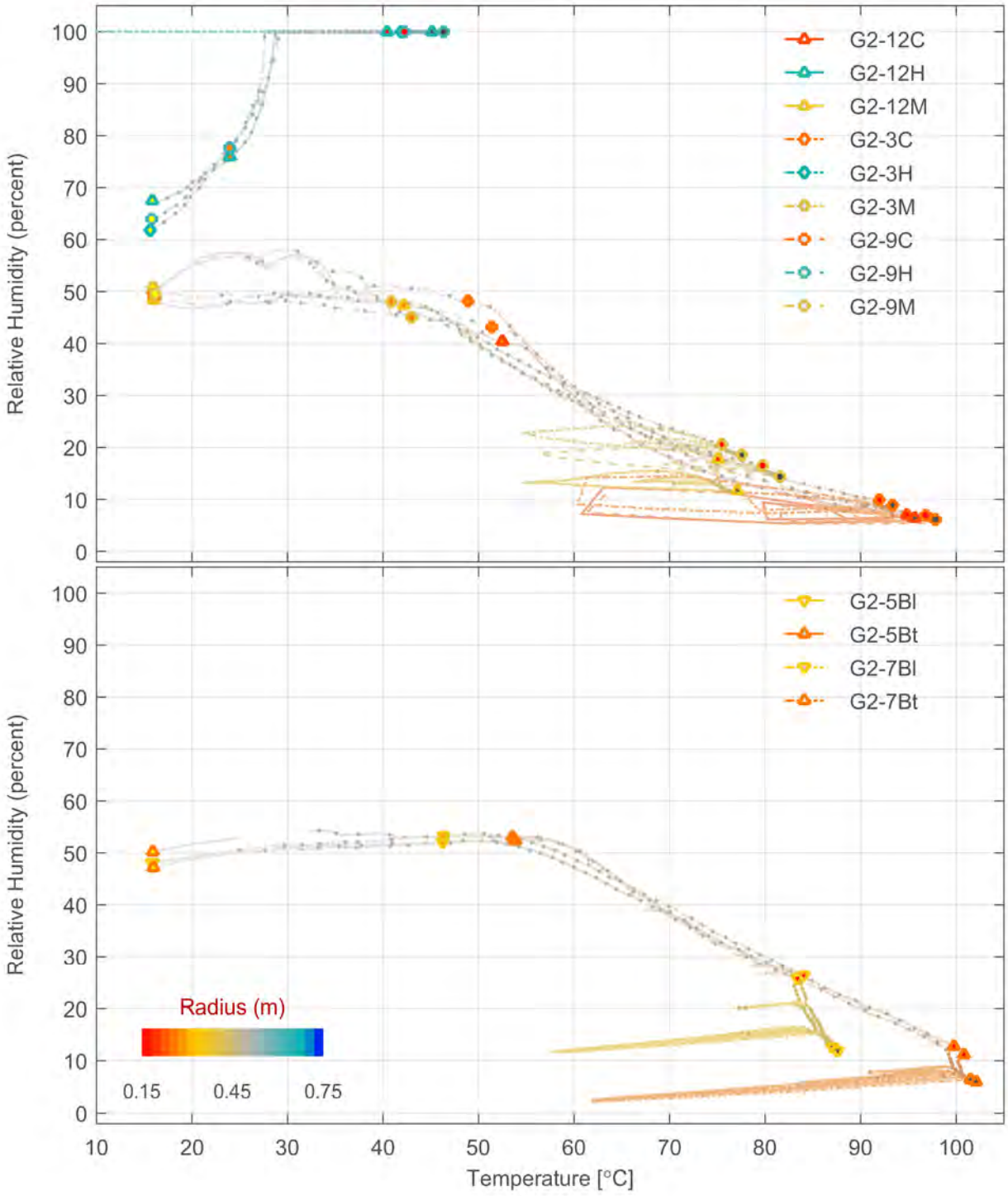

Figure 4-9. Joint Response of Daily Average Measured Temperature and Relative Humidity in the Granular Bentonite Buffer and Host Rock (Top) and in the Bentonite Block Pedestal (Bottom) at the G2 Cross Section. Dots are Spaced 10 Days Apart. [°F = (1.8 × T °C + 32), 1 m = 3.3 ft]

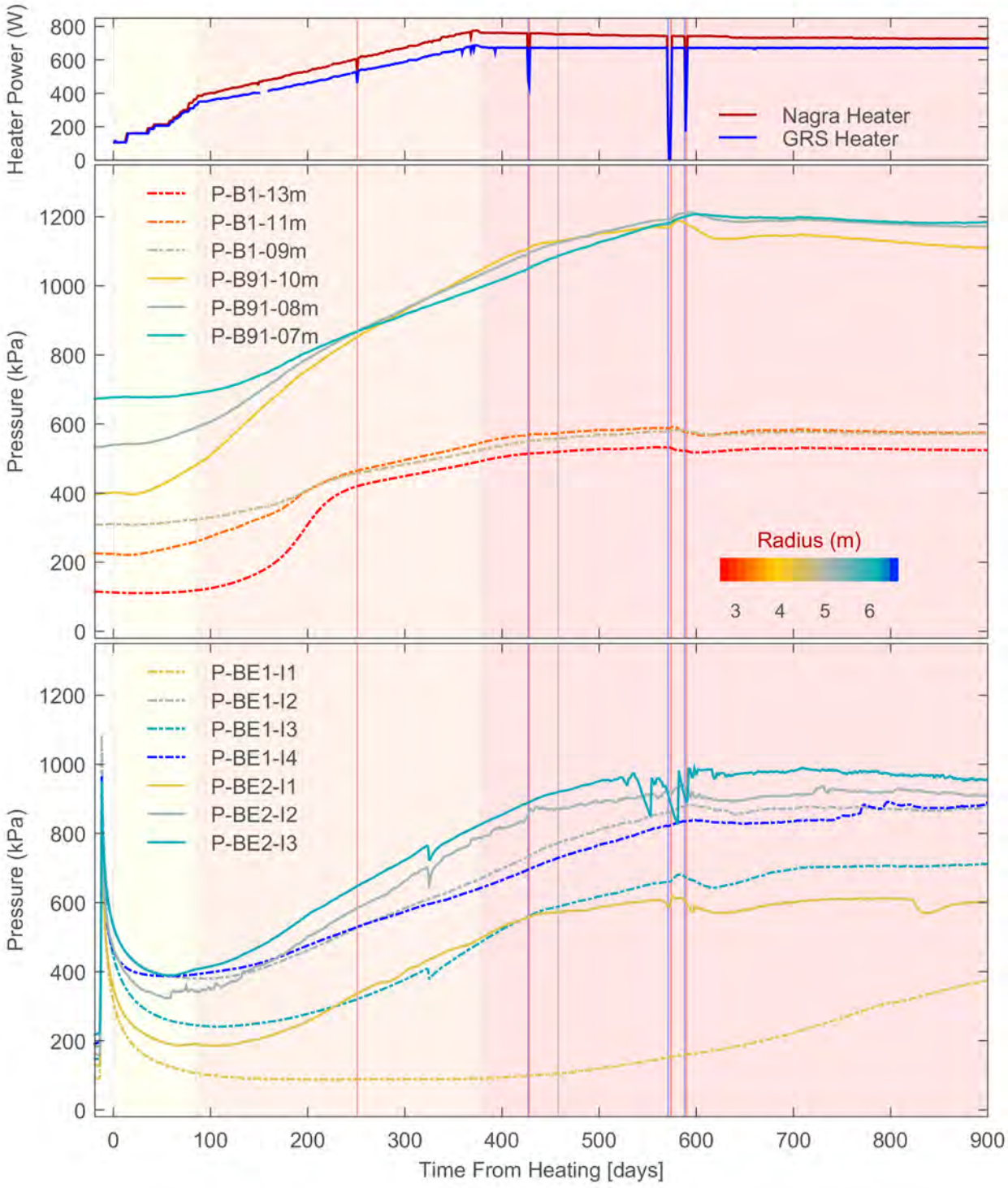

Figure 4-10. Daily Average Measured Heater Power (Top), and Pore Pressure in Slant Boreholes BVE-91 and BVE-1 (Middle) and Subhorizontal Boreholes BE-1 and BE-2 (Bottom). [1 kPa = 0.145 psi, 1 m = 3.3 ft]

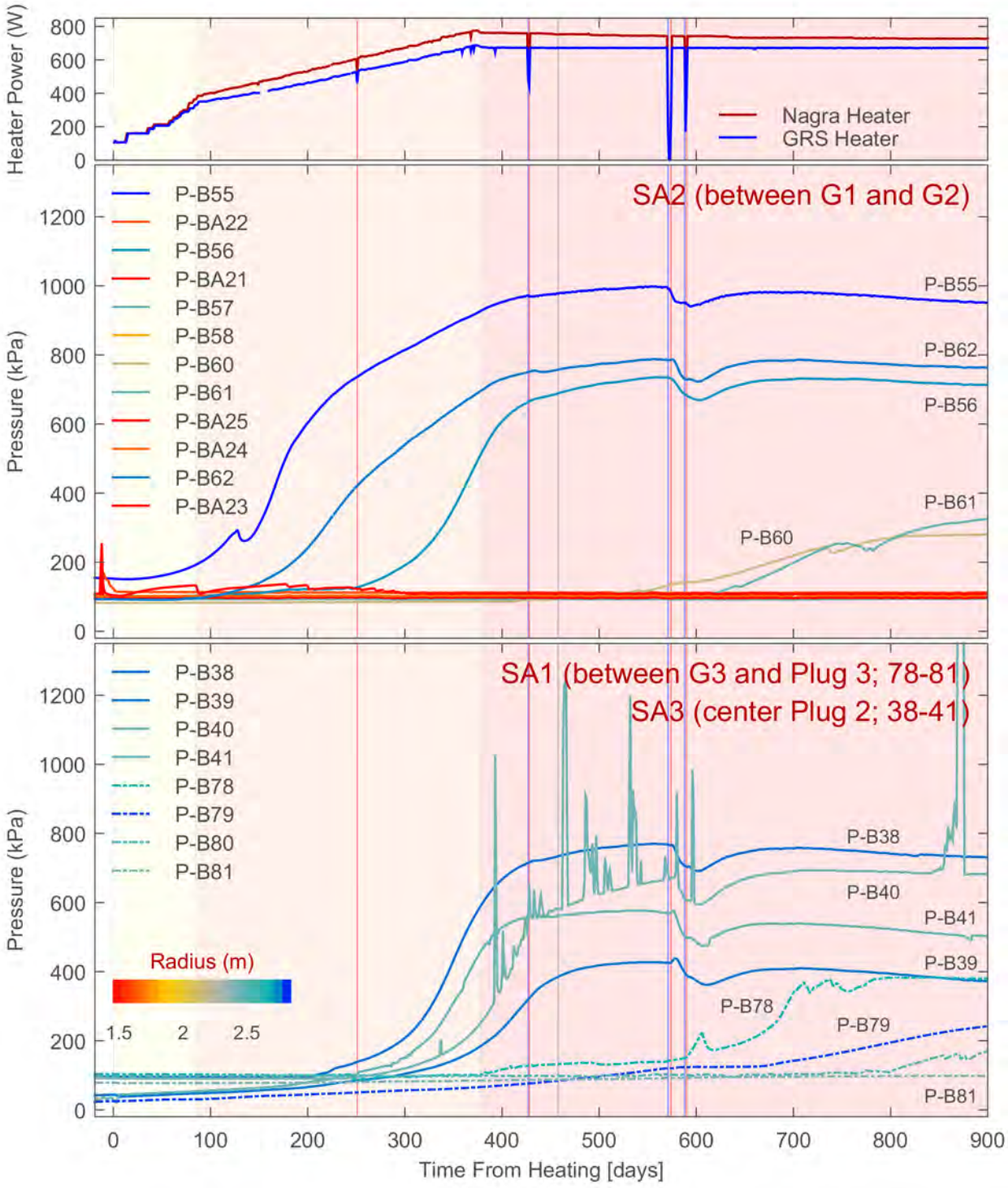

Figure 4-11. Daily Average Measured Heater Power (Top) and Pore Pressure in Boreholes From the Microtunnel (Middle and Bottom), Ordered Clockwise From Vertical in Each Section. [1 kPa = 0.145 psi, 1 m = 3.3 ft]

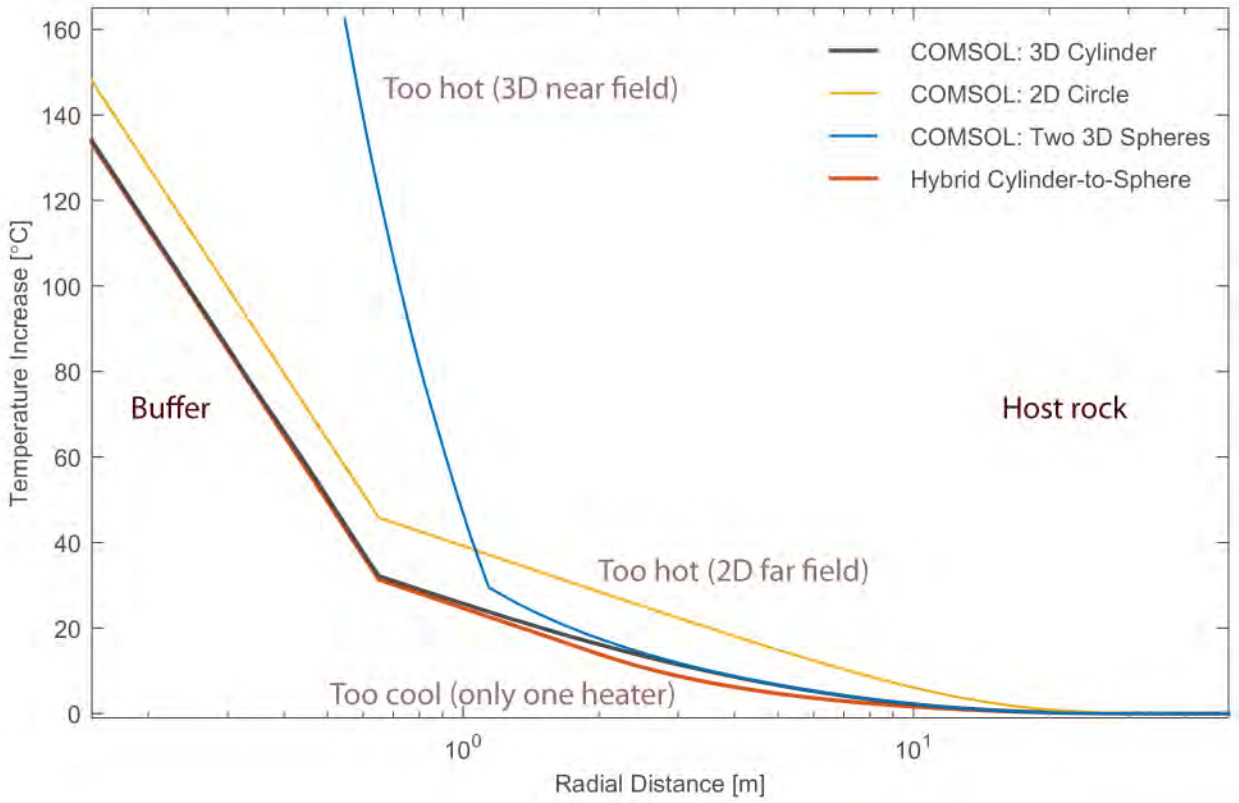

Figure 4-12. Temperature Change After 3 Years in COMSOL and MATLAB Simulations. [°F = (1.8 × T °C + 32), 1 m = 3.3 ft]

5 TASK B1 RESULTS

After task participants presented interim modeling results at the 7th DECOVALEX-2015 meeting, held in April 2015, the Task B1 leader defined the final modeling product as consisting of results from three simulations in two representative cross sections. These simulations were to consider two combinations of input properties (uncalibrated and calibrated) and two long-term heater strategies (the heaters remain on indefinitely and the heaters shut off on June 1, 2019).

Section 5.1 describes xFlo modeling results from the two-dimensional (2-D) cross section model for these three simulations. Section 5.1 also provides a discussion of model results to assess potential model limitations and identify potential future extensions.

As recognized from the start of the HE-E modeling, it is difficult to represent axial fluxes in a 2-D cross section model, and it is useful to use a three-dimensional (3-D) model to assess axial effects. Section 5.2 discusses an initial attempt to extend the 2-D xFlo model into a fully 3-D model, which proved useful for identifying computational limitations in the xFlo code, but the model was too slow to provide results. Section 5.3 describes analyses using a 3-D COMSOL model of steady heat transfer with a detailed representation of the HE-E test. These analyses suggest that (i) relatively little axial heat loss would be expected at the N2 cross section used for the 2-D analysis and (ii) temperature anomalies in the sensor data might be due to poor contact between the buffer and surrounding surfaces.

Section 5.4 describes mechanical analyses using FLAC, which was used to calculate porosity values based on xFlo output as part of the final modeling product. The FLAC analysis provides some insights into deformations that might induce gaps to form at the locations experiencing temperature anomalies.

5.1 Cross-Section Simulations for Task B1

The final modeling product for Task B1 consists of simulation results for three scenarios: (i) the HE-E experiment period, using uncalibrated properties; (ii) the HE-E experiment period extended until rewetting occurs, using calibrated properties and assuming that the heater remains throughout; and (iii) the HE-E experiment period extended until rewetting occurs, using calibrated properties, and assuming that the heater shuts off on June 1, 2019 (7.9 yr after start of heating). The leader devised the two heating strategies to gain additional insight into long-term rewetting processes. The two heating strategies are called the long-heat and short-heat strategies in the following sections.

For each simulation, the task leader requested three types of output: (i) time histories at selected locations, (ii) optional vertical profiles at selected times, and (iii) time histories of summary statistics. The task leader requested time histories for temperature, relative humidity, and liquid pressure; optional vertical profiles of temperature, relative humidity, liquid pressure, porosity, and water content; and time histories of total heat flux into the buffer and total water content in the buffer for both the Nagra (granular bentonite) and GRS (sand–bentonite mixture) sections. Results were requested from the N2 cross section (at the center of the Nagra granular bentonite section) and, optionally, results from the G2 cross section (at the center of the GRS sand–bentonite section). The Center for Nuclear Waste Regulatory Analyses (CNWRA) staff focused exclusively on the N2 cross section simulations, and provided results for all three scenarios.

As discussed in Chapter 4, the NRC/CNWRA team followed an informal model updating process focused on model components with larger uncertainties. In the spirit of the Task B1 comparison, the uncalibrated property set consists of the initial properties for the buffer and bentonite block with a mildly anisotropic but intact host rock (Sections 3.1 and 4.4). The host rock has a horizontal-to-vertical anisotropy ratio of 2.0 for permeability, thermal conductivity, and diffusion coefficients. The cable channel is included in the model in its final configuration, assuming that the lid was made from steel (not Teflon). The cable channel properties remained the same for all subsequent simulations. Note that the uncalibrated property set assumes that the excavation damaged zone (EDZ) is not present (i.e., the EDZ heals soon after heating).

In the spirit of the Task B1 comparison, the calibrated property set (Sections 3.1 and 4.4) consists of the same mildly anisotropic host rock with an EDZ that is sufficiently permeable near the microtunnel to allow rewetting. The model uses the initial host rock retention properties but locally increases permeability around the microtunnel. The interface between the bentonite block and heater liner is adjusted to allow only 20 percent of the block to contact the liner.

5.1.1 Discussion of TH xFlo Simulation Results

This section discusses one of three final simulations for the task in detail. This simulation uses the calibrated parameter set and a transient heater boundary condition consisting of power uniformly applied over the inside of the heater. The other two simulations both use a specified-temperature liner boundary condition with either the uncalibrated or calibrated parameter sets. For the latter two simulations, Appendix B contains equivalent figures corresponding to those presented here.

The spatial distributions of temperature, relative humidity, liquid saturation, pore pressure, and gas pressure as calculated by xFlo at selected points in time are shown in Figures 5-1 to 5-5. The grid is omitted inside the microtunnel for the temperature, relative humidity, and pore pressure figures, and is omitted inside a radius of 1 m [3.3 ft] for the gas pressure plot. The semicircular blank white zone represents the area inside the liner, which is excluded from the domain. The roughly rectangular blank white zone below the liner represents the interior of the cable channel; the grid cells in this zone are disconnected from the simulation. The single grid cell protruding into the cable channel indicates the port in the cable channel wall.

The output times of 0, 180, 367, and 547 days (0, 0.5, 1, and 1.5 years) after start of heating are based on the output dates requested by the Task B1 lead. Days 756 and 1243 (2.07 and 3.4 years after start of heating) are spaced to show simulation progression over time. The simulation imposes total power as the heater boundary condition. To place the output in context of heating, the sparkline in the upper right corner of each subplot indicates the power applied to the heater at the output day. This convention is used throughout section 5 and the appendices.

The initial temperature distribution adjusts approximately in unison with the applied power, especially within the buffer (Figure 5-1). Temperatures are nearly unchanged in the right-hand column. The buffer evolves to be warmest immediately above the liner. The plotting routine does not show the liner itself. Note that the temperature field shows little influence from the cable channel, even though the interior is blocked off from the domain. In fact, the cable channel is a preferential heat pathway because (i) the channel is made of highly conductive steel and (ii) the overlying bentonite block pedestal is more thermally conductive than the surrounding buffer.

The relative humidity distribution, initially uniform by material type, rapidly forms a monotonic profile from dry near the heater to wet in the rock (Figure 5-2). The bentonite block pedestal responds more slowly, with the drying front progressing from the outer top corner towards the bottom interior. Over the same period, a steep relative humidity front builds at the rock wall and gradually progresses inward. The same behavior is visible with respect to saturation (Figure 5-3), except that the bentonite block shows up as distinct from the buffer at all times. The pore pressure distribution (Figure 5-4) also reacts like relative humidity. The pore pressure distribution is clipped in the figure; values adjacent to the liner are more negative than are reflected by the range in the legend.

The evolution of calculated gas pressures (which are the same as pore pressures in the saturated zone) is shown in Figure 5-5 for a larger portion of the model domain. The color scale is in units of kPa, not MPa (as was used for liquid pressure). The red and orange cells on the right side of each box are a result of the atmospheric pore pressure condition applied at Gallery 98. As time progresses, the calculated pore pressures increase several meters from the microtunnel but the zone of near-atmospheric pressure around the microtunnel expands, as well. Note that pressures between the microtunnel and Gallery 98 always form a local trough due to the atmospheric pressures at the tunnels.

The snapshots in time of state variable spatial distributions shown in Figures 5-1 through 5-5 provide insight into the essentially radial evolution of the variables as affected by features such as the bentonite block pedestal and Gallery 98. Comparison with measurements is more precisely illustrated using selected radial profiles approximately aligned with the sensor locations.

The same calculated state variables plotted in Figures 5-1 through 5-5 are also shown in Figures 5-6 to 5-10, but in grid cells along six strategic rays. The color code for the curves indicates the ray orientation. The symbols are plotted using the same color-coding scheme. Note that some curves have a gap where they pass through the cable channel. The interior of the microtunnel is indicated with a white background and the host rock is indicated with a tan background. The profile radius is plotted on a logarithmic scale, which is useful for interpreting behavior when the Laplace equation is governing. Liquid pressures in the saturated zone and temperatures in a conduction-dominated zone are both governed by the Laplace equation once an equilibrium state has been reached, although the thermal and hydraulic conductivities may be anisotropic or heterogeneous.

When steady fluxes are purely radial in a cylindrical coordinate system (i.e., negligible sources or sinks), which appears to be nearly the case based on Figures 5-1 through 5-5, both temperature and pore pressure plot on straight lines with respect to the logarithm of radius in zones with homogeneous material properties. A change in slope indicates a change in material property or local deviation from radial fluxes (e.g., cylindrical or axial fluxes, change in storage). The calculated temperature profiles in Figure 5-6 have nearly straight profiles within the buffer, bentonite block, and host rock that change in slope at the interface between materials. The temperature gradient is steepest near the heater liner and gradually becomes shallower within the buffer, consistent with a smaller thermal conductivity in a drier material. In general, the calculated profiles are consistent with quasi-steady radial fluxes. Cylindrical fluxes are indicated when the profiles have different temperatures at a given radius, but the cylindrical gradients are shallow compared to the radial gradients.

The measured temperatures in Figure 5-6 systematically deviate from the calculated temperatures: (i) the bentonite block temperatures are significantly cooler than the buffer

temperatures, (ii) the temperatures appear to differ from place to place in the microtunnel even though the gradients are similar, and (iii) the calculated temperature range on the heater liner is much larger than the measured temperature range. The calculated temperature gradient in the bentonite block appears to approximately match the gradient between the sensors, but the two are offset by ~15 °C [27 °F]. The calculated temperature profile in the buffer falls between the observations, but has a significantly steeper gradient. The temperatures at the heater liner bracket the observations.

The buffer and bentonite blocks have relatively similar thermal conductivity values at the range of saturations at the inner part of the buffer, and should be essentially constant within the rock. Temperature profiles within a single medium generally follow the linear relationship with respect to the logarithm of radius, but linear projections do not necessarily meet at a joint interface (Figure 5-11). For example, a temperature profile inferred from the 12 o'clock sensor data appears linear from the heater liner through the buffer with a jump of 15 or 20 °C [36 °F] at the microtunnel wall to match the rock profile. The profile inferred from the 6 o'clock sensor data appears to have a jump of ~20 °C [36 °F] at the liner but projected matches at the microtunnel wall agree well. The 3 and 9 o'clock profiles appear to have a jump at the heater liner and microtunnel wall. The 3, 9, and 12 o'clock profiles project to similar temperatures in both the buffer and rock at the microtunnel wall.

The calibration process began addressing the temperature jumps by selectively reducing the contact area between the liner and bentonite block pedestal. This has the effect of reducing the calculated temperature range on the heater liner and altering the gradients in the microtunnel. Section 5.3 further examines the temperature jumps using a fully 3-D COMSOL model, which suggests that the jumps are consistent with a poor interfacial contact.

The calculated relative humidity profiles track the measurements fairly well with respect to timing and reach a similar equilibrium state for the inner buffer and bentonite block sensors and for the rock sensors (Figure 5-7). It should be recognized that misrepresenting the temperature profile may have the side effect of misrepresenting the relative humidity profile, because calculated relative humidity depends on simulated temperature. The corresponding saturation profiles (Figure 5-8) are generally similar to the relative humidity profiles.

The calculated and measured relative humidity profiles differ in potentially significant details, however. In the calculations, the buffer develops an advancing front from the rock wall that has propagated past the outer buffer sensors, especially the 12 o'clock sensor, but the sensors show no sign of any wetting. The calculated relative humidity in the bentonite block responds more slowly than the measurements, but end up in with comparable values. Calculated relative humidity at the rock sensor locations remains somewhat less than 100 percent, but the values may be within the precision level for the sensors. Note that the sensor locations are plotted according to the measured location of the heater axis, which is offset from the microtunnel axis in some locations, but all sensors at the interface are actually located several centimeters into the rock.

The calculated rate of wetting front advance is strongly dependent on xFlo grid resolution. Initial simulations using a prototype 1-D model with various meshes suggested that the front smears over several grid blocks. The mobility is upstream weighted in the xFlo scheme. The combination of upstream weighting and coarse gridding masks the very steep mobility gradients created at the buffer/rock interface as the two materials respond to the required continuity of pressure between materials. Mobility drops many orders of magnitude over the

front, counteracting strong pressure gradients that drive fluxes. The xFlo grid resolves the interface to within a fraction of a centimeter to capture the mobility profile.

Calculated pore and gas pressure profiles are compared to measured borehole pore pressures in Figures 5-9 and 5-10. Note that the pressure units differ by three orders of magnitude between the two figures, and note that xFlo sets gas pressure to pore pressure wherever the porous medium is saturated. The inferred transition from partially to fully saturated conditions is marked by an inflection in the pore pressure profile, usually approximately 2 m [6.6 ft] into the host rock. In Figures 5-9 and 5-10, the symbol color denotes axial position along the microtunnel, with cool colors for the GRS section, gray for Plug 2, and warm colors for the Nagra section. All calculated pore pressure responses are based on xFlo thermohydrological (TH) calculations with no feedback of mechanical responses from FLAC.

The calculated pore pressure profiles evolve over time. The initial 75 days of buffer contact with the host rock developed a strong pore pressure gradient in the host rock as it responded to contact with a medium with a very large initial capillary pressure. Figure 5-9 shows that a sharp pressure gradient is also created in the buffer next to the host rock. These gradients developed as the host rock supplied water to the buffer. The EDZ represented in the parameter set has sufficiently large permeability that the host rock is able to continue supplying water to the buffer. Eventually enough water has moved into the buffer that it becomes nearly saturated at the host rock interface and the wetting front propagates into the buffer. Late pore pressure profiles in the host rock are linear with respect to the logarithm of radius, suggesting that flow of liquid water has reached an approximate steady state. Although not visible with the selected axis scale, a much steeper linear gradient also forms in the buffer as the capillary pressures near the liner drop dramatically in response to heating.

The gas pressure profiles also evolve over time (Figure 5-10). The largest response is in the bentonite blocks, with increased temperatures raising the vapor pressure in the blocks. Over time, the excess pressure in the blocks is relieved as vapor moves into the buffer and the blocks dry. Gas pressure is constrained by the gas pressure boundary condition at the port in the cable channel. Both relative humidity and gas pressure are sensitive to this boundary condition; when the connection is too strong, the buffer dries out excessively, and when too weak, gas pressures in the buffer rise like shown for the blocks.

No gas pressure measurements were available to constrain the model, but indirect evidence suggests that the gas pressures in the buffer may not change much. Pore pressures remain at near-atmospheric conditions within the nearest 1 to 2 m of the microtunnel and have a much larger radial gradient outside this zone (see Section 4.1.2). One way that this condition might occur is if an unsaturated fracture system was connected to the buffer through a saturated host rock in slight tension relative to the gas pressure. If gas pressures were substantially elevated above atmospheric, it would imply that all of the host rock within this zone must have essentially the same elevated capillary pressure in order to remain at atmospheric pressure. Such a capillary pressure distribution would tend to induce radial pore pressure gradients. The lack of observed pressure gradients suggests that (i) the gas pressure is not strongly raised, (ii) insufficient time has passed to develop pore pressure gradients, or (iii) pore pressures are minimally affected by gas pressures.

The calibration process attempted to match the calculated pore pressures in the Gallery 98 boreholes, but microtunnel sensors were not considered in calibration because (i) the data provided by the Task B1 lead were from microtunnel sensors in the GRS section, which was not modeled, and (ii) the data from cross section SA4, which is in a cooler part of the Nagra section,

were not part of the data package. The lack of response in the microtunnel sensor data was counterintuitive and was assumed to be due to sensor failure after the Ventilation Experiment test, but prior to the HE-E test. The one sensor in the SA4 cross section that registered a strong pressure change, P-B7, appeared to fail in the third year of the test, and ultimately dropped to atmospheric pressure consistent with all other sensors in the cross section.

The microtunnel pore pressure sensors cannot be used to draw inferences on gas pressures unless these sensors are reliably reporting pore pressures. Perhaps a packer failure mode is possible where the sensors are reading gas pressure instead of pore pressure, but it is not clear why many microtunnel sensors failed while the Gallery 98 sensors did not. Also, some microtunnel sensors began responding years after the start of heating.

If the microtunnel sensor data is taken at face value, then the calibrated property set results in a substantial misrepresentation of pore pressure responses up to 2 m [6.6 ft] into the rock. The microtunnel sensor data from the SA1 through SA4 cross sections show little inward pore pressure gradient in this region, representing a sharp inflection in the inward gradients implied by the Gallery 98 sensors. The model shows that a strong inward gradient would be expected to form in this region, caused by contact between the buffer and host rock with very different initial capillary pressures. This discrepancy between the calculated response and the observations implies that the buffer and host rock are in poor contact at the microtunnel wall.

The sharp inflection in pore pressure gradients 1 to 2 m [3.3 to 6.6 ft] into the host rock may be explained if the host rock matrix is essentially saturated but gas remains in communication with the microtunnel via fractures penetrating throughout the zone. In the current modeling approach, xFlo uses the host rock retention properties with the EDZ permeability added to the host permeability, which does not fully capture the unsaturated behavior of a fractured rock. xFlo could model this scenario with a dual-continuum or equivalent-continuum approach, where the fractures and matrix each have their own set of water retention relationships. This scenario could be addressed with xFlo in future work.

The inward pore pressure gradients outside the fringe indicate that inward water fluxes are delivering water to the outer fringe. If the system were in a steady or equilibrium condition, the sharp inflection in inward pore pressure gradients implies that these inward water fluxes must be accommodated by inward liquid or vapor fluxes in the fracture system. Outward temperature gradients tend to drive vapor away from the microtunnel, so the presence of inward vapor fluxes would require a significant inward pressure gradient (contradicting observations) to adjust vapor pressures enough to overcome the outward temperature gradient. A more likely explanation is that the fracture system is sufficiently permeable that essentially all of the inward flow transfers to a partially saturated fracture system that requires only a small pore pressure gradient.

Because water moves very slowly in the host rock, pore pressures respond very slowly to water fluxes. As discussed in Chapter 6, pore pressures in the host rock may be dominated by mechanical deformation. In this case, the host-rock pore pressure gradients may be slowly adjusting to the changes in mechanical state and the observed pore pressure gradients may be simply reflecting a slow inward transition to saturated conditions in outer-fringe fractures. The delayed onset of increased pressures in some of the microtunnel sensors is consistent with gradual loss of unsaturated conditions in the outer fringe, either due to rewetting or due to closure of the fractures.

5.1.2 Insights from Sensitivity and Auxiliary Analyses

The auxiliary 3-D analyses performed after completion of the 2-D modeling work suggest that one further calibration step is likely to make the simulated relative humidity and temperature values much closer to the observations in the buffer and near field. The 3-D results strongly suggest that the temperature measurements are consistent with very poor contact between the buffer and host rock. A poor contact would also explain why measured pore pressure gradients in the host rock are small adjacent to the microtunnel despite model calculations indicating that strong pore pressure gradients should develop near the buffer/host rock contact. A poor contact does not restrict vapor transport in any way, however.

Auxiliary analyses of the HE-E displacement data were performed after completion of the 2-D modeling work, described in Section 6.4. The displacement data was provided to the Task B1 teams, but was not considered in any Task B1 model comparisons. The data suggest that the microtunnel wall radius expanded by >17 mm [>0.7 in] after the start of heating, which would have led to poor contact between the buffer and host rock unless the buffer also expanded by the same amount. As discussed in Section 5.4, the current mechanical model calculations, which were intended to focus on buffer deformation processes, show an order of magnitude smaller tunnel expansion than the displacement data. The FLAC code reliably simulates large deformations; the causes for the under-estimate of tunnel expansion may be: (i) the bulk host rock is more thermally expansive than core samples or (ii) the model assumption of linear elasticity for the host rock is inappropriate in the near field. The under-estimate of tunnel expansion makes it difficult to use model calculations to independently estimate how much the buffer would have expanded, and no data are available on buffer displacements. Lateral movement of the buffer material down the slopes formed below the emplacement augur during emplacement promotes preferential segregation of coarser material at the base of the slopes, which would also tend to form a zone with poor thermal and hydraulic conduction between the buffer and host rock.

Auxiliary analyses of the HE-D test, described in Section 6.5, suggest that pore pressures in saturated host rock are almost entirely determined by cumulative mechanical deformation, at least on time scales as short as the HE-E test. If this is the case, xFlo would likely require two-way coupling with FLAC to properly calculate pore pressures in the host rock. Changes in porosity due to host rock deformation would likely be primarily accommodated by an evolving fracture system in the EDZ and by pore deformation outside the EDZ.

5.1.3 Time to Rewetting

The final set of cross section simulations addressed a goal set by the Task B1 leader of estimating time to rewetting for two scenarios: (i) heating continues indefinitely (the long-heat scenario), and (ii) heating turns off at a specified future time (the short-heat scenario). The buffer is considered to be saturated when all the nodes in the buffer have a liquid saturation of at least 99 percent. Two simulations were run using the calibrated property set, which allows rewetting to occur. Both simulations were run for 100 years.

Both scenarios require that power inputs are projected into the future using the current experimental scheme of setting temperatures at the heater liner to 140 °C [284 °F]. This is problematic, because (i) the heater output in the Nagra section experienced a gradual decline after the first year of heating and (ii) measured liner temperatures in the N1, N2, and N3 cross sections experienced a range of ~18 °C [32 °F]. In essence, projecting the future behavior requires (i) explicitly implementing control logic in the model, (ii) projecting future declining

heater output, or (iii) approximating the temperature distribution across the heater liner (which is a potentially significant aspect of the computations).

The short-heat scenario was implemented by imposing a spatially uniform input power to the heater liner interior, following previous modeling. The time history of measured power seemed to show a slowing rate of decline, although the power distribution included measurement gaps and seemed to experience some oscillations later in the experiment. This gradual decline was extrapolated to the shutoff date.

The long-heat scenario was implemented as a constant temperature over the inner heater liner surface, using the measured temperatures in sensor HB_T-TC-H-B-O_1 (the 12 o'clock sensor contacting the heater liner at the N2 cross section). This approach slightly overestimates power into the liner, because radial gradients into the buffer and bentonite blocks are slightly larger with the higher temperatures.

The calculated water mass in the microtunnel projected from the start of the heater period until steady conditions are achieved are shown in Figure 5-12 (top). Three simulations are reported: (i) the initial parameter set with the long-heat scenario, (ii) the calibrated parameter set with the long-heat scenario, and (iii) the calibrated parameter set with the short-heat scenario.

The parameter set used has a strong influence on whether the buffer rewets. The calibrated parameter set primarily differs from the initial parameter set by the inclusion of larger permeabilities in the near field. These simulations suggest that hydraulic properties in the very near field mediate whether the buffer ever rewets. The host rock matrix does not appear to have sufficiently large permeabilities for inward flow to overcome outward vapor fluxes without enhanced permeability immediately next to the microtunnel, and an expanded unsaturated zone forms in the host rock. With a larger permeability to represent near-field fractures (either excavation- or thermally induced) included, however, the buffer rewets. Rewetting is nearly twice as fast if the heater is left on rather than shut down. This is counterintuitive at first, but the faster rewetting occurs because water viscosity decreases with increasing temperature and water flux rates are inversely proportional to viscosity. The viscosity effect is important where the temperatures are elevated, because water viscosity is 2.4 times larger at 15 °C [59 °F] than at 60 °C [140 °F]. Turning off the heater allows a larger mass of water into the microtunnel at saturation, because water becomes more dense with decreasing temperature.

Transient input heat fluxes (Figure 5-12 bottom) are calculated by integrating the heat fluxes over the inner surface of the heater liner. The power needed to maintain a temperature of 140 °C [284 °F] at the liner is a measure of the water content in the buffer, because the buffer thermal conductivity increases with water content. Comparing Figure 5-12 top and bottom shows that the power needed at full saturation is nearly double the power needed when the buffer desiccates.

Staff identified flux inconsistencies while extracting and manipulating fluxes reported in xFlo output files in order to create Figure 5-12 (bottom). The reported radial flux for certain links is reported with two different values near the heater, and the integral of radial flux appears to change with radius near the heater even when equilibrium should have been achieved. These may be a numerical issue related to the sharp contrast in thermal conductivity between the steel liner and the dry buffer or may result from internal bookkeeping inconsistencies. This discrepancy will be investigated as future work.

5.1.4 Discussion of Calculated Rewetting Behavior

Using the calibrated property set, which allows rewetting to occur, the simulations suggest that rewetting occurs significantly faster with the heater left on. The controlling factor appears to be temperature-dependent fluid viscosity near the heater, which influences how quickly the fluid moves through the pore space near the heater. Also, a slightly smaller mass of water is needed to fill the fixed microtunnel volume when the heater remains on, because hot water is less dense than cold water.

The calculated rewetting times are almost certainly too fast because the calibrated property set does not consider poor contact between the host rock and the buffer. It may be the case that, under conditions at the end of the data set, any imbibition into the buffer is balanced by vapor transport to the host rock, so that an equilibrium state forms with no net rewetting. In this case, buffer rewetting would likely be delayed until the host rock and fracture system completely resaturates and allows pore pressures to form inward gradients at the microtunnel wall, likely well after an approximate thermal equilibrium is established. Once the buffer begins to locally resaturate, the buffer should swell and heal the gap. Once this process begins to occur, there presumably would be a positive feedback due to local swelling that allows the contact area to expand relatively rapidly.

The rewetting times calculated by xFlo should be reasonable for the period after contact between buffer and host rock is restored, assuming that the EDZ fractures near the microtunnel wall do not completely heal. The model does not consider healing, which would tend to slow rewetting, but likely underestimates the EDZ permeability prior to heating based on hydraulic tests in the EDZ around Gallery 98 performed during the Excavation Disturbed Zone-B (EDB) experiment (Martin et al., 2004).

5.2 Three-Dimensional Analyses with xFlo

Once the 2-D cross section analyses neared completion, staff performed a few additional auxiliary simulations to build insight into the importance of axial and end effects that are neglected in 2-D cross section simulations. The limited time available precluded developing a coupled xFlo/FLAC model, so only TH processes were considered. The first analysis alternative that CNWRA staff considered was using xFlo to perform transient TH simulations. After it became apparent that very limited progress would be achieved with the developed transient nonlinear 3-D xFlo model due to the computational burden, staff instead used COMSOL to perform steady linear 3-D thermal simulations and develop additional insight (Section 5.3).

Staff considered two approaches for examining axial TH processes using xFlo: (i) an axisymmetric 2-D model or (ii) a fully 3-D model. The axisymmetric 2-D model is usually an appropriate second model for considering axial redistribution, but staff skipped directly to the fully 3-D model. The following rationales justified developing a fully 3-D model:

- An axisymmetric 2-D model inherently cannot consider properties that change in the circumferential direction. Accordingly, effects of the bentonite block pedestal, cable channel, local cable port openings, and host rock anisotropy cannot be addressed. CNWRA staff were especially interested in probing the effects of these features.

- The input files would be created using MATLAB-based preprocessing software extended from the 2-D cross section model. Given that the 3-D grid would be developed by segmenting a 2-D axisymmetric grid, there would be little difference in the

effort required to extend the preprocessor between an axisymmetric 2-D model and a fully 3-D model for the HE-E test.

- An axisymmetric 2-D model and a fully 3-D model of the HE-E test both must consider a fair amount of detail with respect to material properties and the geometry of the zones to which they are assigned. Developing this information requires the same effort for both models, and there is little difference in the effort required to include the information in the preprocessor.

- The current version of xFlo has been used for 1-D and 2-D applications. A fully 3-D model provides an opportunity to evaluate model capabilities in a demanding context.

A detailed 3-D model requires much longer computational times than the 2-D cross section model, thus at most a few preliminary simulations would be possible in the limited time available. Accordingly, the model was intended to (i) focus on factors potentially driving axial mass and energy fluxes, (ii) develop insights into methods for approaching similar problems, and (iii) provide a computational test to assess xFlo performance.

5.2.1 Grid Development and Rationale

The 2-D cross section grid provided the starting point for the 3-D model. The cross section model partitions cylindrical shells along their circumference within a radius of 2 m [6.6 ft], and partitions spherical shells into lune shells outside the 2-m [6.6-ft] radius. A lune is the area bounded by two great circles on a sphere (e.g., longitude lines on a globe). To develop cell dimensions, first a set of discrete radii were selected for the circumferential interfaces between nested cells. Concentric radii had small separations to capture fine detail near contrasting materials and gradually zoomed out elsewhere. In the inner cylindrical zone, the cylinders were assigned the same length as the Nagra heater to calculate the interfacial area between nested cells. In the outer spherical zone, only the radius is needed.

The 2-D model was constructed so that a logically rectangular grid was distorted to be approximately parallel and perpendicular to the flow paths. This approach minimizes numerical dispersion and is readily converted into a FLAC grid.

Simply replicating the 2-D grid at intervals along the axis of the microtunnel works well within the microtunnel walls. Figure 5-13 illustrates the partitioning along the microtunnel. For the 3-D model, cross sections are spaced closely near plugs and further apart near the center of buffer sections to capture material property contrasts. Cross sections are placed to segregate plug material types, subdividing larger material zones to keep spacing relatively consistent.

The far-field grid is calculated and generated by constructing spherical shells and partitioning them into lunes. The lunes were further partitioned to represent the cross sections along the axis of the microtunnel. Splines were used to smoothly interpolate between the microtunnel and far field, requiring that the spline was perpendicular to both the cylindrical microtunnel wall and the sphere marking the transition to the far field. Each spline was subdivided with a set of consistent length fractions to mark off cell boundaries. This procedure yields cell interfaces that are approximately aligned with the microtunnel near the microtunnel, and with the outer boundary in the far field. The end grid should be reasonably well aligned with flow paths, especially in the buffer zones of primary interest.

The grid attempts to be aligned parallel and perpendicular to flow lines, but the boundary makes a 90° turn at the junction between the microtunnel wall and the outside edges of Plugs 1 and 3. This corner creates a singularity in the flow paths. The splines ease the singularity by rounding the corner, but the grid cells are unavoidably deformed near the singularity. The spline curvature is a tuning parameter to adjust the grid shape, and several iterations were needed to mitigate issues with grid distortion, size, and spacing in the rock near the plugs. The distorted grid cells in this area may be prone to convergence issues during computations.

5.2.2 Simulations

The 3-D simulations were intended to focus on interactions between the buffer and host rock. Accordingly, the simulation period started with emplacement of the buffer material 75 days prior to start of heating.

The 2-D and 3-D simulations used the same initial conditions in the buffers, and used the same uniform initial temperature throughout the domain. Two additional initial conditions must be specified to represent the air and water masses in the system, but these are not well known and proved problematic for the host rock and plugs. Under saturated conditions, xFlo expects dissolved air concentration and water pressure. Under unsaturated conditions, xFlo expects gas saturation and gas pressure. For the 3-D simulations, the initial conditions for air and water strongly influenced time stepping during the spin-up phase of simulations.

xFlo uses an adaptive scheme to adjust time steps based on several user-specified convergence criteria. The scheme seeks to increase time step size after successfully converged time steps and repeats failed time steps with a smaller time step size. A time step failure occurs when the solver requires excessive iterations to reach a convergence criterion or it encounters an invalid number. This process typically results in a zig-zag convergence pattern, with steadily increasing step size until a failed step occurs, a sharp drop in step size due to one or more failures, and a return to increasing step sizes. Adaptive time stepping commonly reduced time steps to smaller than micro to milliseconds to achieve convergence during the first simulations, which is too small for practical 3-D simulations using available computational resources. Such a small time step was common during the spin-up phase of simulations whenever the initial conditions did not represent a near-equilibrium state.

To provide a benign near-equilibrium initial condition in the host rock, water pressure was assumed to vary approximately cylindrically with radial distance from the microtunnel wall, consistent with a steady flux from the far field to a specified capillary pressure determined by the relative humidity at the tunnel wall, with a spatially uniform gas partial pressure. This procedure created an unsaturated zone around the microtunnel. A small initial dissolved air concentration was assumed within the saturated zone.

The plug materials were all assumed to be unsaturated. Initial conditions based on estimated material properties were applied; these are uncertain but are unlikely to affect conditions in the middle of the buffer sections. The strong contrast between the host rock and materials in the microtunnel can create very sharp initial saturation gradients. The initial condition for concrete was found to strongly limit time steps when it creates strong pressure gradients; this situation occurs in the concrete unless the concrete is almost saturated.

When the water content and temperature of concrete was set to near equilibrium initial conditions, time stepping is typically controlled by convergence in grid cells at the interface between saturated and unsaturated conditions. This transition forms a shell around the

microtunnel. For an initially saturated host rock, the shell grows steadily over time. In the 2-D simulations, the unsaturated zone reached 1 to 2 m [3.3 to 6.6 ft] into the host rock.

Movement of the saturation transition front controlled time stepping in the 2-D simulations, but proved to be a much stronger control for the 3-D simulations. Relatively large gas fluxes into a cell occur with the threshold increase in gas permeability in a cell transitioning from saturated to unsaturated. In the 2-D grid, movement of the front is essentially perpendicular to the radial direction, so the gas fluxes are essentially 1-D. The 3-D grid is somewhat skewed relative to an advancing front, so convergence along the front is also affected by brief strong lateral gas fluxes along the front.

Model testing was performed to examine the slow convergence rate at the saturation transition front. The xFlo solution procedure uses different state variables for saturated and unsaturated conditions, switching between variables at the transition. The testing revealed a small inconsistency between the two formulations, which had the effect of spuriously creating mass. Removing the inconsistency substantially improved convergence, but convergence rates in transition fronts still strongly control the overall simulation time step.

Only one 3-D simulation completed the entire 75-day period between initial buffer emplacement and started the heating period. Time steps gradually increased over the 75-day period. Prior to heating, the time steps tended to oscillate between roughly 0.05 to 5 minutes, and one day of computational time achieved approximately 6 days of simulation time on a workstation. For comparison, each of the final 2-D simulations (including a 15-year equilibration period used to stabilize conditions and 100 year simulations after start of heating) ran in less than two hours on the same workstation. The simulation continued into the heating period, but the time steps began reducing as the saturation front started receding after the start of heating. By 35 days after start of heating, the average time step dropped by a factor of 4.

The 3-D simulations point to the need to properly address convergence in cells at the transition between saturated and unsaturated conditions.

5.3 Three-Dimensional Analyses with COMSOL

The 2-D cross section analyses inherently assume that the end effects associated with a finite-length heater are negligible at the N2 cross section. After completing the final set of 2-D model runs, CNWRA staff developed a detailed steady-state 3-D thermal model using COMSOL to assess end effects and provide independent confirmation of xFlo calculations. The COMSOL model also offers the opportunity to test assumptions regarding thermal contact between the buffer and other components using a thin resistant layer. Temperature profiles within the microtunnel and near field respond relatively quickly to temperature changes, thus the steady solution should be representative of the test conditions within the first year after peak power has been achieved.

5.3.1 Model and Base Simulation

The detailed 3-D model geometry of the HE-E test components are illustrated in Figure 5-14. Each of the components is described in Section 1.1. Parameter values for the model are based on the xFlo parameter set, as described in Sections 3.1 and 4.4. The horizontal thermal conductivity is twice the vertical thermal conductivity in the rock and isotropic otherwise. The HE-E test is embedded in a cylinder that has a radius of 20 m [65.6 ft] and length of 40.44 m [132.7 ft]. Symmetry is assumed on both sides of a vertical plane, thus only one side of the

plane is considered and a zero-gradient condition is imposed on the vertical plane. The applied power, uniformly spread over the inner surface of the liner between the plugs bounding each section, is comparable to peak applied power during the HE-E experiment (720 W over the Nagra heater and 670 W over the GRS heater).

The model explicitly includes thermal barriers such as rockwool insulation and the Teflon couplings in Plugs 2 and 3. To ease COMSOL gridding, the cable channel is represented as a cylindrical feature with the same effective cross-sectional area for steel used in the xFlo model and the Teflon couplings are centered on the rockwool layer. The as-built drawings suggest that the coupling is offset from the insulation, perhaps allowing additional heat transfer.

The N2 cross section of the Nagra test section is explicitly included in the COMSOL (the half-disk on the left section of Figure 5-14). The cross section only affects gridding, allowing output on selected surfaces and volumes. Three thin resistant layers are imposed on the Nagra section, representing the buffer–heater contact, bentonite block–heater contact, and buffer–rock contact. These thin resistant layers, which were not included in the xFlo model, can be used in COMSOL to represent partial contact with the heater and rock, either due to air gaps or due to poor grain-to-grain contact.

The calculated COMSOL model temperature distribution at the N2 cross section is slightly elliptical (Figure 5-15). The 2:1 thermal conductivity anisotropy yields a slightly flattened temperature ellipse. The hottest temperatures in the cross section are found at the top of the heater liner, but temperatures are warmer below the microtunnel than above because of enhanced heat fluxes through the bentonite blocks and cable channel. The peak calculated temperatures on the heater liner are ~20 °C [36 °F] less than measured, or 86 percent of the observed temperature increase.

The COMSOL-calculated heat flux streamlines at the N2 cross section (Figure 5-16) have release points uniformly spread over the inner surface of the heater liner within three zones, each 20 cm [7.9 in] wide in the axial direction. Dark red streamlines start above the liner springline (horizontal midpoint) and yellow streamlines start where the liner contacts the bentonite block. The red streamlines start in a relatively thin swath above the bentonite blocks and below the springline. All of the streamlines are displaced in the clockwise direction in the liner. Note that all of the red streamlines started where the liner contacts the buffer, but are displaced to pass through the top of the bentonite blocks. Also note that streamlines converge into the cable channel, which acts as a thermal conduit.

The COMSOL-calculated horizontal and vertical temperature profiles for the N2 cross section (Figure 5-17) are similar to the xFlo profiles, with a similar spread of temperature along the heater liner and a similar cluster of profiles within the buffer and bentonite blocks. The COMSOL-calculated profiles are cooler for the same temperature input.

5.3.2 Axial Heat Fluxes

The bentonite block exhibited cooler measured temperatures than were calculated by xFlo in the initial 2-D simulations, and various approaches were considered to better match the temperatures during the model development process. One approach treated the cable channel as a 1-D axial link to the ambient temperature, allowing heat loss. The rationale for considering this axial pathway was based on the column test, which showed a strong influence on thermal redistribution due to the presence of the highly conductive stainless steel sheath. Including the 1-D link in xFlo simulations had a small influence on calculated radial temperature gradients in

the bentonite block, and dropped heater temperatures by 5 to 10 °C [9 to 18 °F]. During model development, the representation of the cable channel was also changed from the initial conceptualization of a void space without any steel walls. Including the steel channel walls in the cross section reduced heater temperatures by a much larger amount than including axial fluxes, leading to the tentative conclusion that axial heat loss in the steel channel may not be necessary to include in the 2-D model after all. The 3-D COMSOL model provides a means to assess this conclusion regarding lateral heat loss.

Figure 5-18 (top) shows heat flux streamlines starting at the inside of the heater liner in a thin swath between the springline and bentonite block (the same circumferential zone indicated by the red streamlines in Figure 5-16). Streamlines starting in the Nagra section are yellow or red, with the streamlines starting in the 20-cm [7.9-in] wide zone at the center of the Nagra section indicated by red. Blue streamlines start in the same thin swath in the heated part of the GRS section. All of the streamlines exit the buffer in the bottom half of the microtunnel. Even though none of the streamlines start in a plug, approximately 14 percent of the Nagra streamlines enter the host rock from Plugs 1 and 2, implying that approximately 14 percent of the power is lost to the plugs. Plug 1 receives 86 percent of the lost power.

The streamlines starting in the N2 cross section exhibit a small amount of axial displacement within the microtunnel, but remain almost parallel (Figure 5-18 bottom). Manually measuring the axial spread between streamlines in a screen plot reveals that the spread is ~2.5 percent larger at the microtunnel wall than at the inner part of the heater, suggesting that axial heat spread within the microtunnel accounts for ~2.5 percent of the applied power near the N2 cross section. The streamlines starting within the N2 section have spread by ~30 percent at the 2-m [6.6 ft] radius. For comparison, in the 20-cm [7.9-in]-long representative N2 cross section, the total heat flux across (i) the inner face of the heater liner, (ii) the tunnel–rock interface, and (iii) a 2-m [6.6-ft] radius is 17.95, 17.5, and 13.77 W, respectively, showing a drop in power of 2.6 and 30.4 percent, respectively.

The periphery of the microtunnel includes four sections: (i) above the springline, (ii) between the springline and the invert, (iii) the floor to the cable channel, and (iv) the bottom of the cable channel. The invert is modeled as having the same properties as the rock. The top half of the microtunnel receives 43 percent of the heat flux, as a result of preferential heat loss through the bentonite pedestal. The average heat flux into the host rock is 35.9 W/m^2 in both the second and fourth sections; above the springline the average flux is 36.8 W/m^2 Along the invert, however, the average flux is 48 W/m^2. This is consistent with the consolidation of streamlines through the bentonite blocks, into the cable channel, and subsequent spreading across the floor shown in Figure 5-16.

Heat fluxes in the steel components are readily calculated in the fully 3-D COMSOL model. Viewed in an orthotropic projection are calculated (i) temperature, (ii) axial heat flux in the metal components (heater liner and cable channel), and (iii) the ratio of axial heat flux to total heat flux in the metal components extracted from a simulation with nominal parameters (Figure 5-19). Figure 5-19 plots these outputs on the inner surface of the metal components. The right side of the heater in Figure 5-19 passes through Plug 3 (the access to MI niche).

The calculated temperature drops of approximately 4 to 5 °C [7.2 to 9 °F] from the top to bottom of the heater liner are similar at all points along the heater liner, just like measured liner temperatures. The axial temperature gradient and the fraction of thermal flux in the axial direction are both nearly zero near the heater center, supporting the assumption that a 2-D cross section captures essential flux patterns near the center of the heater sections, but the

axial gradient is much larger near the plugs. This behavior reflects a gradually increasing axial heat flux towards the plugs. This behavior occurs even though power is applied uniformly over the heater segments between the plugs. The hottest location on the heaters is offset from the heater center towards the central plug.

The axial heat fluxes in the cable channel are much smaller than the axial fluxes in the heater liner. This confirms the tentative conclusion from the 2-D modeling that the 1-D axial link representing axial heat losses in the steel cable channel did not contribute significantly to the 2-D model. A 1-D axial link to the boundary condition applied to the heater liner would have had a larger effect on the energy balance. Note that the xFlo model can only calculate a 1-D axial heat loss in the heater liner when the boundary condition from the heater is represented as heat flux rather than specified temperature. It may be difficult to justify the strength of the connection, however, without insights from full 3-D modeling. Given 3-D model results for guidance, it may be more attractive to simply reduce the applied power by a fixed percentage to account for axial losses.

The average axial heat flux through the heater liner at Plug 1 is 3000 W/m^2. The cross-sectional area of the 8-mm [0.31-in]-thick heater liner is 0.0071 m^2 [0.076 ft^2], so the heat loss out the end is approximately 21 W. The heat loss in the heater liner at Plug 2 is about a third as large, suggesting that the total heat loss from the heater liner is less than 4 percent of the applied power. Heat fluxes in the cable channel are negligible compared to this loss, but lateral heat loss over the much larger area of the plugs may be significant.

These results suggest that axial heat flow in the heaters (which is not included in the modeling) may have comparable effects to axial heat flow in the heater liner, because measured temperatures for the heaters show similar axial temperature gradients as the liner. Teodori and Gaus (2011) describe the heater construction. Each heater comprises three cylinders, two of stainless steel and one of carbon steel. Total metal cross-sectional area is 0.0107 m^2 [0.12 ft^2] suggesting that axial heat flux in the heater exceeds axial heat flux in the liner. The heaters are completely enclosed and separated from the heater liner using Teflon centralizers, with no other physical contact to the liner, so heat fluxes must pass through the liner and do not have direct contact with the plugs. The two heaters are separated by 47.6-mm [1.9-in] diameter PPS-Carbon fiber tube with 1.9-mm [0.07-in] wall thickness and an aluminum tube with similar dimensions extends from the GRS heater through Plug 3. The two rods are wrapped with rockwool for isolation.

With this configuration, heat transfer to the heater liner should be dominated by radiative transfer and therefore transfer is predominantly radial from the axis. Because of axial transfer in the heater, the power transferred to the liner will be slightly smaller than nominal at the center of each test section and slightly larger than nominal at the ends of each test section.
The temperature drop from the heater to the far field is proportional to applied power, so overestimating the effective power load to the N2 cross section by 1 percent (i.e., neglecting axial heat loss of 1 percent) will increase a calculated heater temperature of 140 °C [284 °F] {124.5 °C [225 °F] above the ambient background temperature} by 1.245 °C [2.2 °F]. Neglecting a heat loss of 5 percent of applied power due to axial heat fluxes with accurate thermal conductivities in the buffer and bentonite pedestal would raise heater liner temperatures by 6.25 °C [11.3 °F] in the xFlo 2-D model. Accordingly, it would be expected that the xFlo-calculated liner temperature should be somewhat larger than measured if the buffer thermal properties are accurate.

5.3.3 Temperature Drop at Interfaces

The mismatch between measured and calculated temperature profiles in the radial direction is a second lingering concern with the xFlo simulations. As shown in Figure 5-17, calculated temperature profiles are approximately loglinear with radial distance from the heater liner to the host rock, with a break in slope at the host rock. This is the expected behavior for piecewise constant thermal conductivities in a radially diverging cylindrical system. However, when the measured temperatures within the buffer are loglinearly extrapolated to the heater and host rock (Figure 5-11), there appears to be a substantial temperature drop at some buffer boundary surfaces. This is especially noticeable for the side and bottom of the heater, and at the buffer–host rock interface. A poor contact between the different materials would create such a temperature drop. Presumably, a poor contact at the buffer–host rock interface also would restrict liquid transfer under unsaturated conditions, thereby slowing buffer rewetting.

A thin resistive layer in the COMSOL model can represent a poor contact between materials. The COMSOL model represents a thin layer with a fixed thermal conductivity and thickness, but only thermal conductance (thermal conductivity divided by thickness) affects the temperature drop for a given heat flux. To assess the effect of a thin layer, thin resistive layers were added to three interface segments: (i) buffer–heater side (between the bentonite block and heater springline), (ii) bentonite block–heater bottom, and (iii) buffer–host rock (crown to floor). Each layer was assigned an arbitrary thickness of 5 mm [0.2 in] and a scaled value of the buffer or block thermal conductivity. A series of calibration simulations with different scale factors suggests that the scale factor for each of the resistive layers (heater and buffer, heater and block, and buffer and rock) should be less than unity.

The illustrative simulation shown in Figures 5-20 through 5-22 features an offset between buffer and block temperature profiles of approximately 10 °C [18 °F], temperatures of approximately 140 °C [284 °F] for the heater liner, a relatively small temperature difference across the heater liner, and appropriate temperature jumps at both the heater and the rock. The properties were adjusted manually, with just a few trials. This simulation has scale factors of 0.2, 0.05, and 0.02 for the buffer–heater, block–heater, and buffer–host rock interfaces, respectively. One implication is that there may be a substantial disturbance at the buffer–host rock interface, perhaps due to bridging or fissures developing during the test. The bentonite block also appears to have poor contact with the heater liner, perhaps due to differential swelling or contraction. A better but still poor contact between the buffer and heater liner is necessary to achieve a temperature offset between profiles in the buffer and in the block. The temperature measurements (Figure 5-11) show that the temperature drop is quite small on the top of the heater liner and greater on the sides and bottom, suggesting that the contact is much better where the buffer is resting on top of the heater than where it might form a gap on the sides and bottom.

Thermal resistances at these locations have an important side effect of increasing heat flux into the plugs. Axial heater fluxes at the end of the heater liner increase by about a third. It appears that COMSOL does not calculate normal fluxes correctly when a thin resistant layer is used, so the fluxes into the rock wall cannot be directly calculated. Based on the spread in streamlines (see comparison in Figure 5-18), axial losses for the representative N2 cross section increase from 2.5 to 6.6 percent at the rock wall and from 30 to 37 percent at the 2-m [6.6-ft] radius. By implication, accounting for axial heat loss becomes more important in the 2-D cross section model when resistive features are included.

Moisture redistribution is also largely dominated by diffusive processes. The COMSOL 3-D thermal model suggests that the fraction of moisture fluxes moving axially should be comparable to but smaller than axial thermal flux fractions, because (i) there are no highly conductive pathways for moisture redistribution near the heater liner and (ii) moisture redistribution responds to both capillary pressure and temperature gradients. The dominant axial process for moisture redistribution inside the microtunnel is due to vapor redistribution from hot zones to cold zones (i.e., down temperature gradients). Accordingly, estimates of moisture fluxes at the N2 cross section should be even better represented than estimates of heat flux with the 2-D hybrid grid.

5.4 Calculated Mechanical Response

The Task B1 lead requested that each team provide calculated porosity values at the same locations that TH outputs were provided. To calculate porosity, the FLAC model described in Section 3.2 considered the mechanical responses from a sequence consisting of microtunnel mining, HE-E test materials emplaced in the microtunnel, and TH responses to heating. The FLAC model ran independently of xFlo prior to heating, and was driven with one-way coupling using xFlo temperature, saturation, and gas pressure output during the heating phase. This straightforward approach allows CNWRA staff to assess the need for more complex two-way coupling between xFlo and FLAC in which FLAC-calculated deformations are passed back to influence saturation and pressures internal to xFlo. For this assessment, mechanical responses were calculated using the short-heat (heating stopped 7.9 yr after it began) and long-heat (heating continues indefinitely) scenarios described in Section 5.1.

One set of FLAC simulations illustrates the calculated change in porosity from the initial state while a saturation front is advancing. An advancing rewetting front occurs seven years after start of heating using the calibrated TH property set in the short-heat boundary condition scenario (spatially uniform power is applied to the inner boundary of the liner). The long-heat and short-heat boundary conditions are essentially the same to this point in time, with the heater liner temperature held at approximately 140 °C [284 °F] after the first year of heating. Two other scenarios, the rewetted and dessicated scenarios, were developed using the long-heat scenario with the calibrated and uncalibrated TH material property sets, respectively. Both simulations terminated 100 years after start of heating, but in both simulations equilibrium was reached decades before the end of the simulation.

The temperature and saturation profiles for the advancing front scenario (Figure 5-23) show an advancing front approximately 15 to 20 cm [6 to 8 in] from the rock wall after seven years of heating; Figures 5-3 and 5-8 show the saturation evolution during the first 3.4 years after heating begins. The temperature and saturation profiles for the rewetted buffer scenario (Figure 5-24) show a warmer host rock with complete buffer rewetting after 100 years; this simulation has passed through the advancing-front stage. The temperature and saturation profiles for the desiccated buffer scenario (Figure 5-25) show a cooler host rock with a desiccated buffer and a dryout zone in the host rock; this scenario experienced a brief wetting front adjacent to the host that dissipated within a few years.

The calculated deformation of the microtunnel is small, thus the total pore space within the microtunnel is almost constant (even considering the extensometer measurements, the tunnel expansion is small relative to the tunnel void space). Deformation and change in porosity patterns within the microtunnel are shown in Figures 5-26 to 5-28 for the same three scenarios, with the deformations corresponding to the times shown in Figures 5-23 to 5-25 (7 years after start of heating for the advancing front scenario, 100 years after start of heating for the rewetted

and desiccated buffer scenarios). The change in porosity is an integrated measure of relative or differential deformation from the initial emplacement to the end of the simulation. Figures 5-26 through 5-28 have the same color scales. Change in porosity is indicated with warm colors for increasing porosity (expansion) and cool colors for decreasing porosity (contraction).

Figures 5-26 to 5-28 show that the calculated deformation generally consists of an annular zone of extension (with porosity increase of up to ~0.02) bounded by compression zones (with local porosity decrease of up to ~0.08) around the heater and near the tunnel boundary.

In the advancing front scenario (Figure 5-26), a sharp wetting front is progressing inward from the microtunnel wall, but the inner half of the buffer is drier than the initial condition (Figures 5-3 and 5-8 show the evolution of saturation up to 3.4 years after heating begins). The central extension zone in Figure 5-26 overlies the inwardly progressing saturation front, with the inner edge is approximately at a saturation level of 0.3 to 0.5. The thin compression zone at the top of the liner results from downward deformation. The thicker extension zone below the liner results from the bentonite block expanding approximately parallel to the liner. The thin extension zone at the side of the liner results from deformation approximately perpendicular to the liner.

The rewetted buffer scenario shows substantial swelling in the bentonite block, unlike the advancing front and desiccated buffer scenarios.

The calculated compression zone near the tunnel boundary that developed in all three scenarios is likely a consequence of the high stiffness of the host rock relative to the buffer, causing the buffer material to be compressed against the tunnel boundary as the buffer interior expands. The compression zone around the heater liner likely resulted from net shrinkage (i.e., reduction in pore space) due to moisture loss. The deformation mechanisms in this zone consist of thermal expansion due to temperature increase and shrinkage due to moisture loss. The results indicate shrinkage is dominant, so that the net deformation is compressive. The heater liner is not allowed to expand, so the compression zone around the liner may also result from extension in the buffer interior. The extension zone likely resulted from a combination of balancing deformations in the outer and inner compression zones and swelling due to moisture driven from the heated areas condensing within this zone.

The extension zones are closest to the tunnel boundary along the horizontal mid-plane of the heater where the deformation along the liner is perpendicular to the liner. The buffer is compressed parallel to the tunnel circumference, resulting in relatively high compression away from the horizontal mid-plane of the heater.

Therefore, buffer deformation resulting from time-dependent TH changes (heating and moisture redistribution) varies mostly radially but shows a noticeable circumferential gradient near the tunnel boundary. The deformation pattern is the same for all three TH model cases, but the extension zone is greater at equilibrium in both the wet and dry scenarios after 100 years than in the advancing-front situation after 7 years. The similarity of the compression and expansion zone patterns in the two equilibrium scenarios suggests that early deformation patterns may be preserved during subsequent rewetting.

The calculated compression zones against the microtunnel wall developed because the host rock was stiffer than the buffer in the model. In contrast to these model results, the temperature and pore pressure measurements available during the first 2.5 years after start of heating suggest that the buffer actually had poor contact with the host rock (see Section 5.3), which

implies that the host rock may have pulled away from the buffer during heating. The temperature data further suggest that the buffer may have formed a gap below and to the sides of the heater liner.

The conceptual model implemented for this report assumed that the buffer and bentonite blocks remained pressed against the heater liner and host rock without sliding or pulling away, thus FLAC model capabilities appropriate for examining gap formation were not activated. With the focus on modeling buffer behavior, the host rock deformation was not calibrated to the relative deformation data in this initial work, and further work would be needed to draw conclusions about gaps between the buffer and the host rock. Examination of the calculated buffer and block deformation patterns a year after heating began show that the porosity changes along the heater liner surface (decreasing porosity on top of the liner, increasing porosity along the side and bottom) are consistent with buffer movement towards the top of the liner and lateral block extension that displaces the buffer from the side of the liner. These displacement patterns are consistent with a gap forming at the side of the liner but not the top, as suggested by the temperature data. Lateral extension of a relatively stiff and curved bentonite block may increase the radius of curvature of the block, implying that a gap consistent with temperature data may form between the liner and the pedestal.

Understanding potential interactions between host rock deformation, buffer responses to TH processes, and the likelihood of gaps forming at the heater liner and host rock would require further work. A gap may strongly influence temperature profiles and moisture fluxes, thus modeling gap formation processes would likely require tight two-way coupling between xFlo and FLAC. FLAC can readily model gap formation, because FLAC allows interfaces to be defined where materials can slide past each other, pull apart, and recompress. This process uses a separate grid for each side of the interface, with calculations to ensure that the grids do not overlap. Additional logic would need to be added to xFlo to account for deforming gaps, because mass and heat transfer depend on the degree of contact between the two materials. Further, additional logic would need to be added to represent changes in connection patterns when extensive lateral sliding takes place along an interface.

5.5 Inferences from the HE-E Test Modeling

The following inferences were drawn from the series of model analyses in Sections 4 and 5:

- Energy and moisture balances should be reasonably well represented with a 2-D cross section model with a hybrid grid using cylindrical shells in the near field and spherical shells in the far field.

- The strongly contrasting hydraulic properties for the host rock and buffer requires that grid cells are finely discretized in the radial direction near the microtunnel wall to capture sharp capillary pressure gradients. Moisture redistribution is overestimated when the grid is too coarse to accurately capture the capillary pressure gradients, accelerating rewetting. A strong contrast in hydraulic properties is likely at the buffer and pedestal interface, as well.

- Uncertainties regarding properties of the host rock (e.g., the EDZ) and engineered components (e.g., cement blocks and concrete fill) are large relative to uncertainties in buffer properties. Discrepancies between measured and calculated temperature, relative humidity, and pore pressure arise from uncertainties regarding the host rock and

engineered components. Model calibration should not alter buffer properties until other factors are well established.

- The measured radial temperature profiles within the microtunnel suggest that (i) the host rock has a poor contact with the buffer, (ii) the sides of the heater liner are in poor contact with the buffer, (iii) the top of the heater liner is in good contact with the buffer, and (iv) the bottom of the heater liner is in poor contact with the pedestal. Such behavior is consistent with (i) gaps forming where the buffer is not pressed down on the contact and (ii) deformation of the bentonite pedestal near the heater. Formation of gaps would increase heat loss to the plugs. In a repository situation, unsaturated circumferential gaps would raise the temperature of the waste container.

- Measured pore pressures in the host rock suggest that there is a sharp discontinuity at approximately two tunnel radii, with near-atmospheric pore pressures inside the discontinuity and rapidly increasing pore pressures further into the rock that respond to heating. The inner zone pressures are consistent with radial fractures remaining unsaturated and maintaining a continuous gas contact with the microtunnel while the host rock matrix maintains a mild tension. The calculated host rock pore pressures strongly respond to imbibition into the very dry buffer; the lack of an observed strong suction gradient is consistent with poor contact between the buffer and the host rock. The lack of an observed strong suction gradient also could be consistent with highly permeable unsaturated inner zone fractures that are able to conduct water with little pressure gradient, with a wetting front that has not penetrated to any sensors. A revised xFlo model with a dual continuum or equivalent continuum approach could be used to represent the unsaturated fractures.

- Calculated rewetting times with the calibrated property set are likely too fast if unsaturated fractures and gaps exist, because rewetting will likely require that these features are almost saturated. Little information is available to assess (i) how long it would take to saturate these features and (ii) what the mechanical response would be for such features.

- Time steps in 3-D xFlo simulations are strongly limited by cells transitioning between saturated and unsaturated. This behavior also occurs in 1-D and 2-D simulations. The code was revised to improve consistency when a grid cell transitions between saturated and unsaturated states, which helped convergence considerably. The simulations provide a good test for further work focusing on improving the convergence when capillary pressures are near zero.

- Initial calculations of the buffer mechanical responses indicate that deformation and porosity changes are relatively small in the buffer except for restricted regions. The initial analysis provides hints that gaps might form along the heater liner where sensor data indicate there are temperature anomalies. Modeling gap formation would require a more intensive study, and likely would need tight coupling between xFlo and FLAC to ensure consistency between THM processes.

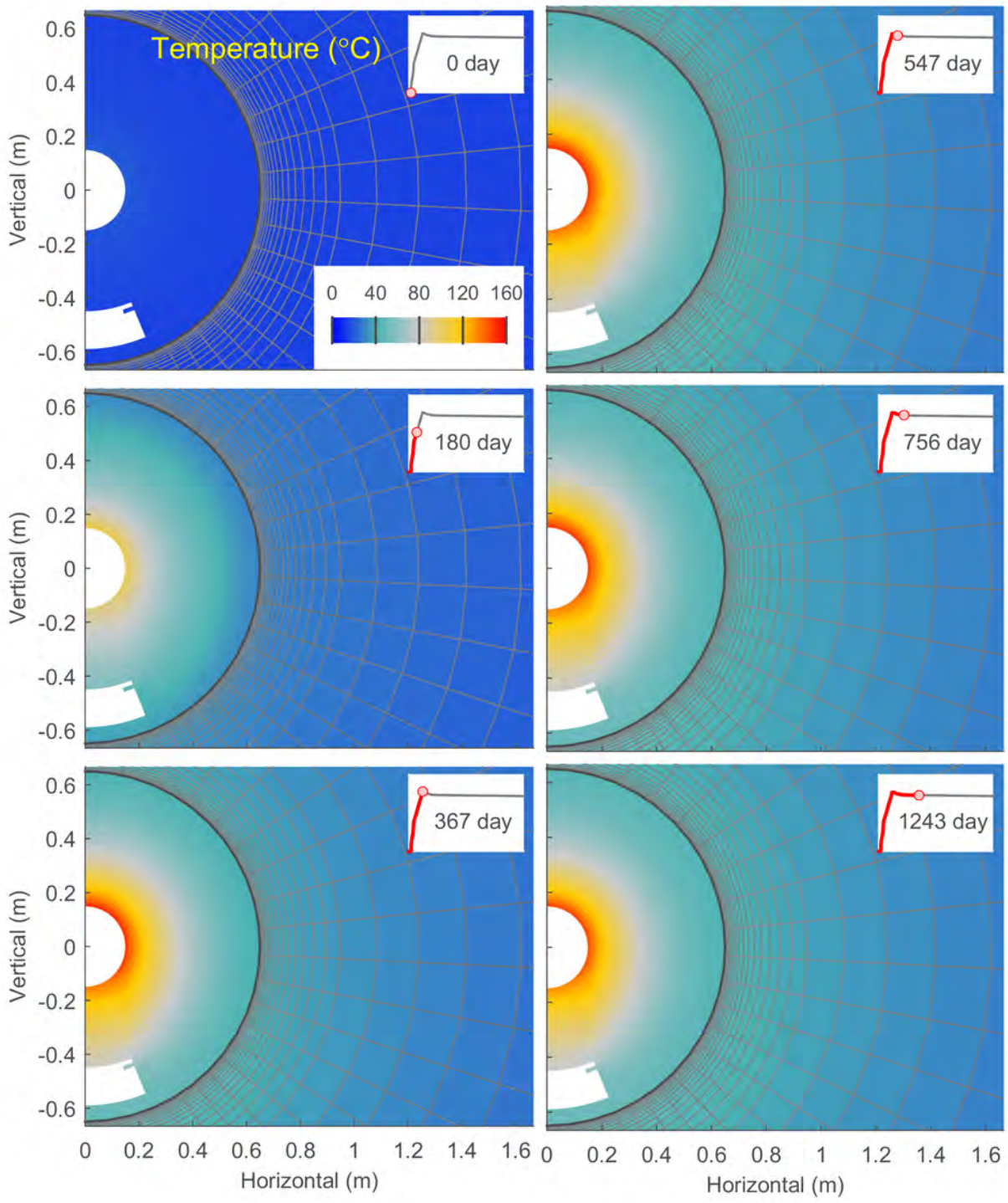

Figure 5-1. Spatial Distribution of Calculated Temperature at Selected Time Instants After Start of Heating for the Final Parameter Set. Inset for Time Instant and Heater Power Added to Each Plot. {°F = [1.8 × T °C + 32]}, 1 m = 3.3 ft]

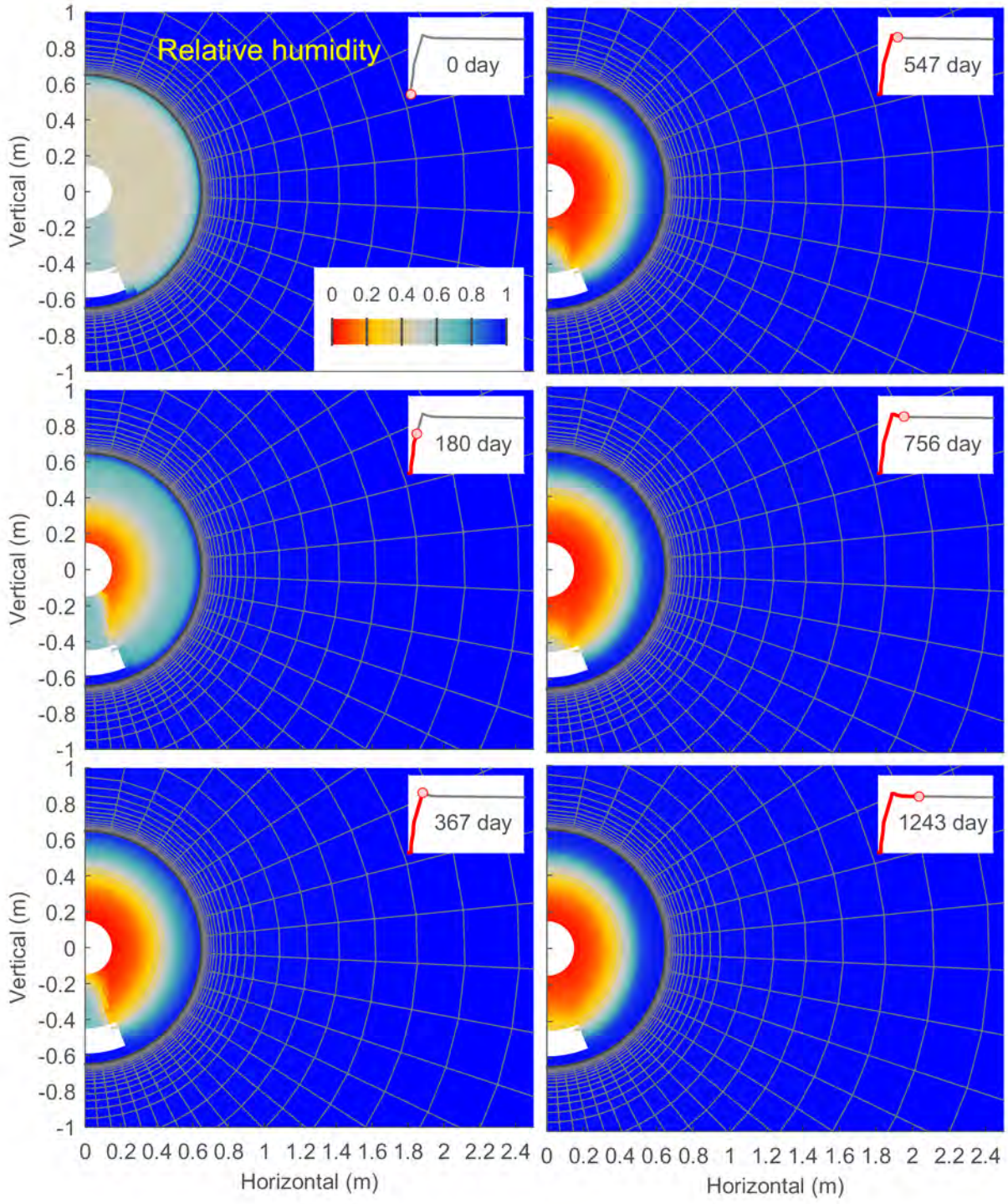

Figure 5-2. Spatial Distribution of Calculated Relative Humidity at Selected Time Instants After Start of Heating for the Final Parameter Set. Inset for Time Instant and Heater Power Added to Each Plot. [1 m = 3.3 ft]

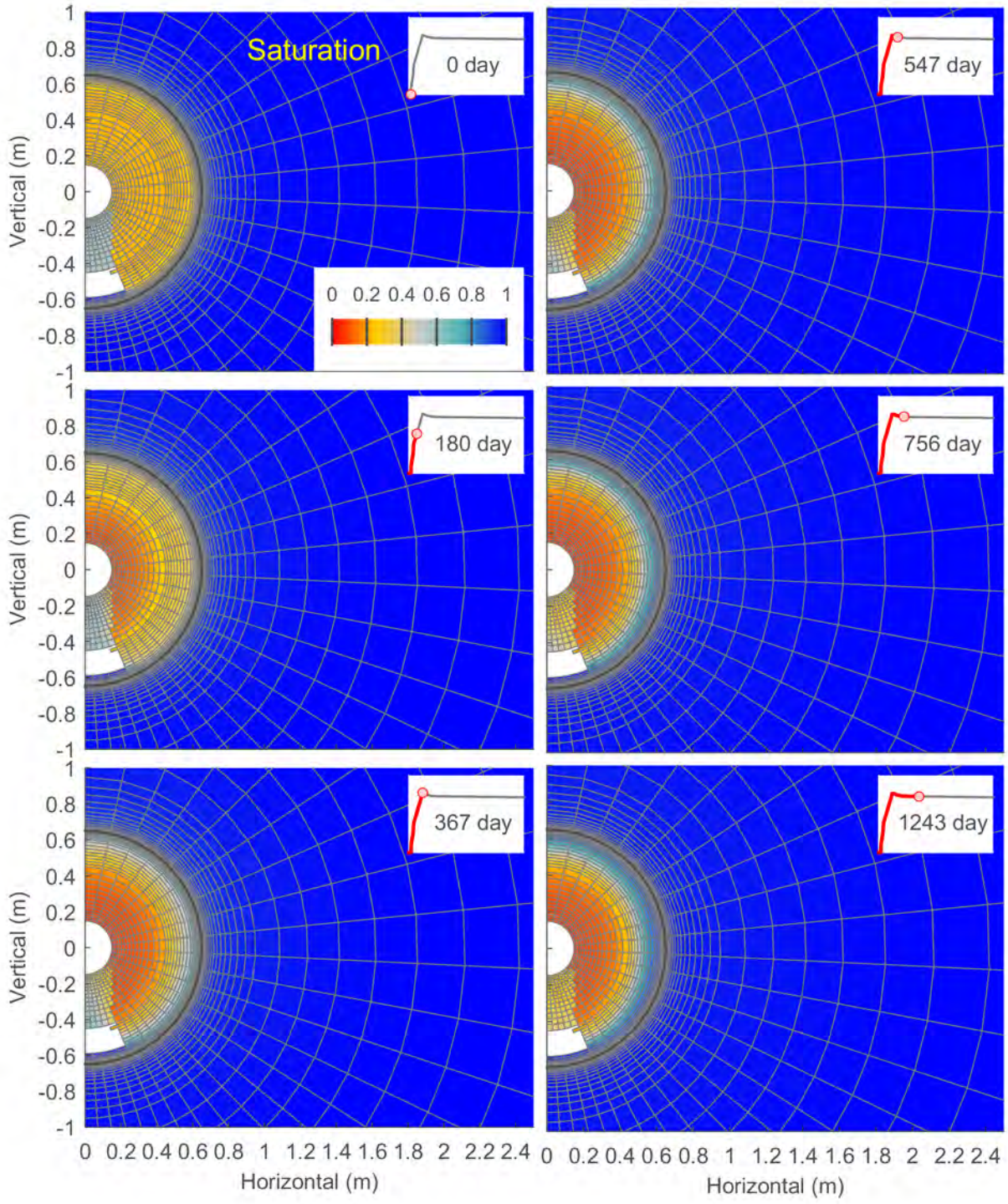

Figure 5-3. Spatial Distribution of Calculated Liquid Saturation at Selected Time Instants After Start of Heating for the Final Parameter Set. Inset for Time Instant and Heater Power Added to Each Plot. [1 m = 3.3 ft]

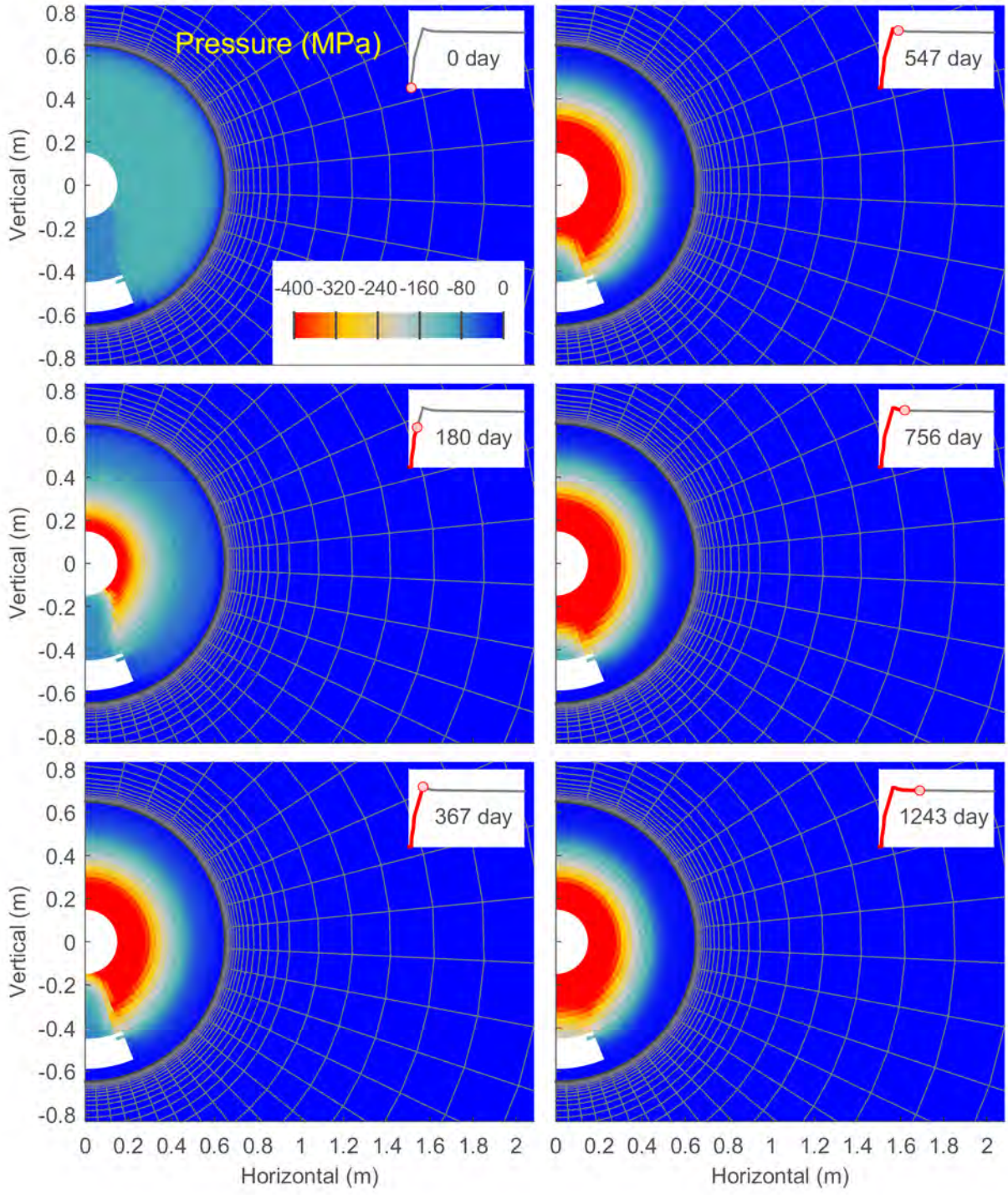

Figure 5-4. Spatial Distribution of Calculated Liquid Pressure at Selected Time Instants After Start of Heating for the Final Parameter Set. Note That Liquid Pressure is Clipped. Inset for Time Instant and Heater Power Added to Each Plot. [1MPa = 145 psi]

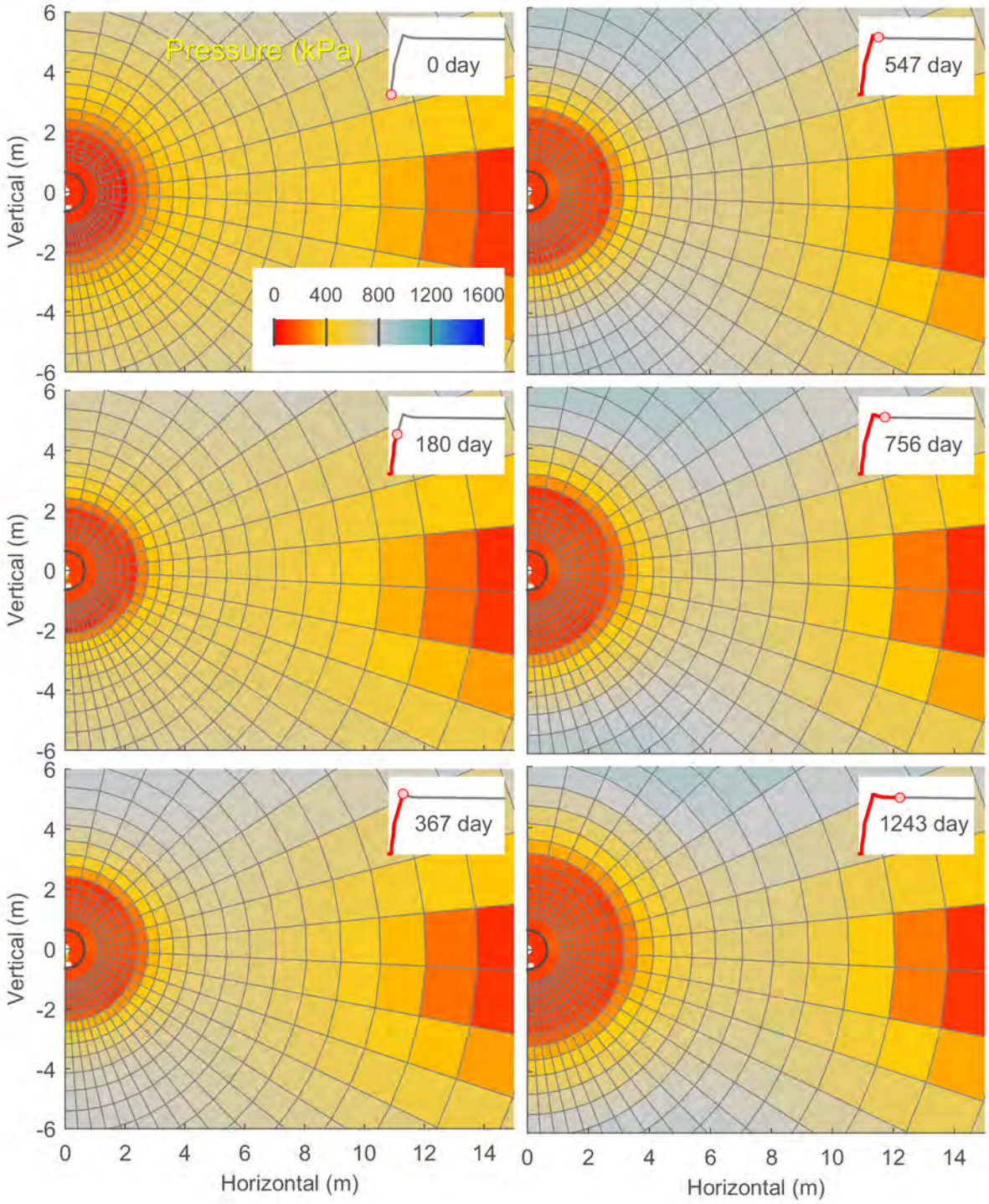

Figure 5-5. Spatial Distribution of Calculated Gas Pressure at Selected Time Instants After Start of Heating for the Final Parameter Set. Note That xFlo Sets Gas Pressure to Liquid Pressure Where Fully Liquid Saturated. Inset for Time Instant and Heater Power Added to Each Plot. [1 kPa = 0.145 psi, 1 m = 3.3 ft]

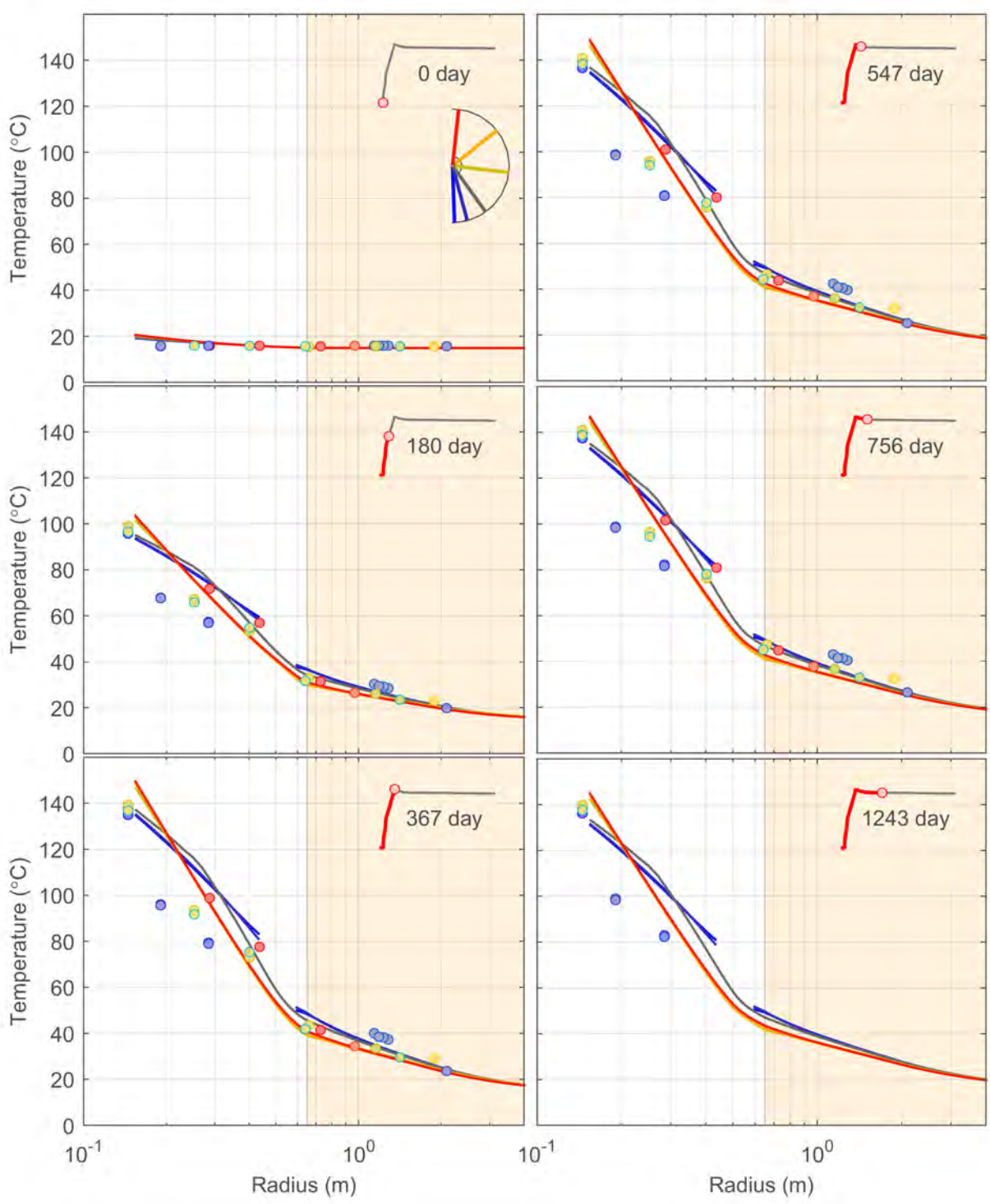

Figure 5-6. Radial Profiles of Calculated and Measured Temperature at Selected Time Instants After Start of Heating for the Final Parameter Set. Insets Show Profile Position, Simulation Time Instant, and Heater Power. [°F = (1.8 × T °C + 32), 1 m = 3.3 ft]

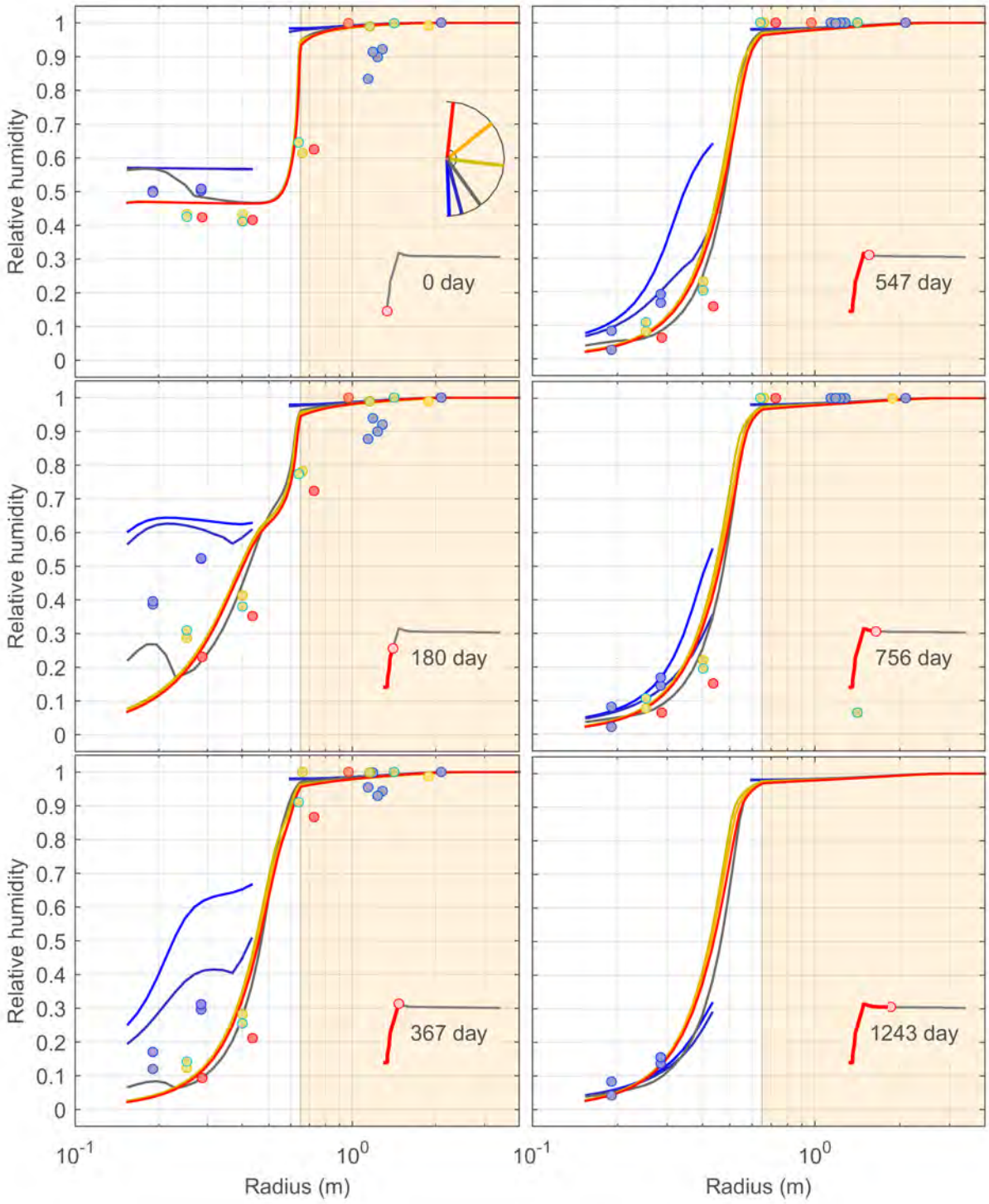

Figure 5-7. Radial Profiles of Calculated and Measured Relative Humidity at Selected Time Instants After Start of Heating for the Final Parameter Set. Insets Show Profile Position, Simulation Time Instant, and Heater Power. [1 m = 3.3 ft]

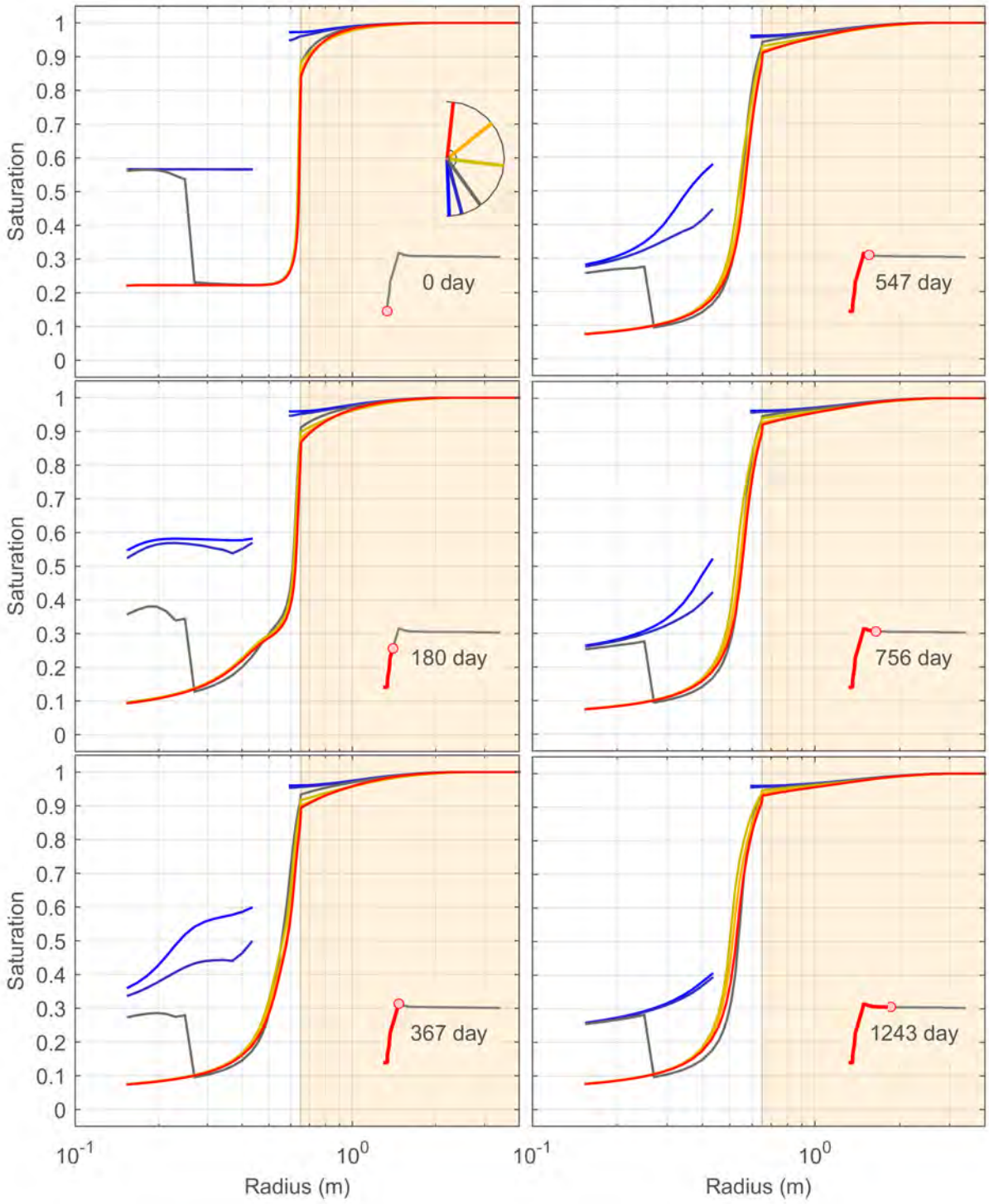

Figure 5-8. Radial Profiles of Calculated Liquid Saturation at Selected Time Instants After Start of Heating for the Final Parameter Set. Insets Show Profile Position, Simulation Time Instant, and Heater Power. [1 m = 3.3 ft]

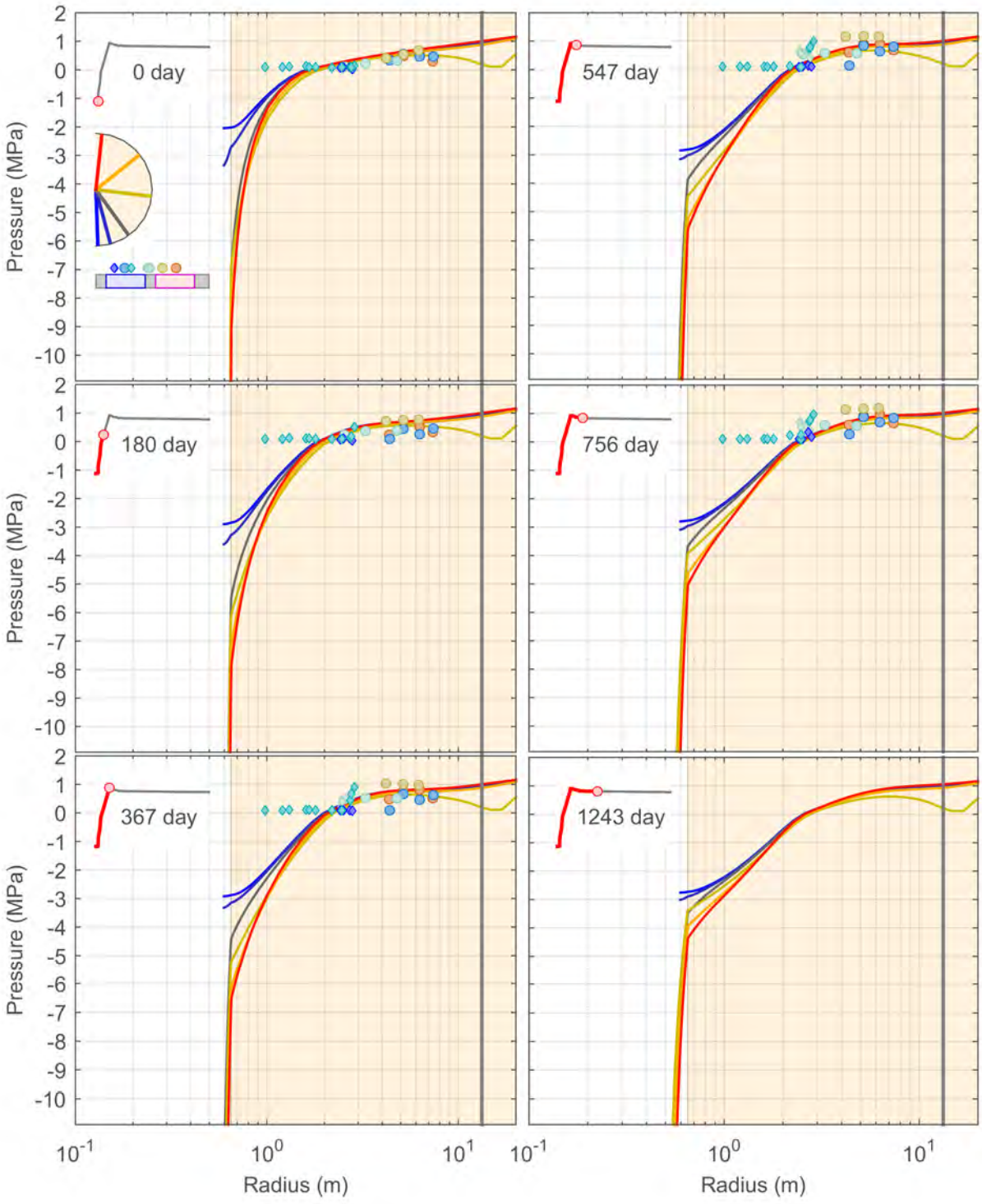

Figure 5-9. Radial Profiles of Calculated and Measured Pore Pressure at Selected Time Instants After Start of Heating for the Final Parameter Set. Circles and Diamonds Indicate Pore Pressure in Gallery 98 and Microtunnel Boreholes, Respectively. BE-1, BVE-1, BVE-91, and BE-2 are Colored Blue, Cyan, Tan, and Orange, Respectively. [1MPa = 145 psi, 1 m = 3.3 ft]

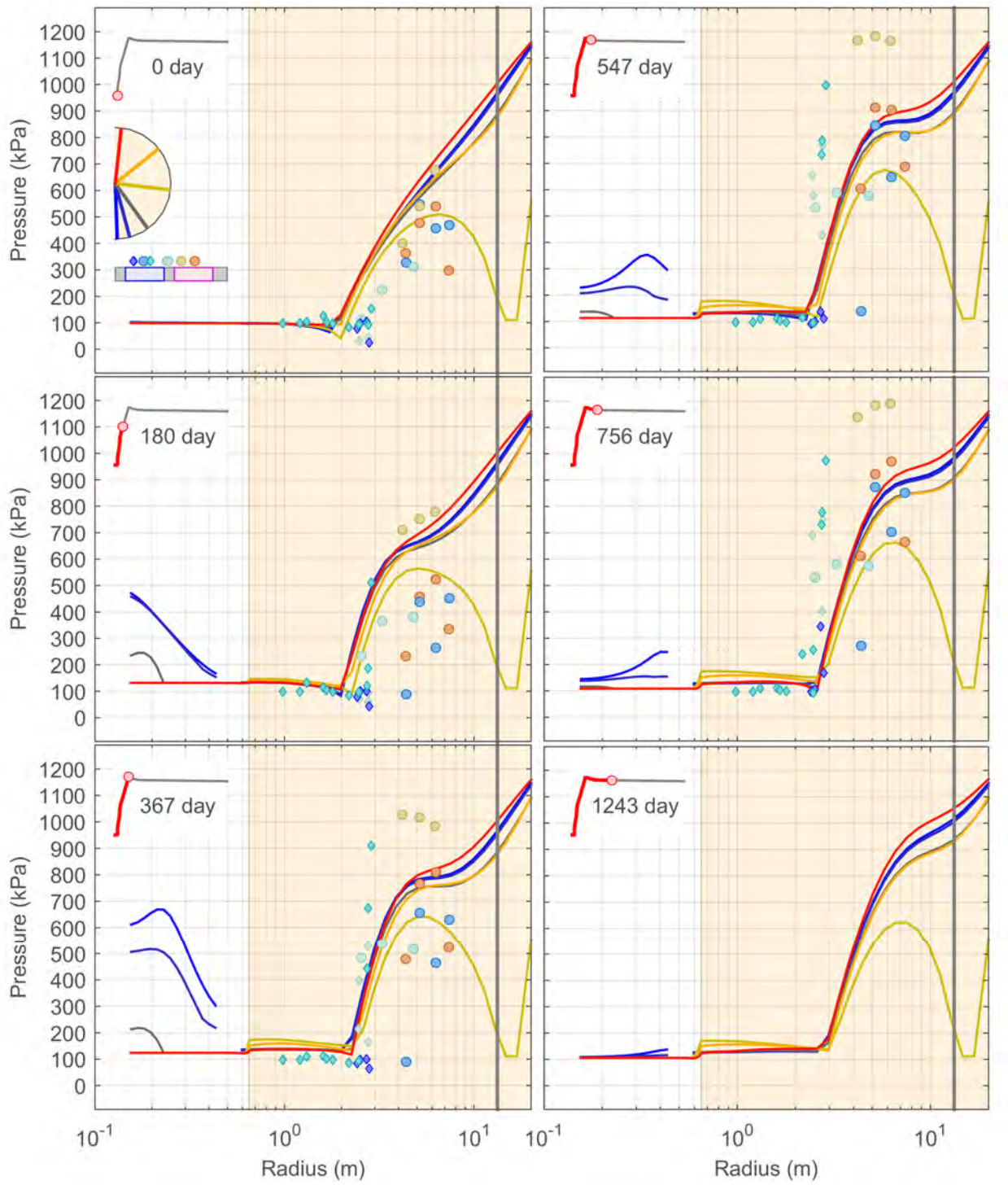

Figure 5-10. Radial Profiles of Calculated Gas and Measured Pore Pressure at Selected Time Instants After Start of Heating for the Final Parameter Set. Circles and Diamonds Indicate Pore Pressure in Gallery 98 and Microtunnel Boreholes, Respectively. Note That xFlo Sets Gas Pressure to Liquid Pressure Where Fully Liquid Saturated. [1 kPa = 0.145 psi, 1 m = 3.3 ft]

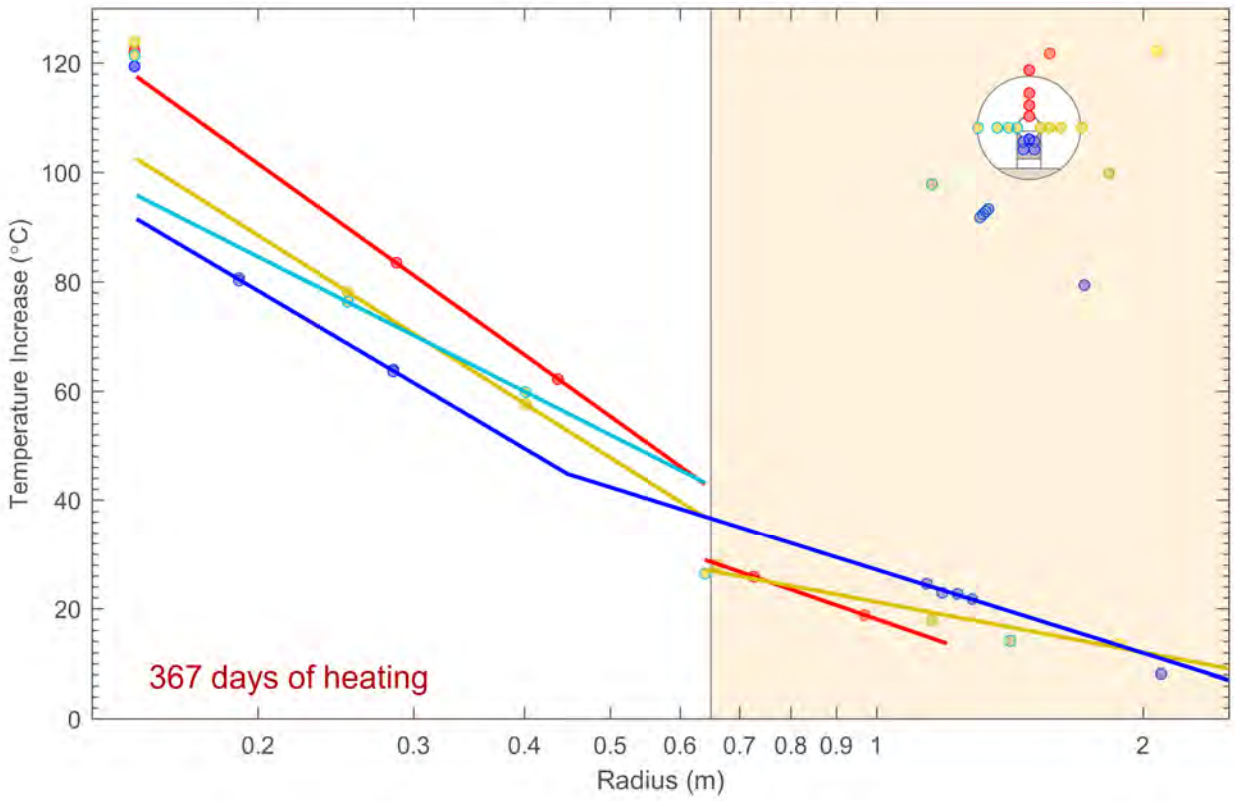

Figure 5-11. Temperature Profiles Projected From Sensor Data After One Year of Heating. Inset Shows Sensor Locations.

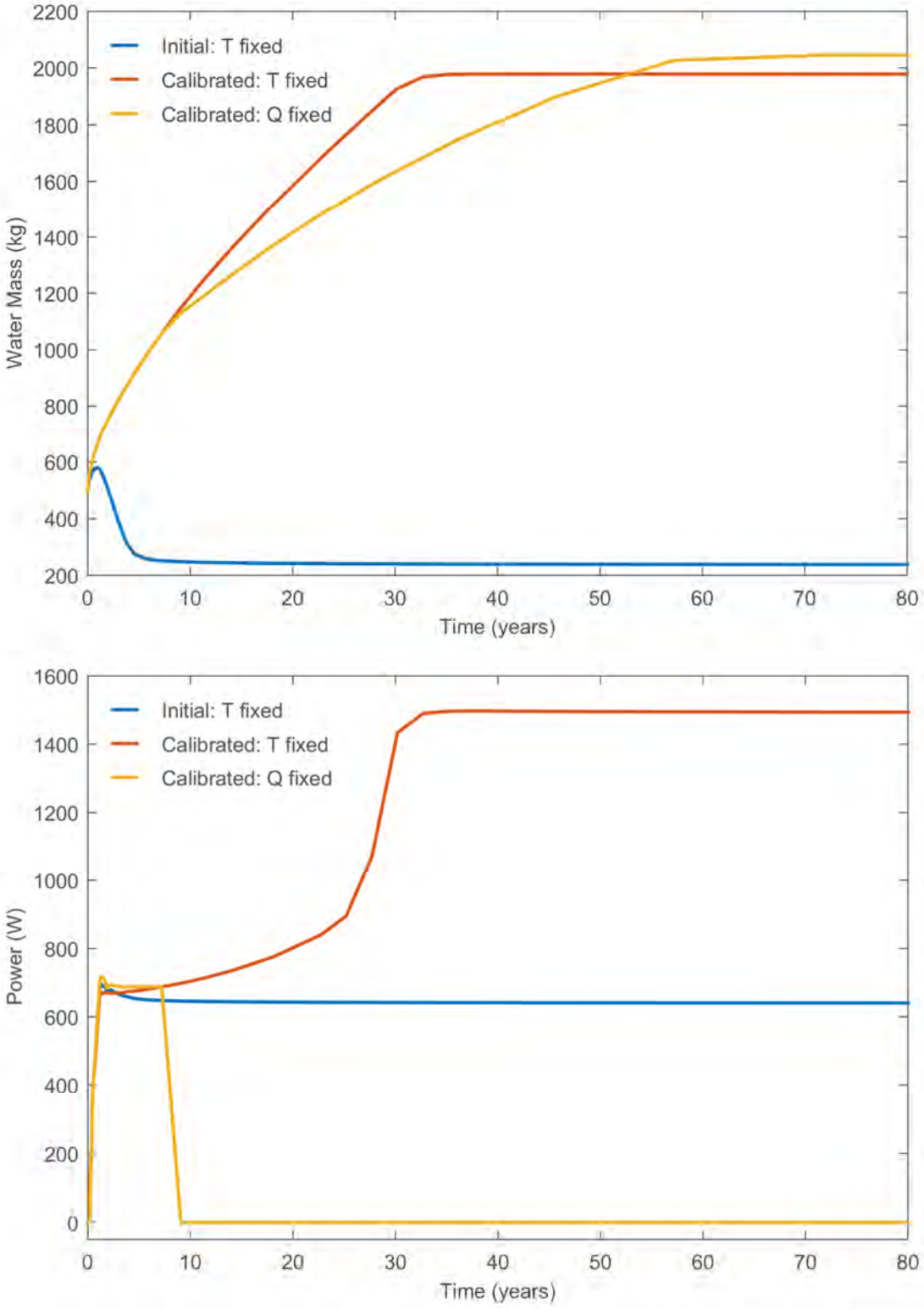

Figure 5-12. Calculated Water Mass in the Nagra Section (Top) and Heat Flux Into the Nagra Section (Bottom).

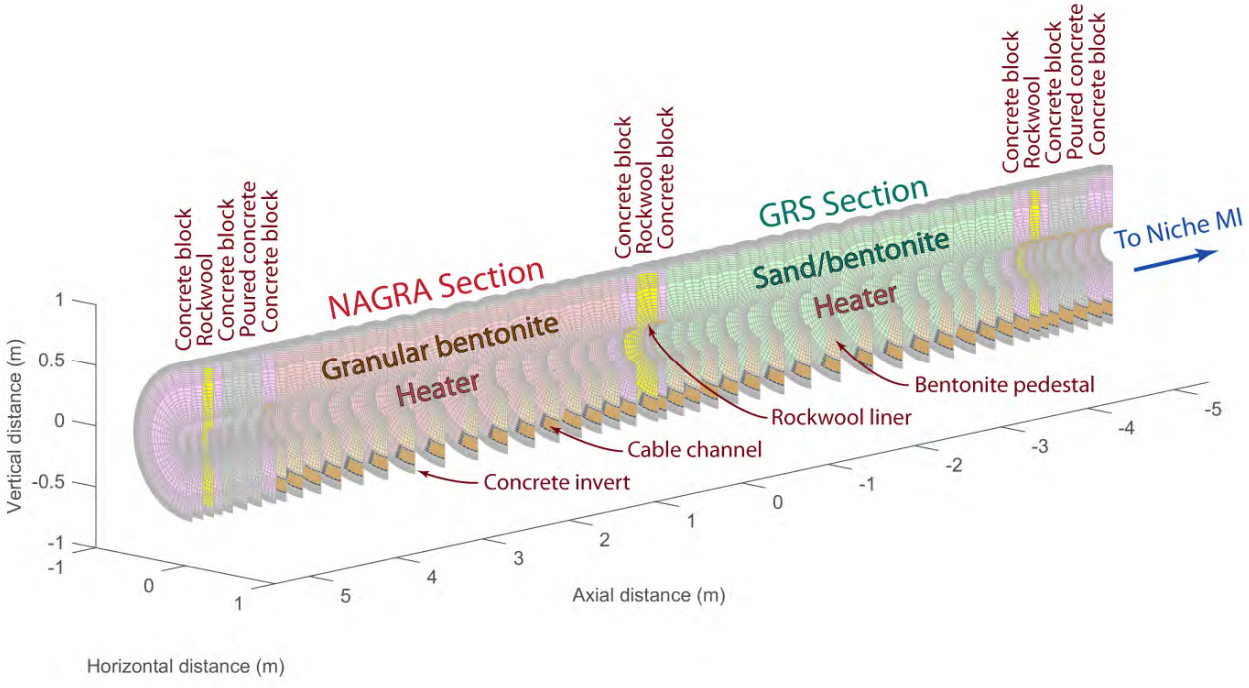

Figure 5-13. Microtunnel and HE-E Components in the 3-D xFlo Model. The Total Domain is a Half-Sphere With Outer Radius of 200 m. Coloring is by the Labeled Material. [1 m = 3.3 ft]

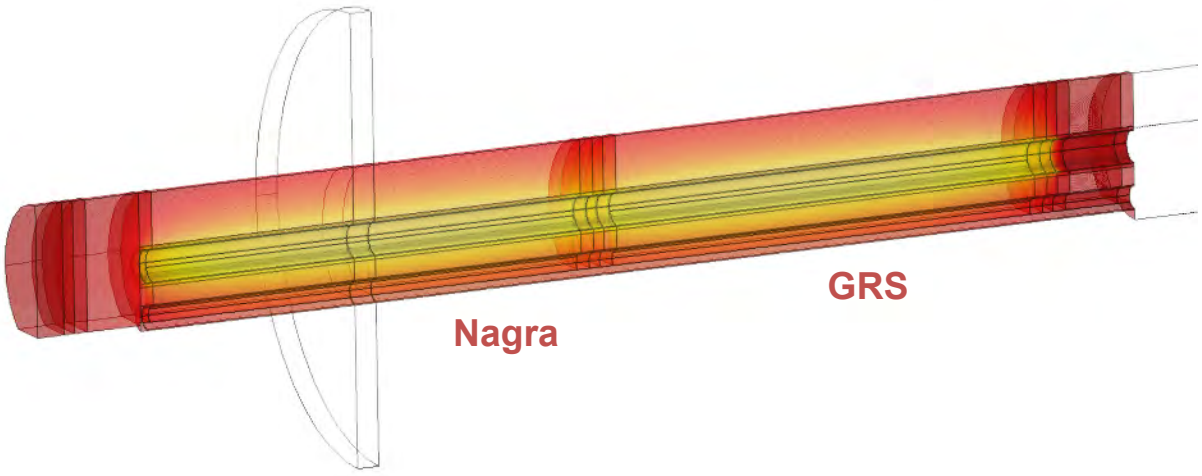

Figure 5-14. HE-E Components in the 3-D COMSOL Thermal Model. The Total Domain is a Half-Cylinder With Outer Radius of 20 m and Length 40.44 m. Coloring Generically Indicates Temperature. The N2 Cross Section is Indicated by a Half-Cylinder With Radius of 2 m. [1 m = 3.3 ft]

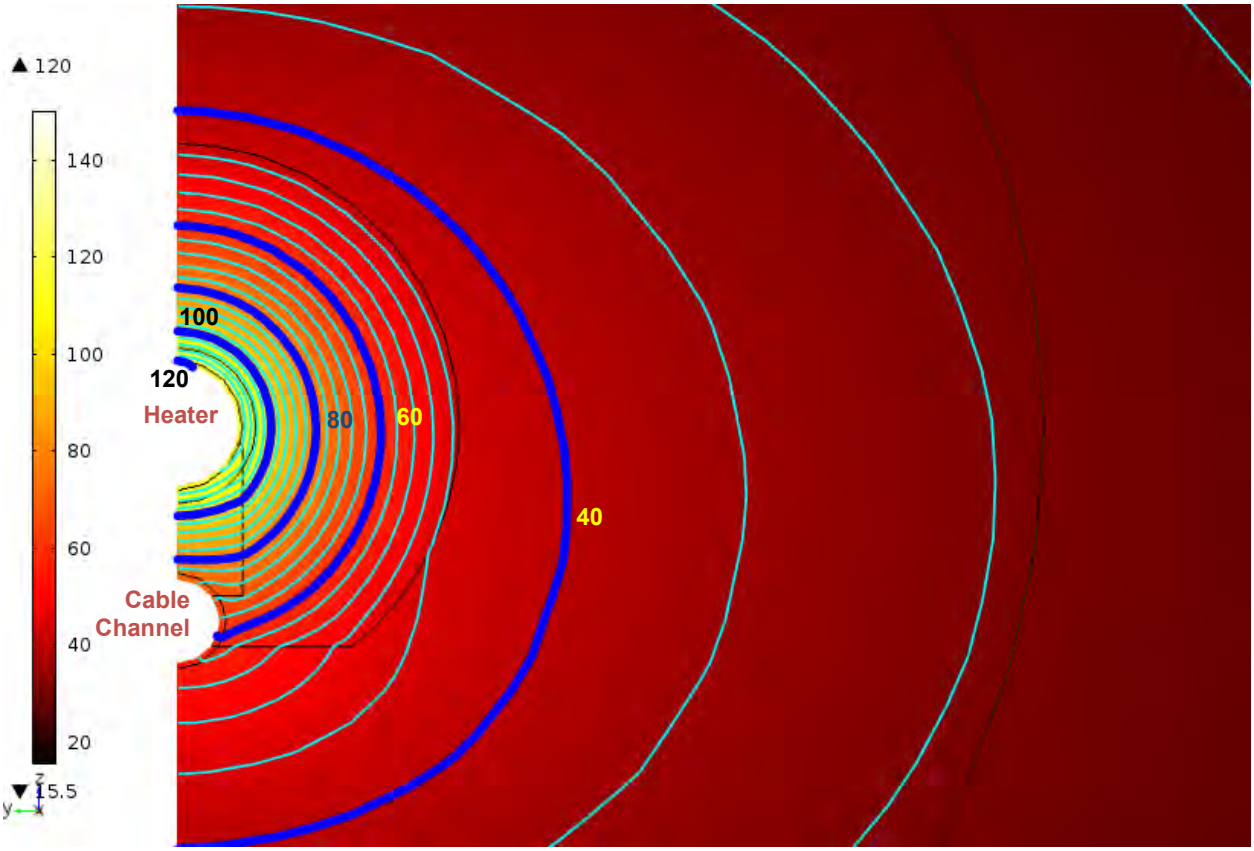

Figure 5-15. Steady State Buffer and Near-Field Temperature (°C) at the N2 Cross Section in the 3-D COMSOL Thermal Model With Nominal Properties. Temperature Contours are Separated by 4 °C [7.2 °F]. [°F = (1.8 × T °C + 32)]

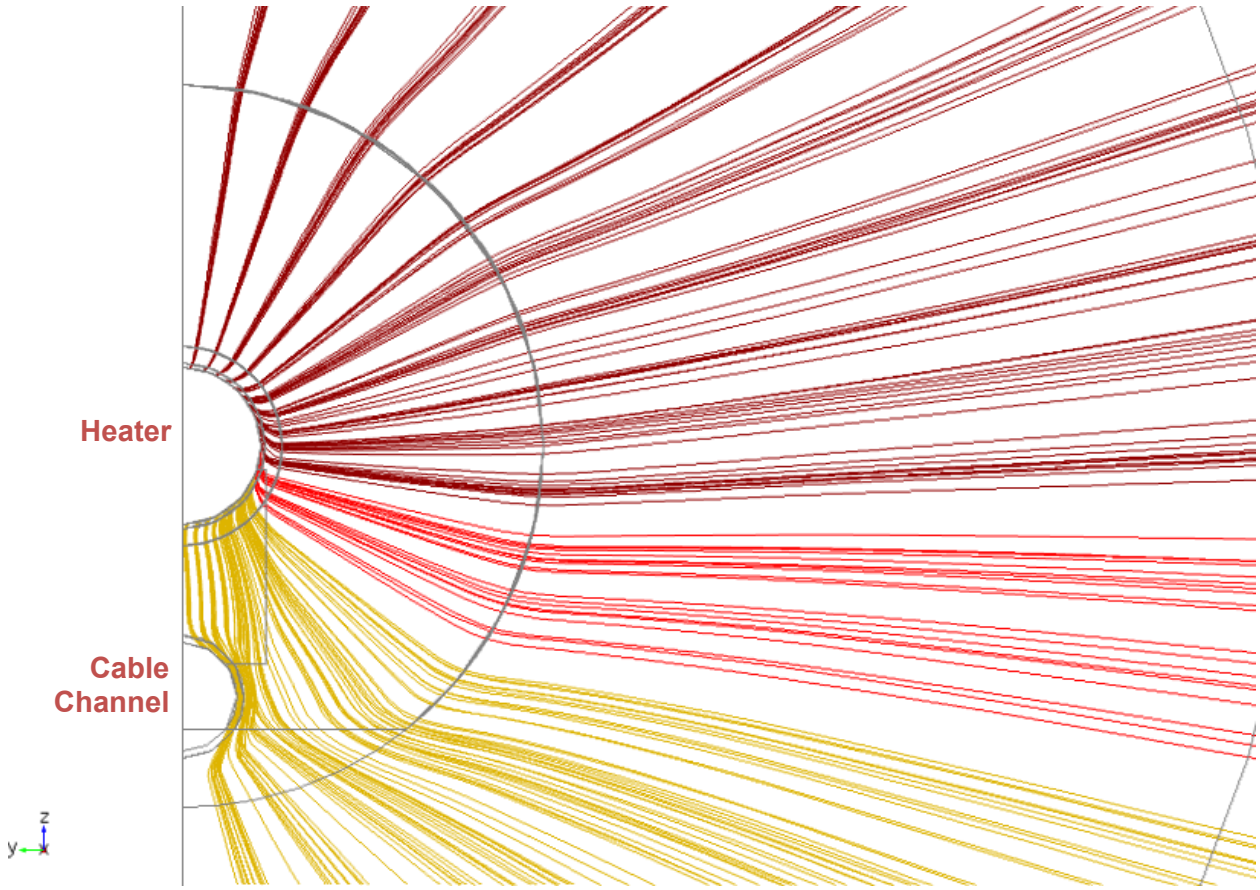

Figure 5-16. Heat Flux Streamlines Starting From a Uniformly Spread Location on the Inner Surface of the Heater Liner Within the N2 Cross Section in the 3-D COMSOL Thermal Model With Nominal Properties. Dark Red Lines Started in the Top Half and Yellow Lines Started at the Bentonite Block.

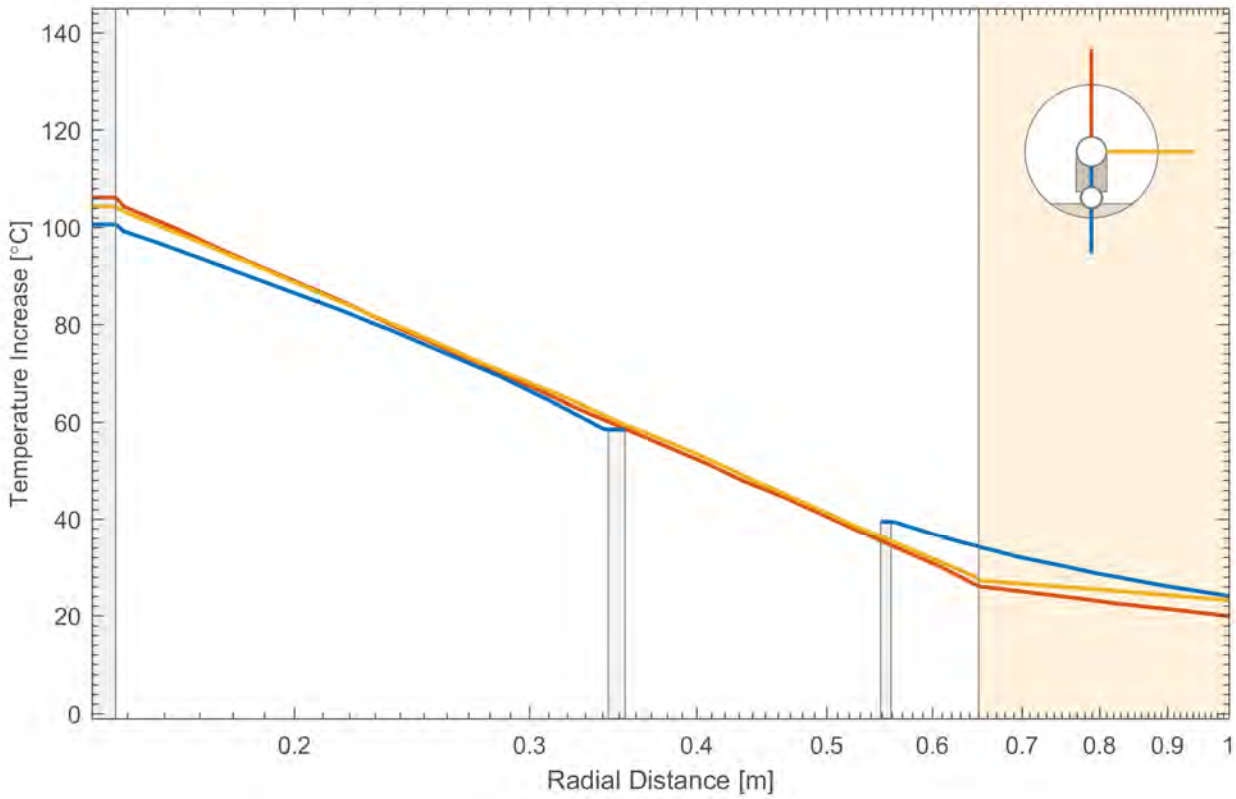

Figure 5-17. Profiles of Steady State Temperature at the N2 Cross Section in the 3-D COMSOL Thermal Model With Nominal Properties. [°F = (1.8 × T °C + 32), 1 m = 3.3 ft]

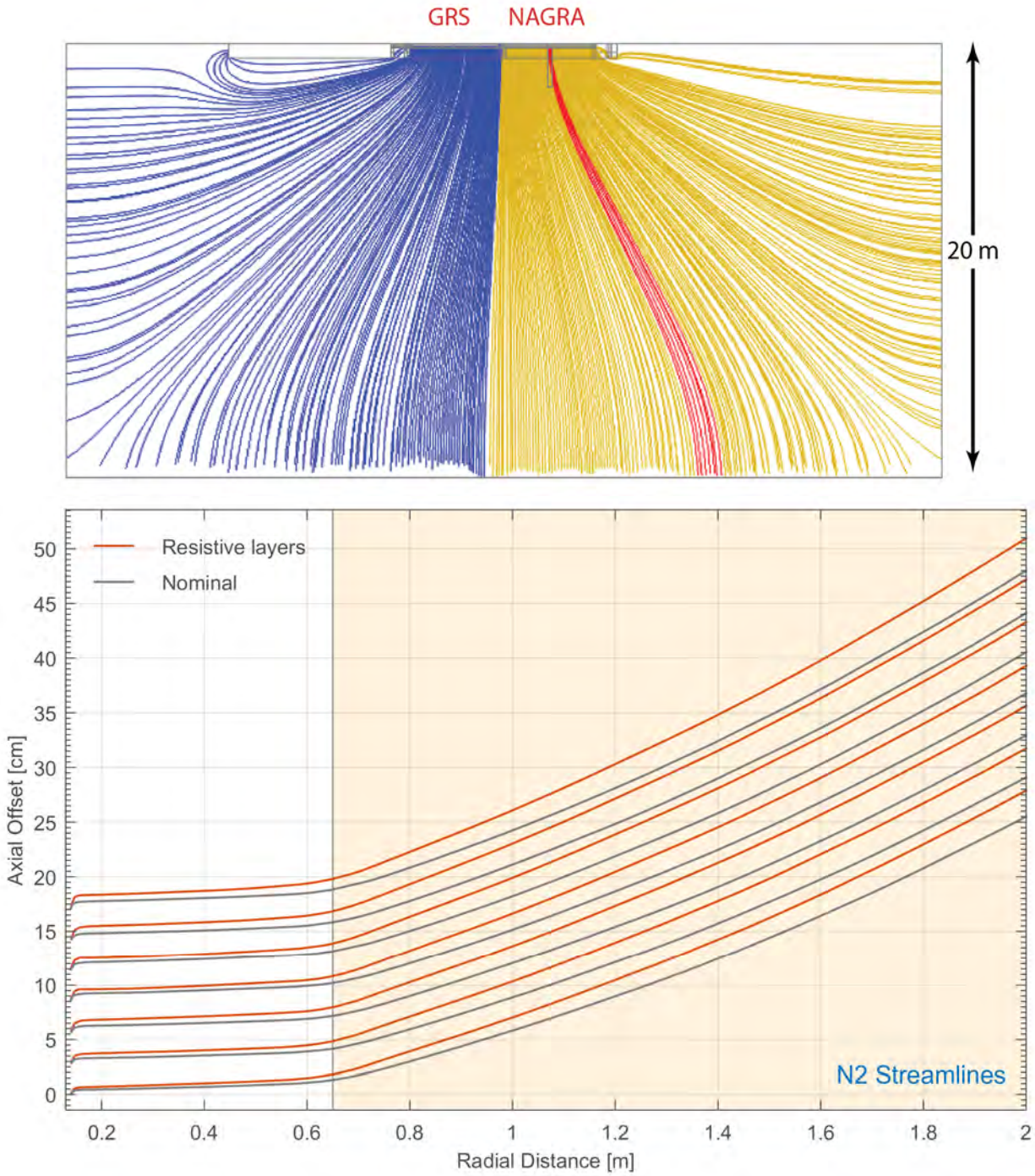

Figure 5-18. Heat Streamlines Released Below the Springline at the Inner Heater Liner Surface for the Nagra and GRS Sections From the 3-D COMSOL Model Results With Nominal Properties (Top). Offset in Axial Direction for Streamlines Starting in the N2 Cross Section With and Without the Thin Resistive Layer (Bottom). [1 cm = 0.39 in, 1 m = 3.3 ft]

Temperature (°C); contour spacing is 2 °C

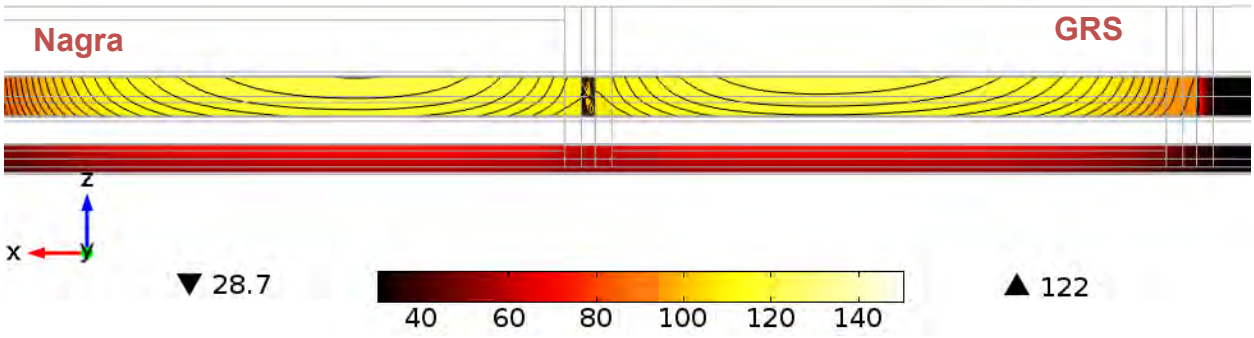

Axial heat flux (kW/m^2); contour spacing is 0.2 kW/m^2

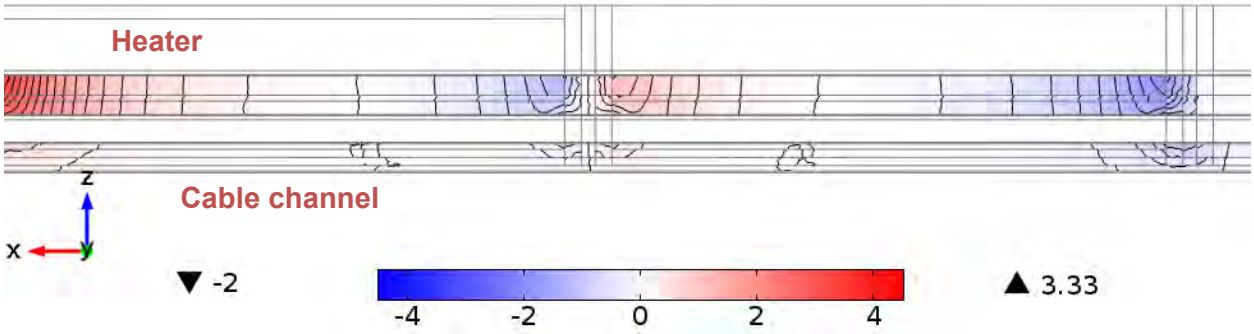

Ratio of axial heat flux to total heat flux; contour spacing is 0.1

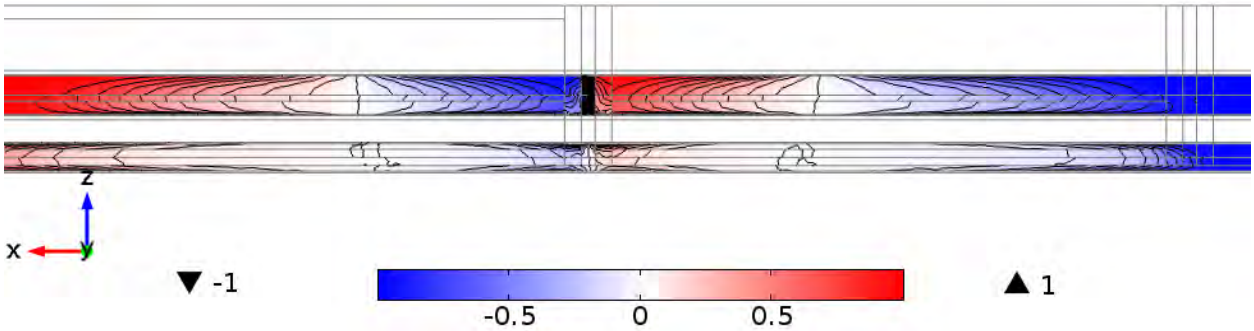

Figure 5-19. Orthotropic Projection to a Vertical Plane of Calculated Temperature (Top), Axial Heat Flux (Middle), and Ratio of Axial to Total Heat Flux (Bottom) for the 3-D COMSOL Thermal Model With Nominal Properties. Extreme Values are Indicated to the Side of the Scales. [°F = (1.8 × T °C + 32), 1 m = 3.3 ft]

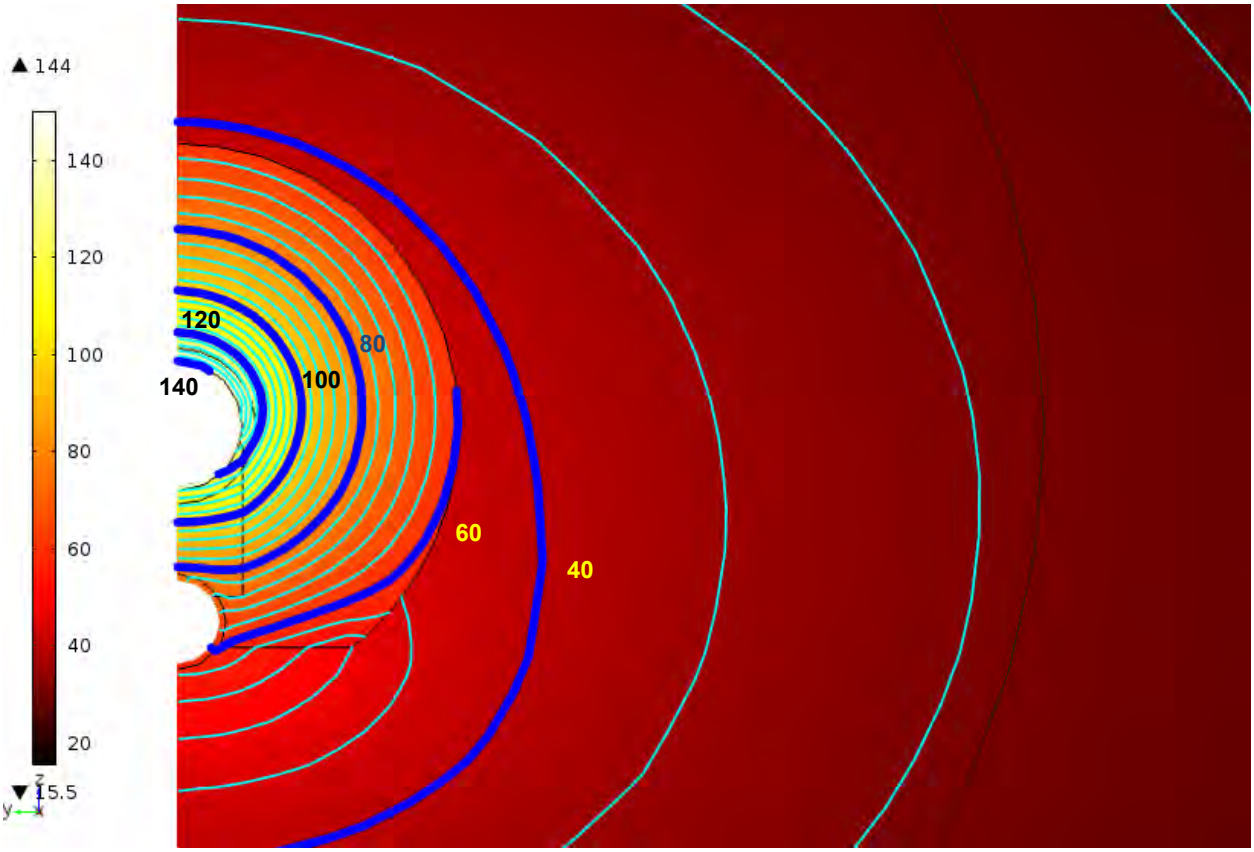

Figure 5-20. Steady State Buffer and Near-Field Temperature (°C) at the N2 Cross Section in the 3-D COMSOL Thermal Model With a Thin Resistive Layer Assumption. Temperature Contours are Separated by 4 °C. [°F = (1.8 × T °C + 32), 1 m = 3.3 ft]

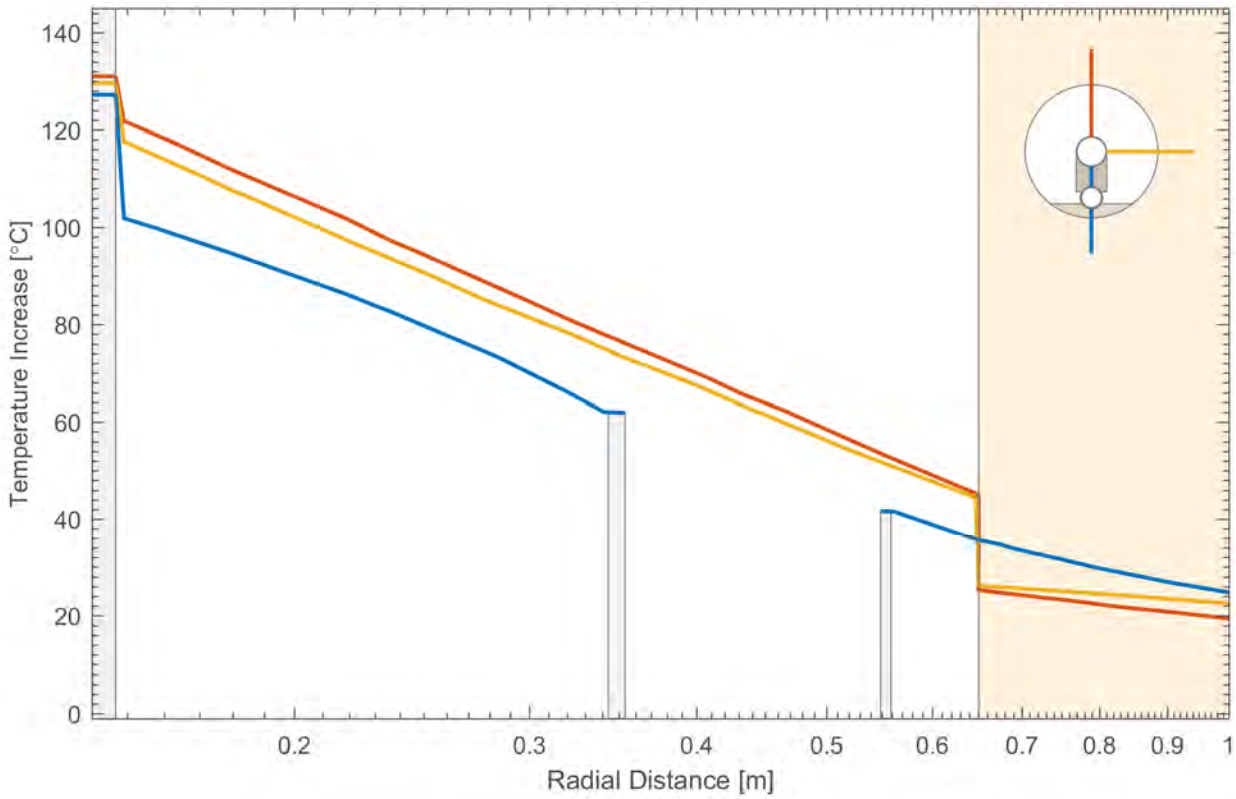

Figure 5-21. Profiles of Steady State Temperature at the N2 Cross Section in the 3-D COMSOL Thermal Model With a Thin Resistive Layer Assumption.
[°F = (1.8 × T °C + 32), 1 m = 3.3 ft]

Temperature (°C); contour spacing is 2 °C

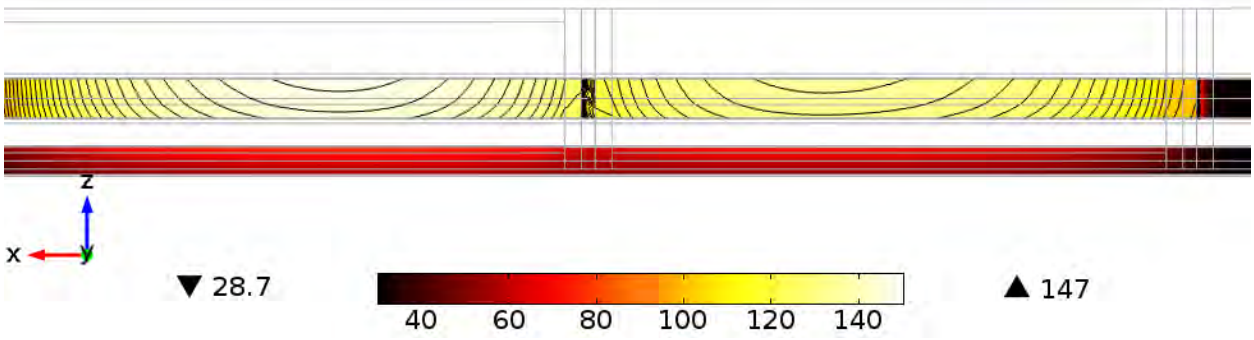

Axial heat flux (kW/m²); contour spacing is 0.2 kW/m²

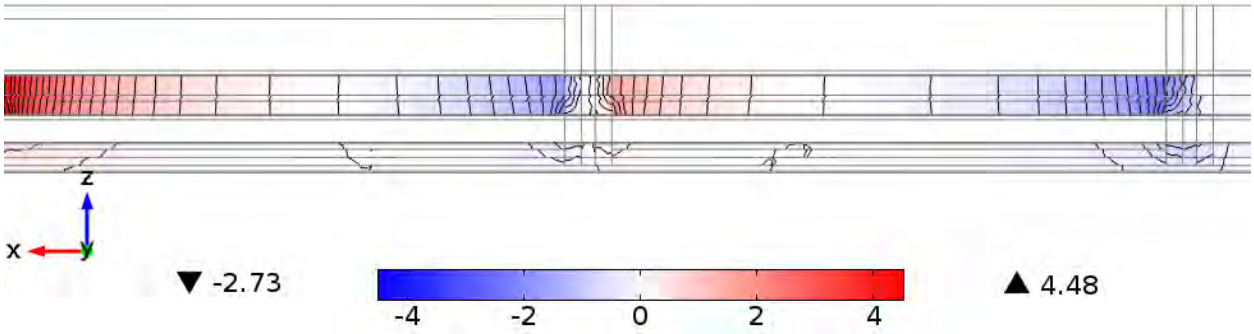

Ratio of axial heat flux to total heat flux; contour spacing is 0.1

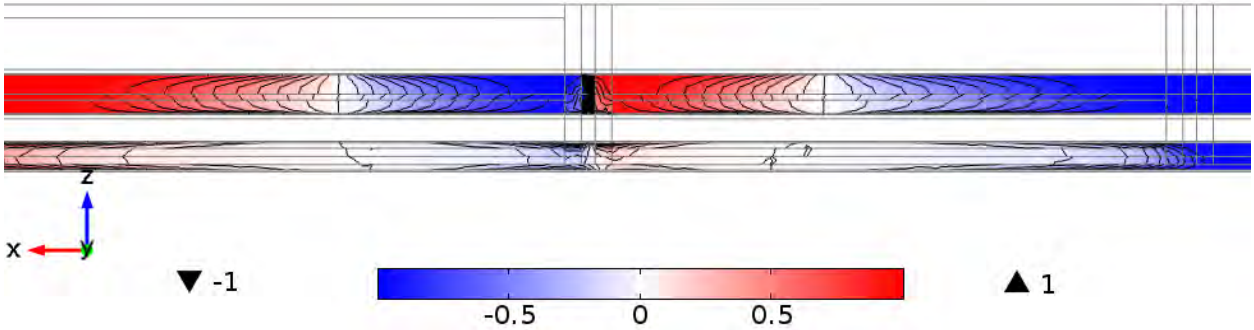

Figure 5-22. Orthotropic Projection to a Vertical Plane of Calculated Temperature (Top), Axial Heat Flux (Middle), and Ratio of Axial to Total Heat Flux (Bottom) for the 3-D COMSOL Thermal Model With Nominal Properties. Extreme Values are Indicated to the Side of the Scales. [°F = (1.8 × T °C + 32), 1 m = 3.3 ft]

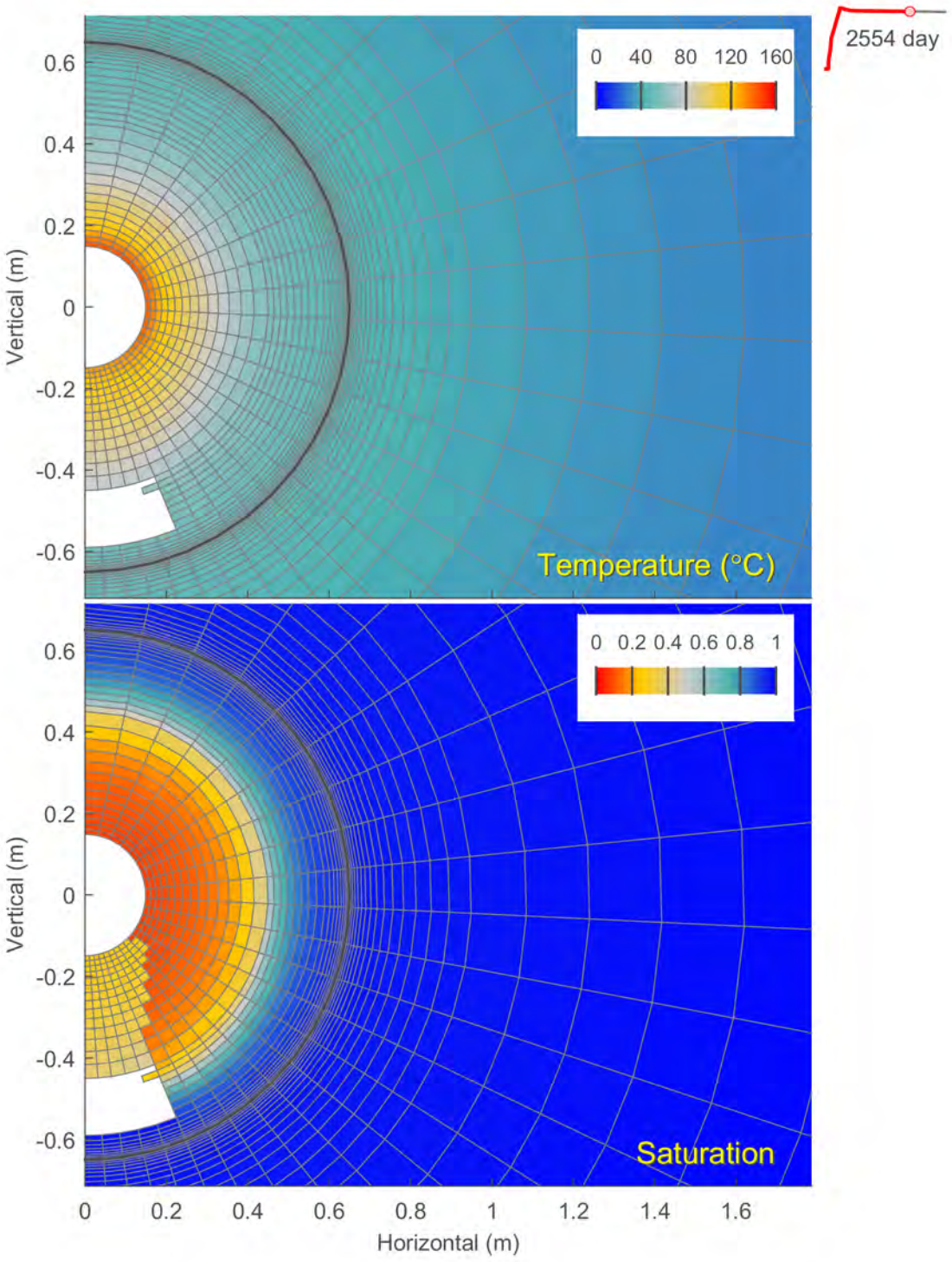

Figure 5-23. Temperature and Saturation Profiles 7 Years After Start of Heating for the Case With Calibrated TH Properties and the Short-Heat Boundary Conditions (Advancing Front Scenario). Tunnel Wall is at Radius of 0.65 m. [°F = (1.8 × T °C + 32), 1 m = 3.3 ft]

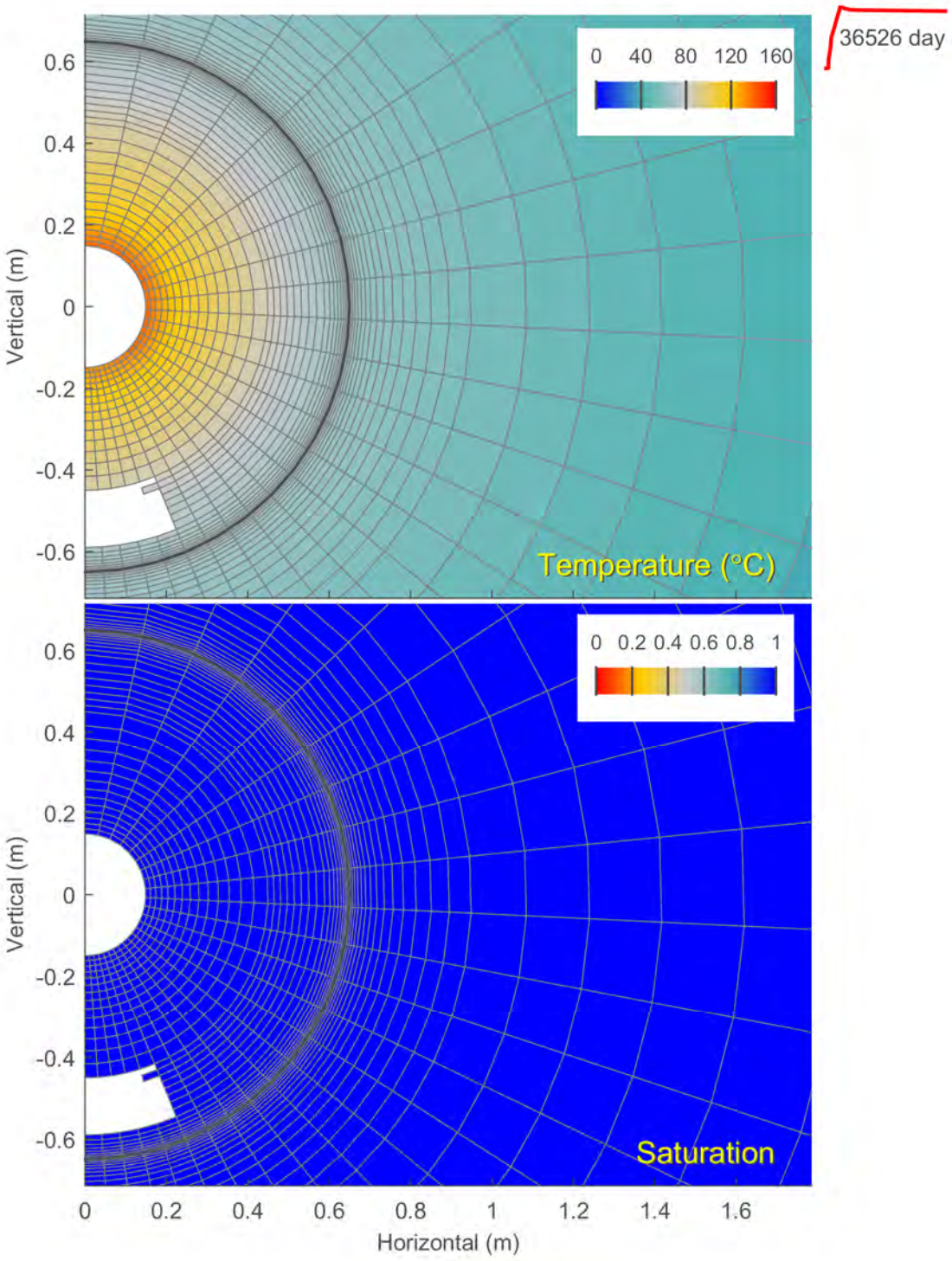

Figure 5-24. Temperature and Saturation Profiles 100 Years After Start of Heating for the Case With Calibrated TH Properties and the Long-Heat Boundary Condition (Rewetted Buffer Scenario). Tunnel Wall is at Radius of 0.65 m. [°F = (1.8 × T °C + 32), 1 m = 3.3 ft]

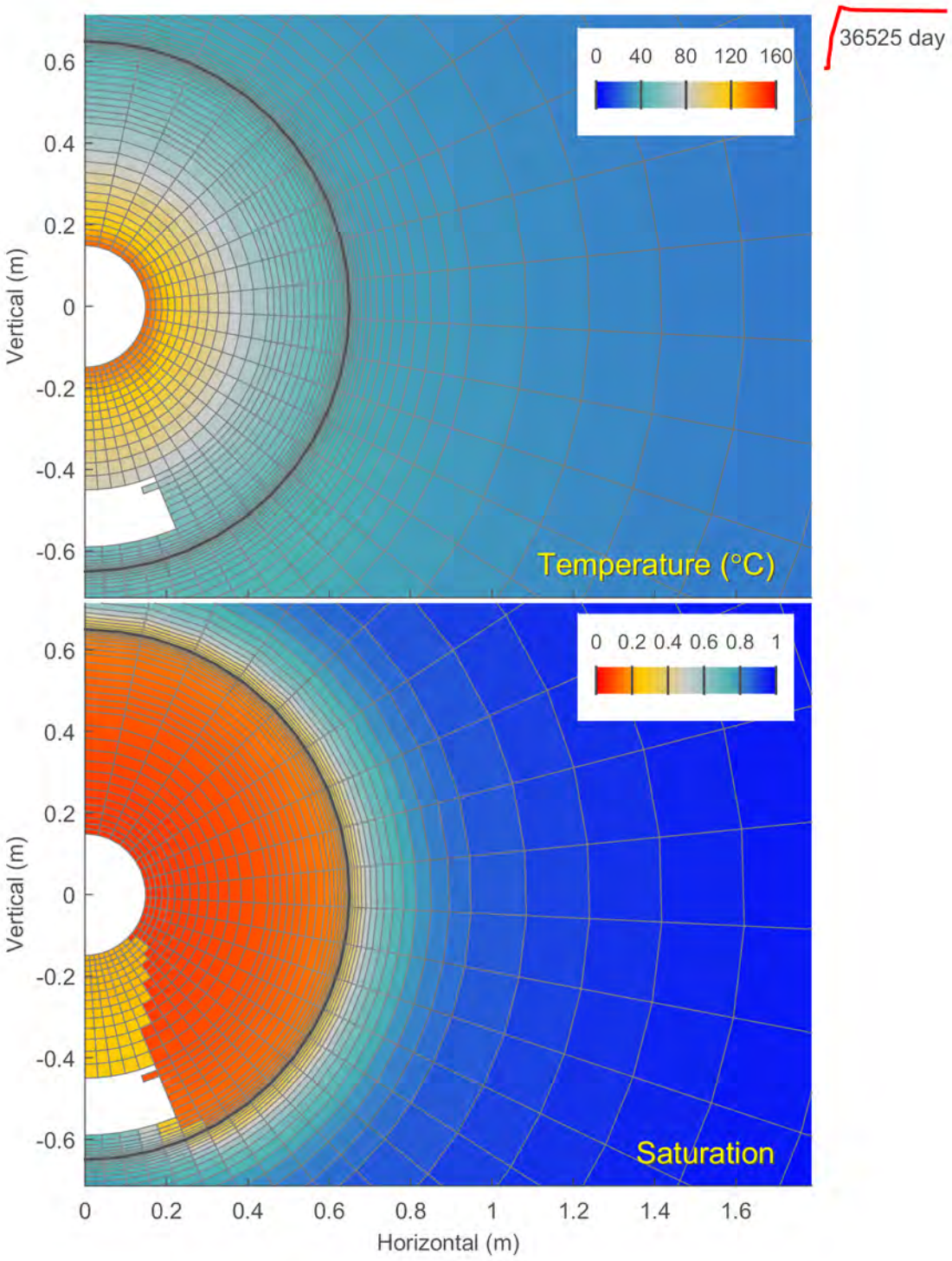

Figure 5-25. Temperature and Saturation Profiles 100-Year After Start of Heating for the Case With Uncalibrated TH Properties and the Long-Heat Boundary Condition (Desiccated Buffer Scenario). Tunnel Wall is at Radius of 0.65 m. [°F = (1.8 × T °C + 32), 1 m = 3.3 ft]

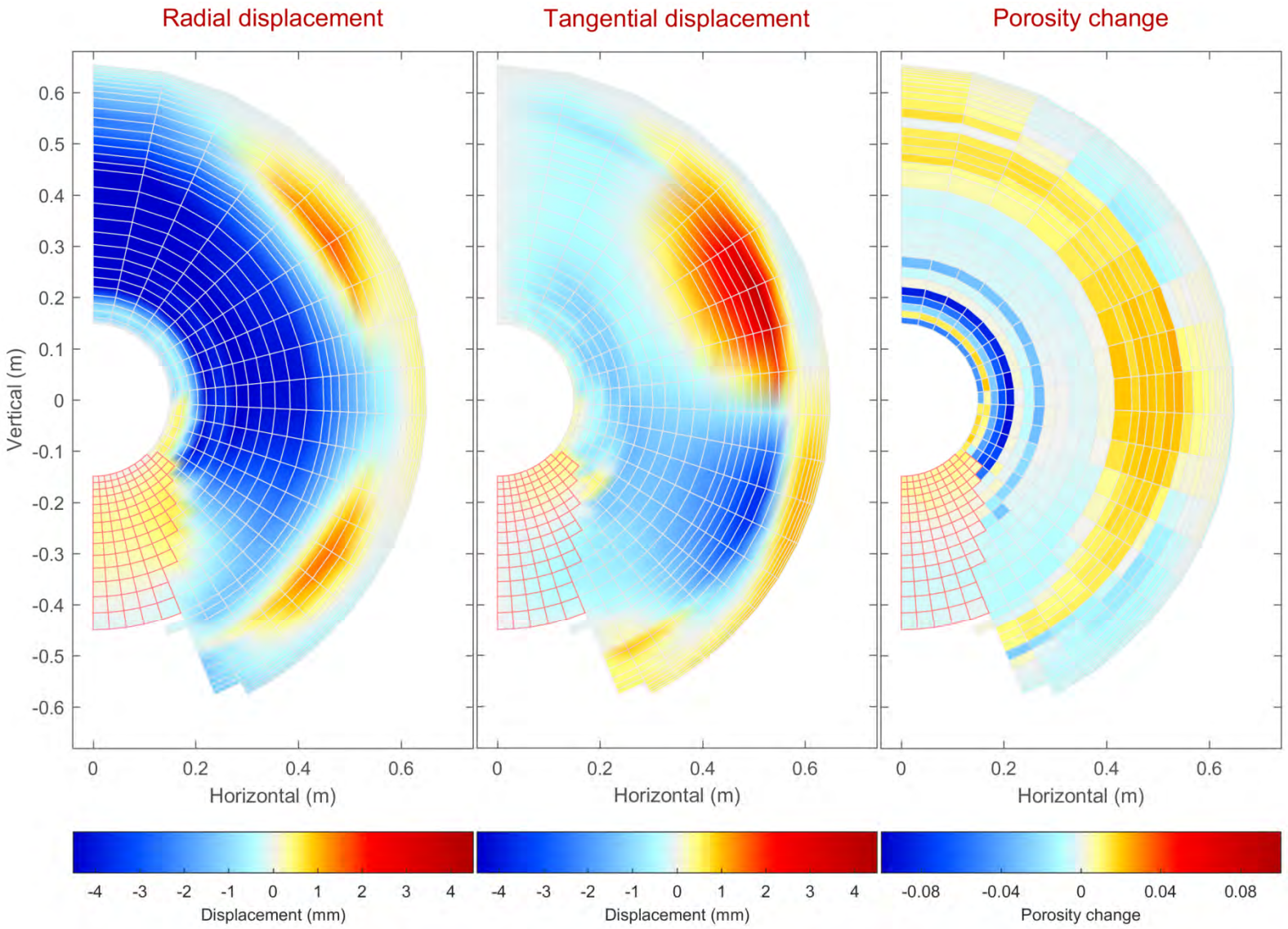

Figure 5-26. Radial and Tangential Displacements, and Change in Porosity, for the Advancing Front Scenario (Granular and Block Bentonite Zones Only). Tangential Displacement is in the Counter-Clockwise Direction.

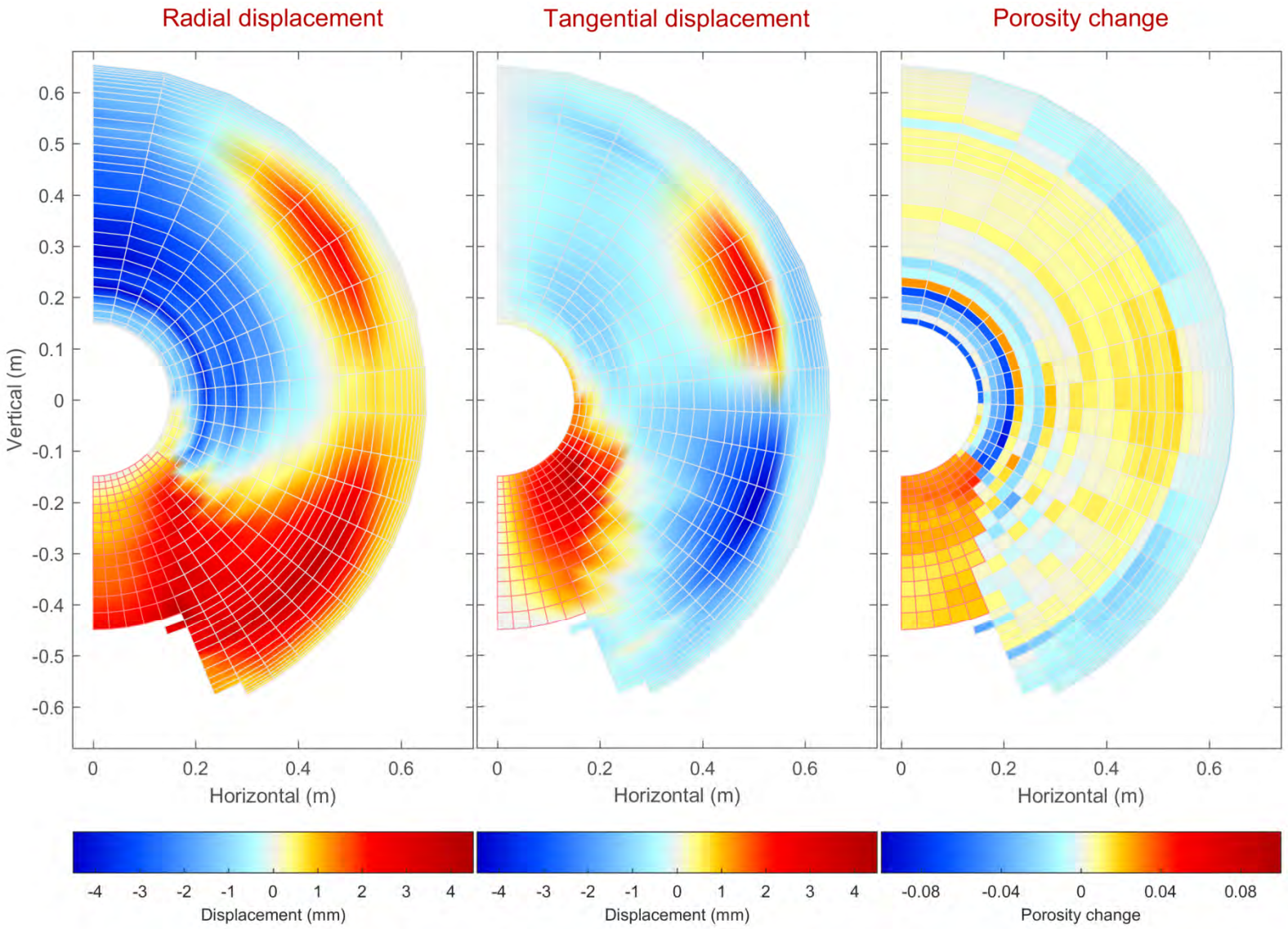

Figure 5-27. Radial and Tangential Displacements, and Change in Porosity, for the Rewetted Buffer Scenario (Granular and Block Bentonite Zones Only). Tangential Displacement is in the Counter-Clockwise Direction.

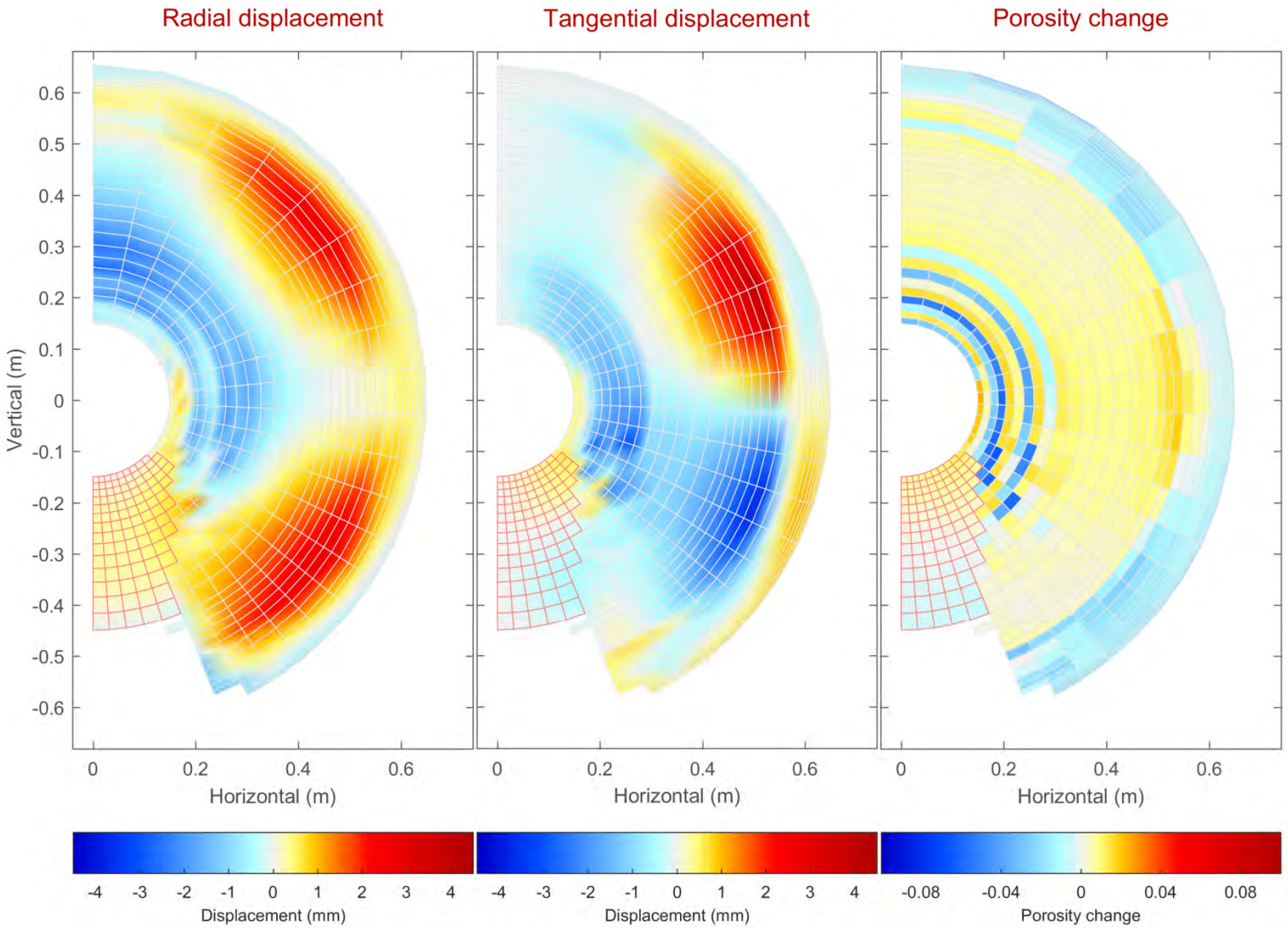

Figure 5-28. Radial and Tangential Displacements, and Change in Porosity, for the Desiccated Buffer Scenario (Granular and Block Bentonite Zones Only). Tangential Displacement is in the Counter-Clockwise Direction.

6 AUXILIARY ANALYSES

The modeling scope for **De**velopment of **Co**upled Models and Their **Val**idation Against **Ex**periments (DECOVALEX)-2015 Task B1 focused exclusively on processes in the microtunnel and near field, particularly emphasizing buffer responses to heating. All inter-model comparisons under Task B1 are at locations within 6.5 m [21 ft] of the microtunnel wall, with heating during the HE-E test expected to cause little temperature change outside this radius. The initial conceptual model behind the simulations assumes that the host rock is water saturated except perhaps for a transient dryout zone adjacent to the microtunnel, the excavation damaged zone (EDZ) rapidly heals, processes in the buffer are minimally affected by the host rock, and all engineered and natural components remain in close contact.

The modeling exercises suggested that mass and energy exchanges with the host rock and engineered components may have a substantial influence on processes in the buffer, and the influence of heating may alter pore pressures much deeper into the host rock. After all modeling was completed for the task, a series of auxiliary analyses were performed to better understand certain anomalies between model calculations and data provided by the task leader.

The auxiliary analyses considered all of the data provided by the task leader, not just the data selected for cross-comparisons between all task participants. Additional information available from other Mont Terri Underground Research Laboratory (URL) studies proved very useful in the auxiliary analyses. The series of analyses stemmed from an effort to (i) replicate the initial pore pressure distribution around the microtunnel prior to heating and (ii) understand rapid observed reverse pore pressure responses to power outages. These analyses (i) yielded estimates of the initial pore pressure distribution across the URL footprint; (ii) identified studies showing that the pore pressure distributions and EDZ permeabilities are anisotropic around openings at the URL (due to stress distributions rather than permeability anisotropy); (iii) illustrated that mechanical, thermal, and hydraulic responses have distinctly different characteristic response times within the host rock; (iv) suggested that reverse pressure fluctuations after power failures observed laterally from the microtunnel stem from changes in the microtunnel cross section due to anisotropic thermal expansivity; and (v) revealed that thermal stresses profoundly influence microtunnel expansion and sudden slippage within the host rock. These analyses are contained within Sections 6.1 through 6.6. Implications for radioactive waste disposal are discussed in Section 6.7.

6.1 Pre-Test History Related to Pore Pressures Near the HE-E Test

The two dimensional (2-D) xFlo model of the HE-E test used initial and far-field pore pressure distributions based on estimates used in previous models, but the basis for the other estimates was not clear. The initial pore pressures have little effect on the model calculations during heating, because the initial pore pressures were altered with an extensive ramp up period forced by estimated relative humidity values in the microtunnel, and responses in the near field should be unaffected by the far-field boundary condition during the HE-E test period. However, sensors in different boreholes suggested that the radial gradients in pore pressure depended on axial position and the angle to the microtunnel axis, both at start of heating and while responding to heating, and it appears that pore pressures were declining with distance from the microtunnel in at least two of the Gallery 98 boreholes. These observations were not fully reproduced in the HE-E model. Accordingly, one auxiliary analysis considered the available information from the Mont Terri URL to better understand the expected pore pressure distributions in the host rock near the microtunnel.

The exploratory tunnel for the Mont Terri motorway tunnel was excavated in 1989 (labeled Security Gallery in Figure 2-2). The Security Gallery (also known as the Reconnaissance Gallery) was accepted for research activities in 1995, and field operations started in January 1996 with the construction of 8 Niches and 18 boreholes.

Horizontal boreholes BED-B1, BED-B2, and BED-B3 are 24-m [78-ft] boreholes drilled from Niche BF towards the location of the HE-E in mid-September 1997 (Möri et al., 1998), reaching to within 1 m [3.3 ft] of Gallery 98 (which had not yet been excavated). Gallery 98 is ~30 m [100 ft] west of the Security Gallery. Marschall et al. (2004; their Figure 4.22) showed sporadic measurements in 11 pressure sensors for the three boreholes starting by the end of May 1997 in these boreholes, with pressures between 1 and 1.5 MPa [145 and 218 psi]. Essentially continuous readings commenced at the end of September 1997, starting with atmospheric pressures.

Pore pressures rapidly rose to approximately 1.3 to 1.5 MPa [188.6 to 217.6 psi] in all 11 sensors by mid- to late-November 1997, which marked an inflection point for all sensors. Afterwards, pressures in all sensors continued to rise at a new rate, reaching 1.8 to 2 MPa [261.1 to 290 psi] in five months (all sensors responded at essentially the same rate). The excavation of Gallery 98 reached the sensor positions in the first week of April 1998 (Martin et al., 2004; their Figure 1-5), causing an initial rapid spike when the cutting face came within 1 m [3.3 ft] of the borehole position, then 10 of the 11 sensors dropped within two weeks, to levels between 0.5 and 1.7 MPa [72.5 and 246.6 psi] lower than their initial value depending on distance from the tunnel wall. Martin et al. (2004) attribute the pore pressure spike to deformation of the observation interval, which increased pore pressure within the rock.

A sensor (BED-B2 I4) located 12 m [39 ft] from Gallery 98 (almost midway between Gallery 98 and the Security Gallery) experienced a small spike and returned to just below 2 MPa [290 psi]. The rate of rise flattened in all sensors for this borehole, achieving levels slightly below 2 MPa [290 psi] several weeks prior to the Gallery 98 signal, and this may have represented an equilibrium state with respect to the Reconnaissance Gallery drawdown. Sensor BED-B1 I4, approximately the same distance from Gallery 98, held near 1.5 MPa [217.6 psi] with episodic fluctuations to 2 MPa [290 psi] after drilling operations.

Marschall et al. (2004; their Figures 4.23 and 4.24) also present data from others of the original boreholes to the end of June 2000. All of the sensors exhibited a gradual decline over the previous year (Marschall et al., 2004; their Figure 4.23), presumably reflecting gradual loss of water to the gallery ventilation. Sensor BED-B2 I4 had dropped to 1.8 MPa [261.1 psi] by this time. The data at the end of June show trends with respect to distance from a borehole and position along the Security Gallery. The boreholes deepest in the Opalinus showed larger pore pressures. This is consistent with a sloping water table above the Opalinus. An average water table slope in the overlying aquifer of 45° (representing a reasonable upper bound for the sloping water table) would result in a drop in 1.7 MPa [246.6 psi] over the 175-m [574 ft] range of borehole locations. At this separation and approximately the same radial distance, sensor BGP-1 registered ~0.25 MPa [36.3 psi] in September 1996 and sensor BPP-1 registered ~1.85 MPa [268.3 psi] in June 2000.

A steady-state three-dimensional (3-D) isothermal groundwater flow model with a simplified 3-D representation of the microtunnel, nearby mined features, Opalinus Clay aquifer, and underlying aquitards, was developed to estimate the equilibrium hydraulic gradient that might be expected near openings assumed to be at atmospheric pressure. The equilibrium gradient may take decades to centuries to achieve, once pore pressures redistribute after excavation-induced

strains. The COMSOL groundwater flow model used to consider this system (Figure 6-1) includes bedding planes aligned with the aquifer, which has a 30° tilt to represent the anticline above the laboratory. The model does not account for the additional rotation to 55° occurring across the laboratory. Note that the Main Fault is not represented in the model, but is located approximately 10 to 20 m [33 to 66 ft] above the HE-E test section based on dips measured in the microtunnel.

In the COMSOL model, permeability is assumed to be twice as large parallel to bedding than it is perpendicular to bedding. The top boundary is assumed to have a water table parallel to the top of the Opalinus Clay, and the bottom boundary is assumed to be a confined with piezometric surface sloping at 90 percent of the dip. These boundary conditions are based on the exposures at the top of the anticline and the two piezometers reported by Marschall et al. (2004; their Figure 4.21) that are separated by ~1 km [0.6 mi] at the motorway reference elevation. The presumed boundary conditions would need additional data to be confirmed.

Calculated equilibrium head distributions in the Opalinus Clay (Figure 6-2 top) drop with elevation at the top of the Opalinus Clay according to the boundary condition, thus pore pressure gradients are nearly perpendicular to the dip direction (Figure 6-2 bottom). The calculated flow is downward, approximately perpendicular to dip. This pattern is a consequence of two aquifers exposed to the atmosphere but offset in elevation. Flow patterns are likely to deviate further downdip, away from the atmospheric boundary. Atmospheric pressure near the laboratory forms a large sink. Including all of the mined openings in the model would create a much more laterally extensive sink, but this would likely not substantially affect pressure distributions near the microtunnel because of the boundary conditions represented by the top and bottom aquifers and the galleries and niches surrounding the microtunnel.

The equilibrium pore pressure distribution at approximately the center of the Nagra section of the HE-E (Figure 6-3) assumes that the HE-E test was not installed and that the microtunnel is at atmospheric pressure. The anisotropic permeability creates an oval shape to the drawdown, with vertical gradients steeper than horizontal gradients at the microtunnel. The region between the microtunnel and Gallery 98 has particularly shallow gradients due to the overlapping drawdowns around these features. All of the pressure sensors used for the HE-E test, including the subhorizontal boreholes extending from Gallery 98 towards the microtunnel, would experience pressures less than 400 kPa [58 psi] based on this calculation.

Measured local radial gradients near the galleries appear to be dependent on the borehole orientation (horizontal, slant, or vertical, in order of largest to smallest gradient) and the position with respect to the Main Fault. This conclusion is based on observations from vertical and horizontal boreholes on the northwest (deeper) side of the Main Fault, and vertical and slant boreholes on the southeast side of the Main Fault. These observations contrast with the COMSOL model equilibrium calculations, which show that pressure gradients are lowest in the bedding plane because pore pressures are responding to larger permeabilities along bedding planes.

Marschall et al. (2004) note that (i) the Main Fault appears to be even less permeable than the rest of the Opalinus and (ii) permeability measurements of the sandy facies based on packer tests are quite similar to permeability measurements of the shaly facies. These observations suggest that the Main Fault may affect flow patterns and pressure distributions, but the different intervals within the Opalinus Clay may have similar flow behavior.

Pressure distributions also may result from different stress configurations around openings. Martin et al. (2004) consider the Gallery 98 EDZ in detail, and findings from this study are directly applicable to the microtunnel, which is parallel to Gallery 98. Simulations of instantaneous pore pressure changes in response to drilling suggest that pore pressures rapidly increased by up to 1 MPa [145 psi] on the sides of Gallery 98 and decreased by up to 1 MPa [145 psi] on the top and bottom (Martin et al., 2004; their Figure 4-17), with perturbations becoming small 20 m [66 ft] from the gallery. If pore pressure disturbances require decades to dissipate, stress changes might explain the observed large gradients in the horizontal boreholes. Martin et al. (2004; their Appendix D) estimated that response time for 50 percent of a pore-pressure disturbance to propagate the diameter of the opening into the host rock is decades for Gallery 98, years for the microtunnel, and days for 100-mm [3.9-in] boreholes, given material properties similar to Opalinus Clay.

Martin et al. (2004; their Figure 6-20) also document several hydraulic conductivity measurements from the first meter of rock around Gallery 98. Seven reported hydraulic conductivities range from 10^{-7} to 10^{-10} m/s, compared to the undisturbed values of approximately 10^{-13} m/s, with the smallest values in the vertical and the largest values at opposing 45° locations (top on the side closer to the Security Gallery and bottom on the opposite side). The increase in hydraulic conductivity is reportedly due to circumferential cracks. Martin et al. (2004) concluded that this increase in the EDZ is local and does not form continuous flow paths. These hydraulic conductivity measurements suggest that the EDZ permeability around the opening is three to six orders of magnitude larger than that of the host rock.

6.2 Ventilation Experiment Test History

The Ventilation Experiment (VE) test changed the relative humidity over a range of 0 to 100 percent in the microtunnel for a period of several years prior to the HE-E test, and many of the sensors used for the HE-E test were inherited from the VE test. The HE-E model indirectly accounts for the ventilation perturbations by extending the ramp up period. The VE documentation was examined to understand if measured responses during the VE test had potential implications with respect to the HE-E test.

The microtunnel for the VE was excavated in February 1999. The microtunnel was sealed for VE testing 3.4 years later. The VE test included eight phases (Phases 2 through 9) from August 2002 through December 2006 (Mayor and Velasco, 2008), then the system was allowed to resaturate until the start of the HE-E preparation in December 2010 (Teodori and Gaus, 2011). Active desaturation occurred in VE Phases 4 through 6 (June 2003 through January 2004) and Phase 9 (July 2005 through December 2006). Phases 2 and 3 (August 2002 through June 2003) and Phase 7 (February 2004) ventilated with air at greater than 92 percent relative humidity. Phase 8 (March 2004 through July 2005) consisted of resaturation without ventilation.

The most extreme testing occurred in Phase 9, with relative humidity established at 5 to 10 percent in the test section after approximately 4 months and held at this level for 11 out of the next 13 months. During the first two or three months, the outflow rate per unit wall area dropped from 10 to <2 $g/m^2 \cdot hr$, and maintained at ~1 $g/m^2 \cdot hr$ over most of the last year with a relative humidity of 5 percent (Mayor and Velasco, 2008; their Figure 3).

The generated vapor outflow during the extreme testing period can be used to estimate how quickly pressures would respond in a saturated host rock using an analogy to pumping from a

borehole in an aquifer. The transient pressure response around a line sink given a constant pumping rate and constant isotropic hydraulic properties is illustrated in Figure 6-4 using the Theis equation (Theis, 1935). The radius represents distance from the axis of the tunnel. This represents the changes in the host rock if Phase 9 were held indefinitely. For this calculation, the permeability is 2×10^{-20} m^2, specific storage is 10^{-5} m^{-1}, and pumping rate per unit length of tunnel is 1.13×10^{-9} m^3/s·m. The pumping rate is equivalent to 1 g/m^2·hr mass flux per unit area at the radius of the microtunnel wall. For nominal Opalinus Clay properties, the propagation of a pore water pressure pulse to depth of several meters within the host rock would take years to decades. This rate of change is in stark contrast to the equilibration time of days to weeks for sensors in boreholes near Gallery 98 after cutting surfaces passed each borehole location. Rapid responses occurred for sensors located up to 10 m [33 ft] into the surrounding rock mass.

Garitte et al. (2013; their Figure 33) provided observations and modeling results for the VE test from the previous DECOVALEX phase, including pore-pressure observations 3.5, 4.5, and 5.6 m [11.5, 14.8, and 18.4 ft] from the microtunnel wall in borehole BVE-91 (also used in the HE-E test). The BVE-91 borehole was installed in April 2005 and the sensors were still equilibrating at the start of the Phase 9 ventilation (Mayor and Velasco, 2008; their Figure 6). Peak pressures ranged from 750 to 1100 kPa [109 to 160 psi]. The pore pressures in BVE-91 exhibited an annual oscillation of 100 to 200 kPa [14.5 to 29 psi], with a maximum in February, superimposed on a gradual decline of approximately 100 kPa/yr [14.5 psi/yr] over 4 years (December 2005 through December 2009). Annual changes in barometric pressure can only explain a very small fraction of the total change. The close correspondence between the different sensors might be consistent with an oscillating water table, because a change in pressure of 100 kPa [14.5 psi] corresponds to a water column 10 m [33 ft] deep and average annual precipitation in the region is between 1 and 1.4 m [3.3 and 4.6 ft]. Accounting for the karstic nature of the overlying limestone aquifer, the water table could oscillate more than 10 m [33 ft]. However, the low-permeability Opalinus Clay should strongly dampen the annual cycle at the depth of the Mont Terri URL. The annual change in water mass on total overburden mass above the Opalinus Clay could cause a stress change at depth, so annual fluctuation in water mass might explain a few percent of the observed fluctuations.

Garitte et al. (2013) suggested that annual temperature cycles propagating from Gallery 98 explain the pore pressure changes. It is more likely that temperature fluctuations at the microtunnel are the cause of BVE-91 fluctuations, because all sensors are closer to the microtunnel and the cycle is progressively delayed with distance from the microtunnel wall, consistent with propagation outward from the microtunnel. Note that these sensor readings increased by 600 to 800 kPa [87 to 116 psi] during the HE-E test, with temperature changes outside the microtunnel wall of 30 to 35 °C [86 to 95 °F], suggesting that a temperature fluctuation on the order of 5 °C [9 °F] might explain the annual cycle. Average air temperature in nearby Swiss cities fluctuates by ~18 °C [32.4 °F], but this variability may be strongly buffered by the rock mass before reaching the microtunnel. Peak atmospheric temperatures (i.e., during July) lead peak pore pressures (February) by ~7 months.

During the VE test, the sensor at 3.5 m [11.5 ft] distance led the sensors at 4.5 and 5.6 m [14.8 and 18.4 ft] distance by ~2 months at BVE-91 (Mayor and Velasco, 2008; their Figure 6). Between the VE and HE-E test, it appears that all sensors are synchronized (Garitte et al., 2013; their Figure 33), at least to within a month or so. After 500 days of the HE-E test, small {<40 kPa [5.8 psi]} changes in pressure are synchronized within days. The phase lag is proportional to distance in an isotropic medium, so a phase lag of 7 months at 4.5 m [14.8 ft] depth would imply that the signal leads by 1.6 months at 3.5 m [11.5 ft] and lags by 1.7 months at 5.6 m [18.4 ft]. This discrepancy may be partially due to anisotropic thermal conductivity

preferentially aligned with bedding; BVE-91 is slanted with respect to the bedding, so that the sensors are aligned with slightly different angles with respect to bedding.

The link between temperature and pore pressure can be seen clearly for BVE-91 in the HE-E test (data provided for DECOVALEX-2015) during a power outage lasting several days (days 572 through 575). Pressure immediately started to increase at all three sensors when the heating stopped, although the peak increase of ~20 kPa [3 psi] lagged onset by ~10, ~20, and ~30 days, respectively. It is not clear why pore pressures increased as a result of a cooling event, but the responses suggest that pore pressure responses in the Opalinus Clay are rapidly influenced by changes in rock stresses, more slowly influenced by propagating temperatures, and much more slowly affected by water movement.

Millard et al. (2013) discusses anisotropic effects around the VE test, including anisotropic permeability, stress, and mechanical properties. This work was performed under the previous phase of DECOVALEX. These analyses neglected temperatures and apparently did not consider BVE-91, but the analyses showed that changes in stress rapidly alter pore pressures and anisotropic mechanical properties amplify effects on pore pressures.

Thöny (2014; his Figure 2-25) plots temperature in borehole BRC-2 (off of Gallery 08) between April 2008 and May 2011. BRC-2 is a horizontal borehole at an 8° angle to Gallery 08 at the elevation of the Gallery 08 axis, so temperatures from Gallery 08 propagating to the sensors move along bedding planes. Temperatures in the sensor at 1.3 m [4.3 ft] (Sensor 1) range over 9 °C [16.2 °F], although the annual variation is smaller and changes from year to year. Peak rock temperatures lag the annual meteorological cycle by several months, with additional lag of ~2 months and ~3.5 months to the deeper sensors at 3.0 and 4.6 m [9.8 and 15 ft] depth. The lags in borehole BRC-2 are more distinct than lags in BVE-91. Sensor 1 was warmer than 16 °C [61 °F] from April 2008 (start of data) through January 2009, remained cooler than 16 °C [61 °F] until November 2010, and remained above 16 °C [61 °F] until May 2011 (end of data). Temperatures climbed 9 °C [48 °F] in Sensor 1 almost continually from April 2010 through April 2011. It appears that ventilation temperatures in the laboratory only partly follow the annual surface temperatures.

The literature related to the VE test provides background information on pore pressures in the Opalinus Clay around the microtunnel. This work suggests that anisotropic responses were observed prior to the HE-E test, and provides a limited indication that pore pressures respond strongly to thermal changes. Additional data from the start of the VE test up to the HE-E test would be useful in testing the thermal responses, especially if the air temperature in the MI Niche were available. These data do not appear to be readily available on the Mont Terri URL website.

6.3 HE-E Test Observations in Opalinus Clay

The Task B1 leader provided temperature, relative humidity, and pore pressure measurements from a set of sensors in the microtunnel and the Opalinus Clay host rock during the HE-E test, as well as the total power to each heater. The sensor data started 19 days prior to turning on the heater. Note that the only provided pore pressure data in the Nagra section is from boreholes drilled from Gallery 98. Chapter 4 discusses the thermal and hydraulic response of the buffer and near field in more detail, in the context of comparing observations with model results. The xFlo simulations were run uncoupled from stress feedbacks, so pore pressures in the host rock can only respond to changes in evaporation rates, fluid transfers across the microtunnel–host rock interface, and fluid and rock density responses to temperature change.

The previous discussion in Section 2.3 suggests that pore pressure may respond to these forcings more quickly and at greater depth than thermal and hydraulic conduction can explain.

A rapidly changed forcing provides a more distinct signal than a gradual change. Accordingly, an auxiliary analysis compared the rapid responses following transient power outages to the gradual responses during the normal test protocol.

The temperature and pressure observations from sensors located in the host rock are compared with the applied power load in Figure 6-5. The power load was ramped up over the first year in a series of steps. After the first year, computer-controlled power adjustments maintained the peak temperature at ~140 °C [284 °F] for each heater. Twelve sensors measured temperature on each heater surface, and temperature varied substantially across the heater surface. Based on the temperature readings for all 24 sensors, it appears that the top sensor in the center of each heater was used to adjust the applied power. The power applied in the GRS (sand–bentonite) section remained essentially constant once the initial ramping completed, implying that the thermal properties (thus water content) in the GRS section did not change. The power applied in the Nagra (granular bentonite) section gradually decreased over the next two years, implying that the effective thermal conductivity across the granular bentonite (and its water content) decreased slightly over time.

The temperature and pressure readings were detrended for Figure 6-5 to better visualize the response to the heater. Observations were typically made at hourly intervals. To detrend, first the observations were converted to average daily values, then an extrapolated linear rate of change was calculated for each sensor based on the first and last readings prior to turning on the heater. The extrapolated linear trend was removed from the average daily values to create the detrended series.

The detrended responses in Figure 6-5 are color-coded based on distance from the microtunnel axis. Red lines are responses adjacent to the microtunnel and yellow-tan lines are responses approximately 2 m [6.6 ft] from the microtunnel, all obtained from boreholes drilled from the microtunnel. Blue-green and blue lines are from sensors in boreholes BVE-91 and BVE-1, which were drilled with a declination of 5° from Gallery 98, and therefore the sensors are to the side and somewhat below the microtunnel. Estimated angles range from 22° to 35° (BVE-91) and 27° to 75° (BVE-1) from the horizontal, based on illustrations by Teodori and Gaus (2011; their Figures 5.19 and 5.20). The lines are also coded by weight and style to distinguish whether the observations are generally from above, below, or to the sides of the microtunnel. The only measurements further than ~2 m [6.6 ft] from the microtunnel wall are from BVE-91 and BVE-1. Two additional lateral boreholes were drilled from Gallery 98 for the HE-E test, BHE-E1 and BHE-E2, that dip by 6.2° from the microtunnel axis; these sensors had not equilibrated at the start of the test.

Temperature responses behaved generally as expected, with the responses tracking the power increase over the first year and continuing to warm more slowly once the power load stabilized (Figure 6-5). This behavior is consistent with gradual propagation of a thermal front into the host rock. The largest responses are from sensors near the buffer/rock interface and near the center of each section, with temperatures dropping both with radial distance and along the microtunnel axis.

A variety of pressure responses are exhibited (Figure 6-5). The observations suggest that the pore pressure responses do not track synchronously with temperature changes. Essentially no pore pressure changes are observed where the rock heats the most (at the microtunnel wall),

and the largest responses are meters into the rock where the temperature changes are small. The largest pore pressure responses occur ~2 m [6.6 ft] above the microtunnel; the earliest responses are from the middle of the GRS test section (cross section SA2), with later responses from the plug between test sections (cross section SA3). Near-field sensors from below and to the side of the microtunnel have modest and delayed responses. The near-field sensors have a characteristic “front-like” signature, with a delay, followed by a relatively rapid rise, followed by a relatively persistent pore pressure. Only one near-field sensor (in cross section SA3) exhibited a rise followed by gradually declining pressure.

All but one of the pore pressure sensors in the four Gallery 98 boreholes began responding within 50 to 150 days after the start of heating. These sensors have a smoother signal with smoother rise than the near-field response. The sensor in BVE-1 that is less than 2 m [6.6 ft] below the microtunnel does exhibit a front-like rise, but much earlier than other near-field sensors below and to the sides of the microtunnel. Some of the borehole sensors exhibit a gradual decline in pore pressures.

The power outages occurring 571 and 589 days into the experiment provided an opportunity to examine the responses due to a sudden change in conditions. This is akin to a slug test in examining aquifer properties. The detrended responses for temperature and pressure during the 60 days after the start of the first outage (which lasted ~3 days) are shown in Figure 6-6. The heater power is colored peach to indicate changes in power from 20 days before the outage.

The temperature responses to the outage exhibit the classic behavior of decay and delay, where increasing distance from the perturbation source results in a smaller response that is increasingly delayed. Temperatures vary significantly along the microtunnel axis, even though the power is uniformly applied. The magnitude of the temperature response also differs along the microtunnel, as shown when responses from different locations are compared.
The temperature response does not show a strong difference between vertical and horizontal, suggesting that anisotropy in thermal conductivity is not very large.

The pore pressure responses to the outage show an interesting pattern. Pressure ~2 m [6.6 ft] above the center and side of the GRS test section (SA2) begins dropping almost immediately after the outage starts, recovering after the heater resumes. The second outage causes a secondary decline. At the center plug (SA3), a small pressure rise occurs above the plug, followed by a slightly larger and longer decline and recovery. A larger (but still small) rise occurs below the plug, followed by a similar decline and recovery. A distinct rise is visible in most of the sensors in the boreholes from Gallery 98, followed by a longer decline. The two nearest pore pressure sensors, located 1.9 and 2.8 m [6.3 and 9.2 ft] below the microtunnel, do not exhibit the anomalous rise. The one sensor in SA4 (near the N1 cross section) showing above-atmospheric pressures, P-B7, which is located >2 m [6.6 ft] from the microtunnel wall at the 7:30 o’clock position (45 degrees below horizontal), has a particularly strong reverse pressure response of 40 kPa [psi] following the outage on day 571.

The anomalous rise in pore pressure appears to be an example related to the Noordbergum and Rhade effects, which refer to transient reverse water level changes in clayey aquitards when pumping starts or stops in wells completed in the adjacent aquifers. The reverse water level change is due to rapid strain response to a change in pumping, and has been observed in fractured crystalline rock as well (Burbey, 2013). When observed in aquitards, the reverse pressure typically dissipates within minutes to hours, followed by a more typical pressure

response. A reverse-pressure response to changes in thermal stress does not appear to have been described in the literature, at least not linked to the Noordbergum effect.

The detrended responses for temperature and pressure during the 340 days after the start of the first outage are shown in Figure 6-7. The near-field pore pressure responses appear to be responding to the gradual decline in power to the Nagra heater. The long-term declines in the borehole pressures also may be partly due to the normal dissipation of pore pressures, which coincidentally may have begun to become significant when the outages occurred.

6.4 Thermally Induced Deformation in the HE-E Test

The observed rapid pore pressure responses to thermal events discussed in Section 6.3 implies that thermally induced deformation of the host rock may be responsible for rapid propagation of strains. Available deformation data were examined to identify whether thermal stresses induced significant strains around the microtunnel.

The Task B1 leader provided spreadsheets with hourly relative deformation measurements from cross sections SD1 and SD2. Each cross section has three of four operating extensometer sensors measuring relative radial displacement between the microtunnel face and 2 m [6.6 ft] into the host rock. Cross section SD1 is in the GRS section near Plug 2 and cross section SD2 is near cross section N2.

The extensometers were installed for the VE. During the VE test phases, the extensometers recorded host rock contraction (tunnel expansion) while the host rock was drying and rock expansion (tunnel shrinkage) while the host rock was rewetting. Individual extensometers typically varied in length by <2 mm [0.79 in] between phases (Figure 6-8).

The extensometers recorded an average deformation approximately one order of magnitude larger during heating (Figure 6-9). At the start of the HE-E heating phase, two of the three extensometers in each cross section were within 0.5 mm [0.02 in] of the original length. The other two were deformed by 6 to 7 mm [0.24 to 0.28 in], one by extension and the other by contraction. These data suggest that the microtunnel deformed asymmetrically since the extensometers were installed.

During the heating phase, all of the extensometers registered strong contraction linked to power input. The extensometers expanded and contracted synchronously to stimuli, with some responses linked to steps in power and other responses not obviously linked to power changes. Mean deformation across the extensometers responded as approximately the square root of applied power, consistent with the area of the microtunnel increasing proportionately to applied power. Contraction stalled or greatly slowed approximately a month before peak power was reached, with all relative displacements between 13 and 17 mm [0.51 and 0.67 in].

Several months after peak power stabilized, all six extensometers registered a rapid contraction over two to three hours, with all extensometers ending with displacements between 17 and 17.5 mm [0.67 and 0.69 in]. Host rock pore pressures were unaffected by the rapid contraction event, but there was an inflection in the rate of pore pressure increase approximately 10 days prior to the contraction event at several locations. The rate of pore pressure increase reduced by a factor of two to three at the inflection, suggesting that some feature contacted by the growing pressures was able to relieve the excess.

The uniform relative displacements suggest that the microtunnel reached an essentially circular cross section after the rapid contraction, with its radius increased by at least 2.6 percent from the initial state when the extensometers were installed. A larger diameter increase may have occurred if radial movement of the host rock away from the tunnel occurred more than 2 m [6.6 ft] into the host rock.

Subsequent power outages had very little effect on the extensometers, if anything, causing a slight increase to the extensometer contraction. The extensometers continued to contract slightly over time, even though the applied power in the Nagra heater gradually decreased over the same period. The magnitude of the contraction during this period is comparable to the magnitude of contraction during rewetting in the VE test (Figure 6-8).

6.5 HE-D Responses

The reverse pressure and relative deformation responses in the host rock described in Sections 6.3 and 6.4 suggest that the host rock responds strongly to thermal stresses. The available sensor density in the HE-E test is enough to identify that these processes are occurring, but is not designed to probe the host rock responses. The first subtask under Task B1 modeled the HE-D test, which was specifically designed to evaluate host rock responses to heating. Accordingly, the HE-D test data was re-examined to assess relationships between pore pressures and thermal stresses.

The HE-D test explicitly probed the responses of the saturated Opalinus Clay to a pair of adjacent heaters located in a single borehole. The HE-D test occurred at a smaller scale than the HE-E test, with a borehole diameter of 0.3 m [0.98 ft] instead of 1.3 m [4.3 ft] and a total effective heater length of 5.16 m [16.9 ft] instead of 8 m [26.2 ft]. The host rock reached approximately 100 °C [212 °F] at the borehole wall during the second phase of the HE-D test, compared to estimated peak temperatures of approximately 50 °C [122 °F] below the microtunnel for the HE-E test. The horizontal heater borehole is approximately perpendicular to the HE-E test microtunnel, installed along a bedding plane perpendicular to dip. The HE-D heater borehole has approximately the same azimuth as the minimum principal stress, whereas the HE-E microtunnel has approximately the same azimuth as the intermediate principal stress.

Instrumentation for the test included (i) 12 co-located temperature and pressure sensors, (ii) numerous additional temperature sensors, and (iii) extensometers in three boreholes. The first subtask of Task B1 compared the measurements to model predictions of the THM behavior of the saturated host rock (Ofoegbu et al., 2015a).

Pore pressures responded to mechanical events in the HE-D test (Figure 6-10). Pressures in the D14, D15, and D16 sensors near the D0 (heater) borehole suddenly dropped during the last stage of borehole advance or more slowly increased during the borehole drilling. These sensors are between 94 and 135 cm [3.08 and 4.43 ft] of the heater borehole. Sensors D03 (the nearest sensor to the heater borehole in the bedding plane, on the distal side from MI Niche) and D08 (also in the bedding plane, on the proximal side to MI Niche) recorded a gradual pore pressure increase starting with start of the borehole installation. Sensor D03 also recorded a pore pressure drop of ~0.2 MPa [29 psi] when the heater packer initially inflated to a pressure of 1 MPa [145 psi]; this is the reverse of what would be expected when the host rock is compressed. Rapid pressure drops also occurred in sensors D03 {<0.1 MPa [15 psi]}, D14 {0.4 MPa[58 psi]}, and D15 {0.6 MPa[87 psi]} when the heater packer failed, with slower recovery after the heater packer was repaired.

Pore pressures also responded to heating events (Figure 6-10). Note that some heating events featured different temperature responses on heaters H1 and H2, which may have influenced thermal responses in the adjacent host rock. The heater packer failure between July 24 and 29, 2004, appeared to locally redistribute heat fluxes due to altered contact with the host rock. The power interruption between December 15 and 17, 2004 appeared to start with heater H2 failing and more than a day later H1 failing. Total power may have been maintained for more than a day by transferring power from heater H1 to H2 before H1 failed. Note that the December 2004 power interruption triggered a continued packer pressure drop of <0.1 MPa [15 psi], and the final cooling phase triggered a continued packer pressure drop of >0.1 MPa [15 psi] (Wileveau and Rothfuchs, 2007, Figure 2-19).

Like the HE-E test, reverse pressures occurred in the HE-D test due to thermal events. The HE-D synthesis reports (Wileveau and Rothfuchs, 2007; Wileveau, 2005) recognize that reverse pressures occurred without proposing a cause. The largest reverse pressures were ~0.2 MPa [29 psi], occurring after sudden temperature changes at sensors that were roughly in the same bedding plane as the heater. Reverse pressures were not observed in the direction roughly perpendicular to the bedding plane.

Thermally induced reverse pressure events initiate shortly after the change in temperature at the heater. The magnitude of the reverse pressure at a particular location continued to increase until the temperature front reached the location, then the pressure started to respond normally. At three locations with reverse pressure responses (sensors D03, D16, and D17), temperature changes lag the reverse pressure response by ~13, ~18, and >48 hr at 0.93, 1.42, and 2.96 m [3.05, 4.66, and 9.71 ft] from the heater axis {0.78, 1.27, and 2.81 m [2.56, 4.17, and 9.71 ft] from the borehole wall}. At the nearest location in the perpendicular direction (sensor D14), 0.93 m [3.05 ft] from the axis, only the normal pressure response occurred but it started ~1 hr after the heater temperatures began responding and ~12 hr prior to the temperature response at the same location. This behavior is consistent with a gradually accumulating differential strain ahead of the temperature front that is overwhelmed by local responses to temperature changes at the sensor location.

The reverse pressure occurrences in the HE-D test are consistent with the observations from the HE-E test, insofar as reverse pressures (i) repeatedly occur soon after sudden temperature changes, (ii) appear to be aligned with the bedding plane, and (iii) propagate more rapidly than the temperature signal itself.

6.6 Inferences

The additional information gleaned from other studies at the Mont Terri laboratory has provided insights into several aspects of the recent modeling work.

Initial Pore Pressures

The available information suggests that the pressure distribution within the laboratory prior to any excavation is likely consistent with a sloping water table above the Opalinus Clay and a sloping piezometric surface below the Opalinus Clay, with flow generally downwards through the clay. Pressures in the thick overlying karstified limestone aquifer, approximately 100 m [330 ft] above the HE-E test location, likely are unaffected by interactions with the Opalinus Clay, but pressures in the thinner underlying aquifer may be affected by interactions with the Opalinus. The effective distance to the boundary condition must be larger than the minimum distance. The xFlo modeling work assumed that the pressure condition was consistent with a

water table ~170 m [560 ft] above the HE-E test, and used the distance to the water table as the outer model domain. The actual water table is probably somewhat higher in elevation, increasing pressure, but the effective domain radius may be a bit smaller based on the Opalinus Clay thickness. The effective domain radius must be larger than the 100 m [330 ft] thickness to account for longer flow paths at the side of the domain. In 3-D models, it is probably unnecessary to use a model domain that exceeds a cube co-located with the top and bottom of the Opalinus Clay.

Links Between THM Processes

Other studies from the laboratory combine with the HE-D and HE-E tests to illustrate important links between thermal, hydraulic, and geomechanical processes in the Opalinus Clay. These processes operate at quite different time scales. Geomechanical responses to a perturbation propagate much faster than thermal responses, which in turn propagate much faster than water can redistribute. Both geomechanical responses and temperature changes have a strong effect on pore pressures under saturated conditions in the Opalinus Clay. Pore pressure distributions in the host rock are dominated by changes in strains due to excavation for years to decades after excavation, depending on the diameter of the excavation. Excavation rapidly modifies pore pressures even multiple excavation diameters from the excavation wall. Changes in temperature at the excavation boundary can modify thermal stresses in the host rock, resulting in pore pressure changes distal to the excavation without affecting pore pressures in the unsaturated zone at the excavation wall. Even changes in ventilation temperatures of several degrees appear to be sufficient to change pore pressures by 100 to 200 kPa [15 to 29 psi] several meters from the HE-E microtunnel, long before the resulting small temperature change can propagate to this depth.

Over the time scales of the HE-E and HE-D tests, changes in pore pressures within the host rock appear to be almost completely determined by passive responses to TM perturbations. Only pore pressures very near the microtunnel, niches, and galleries are likely to respond to evaporative exchanges or transfers with the buffer medium during the tests, and studies in other parts of the URL indicate that the pore pressure distribution near openings may simply be due to expansion of the host rock into the openings as influenced by the stress field. This implies that measured pore pressure changes may be a useful indicator of local changes in porosity given local temperature.

The NRC/CNWRA team did not consider the effect of excavation on initial pore pressures in modeling the HE-E test, nor did they consider the effect of thermally induced strains on pore pressures. The FLAC model did consider the effect of excavation, but was not calibrated to the relative deformation data and underestimated the microtunnel expansion because of heating. From the modeling perspective, the calculated pore pressure results are probably best interpreted with respect to changes from the initial state. It will be necessary to complete the two-way coupling between xFlo and FLAC to capture the important TM processes that dominate changes to pore pressure distributions within the Opalinus Clay.

Reverse Pore Pressure Responses

The pore pressure observations in the Opalinus Clay during the HE-E test clearly reveal a reverse-pressure phenomenon occurring several meters into the host rock due to a power outage. Revisiting the HE-D test shows that reverse pressures were also seen in several sensor locations following mechanical and temperature changes at the heater. Reverse pressures mediated by mechanical responses have been observed in groundwater applications

since the 1960s, commonly seen in a soft aquitard deforming due to sudden pumping changes in an adjacent aquifer. Recently the same reverse-pressure response to pumping was observed in fractures in hard crystalline rock. This may be the first documented instance of reverse pressures resulting from mechanical deformation induced by changes in thermal stresses.

Reverse pressures in the Opalinus Clay are a direct indication of interaction between THM processes that cause changes in available pore space. Because the rock is fully saturated, changes in the volume available for pore water induce a change in pore water density. Because water is nearly incompressible, only a small change in water density is sufficient to induce a large change in pore pressure.

The HE-D heaters are oriented perpendicular to the HE-E heaters. In both tests, reverse pressures are only seen when the pressure sensor is offset from the heater mostly in the bedding plane. The HE-D test sensors indicate that both reverse and normal pressure responses initiate before the temperature responses at a given location. Reverse pressures accumulate until the temperature front reaches the location, then the normal response takes over. These characteristics are consistent with preferential thermal expansivity perpendicular to the bedding plane, which implies that disproportionate strains perpendicular to the bedding plane tend to be compensated by the reverse strains parallel to bedding.

Laboratory measurements by Wileveau (2005; their Table 7-4) indicate that thermal expansion is 1.7 to 3.8 times greater perpendicular to bedding in the Opalinus Clay. Measurements by Wileveau and Rothfuchs (2007; their Table 3-2) indicated that thermal expansion is 10 times larger perpendicular to bedding. With such anisotropy, a cooling event causes contraction in all directions in the host rock, but the larger thermal contraction perpendicular to bedding requires compensating strains parallel to bedding that temporarily overwhelm the small amount of thermal contraction along the bedding plane.

The reverse pressure observation in the D03 sensor following the initial pressurization of the heater packer in the HE-D test combined with the response of the radial extensometers during heating in the HE-E test, further suggests that the reverse pressures may be primarily due to changes in the shape of the openings in the host rock. The HE-E extensometers demonstrated that thermal expansion due to heating made the microtunnel opening more circular and pressurization of the heater packer also must have made the HE-D borehole more circular. The maximum principal stress is subvertical, oriented with N210° azimuth (southwesterly) and 70° dip (Wileveau, 2005), and the other principal stresses are subhorizontal and approximately aligned with the HE-D borehole and HE-E microtunnel axes. These orientations will tend to flatten the openings in a subvertical direction. The bedding planes dip 25° (HE-E test) to 45° (HE-D test) to the southwest, generally 25° to 45° of the principal stress direction, which may modify the deformation directions if there is anisotropy in the bedding directions.

6.7 Implications for Radioactive Waste Disposal

The HE-E test and associated studies from the Mont Terri URL reveal several responses of the host Opalinus Clay to heating that are pertinent to radioactive waste disposal.

- *Buffer rewetting*. The observed heating-induced expansion of the host rock results in a larger mined opening. Observed temperature profiles within the buffer and host rock in the HE-E test are consistent with poor contact between (i) the buffer and the top and sides of the microtunnel and (ii) the media surrounding the heater liner and the liner

sides and bottom. A gap in either location would tend to increase the temperature of an emplaced waste package. Further, a gap between the buffer and the host rock would tend to delay rewetting. The earliest rewetting would likely occur at the bottom of the opening, where the best contact between buffer and host rock remains. A modest amount of swelling at the bottom of the buffer might be sufficient to restore good contact between the buffer and the host rock.

- *Rapid host rock deformation*. The host rock is expected to undergo deformation in response to TH processes. Unexpected rapid and sudden deformation occurred during the HE-E test during an apparently quiescent period; such limited rapid deformation may not strongly affect the barrier capability of the rock, but this process should be explored further to bound the effects.

- *EDZ modification*. The observed radial deformation of the near field host rock during heating is likely to cause preferential circumferential and radial fracturing, or open existing fracture sets. Presumably the circumferential fractures will be compressed, but radial fractures may locally open. An open radial fracture set in the EDZ may permit rapid transfer of water between the host rock and buffer, and may provide a preferential conduit for axial flows along drifts.

- *Reverse pressure responses*. The observed reverse pressures require rapid changes to the mechanical state due to thermal changes, although rapid thermal changes are unexpected in a repository setting. Rapid changes may be very useful for identifying parameter values in coupled THM processes that would be difficult to characterize with tests based on slow changes. With this in mind, future field tests might benefit from test protocols that change stresses at several different time scales and several different magnitudes.

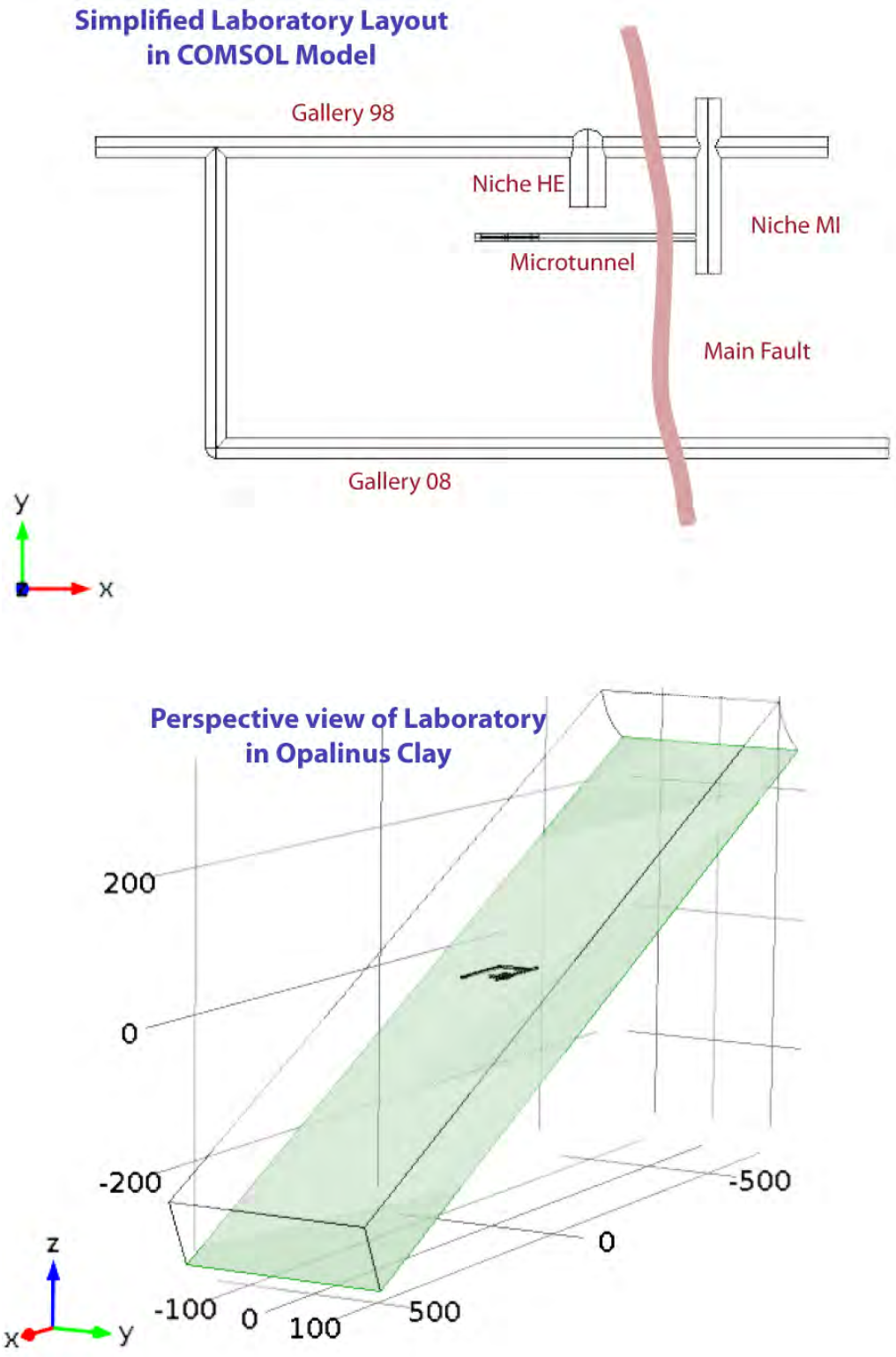

Figure 6-1. Schematic Layout of Mont Terri URL Features (Top) and Orientation of URL With Respect to the Opalinus Clay in the 3-D COMSOL Groundwater Model (Bottom). Axes are in Units of Meters [1 m = 3.3 ft].

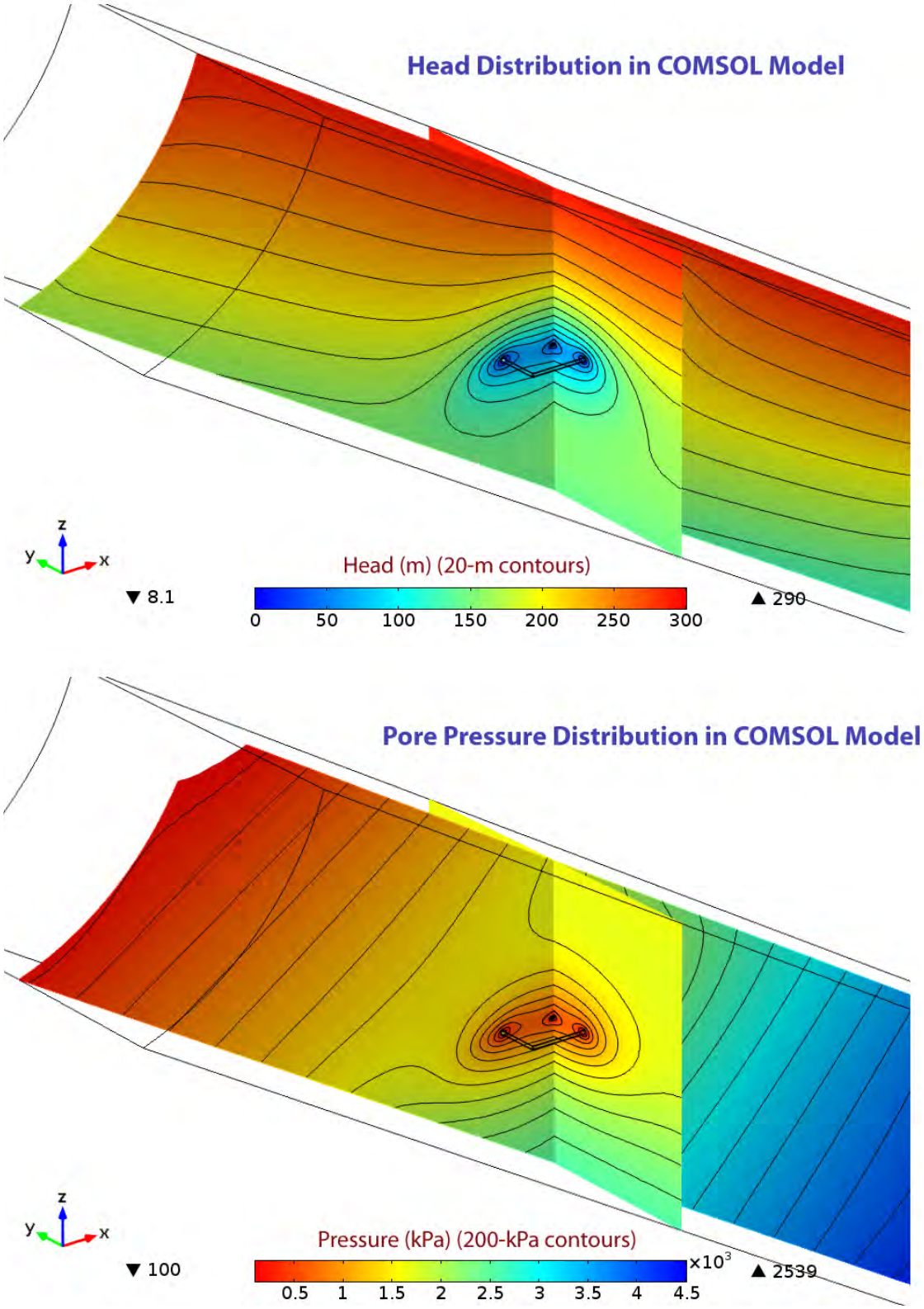

Figure 6-2. Head (Top) and Pore Pressure (Bottom) in the Opalinus Clay Calculated by the 3-D COMSOL Groundwater Model. [1 m = 3.3 ft, 1 kPa = 0.145 psi]

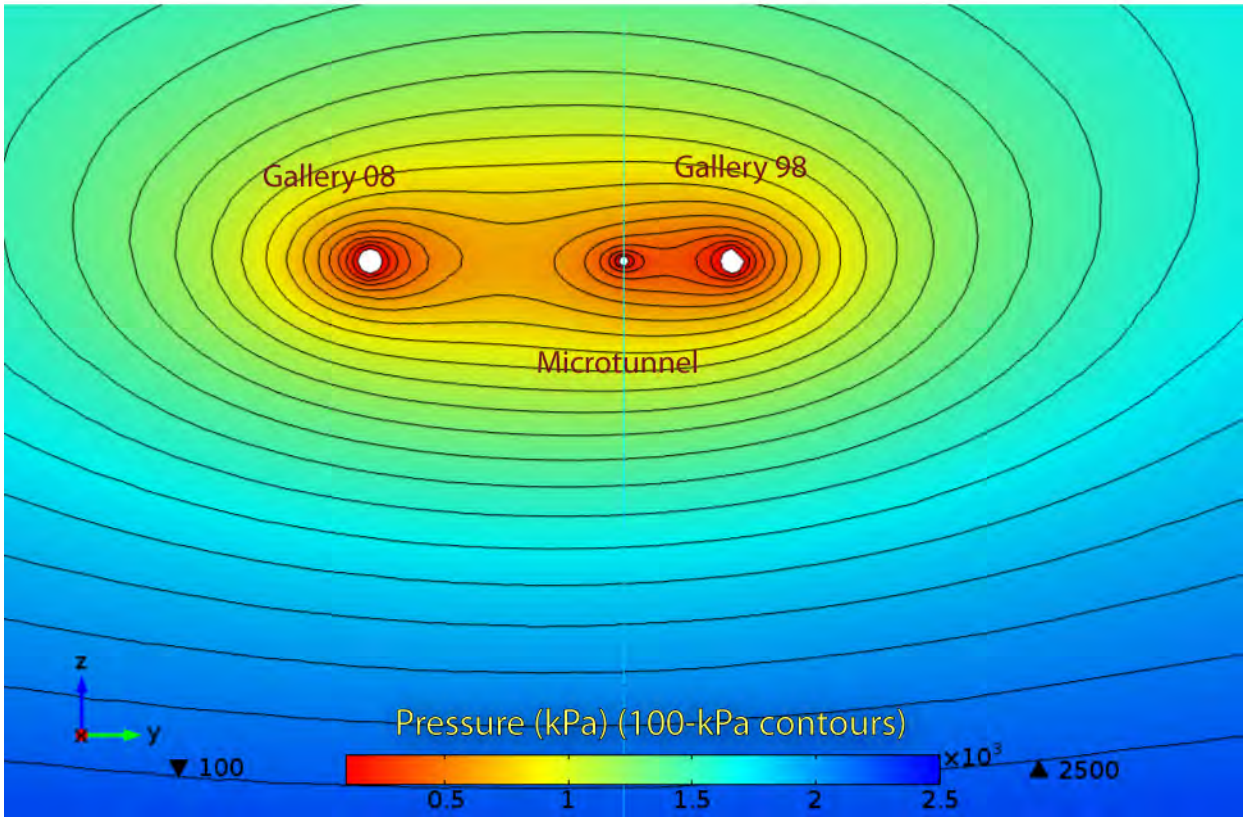

Figure 6-3. Pore Pressure in the Opalinus Clay Calculated by the 3-D COMSOL Groundwater Model at a Vertical Cross Section Passing Through the Center of the Nagra Section of the HE-E Experiment. [1 kPa = 0.145 psi]

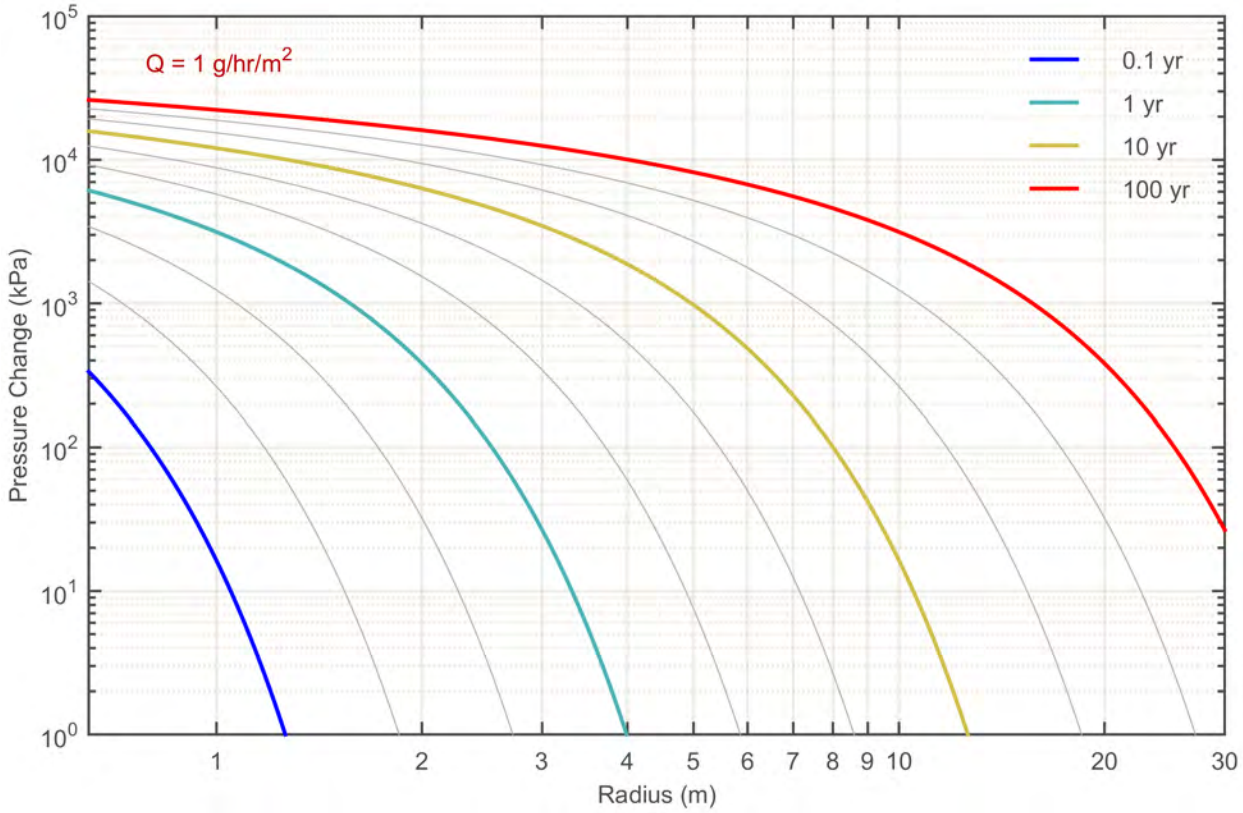

Figure 6-4. Transient Pressure Response to Constant Pumping Corresponding to Phase 9 of the VE test, Using Nominal Opalinus Clay Properties. [1 m = 3.3 ft, 1 kPa = 0.145 psi]

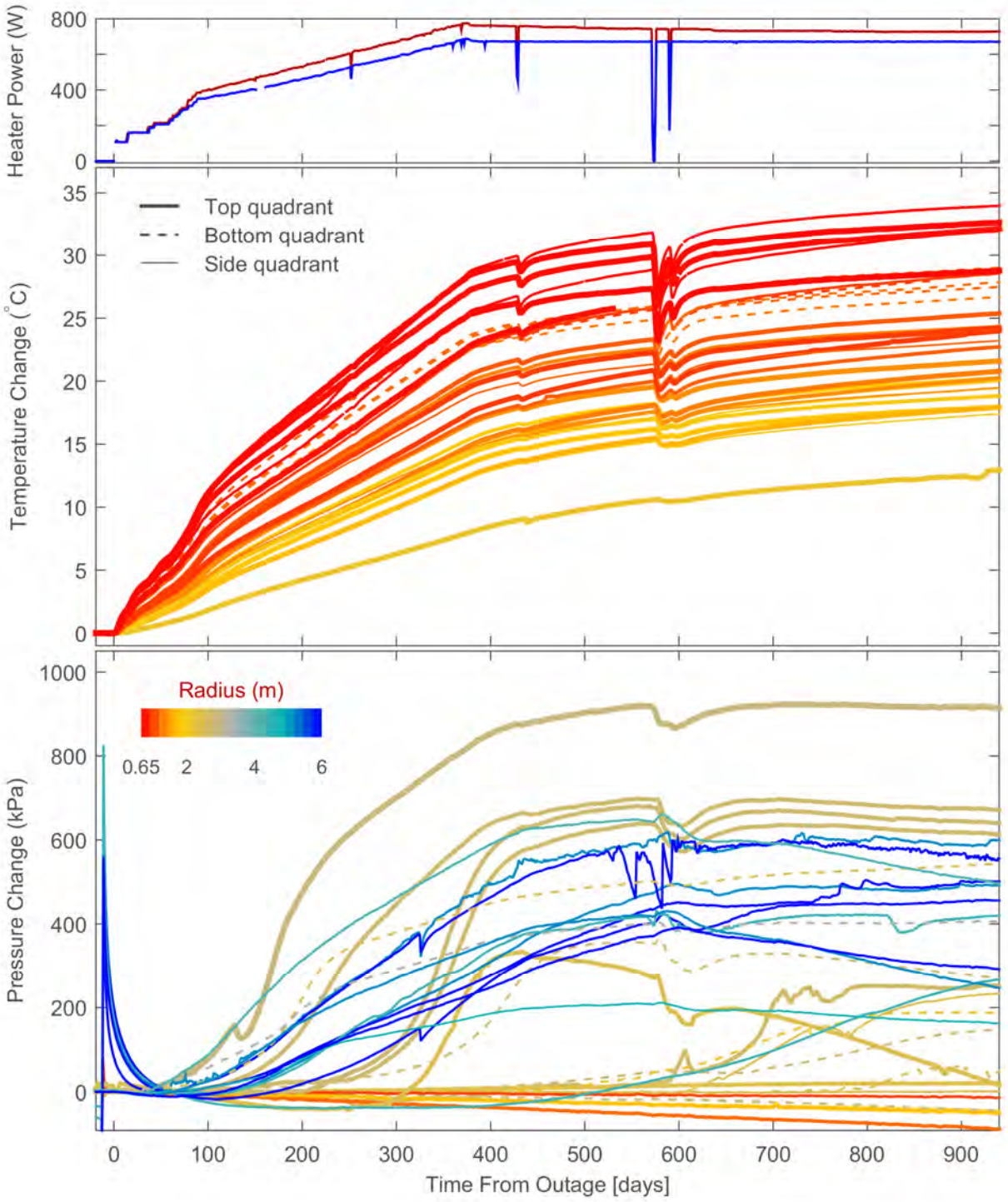

Figure 6-5. Measured Power to Granular Bentonite (Red) and Sand–Bentonite (Blue) Heaters (Top), and Detrended Observed Temperature (Middle) and Pressure (Bottom) During the HE-E Test. Color Coding by Distance to Microtunnel Axis; Line Style is According to Quadrant. [1 kPa = 0.145 psi, (ΔT)°F = (1.8) (ΔT)°C Where (ΔT = Temperature Change), 1 m = 3.3 ft]

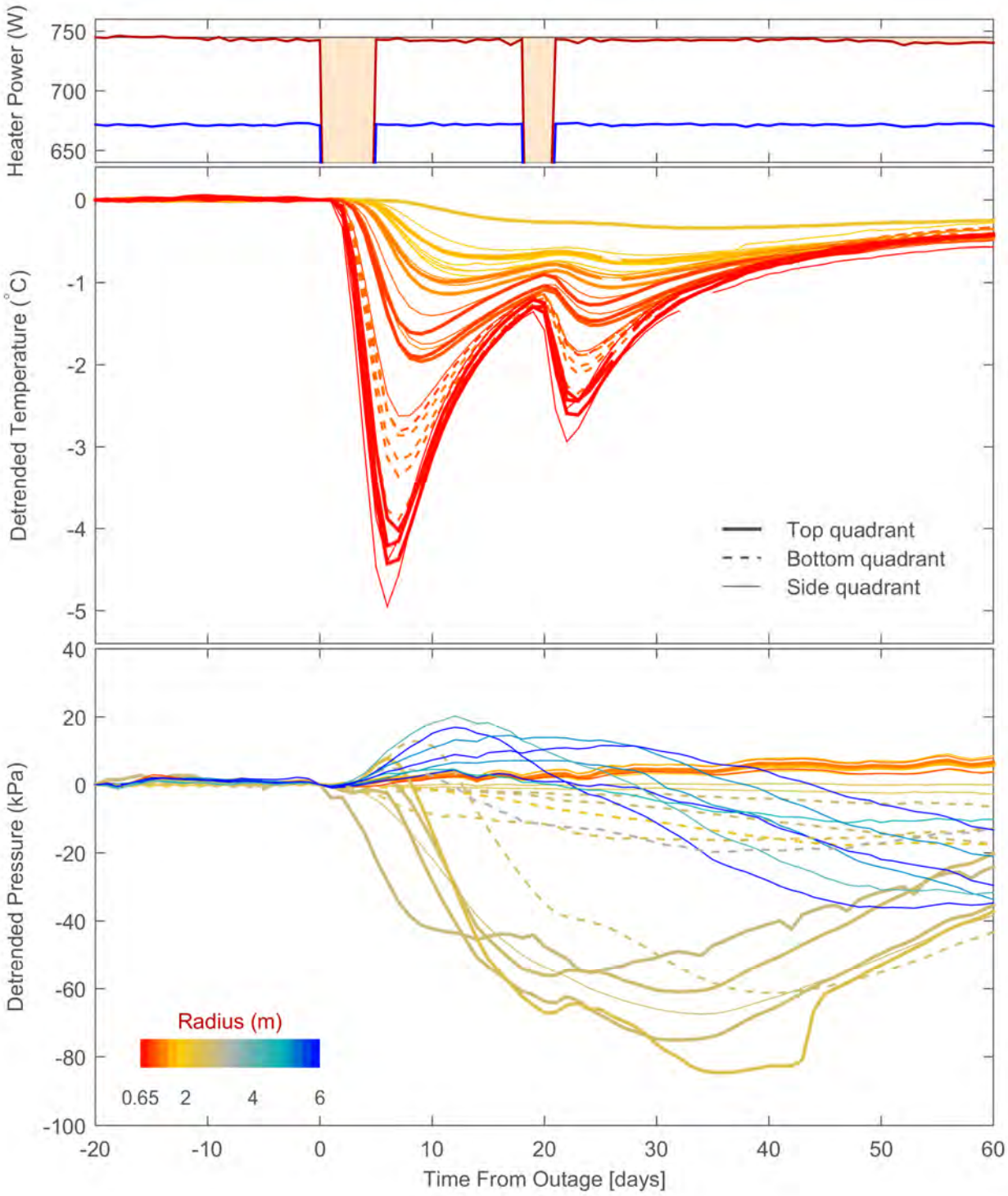

Figure 6-6. Measured Power to Granular Bentonite (Red) and Sand–Bentonite (Blue) Heaters (Top). Detrended Observed Temperature (Middle) and Pressure (Bottom) for 60 Days After a Power Outage. Color Coding by Distance to Microtunnel Axis; Line Style is According to Quadrant. [1 kPa = 0.145 psi, (ΔT)°F = (1.8) (ΔT)°C Where (ΔT = Detrended Temperature), 1 m = 3.3 ft]

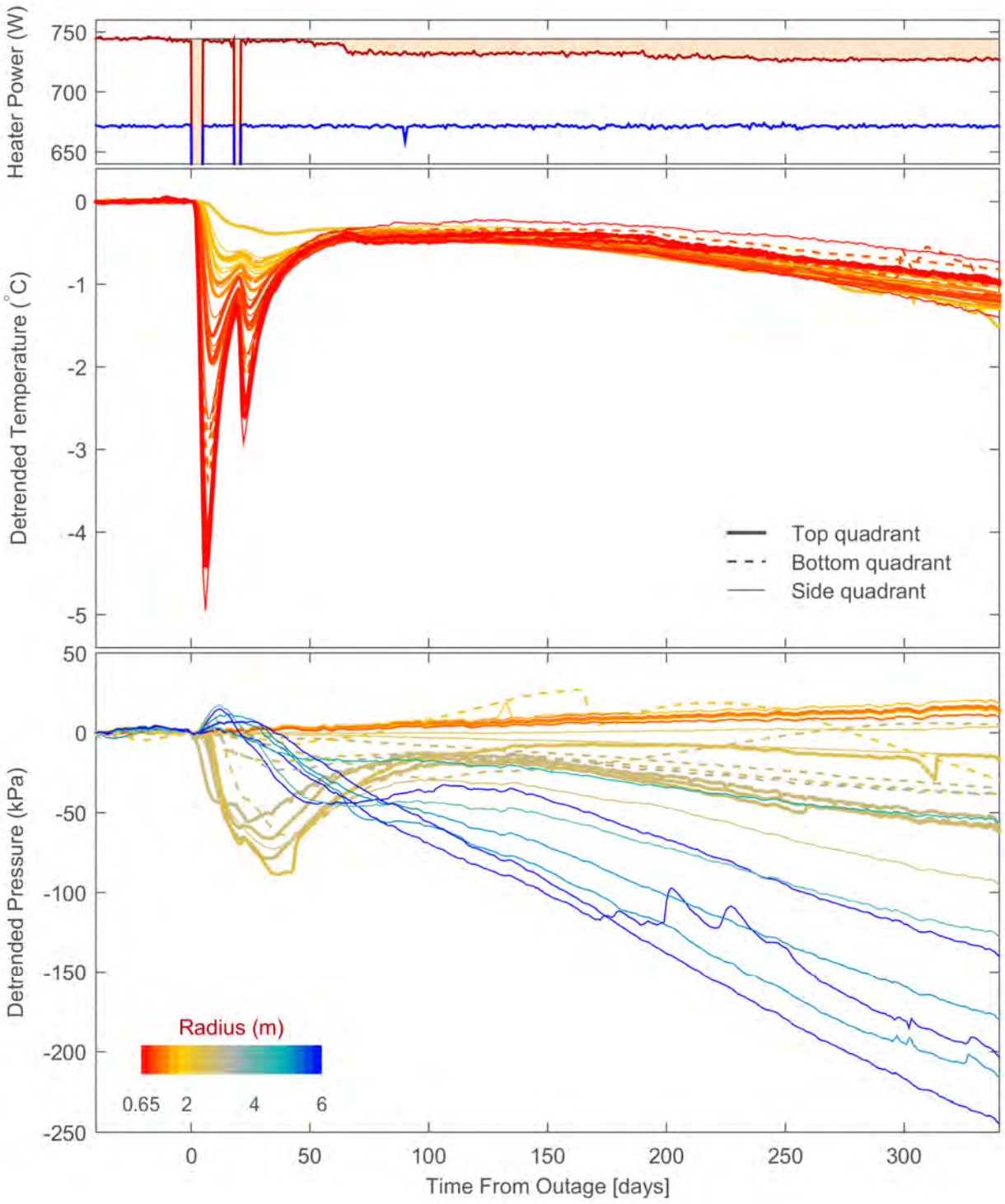

Figure 6-7. Measured Power to Granular Bentonite (Red) and Sand–Bentonite (Blue) Heaters (Top). Detrended Observed Temperature (Middle) and Pressure (Bottom) for 340 Days After a Power Outage. Color Coding by Distance to Microtunnel Axis; Line Style is According to Quadrant. [1 kPa = 0.145 psi, (ΔT)°F = (1.8) (ΔT)°C Where (ΔT = Detrended Temperature), 1 m = 3.3 ft]

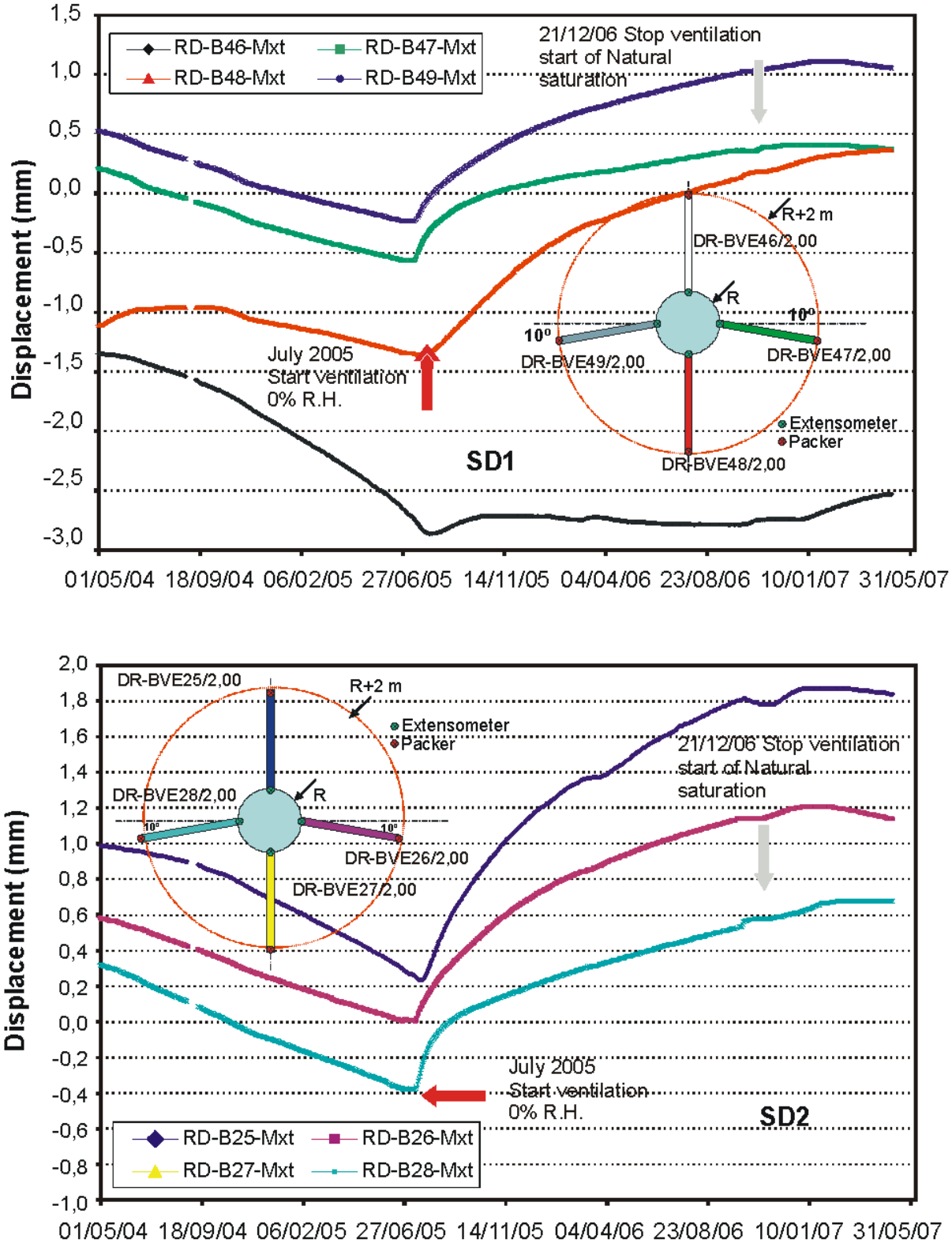

Figure 6-8. Representative Responses of Extensometers During Several Phases of the VE Test. Reproduced From Mayor and Velasco (2008, Figure 10). [1 mm = 0.039 in]

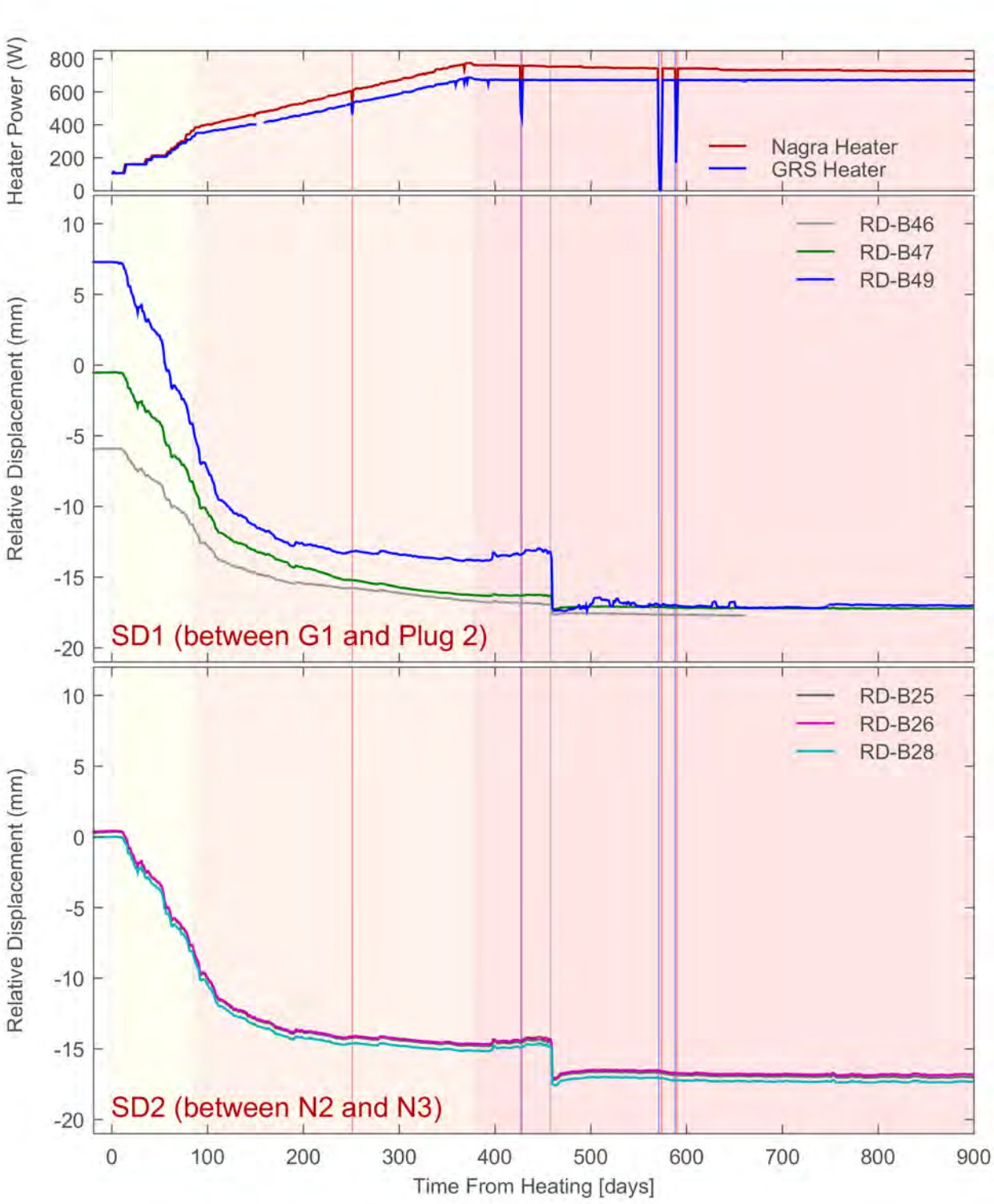

Figure 6-9. Relative Displacements in Top and Side Extensometers. [1 mm = 0.039 in]

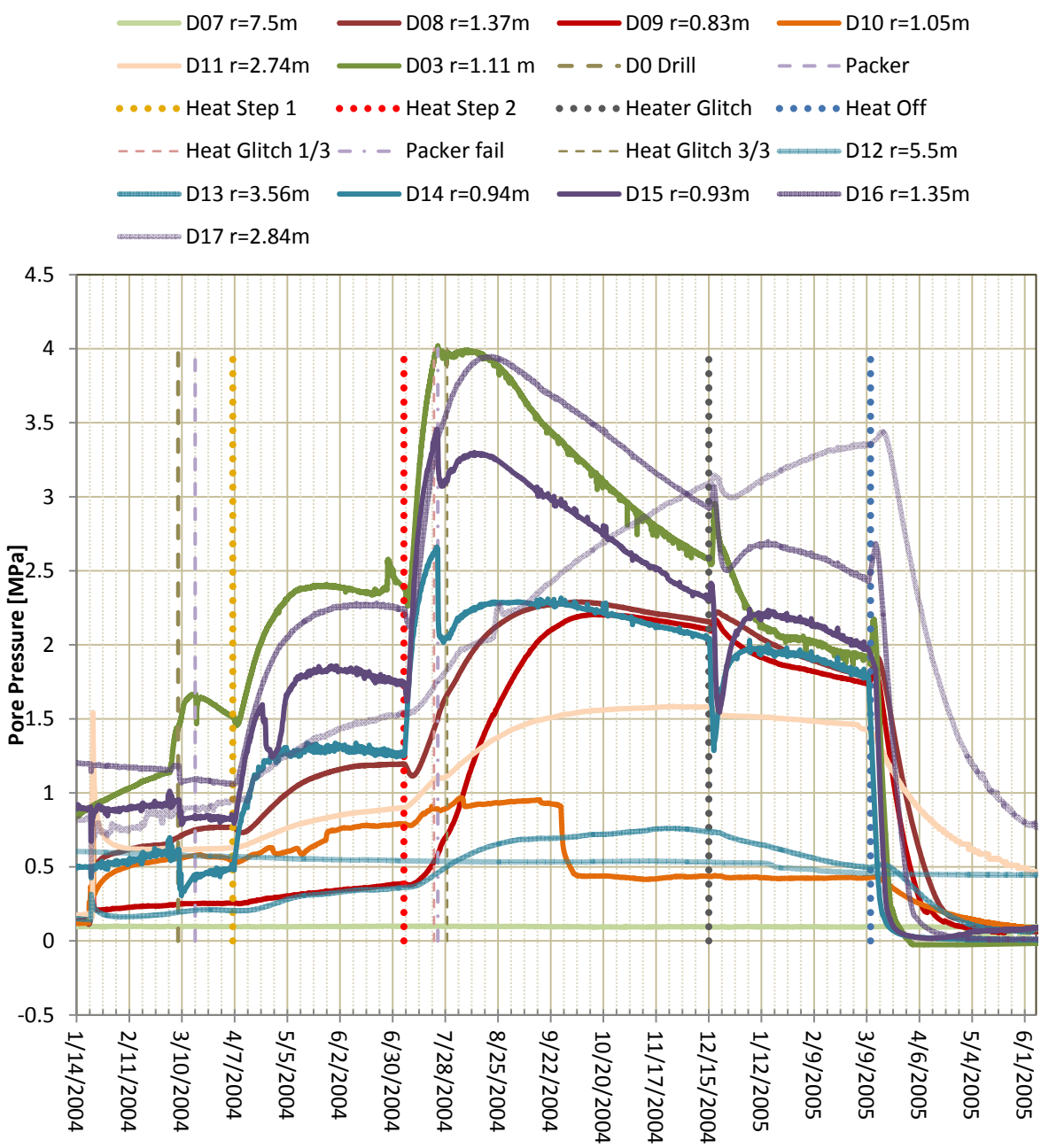

Figure 6-10. HE-D Pore Pressures Responding to Thermal and Mechanical Events at Various Monitoring Locations. [1 MPa = 145 psi, 1 m = 3.3 ft]

7 UPDATE ON DEVELOPMENT OF CONSTITUTIVE AND COMPUTATIONAL MODELS FOR THM BEHAVIOR OF UNSATURATED EXPANSIVE SOILS

Work stemming from the column test was documented in two conference papers on thermohydrologic (TH) constitutive properties presented at the 2015 International High-Level Radioactive Waste Management conference (Manepally et al., 2015; Stothoff et al., 2015b). Section 7.1 summarizes highlights of the TH constitutive model work presented in these conference papers. Additionally, a paper documenting work on mechanical constitutive modeling of unsaturated expansive soils (e.g., granular bentonite and sand–bentonite mixture) was prepared (Ofoegbu et al., 2015b).

Development of **Co**upled Models and Their **Val**idation Against **Ex**periments (DECOVALEX) model exercises are very useful for revealing limitations in the existing computational capabilities that are intended to support performance assessment activities. The series of DECOVALEX subtasks pointed out areas where the xFlo model and xFlo/FLAC combination of models would strongly benefit from additional development before considering repository conditions. Some work was performed developing a prototype model expanding the xFlo capabilities to allow rapid and robust addition of TH constitutive models. Section 7.2 summarizes the work performed on the xFlo model and discusses areas where future efforts would be useful for improving these model capabilities.

Section 7.3 summarizes the constitutive and computational model enhancements that would be most usefully addressed in future work.

7.1 Update on TH Constitutive Model Work

Constitutive model work over the past year focused on documenting insights into key aspects of the granular bentonite buffer material that were gained from the earlier column test. The granular bentonite buffer material has distinct pore scales ranging from nanometers to millimeters.

Surface forces between clay tactoids and the first few layers of water molecules operate at the nanometer scale, and are responsible for the swelling behavior of montmorillonite. The disjoining pressure operating at this scale balances bulk water potential and material stresses. Disjoining pressure is proportional to the square of temperature and inverse square of surface separation. Because swelling is proportional to the surface area of clay tactoids per unit volume, swelling pressure in a given medium is also proportional to the bulk density and the clay fraction. Water storage within individual tactoid layers is small, only a few molecules thick.

Tactoids join end to end, forming platy sheets. At intervals, several sheets form a flexible junction. A collection of many plates forms a honeycomb structure, or aggregate. Depending on the bulk water potential and water content, the sheets may lie flat or may expand into large pores. The void space in an aggregate has a large storage capacity, but flow through the pores is negligible.

Buffer materials intended for emplacement around radioactive waste packages are typically constructed using reworked bentonite, sometimes including sand and sometimes dried and formed into pellets. The pores between aggregates are much larger than the intra-aggregate pores, thus offer much larger liquid and gas flow capacity, but these pores can be closed off as

the aggregates swell. Because the aggregate pores strongly respond to bulk water potential (and to a lesser extent temperature), the pore configurations and therefore intrinsic permeability of the medium is strongly dependent on bulk water potential and temperature.

The changing pore configurations imply that the retention properties are dependent on bulk water potential. Stothoff et al. (2015b) discussed models from the literature that are intended to capture changing pore configurations in the context of water retention in media with two pore scales. Measured pore size distributions have two or more distinct modes representing characteristic pore sizes, and each mode is approximately lognormally distributed. The models from the literature represent each mode with a van Genuchten distribution, and combine the modes assuming that bulk water potential is the same for all pores. This approach essentially treats the set of pore size modes as overlapping continua, where each mode is a distinct continuum, and sums the continua into an equivalent continuum. The models are capable of reproducing retention behavior, but need adjustment to estimate permeability.

Stothoff et al. (2015b) indicated that measured pore configurations with more than two pore size modes can be reasonably well represented with overlapping van Genuchten models, but data are lacking to link changes in pore size modes to bulk pressure or saturation. The existing literature suggests that linking characteristics describing each mode to bulk saturation may be a reasonable approach. It is likely that bulk density and chemical concentrations may also play roles in determining pore size distributions.

Stothoff et al. (2015b) also considered available data for representing thermal conductivity. Across different materials, thermal conductivity appears to vary between concave up, concave down, or S-shaped with saturation. The single available xFlo model does not permit an S-shaped function, but it can represent concave-up and concave-down functions with respect to saturation. Note that the single available xFlo model does not consider temperature-dependent changes in thermal conductivity, which Campbell et al. (1994) showed may affect measured thermal conductivity increases by a factor of 3 under moderately dry conditions when temperature increases from 30 to 90 °C [86 to 194 °F]. This effect becomes negligible in the limit as either the liquid or vapor disappears (saturation goes to zero or unity).

7.2 xFlo development

7.2.1 Current Status

The existing xFlo model is based on the general approach of the TOUGH (i.e., Transport of Unsaturated Groundwater and Heat) model family (Pruess et al., 2012). As implemented, xFlo considers a set of finite volumes separated by one-dimensional (1-D) links. An arbitrary number of links can be imposed. A single equation set is assumed to apply to the entire domain, with two equation sets implemented: (i) air/water/energy for above-freezing conditions and (ii) air/water/ice/energy for below-boiling conditions. An input flag determines whether the second equation set is implemented for Earth or Mars; a Mars simulation uses a different gravitational constant and uses carbon dioxide for the “air” species. The first equation set is formally documented in a user’s manual (Painter, 2006), and the second equation set is documented in a journal article (Painter, 2011). Only the first equation set is utilized for DECOVALEX-2015 modeling. The functionality of the second set of equations in xFlo was not confirmed as part of the DECOVALEX project.

As implemented, xFlo consists of two modules. These modules handle generic components, such as gridding, interpolation, and equation solvers. Each equation set has its own module.

Some constitutive equations are hard-coded in the module; others are available as associated modules. The original intent of the coding approach was to make each module self-contained, allowing replacement of a module without disrupting other code. However, as implemented the partitioning of code among the modules turns out to be highly repetitive, so modifying a single aspect of the code means that the same coding change must be made in several places.

An initial interface between xFlo and FLAC has been developed to consider coupled thermal-hydrological-mechanical (THM) processes. The current implementation of the xFlo/FLAC interface uses semiautomatic one-way coupling between models.

7.2.2 Issues Identified During Modeling

Modeling the column test and the HE-E experiment for DECOVALEX Task B1 identified several issues in xFlo that should be addressed prior to additional modeling similar to the HE-E experiment.

- Some important parameters are hard coded, appropriate constitutive models for the buffer are not included, heat transfer by radiation is not included, and only special cases of material anisotropy can be included.

- Memory requirements demand that each cell with a boundary condition has its own associated boundary condition cell, which can create large input files for two-dimensional (2-D) and three-dimensional (3-D) problems, and it is difficult to specify some boundary conditions.

- Handling the transition between saturated and unsaturated conditions proved to be problematic.

- Feedbacks from mechanical deformation to TH properties were not implemented, and may have been very useful for representing the response of pore pressure in the host rock.

Radiation boundary conditions would have been very useful for the column test and would be needed if xFlo were used with an atmosphere boundary condition in the future. Internal radiation conditions would have been useful in modeling the HE-E experiment to consider axial heat transport in the heater, and would be useful in a repository setting without backfill in the unsaturated zone.

Currently xFlo does not explicitly consider anisotropy, which proved problematic when modeling the HE-E experiment. For this scenario, the host rock features two types of anisotropy: (i) bedding-plane anisotropy, and (ii) excavation damaged zone anisotropy. For the modeling task, anisotropy was approximated by scaling distances in the grid definition, but this is unsatisfactory when different material properties have different anisotropies.

Because of internal bookkeeping that includes an array sized by the number of links to each cell, it is impractical to link a single boundary condition cell to numerous internal cells. In the 2-D and 3-D models, the same time-dependent boundary condition sequence representing a heater or external boundary must be repeated hundreds or thousands of times in the input file for boundary conditions. In addition, it is not possible to specify a pressure or temperature gradient as a boundary condition, which would be useful in some repository applications.

Computations for grid cells at the transition between the unsaturated and saturated zones proved to be a constraint on the size of the time step for modeling the HE-E experiment. This is a classic issue in variably saturated modeling that arises from the discontinuity in the derivative of storage capacity with respect to pressure at the transition. The sharp discontinuity can make Newton-Raphson approaches diverge unless the time step is small. Further work would be required to improve convergence rates.

The current implementation of the xFlo/FLAC interface uses semiautomatic one-way coupling between models. Values of temperature, liquid saturation, and gas pressure calculated in xFlo are the main input to mechanical response calculations in FLAC. MATLAB software has been developed to transform the xFlo grid and output into the corresponding FLAC grid and input. Currently some manual steps are needed to tune the software when a new grid is first created, but once these steps have been performed FLAC simulations can be performed automatically with each new set of xFlo output for a given grid. Two-way coupling has not yet been implemented, where changes to the mechanical state are fed back to xFlo. Two-way coupling would require modifications to xFlo that allow xFlo to pause and restart with updated inputs.

7.2.3 Prototype Development

The xFlo code used for the TH analyses was developed in the mid-2000s with the intention of eventually replacing the existing coupled-process MULTIFLO simulator (Painter, 2006). MULTIFLO (Painter and Seth, 2003) consists of two codes (METRA and GEM) that can be run as stand-alone codes or coupled using the MULTIFLO driver program. The METRA code solves one- and two-phase nonisothermal flow equations in one or two continua for an arbitrary number of spatial dimensions (0-D to 3-D) using an unstructured grid. The GEM code solves multicomponent and multiphase nonisothermal reactive mass equations in 1-D to 3-D. MULTIFLO, METRA, and GEM are coded in ANSI FORTRAN 77.

The xFlo code has a different design philosophy. It is designed to be a general computational framework for solving conservation equations, with strict separation between numerical routines and physical models. Version 1.0β was developed with the philosophy that particular physics models should be encapsulated into packages that contain all secondary variables and physics-specific calculations (Painter, 2006). The initial beta release, written in Fortran 90, reproduced most of the METRA functionality in a single package but omitted some capabilities, such as some boundary conditions. xFlo Version 1.0β heavily uses updated features in Fortran 90, such as dynamic memory allocation, to provide coding flexibility. Two additional multiphase packages have been added to the beta release (Stothoff and Painter, 2016).

As the Center for Nuclear Waste Regulatory Analyses (CNWRA) staff exercised the xFlo 1.1β code, it became clear that future modeling work, including two-way coupling with FLAC, would be greatly facilitated if the xFlo Version 1.1β code structure was reorganized to improve modularity by transferring some of the functions that are currently implemented in the physics packages into the general computational framework. Code revision is not uncommon once an initial experience base is developed with a code exploiting new programming capabilities.

The NRC/CNWRA team identified the following areas as prime candidates for updates:

- *Additional equation sets*. An additional capability for considering hydrogen generation has been discussed. Use of xFlo for transport calculations is being considered. Sensitivity studies may benefit from simplified equation sets (e.g., thermal only).

- *Additional TH constitutive relationships*. Additional constitutive relationships should be easy to add, and accessible across the relevant governing equation sets. For example, it should be easy to define an alternative thermal conductivity relationship and have it robustly accessible to any appropriate equation set.

- *Input/output structure*. It would be useful to have additional flexibility for defining units, including additional input parameters, and customizing output streams. Additions to the equation sets and constitutive equations should be easily and robustly accommodated.

- *Boundary conditions*. Robust and streamlined definitions for boundary conditions would greatly aid in model setup.

- *Improved flexibility in link definitions*. The current implementation of links assumes that material-dependent properties are isotropic. Adding scale factors for relevant fluxes according to a link-dependent parameter would include anisotropy in xFlo capabilities.

- *On-the-fly input*. Fully coupled linkages between xFlo and other codes, such as FLAC, would require that xFlo pauses after a computation, waits for return information, and updates internal variables. Currently this can only be performed by ending a simulation, performing manipulations in external software, and starting a new simulation. At the very least, the internal variables should be saved and read in a binary format to minimize round-off errors.

The following areas were identified as prime candidates for reorganization:

- *Input/output centralization*. Each generic and physics-dependent module is responsible for handling its own input and output. Centralization transfers this repetitive coding to a single set of grouped routines, allowing consistency across packages and permitting easier upgrades.

- *Memory allocation centralization*. Each generic and physics-dependent module is responsible for handling memory allocation for its own variables. Centralization transfers this repetitive coding to a single set of grouped routines, allowing consistency across packages and permitting easier upgrades. Centralized management supports the use of generic input and output.

- *Interfaces between generic and physics-dependent routines*. As implemented, the interface between generic and process-specific code is implemented using a host of nested conditional evaluations to select functions. These conditionals are evaluated every solution iteration for every grid cell, and are spread across the modules, but always have the same answer for a given simulation. Adding a new equation set, constitutive relationship, or boundary condition requires a cascade of repetitive code changes to maintain consistency. Transferring the logic to a one-time evaluation prior to entering the computational phase would speed calculations and make the code logic more transparent.

Fortran 2003/2008 has extended the functionality of pointers beyond the capabilities of Fortran 90. A prototype revision of xFlo was implemented as an offline version of xFlo, avoiding interfering with DECOVALEX-2015 simulations. The prototype was used to explore whether xFlo could be streamlined by taking advantage of the extended pointer capabilities to clarify

overall program logic. The prototype provides a test bed for re-coding in Fortran 2003/2008 and to evaluate whether Fortran 2003/2008 compilers are sufficiently mature to revise xFlo.

The prototype was developed to test whether generic code can be developed common to a wide range of conservation equation sets. Function pointers are used to execute logic specific to a particular equation set, constitutive model, or boundary condition. The particular function pointers are assigned before the start of computations based on input instructions, replacing the repetitive evaluation of nested run-time logic. Memory allocation is handled centrally, with each module accessing the memory using module-specific pointers and with generic input and output routines using generic pointers. Each physics-based module provides logic defining all options and associated parameter characteristics prior to start of input, so that the generic input routines can check for internal consistency of the input and request memory as needed. With the logical structure defined by the physics modules, a new physics-based component can be dropped in without affecting input and output routines.

The prototype uses essentially the same grid and solver routines as xFlo. The overall simulation logic is retained, but reorganized into a generic simulation module, equation assembly modules, and a constitutive property module. The input/output structure is completely revised, supporting easy selection of existing models and permitting modular updates to computational capabilities without modifying the input/output structure. A new module handles parameter definition and storage allocation functions.

Under the prototype logic, the entire code is generic except for the constitutive models and, to some extent, the equation assembly routines. The generic routines are responsible for all of the bookkeeping chores associated with defining storage for variables, handling input and output, and associating constitutive functions with their computational routines. Each constitutive model is responsible for providing definitions for parameters and appropriate function pointers, and the generic routines handle the rest of the bookkeeping. With this strategy, adding a constitutive function requires a small amount of upfront work to add its particular requirements to the generic interface, but adding a constitutive function does not affect coding for the generic routines. Centralizing the input/output and memory management routines will also centralize future logic for pausing and restarting simulations that would be necessary for two-way coupling with other codes, such as FLAC.

The prototype code is intended to identify whether an enhanced generic approach can be usefully applied to xFlo. Several iterations of the core generic routines for handling storage, input, and output have been developed and tested. Testing has shown that a command-driven interface can be successfully and robustly implemented using Fortran 2003/2008, including commands to define the simulation characteristics, read all relevant input, and echo the variables to output. Several methods for assigning input parameters to particular grid cells are implemented. Command-driven input is very advantageous for developing a flexible code, because the command sequence defines the input format rather than some predefined specification. The commands also provide a self-documenting capability to the input.

The particular format of the command-driven language may be modified based on further evaluation and feedback, but the underlying core functionality is reaching a state of maturity. The current language implementation provides a usable interface, but better robustness and power would be available using a standard parsing tool.

Initial prototype development was hampered because Fortran 2003/2008 standards were incompletely implemented in early releases of the compilers. The compilers simply did not recognize the language as coded. Newer releases implement the necessary standards.

Generic equation assembly routines, the air/water/energy equation set from xFlo, and relevant constitutive equations have been coded to test the computational approach. Initial testing is focusing on the interface between these routines and the constitutive equations to refine protocols. Subsequent testing will compare simulation results to the existing xFlo model to verify that the computations are being performed correctly.

7.3 Proposed Future Work

Retention, Permeability, and Porosity

Additional work is required to generalize the retention and permeability models, especially when considering multiple pore scales above the aggregate scale (e.g., inter-aggregate pores embedded in pellets). The work to date provides estimates of retention and permeability given pore size distributions, but defining how the pore size distributions change with water content remains to be developed. The available literature suggests that pore size distributions may smoothly change with water content, giving a potential path forward.

The multiporosity approach has not been implemented in xFlo. This will require coding the equations and revising the xFlo code to permit additional constitutive relationships.

Thermal Conductivity

The current implementation of thermal conductivity in xFlo depends only on saturation. Thermal conductivity of water increases with temperature, whereas mineral thermal conductivity tends to decrease with temperature. Further, latent heat transfer can strongly augment effective thermal conductivity under unsaturated conditions when refluxing occurs within pores (vapor moving away from a heat source balanced by liquid moving towards the heat source). Campbell et al. (1994) showed that measured thermal conductivity increases by a factor of 3 under moderately dry conditions when temperature increases from 30 to 90 °C [86 to 194 °F]. This effect becomes negligible in the limit as either the liquid or vapor disappears (saturation goes to zero or unity).

Available data may not be sufficient to verify whether bentonite-based media exhibit this behavior. Additional work is needed to clarify whether xFlo already captures the refluxing process adequately. If not, constitutive models should be provided to xFlo that capture the effect of refluxing.

Computational Model Development

DECOVALEX model exercises are very useful for revealing limitations in the existing computational capabilities that would be used to support performance assessment activities. Future efforts related to xFlo-FLAC code development include

- Address computational issues associated with saturated/unsaturated transition nodes
- Implement two-way links between xFlo and FLAC based on the approach described in Stothoff et al. (2015a)

- Improve xFlo input/output structure
- Update xFlo documentation
- Prepare for future modeling tasks

Before addressing these tasks, the recommended first task would be to complete testing of the prototype. The prototype incorporates core routines from xFlo. Current testing is focusing on routines that should be able to reproduce model results from DECOVALEX-2015 simulations at the end of a relatively short test phase.

If the prototype is able to provide accurate simulations reproducing xFlo results, it is strongly recommended that staff move forward with a new generation of xFlo based on the prototype. The prototype design addresses many of the important modeling constraints learned from working with xFlo during the DECOVALEX-2015 modeling work. The prototype is designed to provide a robust and flexible computational platform readily expanded for future modeling needs. Addressing the important tasks identified for completion prior to potential participation in the DECOVALEX 2019 phase would be much easier to address with a platform based on the prototype.

A pre-processing, post-processing and visualization tool (mView)[1] is being considered to aid xFlo modeling efforts. Staff are currently evaluating its capabilities, including capabilities for (i) generic grid generation (2-D and 3-D), (ii) generating xFlo-specific input files, and (iii) visualizing xFlo and FLAC results.

Support Disposal-Related Integrated Spent Nuclear Fuel Regulatory Activities

Developing an in-depth understanding of the behavior of buffer, engineered barrier system (EBS) components and argillaceous host rocks and developing modeling tools to represent complex THM behavior will enable supporting other subtasks that are a part of the disposal-related integrated spent nuclear fuel regulatory activities, such as

- Developing numerical models to support performance assessment for specific scenarios and repository design configurations (Osidele et al., 2015). Some of the scenarios identified to be evaluated in detail include (i) heterogeneous resaturation within the buffer material and corresponding impacts to the barrier capability, (ii) buffer damage adjacent to the waste package resulting from temperatures exceeding 100 °C [212 °F], and (iii) large-scale heterogeneity on the state of the buffer throughout the repository.
- Evaluating the evolution of THM conditions for cases where the waste package surface temperatures are very high {i.e., around 200 °C [392 °F]}. Numerical modeling (Colón et al., 2014) has demonstrated that the pressure build-up can occur if the temperatures are very high and the repository is air tight. However, field experiments such as the HE-E test in Mont Terri suggest that pressure build-up in the tunnel may be limited because of connections to the outside galleries and tunnels (see Section 4.1). Some pressure build-up inside the EBS may be expected in an actual repository, because it will not have a designed connection to the outside. Geomechanical properties and swelling behavior (in response to resaturation) will significantly influence

[1] http://geofirma.com/software/mview/

the potential for pressure build-up. If the pressure reaches a threshold level, then micro-cracks in the buffer and host rock may serve as pathways for pressure dissipation.

- Evaluating the potential for gas generation and migration in the EBS: Small-scale laboratory experiments conducted under the Fate of Repository Gases (FORGE) program suggest that gas migration occurs through dilational pathways in the rock; however, the metrics defining travel time and breakthrough conditions are difficult to determine (Graham and Harrington, 2014). Furthermore, larger scale field experiments conducted at the Äspö Hard Rock Laboratory in Sweden do not suggest a consistent pattern of gas migration (Cuss et al., 2010). Numerical models, using xFlo–FLAC, could be developed to understand the conditions such as temperature and pressure that could strongly influence gas generation and transport in the buffer.

8 SUMMARY

U.S. Nuclear Regulatory Commission (NRC) and Center for Nuclear Waste Regulatory Analyses (CNWRA) staff have been participating in Task B1 of the 6th phase of the **De**velopment of **Co**upled Models and Their **Val**idation Against **Ex**periments (DECOVALEX) program (DECOVALEX-2015) since 2012. Task B1 focuses on understanding thermohydrological-mechanical (THM) processes in bentonite buffer and argillaceous host rock, using information and data from laboratory and field tests. This report summarizes numerical modeling of the HE-E experiment, a heater test conducted at Mont Terri Underground Research Laboratory (URL), Switzerland. It also summarizes auxiliary analyses, based on HE-E data supplemented by other URL data from the same site, to provide additional insight into barrier capability functions for the buffer and host rock.

The HE-E experiment heated two test sections in the microtunnel, separated by a plug, that were filled with either granular bentonite or sand–bentonite buffer materials (Section 1.1). The heater was placed on bentonite blocks and plugs were used to isolate the test sections. Each test section was 4 m [13 ft] in length with a diameter of 1.3 m [4.3 ft]. Temperature, relative humidity, and pore pressure measurements in the buffer, bentonite block and in the Opalinus Clay (host rock) were provided to the Task B1 modeling teams, supplemented with heater power inputs and limited relative displacement data.

A two-dimensional (2-D) cross section model, focusing on the granular bentonite section, was developed using xFlo and FLAC to represent thermodydrological (TH) and geomechanical processes, respectively. The 2-D model used a hybrid grid consisting of cylindrical shells in the near field and spherical shells in the far field (Section 4.2). Grid cells were finely discretized at the buffer–host rock interface (i.e., the tunnel wall) to account for the sharp capillary gradients expected because of contrasting hydraulic properties for the host rock and buffer. The xFlo model included features to represent engineered barrier system (EBS) components such as the cable channel and Gallery 98, and considered anisotropy in the Opalinus Clay (Sections 3.1.3 and 3.1.1). Comparison of temperature and relative humidity measurements and simulation results indicated that, in general, xFlo was able to capture the TH processes in the buffer, bentonite block, and Opalinus Clay (Section 5.1). The differences between measurements and xFlo simulation results can be attributed to uncertainties regarding the host rock, especially the excavation damaged zone (EDZ) and engineered components such as cement blocks and concrete fill, so model calibration did not alter buffer properties significantly from the column test model.

The Task B1 participants were assigned three modeling cases to facilitate comparison of THM modeling results for the HE-E experiment and to forecast the THM response to potential future buffer rewetting. These cases included modeling with the (i) uncalibrated parameter set, (ii) calibrated parameter set assuming the heaters are shut down at a specified time, and (iii) calibrated parameter set assuming heating continued indefinitely while maintaining a temperature of 140 °C [284 °F] at the liner. xFlo simulations indicated that the buffer resaturation rate was twice as fast when the heater remained on, which is consistent with the decrease in water viscosity (hence increase in hydraulic conductivity) at higher temperatures (Section 5.1.3). The presence and nature of the EDZ fractures also strongly influences the time of rewetting. The xFlo estimate of the time to rewetting is highly uncertain because swelling processes in the Opalinus Clay EDZ fractures during rewetting were not included in the xFlo model.

Geomechanical modeling using FLAC focused on the geomechanical response of the granular bentonite and bentonite blocks in the unsaturated regime, assuming that the Opalinus Clay was essentially saturated (Section 5.4). FLAC estimates of deformation and porosity changes indicate that these changes occur in specific circumferential bands. Model results indicated (i) zones of compression (i.e., decrease in porosity) occur near the heater liner and near the host rock and (ii) zones of extension occur in the buffer interior and locations immediately adjacent to the side and bottom of the heater liner.

Staff performed auxiliary analyses that focused on pore pressure measurements in the Opalinus Clay, impact of power failures during the HE-E and HE-D tests, and extensometer data from the Opalinus Clay (Chapter 6). One supplemental analysis was intended to better understand the initial pore pressure distributions in the host rock around the microtunnel before heating (Sections 6.1 and 6.2). Staff developed auxiliary three-dimensional (3-D) COMSOL groundwater models, taking into account the bedding anisotropy, mountain-scale geology, and likely water tables in the overlying and underlying aquifers. These models clarified how the initial pore pressures were likely distributed throughout the URL prior to any tunnels, but poorly reproduced pore pressure distributions around mined openings (Section 6.6). Additional information from other parts of the URL suggests that pore pressures respond very quickly to changes in mechanical stress and very slowly to changes in surface humidity on tunnel walls (e.g., desiccation during ventilation). This, in turn, implies that current pressure patterns around openings are still largely determined by mechanical stresses induced by construction.

Other auxiliary analyses used a series of power failures as miniature tests within the overall HE-E experiment and the predecessor HE-D experiment (Sections 6.4 and 6.5). Although THM properties were not estimated, the observed responses to rapid changes in power suggest that such events may be useful for estimating THM properties. The responses during and after the power failures suggested that pore pressures responded synchronously at least 6 m [20 ft] into the host rock during the power failures. Pore pressures within 1.5 m [5 ft] of the microtunnel remained largely unaffected by the power failure, but more distal pore pressures decreased above and below the microtunnel (expected from the sudden drop in thermal load), and temporarily increased before decreasing to the sides of the microtunnel (unexpected). The anomalous reverse pressure responses suggest relationships between thermal-mechanical changes in the host rock and pore pressures in the near field. The reverse pore pressures appear to be related to anisotropic host rock thermal expansivity, which was measured in the lab as approximately 3 to 10 times larger in the direction perpendicular to bedding than it was parallel to bedding (Section 6.6).

Variability in the emplacement density and heterogeneity in bentonite shrinkage could lead to gaps between the buffer and surrounding material that reduce the effective thermal conductivity of a dry buffer. Anomalies in measured temperature profiles from the heater liner to the host rock may have been caused by gaps forming around the heater liner and tunnel wall. Subsequent analysis of the extensometer data suggested that the microtunnel diameter increased by 2.6 percent during heating, suggesting that the 2-D model parameters should be adjusted (Section 6.4). The final stage of microtunnel expansion consisted of a rapid contraction simultaneously observed in all extensometers {0.5 to 4 mm [0.02 to 0.16 in] over a period of approximately 2 hr} that occurred a few months after the temperature peak, which may be evidence of a sudden tension failure event in the host rock. The microtunnel expansion returned the tunnel to essentially identical relative deformations in all extensometers. Microtunnel expansion that resulted in host rock pulling away from the buffer may have led to

poor contact on the top and sides of the tunnel, and bottom and sides of the heater liner, although bentonite block expansion also may have caused gaps at the liner (Section 6.6).

Staff identified several potential areas for future work related to xFlo code development, xFlo–FLAC coupling, and activities to support disposal-related integrated spent nuclear fuel regulatory subtasks (Section 7.3). The potential xFlo code development topics identified by CNWRA staff aim to improve computational efficiency and enhance flexibility in maintaining, modifying and expanding the code. The xFlo-FLAC approach can provide insights to specific scenarios relevant to performance assessment and corrosion subtasks. These scenarios include evaluation of (i) buffer and argillaceous host rocks responses to high temperatures (200 °C [392 °F]) and (ii) the potential for gas generation and migration in the EBS.

9 REFERENCES

Bath, A., A. Gautschi, T. Gimmi, F.J. Pearson, and A. Rübel. Chapter 6: Geochemical Evolution. In "Mont Terri Project – Geochemistry of Water in the Opalinus Clay Formation at the Mont Terri Rock Laboratory". Reports of the Federal Office for Water and Geology (FOWG), Geology Series, No. 5. Bern, Switzerland: Federal Office for Water and Geology. 2003.

Burbey, T.J.. "Poroelastic Effects on Fracture Characterization." *Groundwater*. Vol. 51, Issue 6. DOI: 10.1111/gwat.12022. pp. 904–913. 2013.

Campbell, G.S., J.D. Jungbauer, Jr., W.R. Bidlake, and R.D. Hungerford. "Predicting the Effect of Temperature on Soil Thermal Conductivity." *Soil Science*. Vol. 158, Issue 5. 1994.

Colón, C.F., P.F. Weck, D.H. Sassani, L. Zheng, J. Rutqvist, C.I. Steefel, K. Kim, S. Nakagawa, J. Houseworth, J. Birkholzer, F.A. Caporuscio, M. Cheshire, M.S. Rearick, M.K. McCarney, M. Zavarin, A. Benedicto, A.B. Kersting, M. Sutton, J. Jerden, K.E. Frey, J.M. Copple, and W. Ebert. "Evaluation of Used Fuel Disposition in Clay-Bearing Rock." Technical Report SAND2014–18303R. Albuquerque, New Mexico: Sandia National Laboratories. 2014.

Cuss, R.J., J.F. Harrington, and D.J. Noy. "Large Scale Gas Injection Test (Lasgit) Performed at the Äspö Hard Rock Laboratory: Summary Report 2008." Technical Report TR–10–38. Stockholm, Sweden: Swedish Nuclear Fuel and Waste Management Co. February 2010.

Garitte, B., A. Bond, A. Millard, C. Zhang, C. Mcdermott, S. Nakama, and A. Gens. "Analysis of Hydro-Mechanical Processes in a Ventilated Tunnel in an Argillaceous Rock on the Basis of Different Modelling Approaches." *Journal of Rock Mechanics and Geotechnical Engineering*. Vol. 5. pp. 1–17. 2013.

Gaus, I., B. Garitte, R. Senger, A. Gens, R. Vasconcelos, J.-L. Garcia-Sineriz, T. Trick, K. Wieczorek, O. Czaikowski, K. Schuster, J.C. Mayor, M. Velasco, U. Kuhlmann, and M.V. Villar. "The HE-E Experiment: Lay-Out, Interpretation and THM Modelling." NAB 14-53. Wettingen, Switzerland: Nagra. 2014a.

Gaus, I., K. Wieczorek, K. Schuster, B. Garitte, R. Senger, R., Vasconcelos and J.C. Mayor. "EBS Behaviour Immediately After Repository Closure in a Clay Host Rock: HE-E Experiment (Mont Terri URL)." Geological Society. London, England: Special Publications. doi: 10.1144/SP400.11. 2014b.

Gräfe, K. and U. Rösli. "Mont Terri PEBS: HE-E Experiment: Monitoring and Maintenance, D.2.2-8 HE-E Annual Monitoring Report, (01/03/2013 – 28/02/14)." Solexperts AG, Möntchaltorf, Switzerland. 2014.

Gräfe, K. and U. Rösli. "Mont Terri PEBS: HE-E Experiment: Monitoring and Maintenance, D.2.2-8 HE-E Annual Monitoring Report, Monitoring period 01/03/12 – 28/02/13." Solexperts AG, Möntchaltorf, Switzerland. 2013.

Graham, C.C. and J.F. Harrington. "Final Report of FORGE 3.2.1: Key Gas Migration Process in Compact Bentonite. British Geological Survey Internal Report. CR/14/064. 51pp. 2014.

Grava, E., P. Achtziger, and U. Rösli. "Mont Terri PEBS: HE-E Experiment: Monitoring and Maintenance, D.2.2-8 HE-E Annual Monitoring Report." Solexperts AG, Möntchaltorf, Switzerland. 2012.

Manepally, C., S. Stothoff, G. Ofoegbu, B. Dasgupta, and R. Fedors. "Modeling Thermohydrological-Mechanical Behavior of Granular Bentonite." 2015 International High-Level Radioactive Waste Management Conference, Charleston, SC, April 12–16, 2015.

Marschall, P., J. Croisé, L. Schlickenrieder, J.-Y. Boisson, P. Vogel, and S. Yamamoto. Synthesis of Hydrogeological Investigations at the Mont Terri Site (Phases 1 to 5). In "Mont Terri Project – Hydrogeological Synthesis, Osmotic Flow". Reports of the Federal Office for Water and Geology (FOWG), Geology Series, No. 6. Bern, Switzerland: Federal Office for Water and Geology. 2004.

Martin, C.C., G.W. Lanyon, P. Bossart, and P. Blümling. "Mont Terri Project – Excavation Disturbed Zone (EDZ) in Clay Shale: Mont Terri." Technical Report 2001-01. Falmouth, England: GeoScience Ltd. 2004.

Mayor, J.C. and M. Velasco. "Ventilation Test (VE) Experiment: Final Activity Report for ENRESA, WP 4.3; The Ventilation Experiment Phase II (Synthesis Report)." Technical Report 2008-01. Bern, Switzerland: Empresa Nacional de Residuos Radiactivos, S.A. 2008.

Mayor, J.C., M. Velasco, and J.L. Garcia-Sineriz. "Ventilation Experiment in the Mont Terri Underground Laboratory." *Physics and Chemistry of the Earth*. Vol. 32. pp. 616–628. 2007.

Möri, A., P. Cabal, P. Bossart, M. Adler, and S. Wermeille. "Mont Terri Project – Results of the Phase 3 Drilling Campaign." Technical Report 98-01. Geotechnical Institute Ltd.: Berne, Switzerland. 1998.

Millard, A., A. Bond, S. Nakama, C. Zhang, J.-D. Barnichon, and B. Garitte. "Accounting for Anisotropic Effects in the Prediction of the Hydro-Mechanical Response of a Ventilated Tunnel in an Argillaceous Rock." *Journal of Rock Mechanics and Geotechnical Engineering*. Vol. 5. pp. 97–109. 2013.

Mualem, Y. "A New Model for Predicting the Hydraulic Conductivity of Unsaturated Porous Media." *Water Resources Research*. Vol. 12, No. 3. pp. 513–522. 1976.

Nussbaum, C., O. Meier, N. Badertscher, and P. Bossart. "VE Experiment (Phase II): Photodocumentation of the Test Interval and Water Content Measurements." Unpublished Mont Terri Technical Note (TI 2005-16). 2004.

Ofoegbu, G., B. Dasgupta, C. Manepally, and R. Fedors. "Thermal-Hydrological-Mechanical Modeling of a Saturated Clay Shale—Report on HE-D Test Modeling." IM 17860.09.001.315. San Antonio, Texas: Center for Nuclear Waste Regulatory Analyses. 2015a.

Ofoegbu, G.I., B. Dasgupta, C. Manepally, S.A. Stothoff, and R. Fedors. "Modeling the Mechanical Behavior of Unsaturated Expansive Soils Based on Bishop Principle of Effective Stress". San Antonio, Texas: Center for Nuclear Waste Regulatory Analyses. Journal paper manuscript submitted to U.S. Nuclear Regulatory Commission. 2015b.

Ofoegbu, G., B. Dasgupta, C. Manepally, H. Basagaoglu, and R. Fedors. "Modeling Swelling and Swelling Pressure in Expansive Clays." 2013 International High-Level Radioactive Waste Management Conference, Albuquerque, New Mexico, April 28–May 2, 2013. La Grange Park, Illinois: American Nuclear Society. 2013.

Osidele, O., J. Gwo, O. Pensado, T. Ahn, R. Fedors, X. He, C. Manepally, C. Markley, S. Mohanty, P. Shukla, and S. Stothoff. "Summary Report: Workshop on Buffer Conceptualization for Performance Assessment." San Antonio, Texas: Center for Nuclear Waste Regulatory Analyses. 2015.

Painter, S.L. "Three-Phase Numerical Model of Water Migration in Partially Frozen Geological Media: Model Formulation, Validation, and Applications." *Computational Geosciences*. Vol. 15 Issue 1, pp. 69–85. DOI 10.1007/s10596-010-9197-z. 2011.

Painter, S. "*xFlo* Version 1.0β User's Manual." San Antonio, Texas: Center for Nuclear Waste Regulatory Analyses. 2006.

Painter, S. and M. Seth. "MULTIFLO User's Manual." Two-Phase Nonisothermal Coupled Thermal-Hydrologic-Chemical Flow Simulator. Version 2.0. San Antonio, Texas: Center for Nuclear Waste Regulatory Analyses. 2003.

Pruess, K., C. Oldenburg, and G. Moridis. "TOUGH2 User's Guide, Version 2.1." Report LBNL–43134. Berkeley, California: Lawrence Berkeley National Laboratory. 2012.

Rizzi, M., A. Seiphoori, A. Ferrari, D. Ceresetti, and L. Laloui. "Analysis of the Behaviour of the Granular MX-80 Bentonite in THM-Processes." AN 12-102. Wettingen, Switzerland: Nagra. 2012.

Rutqvist, J., F. Chen, and J. Birkholzer. "Modeling of THM Column Experiment on Bentonite for DECOVALEX-2015 Task B1." DECOVALEX 2015–4th Workshop, November 11–15, 2013. Mont Terri, Switzerland. 2013.

Stothoff, S., C. Manepally, G. Ofoegbu, B. Dasgupta, and R. Fedors. "Modeling Thermohydrological-Mechanical Behavior of Granular Bentonite in a Laboratory Column Test." IM 17860.09.001.410. ML15324A128. San Antonio, Texas: Center for Nuclear Waste Regulatory Analyses. 2015a.

Stothoff, S., C. Manepally, and R. Fedors. "Constitutive Model Developments for Bentonite Buffer Behavior." 2015 International High-Level Radioactive Waste Management Conference, Charleston, SC, April 12–16, 2015b.

Stothoff, S. and S. Painter. "xFlo Version 1.1β User's Manual." San Antonio, Texas: Center for Nuclear Waste Regulatory Analyses. ML16167A315. 2016.

Tang, A.M. and Y.J. Cui. "Effects of Mineralogy on Thermo-Hydro-Mechanical Parameters of MX80 Bentonite." *Journal of Rock Mechanics and Geotechnical Engineering*. No. 2. pp. 91–96. 2010.

Teodori, S.-P. and I. Gaus (eds.). "Long Term Performance of Engineered Barrier Systems (PEBS). Mont Terri HE-E Experiment: As-Built Report." NAB 11-025. Wettingen, Switzerland: Nagra. 2011.

Theis, C.V. "The Relation Between the Lowering of the Piezometric Surface and the Rate and Duration of Discharge of a Well Using Ground-Water Storage." *Transactions, American Geophysical Union*. Vol. 16. pp. 519–524. 1935.

Thöny, R. *Geomechanical Analysis of Excavation-Induced Rock Mass Behavior of Faulted Opalinus Clay at the Mont Terri Underground Rock Laboratory (Switzerland)*. PhD Dissertation: ETH Zurich: Switzerland. 2014.

van Genuchten, M.T. "A Closed-Form Equation for Predicting the Hydraulic Conductivity of Unsaturated Soils." *Soil Science Society of America Journal*. Vol. 44. pp. 892–898. 1980.

Villar, M.V., P.L. Martin, R. Gomez-Espina, and F.J. Romero. "Long-term THM Tests Reports: THM Cells for the HE-Test: Update of Results Until February 2014." PEBS Report D2.2-7.3. Madrid, Spain: Long-Term Performance of Engineered Barriers Systems Project. 2014.

Villar, M.V., P.L. Martin, R. Gomez-Espina, F.J. Romero, and J.M. Barcala. "THM Cells for the HE-E Test: Setup and First Results." PEBS Report D2.2.7a. Madrid, Spain: Long-Term Performance of Engineered Barriers Systems Project. 2012.

Wieczorek, K., R. Miehe, and B. Garitte. "Measurement of Thermal Parameters of the HE-E Buffer Materials." PEBS Deliverable D2.2-5. 2011.

Wileveau, Y and T. Rothfuchs. "THM Behaviour of Host Rock (HE-D) Experiment: Study of Thermal Effects on Opalinus Clay." Mont Terri Project, TR 2006-01. 2007.

Wileveau, Y. "THM Behaviour of Host Rock (HE-D experiment): Progress Report September 2003 – October 2004." Mont Terri Project, TR 2005-03. 2005.

APPENDIX A

TIME HISTORIES OF RELATIVE HUMIDITY AND TEMPERATURE IN NAGRA (N1, N2, N3) AND GRS (G1, G2, G3) CROSS SECTIONS

Time Histories of Relative Humidity and Temperature in Nagra (N1, N2, N3) and GRS (G1, G2, G3) Cross Sections

The figures in Appendix A provide the time histories of relative humidity and temperature in the N1, N2, N3, G1, G2, and G3 cross sections for sensors installed for the HE-E experiment. These consist of the three layers of sensors (close, middle, and host) at the 3, 9, and 12 o'clock positions and the two layers (top and lower) of paired sensors (5 and 7 o'clock).

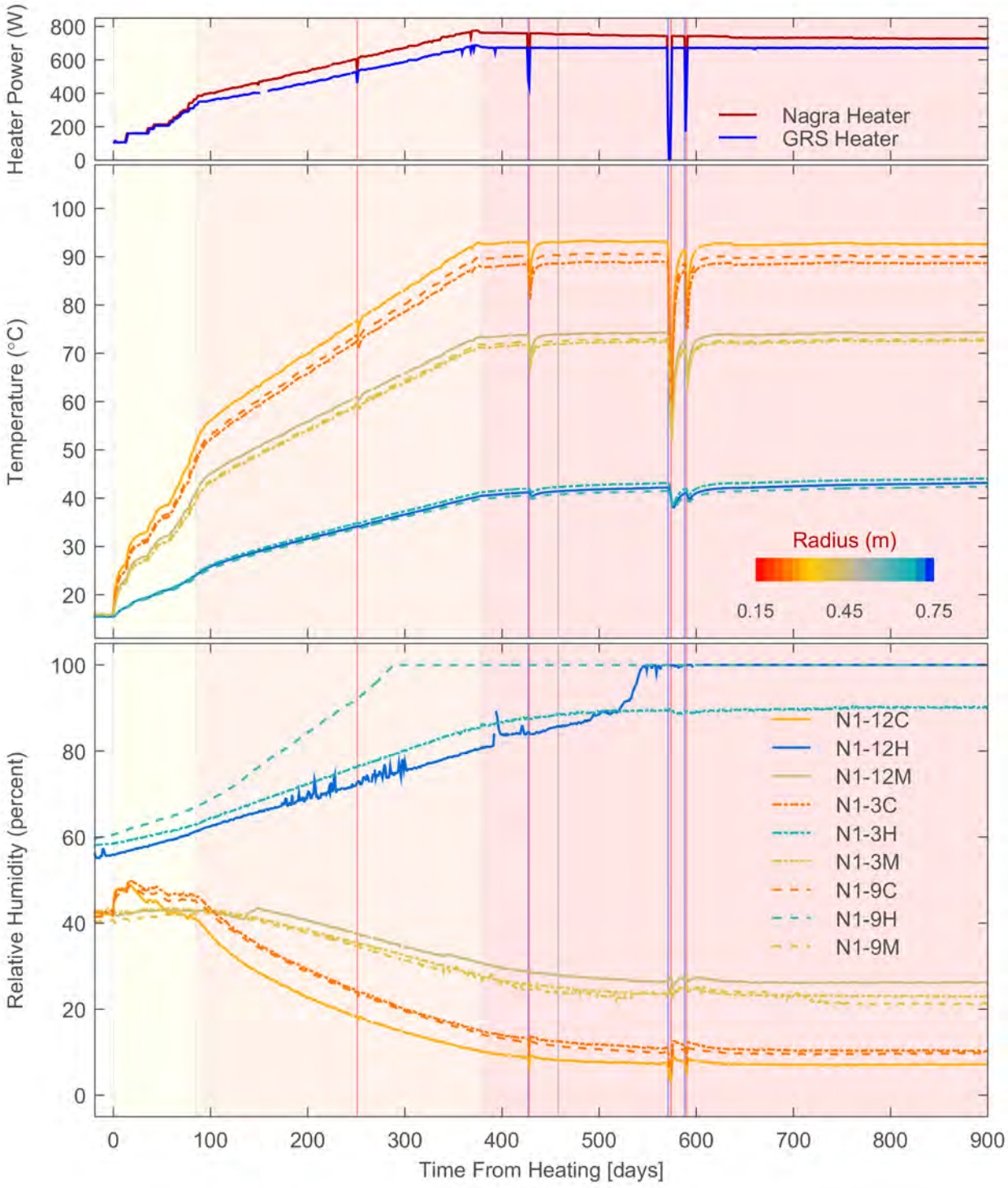

Figure A–1. Daily Average Measured Heater Power (Top), Temperature (Middle), and Relative Humidity (Bottom) in the Granular Bentonite Buffer and Host Rock at the N1 Cross Section [°F = (1.8 × T °C + 32), 1 m = 3.3 ft]

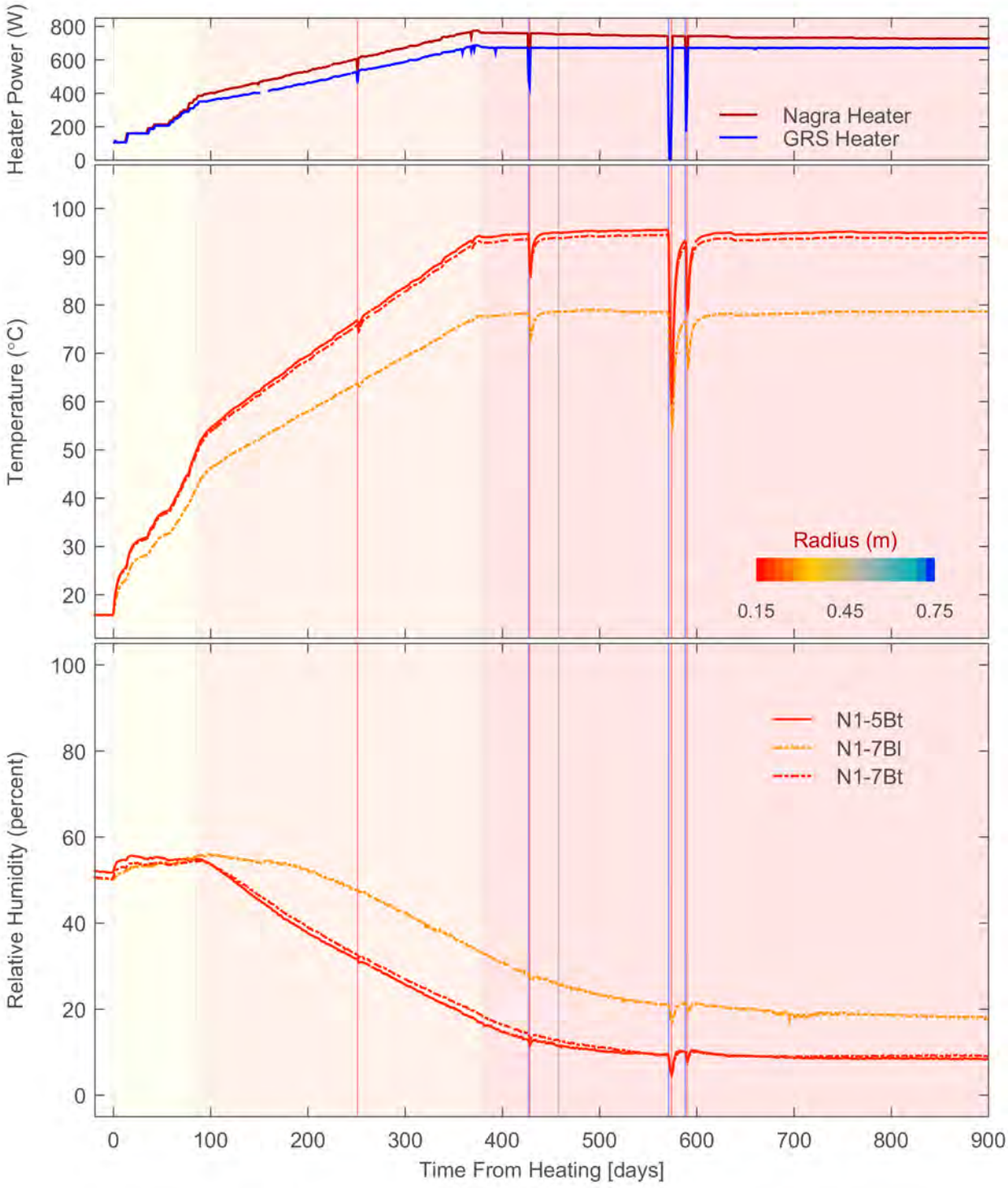

Figure A–2. Daily Average Measured Heater Power (Top), Temperature (Middle), and Relative Humidity (Bottom) in the Bentonite Block Pedestal at the N1 Cross Section [°F = (1.8 × T °C + 32), 1 m = 3.3 ft]

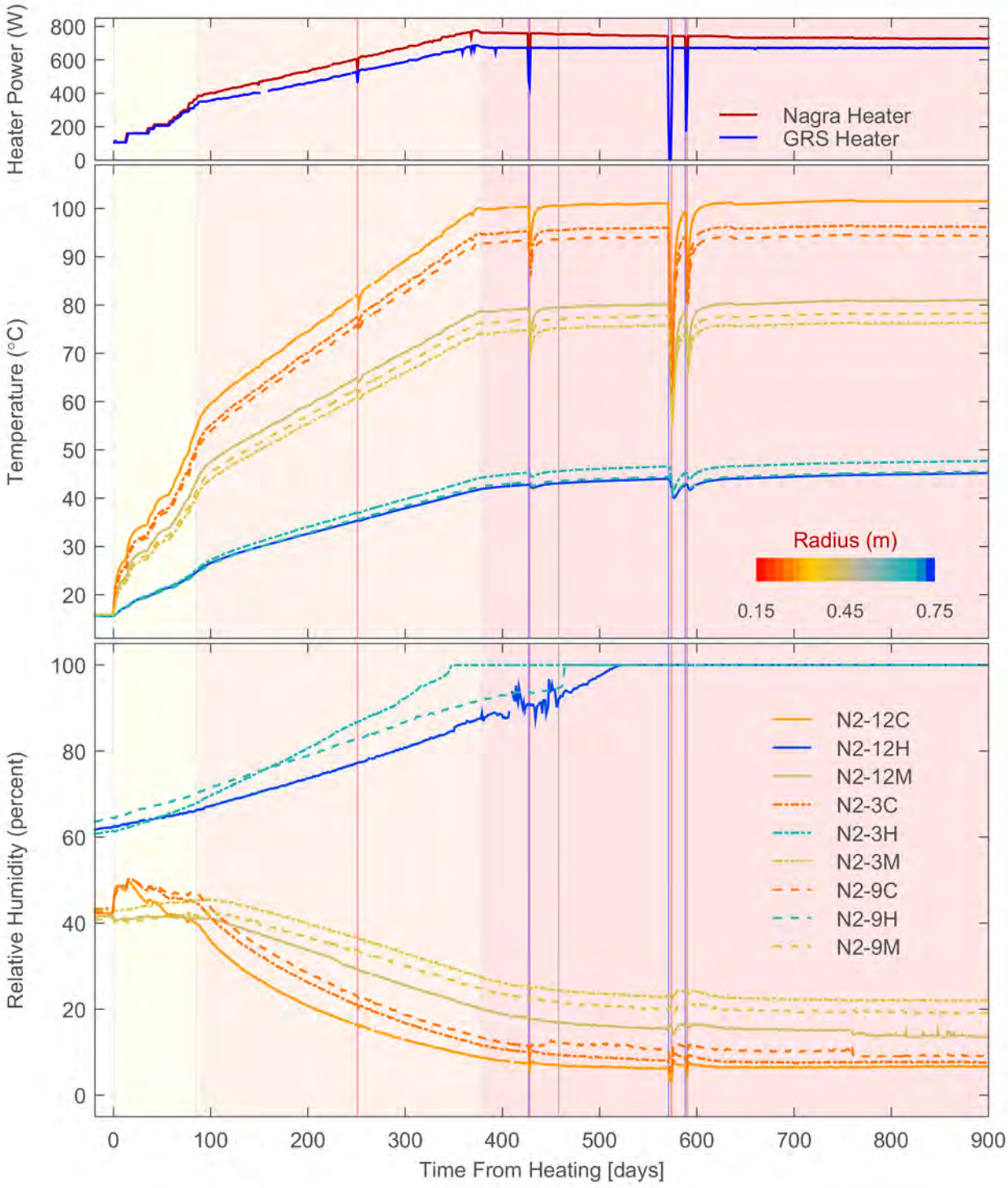

Figure A–3. Daily Average Measured Heater Power (Top), Temperature (Middle), and Relative Humidity (Bottom) in the Granular Bentonite Buffer and Host Rock at the N2 Cross Section [°F = (1.8 × T °C + 32), 1 m = 3.3 ft]

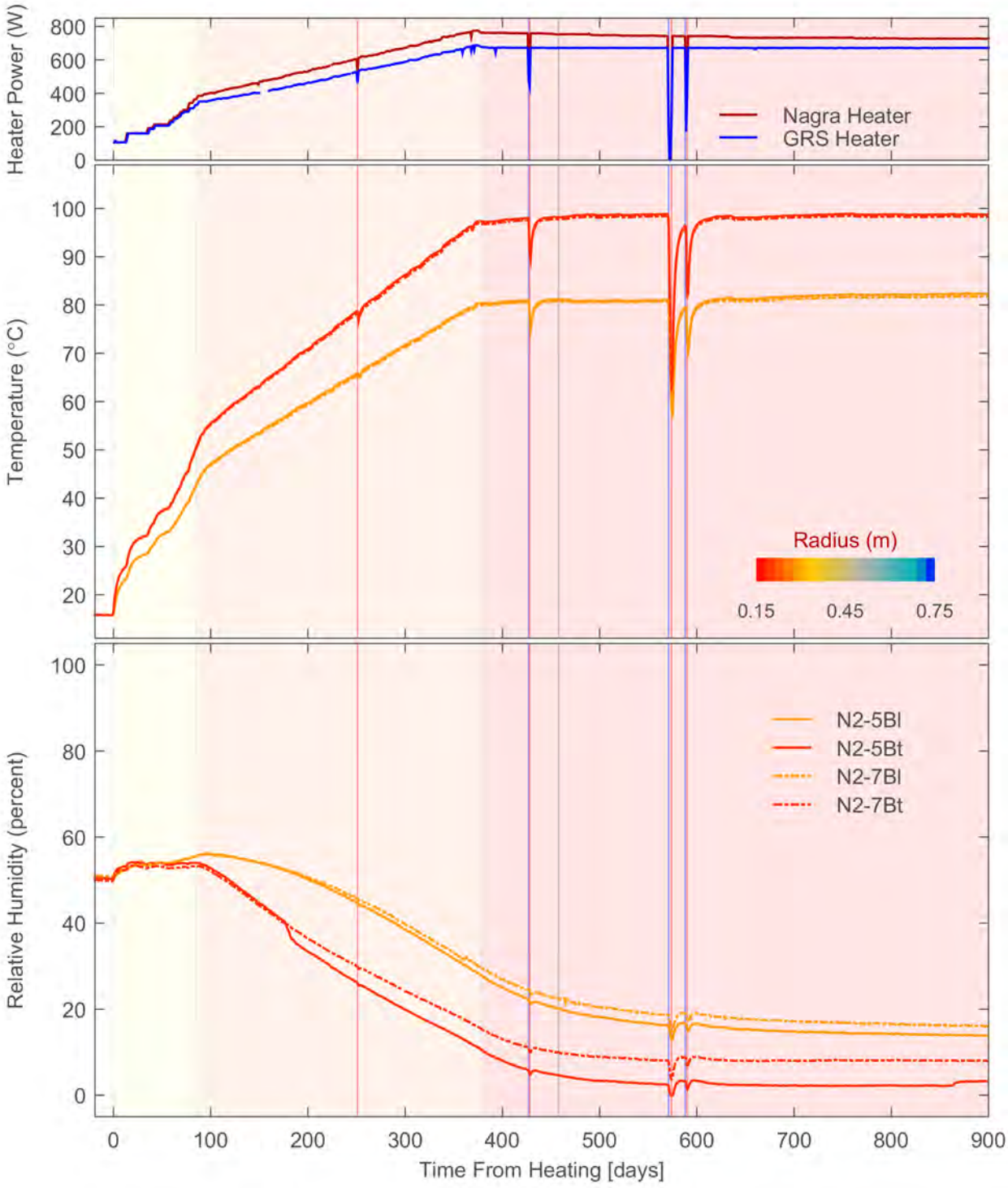

Figure A–4. Daily Average Measured Heater Power (Top), Temperature (Middle), and Relative Humidity (Bottom) in the Bentonite Block Pedestal at the N2 Cross Section [°F = (1.8 × T °C + 32), 1 m = 3.3 ft]

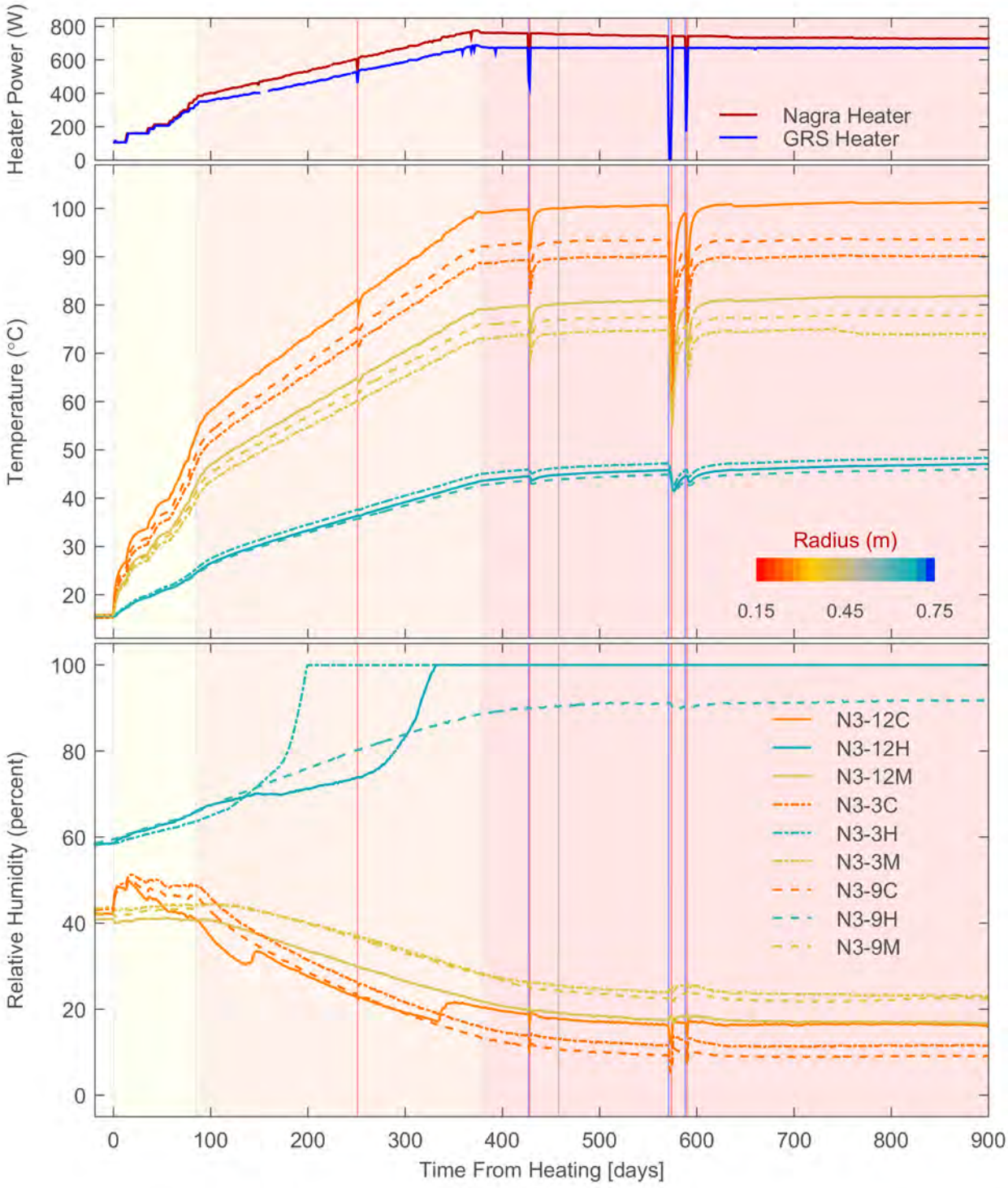

Figure A–5. Daily Average Measured Heater Power (Top), Temperature (Middle), and Relative Humidity (Bottom) in the Granular Bentonite Buffer and Host Rock at the N3 Cross Section [°F = (1.8 × T °C + 32), 1 m = 3.3 ft]

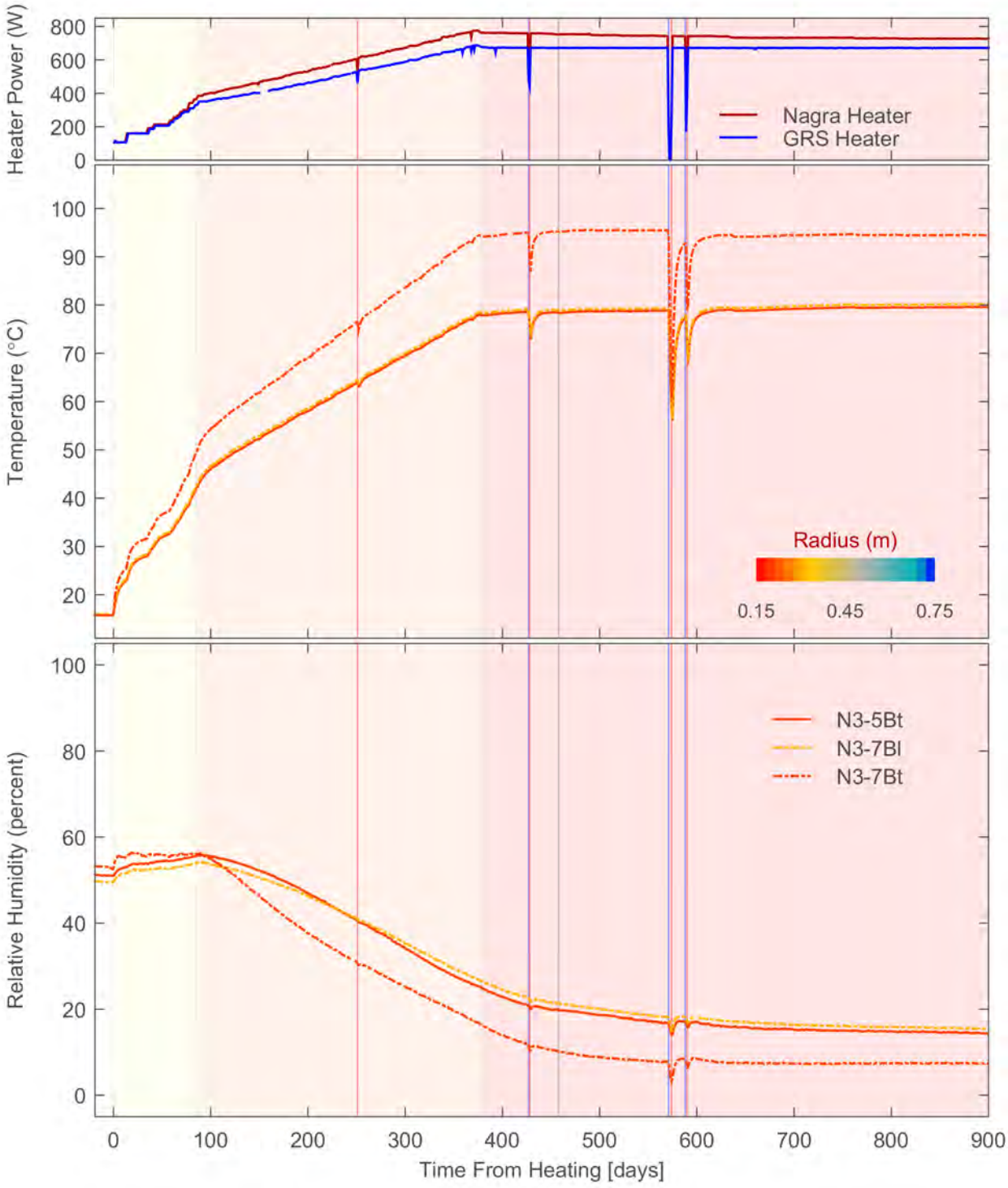

Figure A–6. Daily Average Measured Heater Power (Top), Temperature (Middle), and Relative Humidity (Bottom) in the Bentonite Block Pedestal at the N3 Cross Section [°F = (1.8 × T °C + 32), 1 m = 3.3 ft]

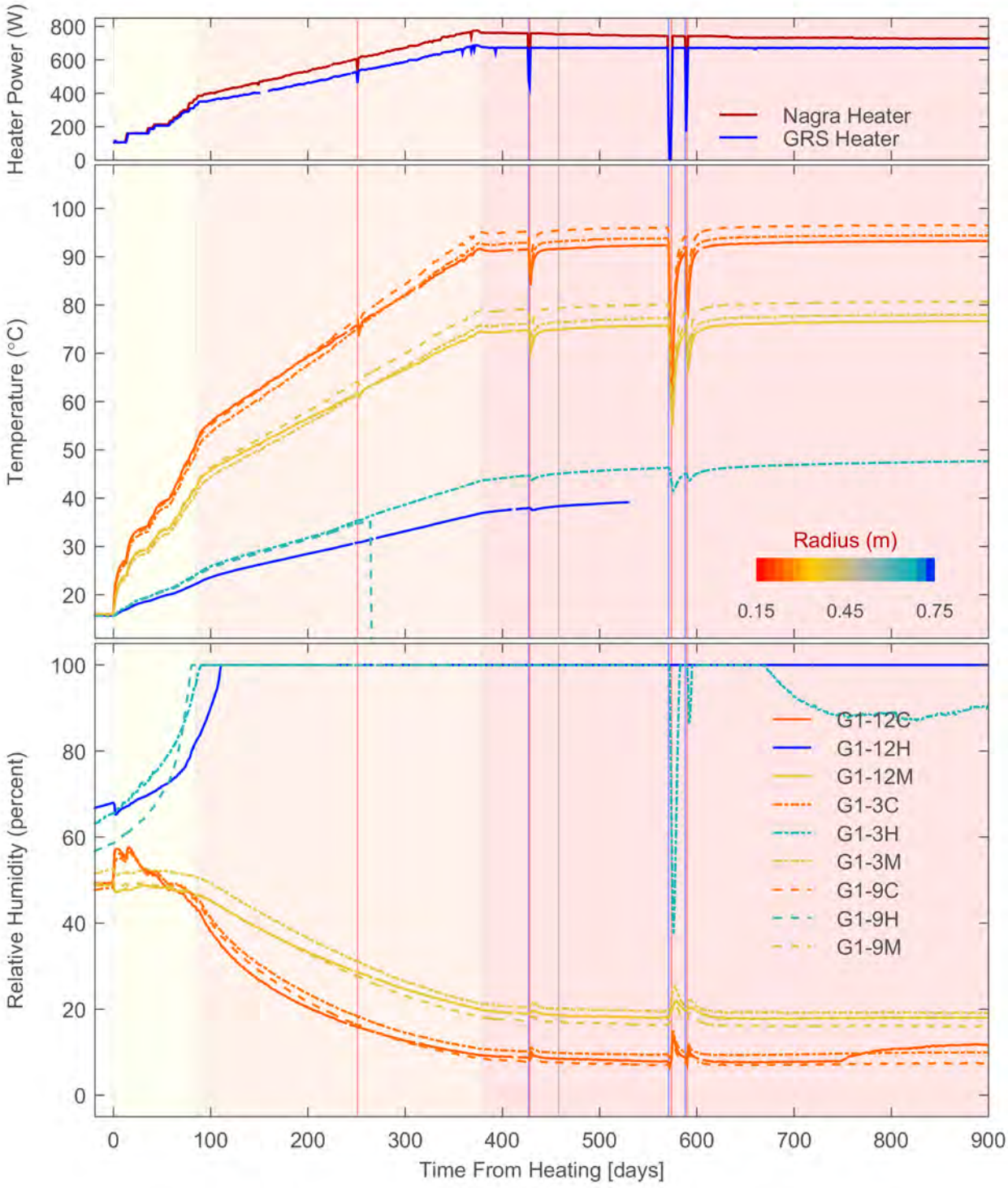

Figure A–7. Daily Average Measured Heater Power (Top), Temperature (Middle), and Relative Humidity (Bottom) in the Sand–Bentonite Buffer and Host Rock at the G1 Cross Section [°F = (1.8 × T °C + 32), 1 m = 3.3 ft]

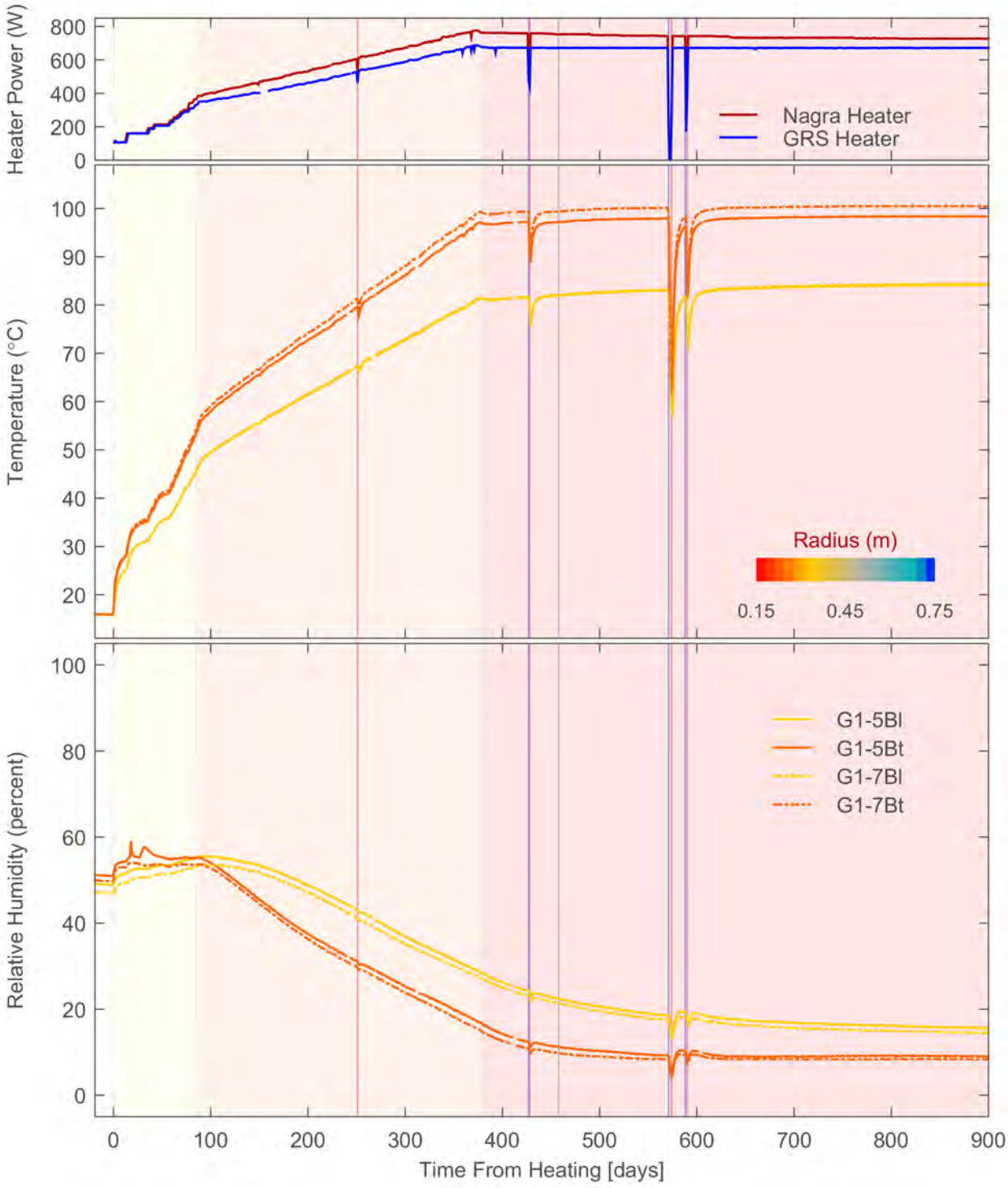

Figure A–8. Daily Average Measured Heater Power (Top), Temperature (Middle), and Relative Humidity (Bottom) in the Bentonite Block Pedestal at the G1 Cross Section [°F = (1.8 × T °C + 32), 1 m = 3.3 ft]

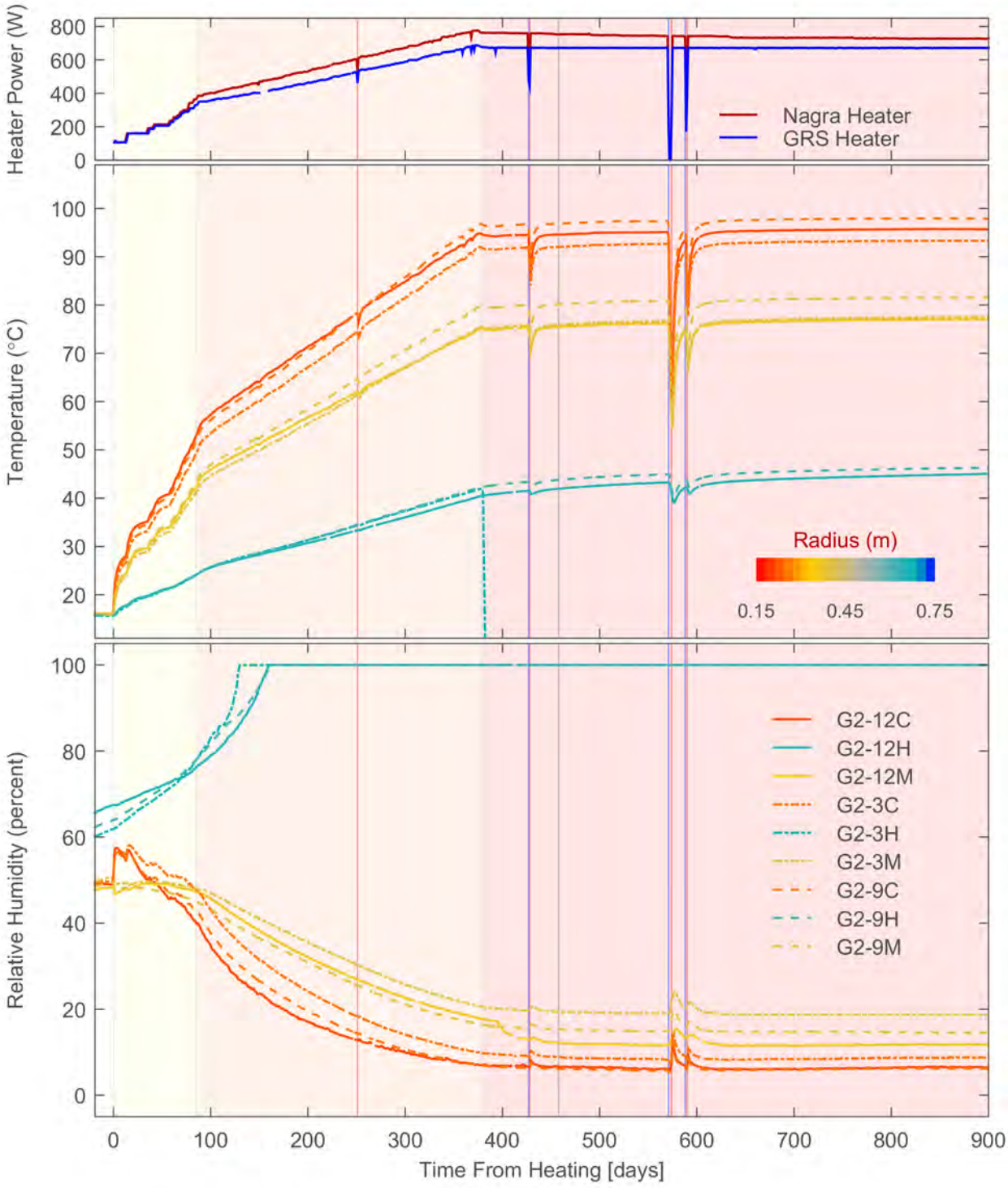

Figure A–9. Daily Average Measured Heater Power (Top), Temperature (Middle), and Relative Humidity (Bottom) in the Sand–Bentonite Buffer and Host Rock at the G2 Cross Section [°F = (1.8 × T °C + 32), 1 m = 3.3 ft]

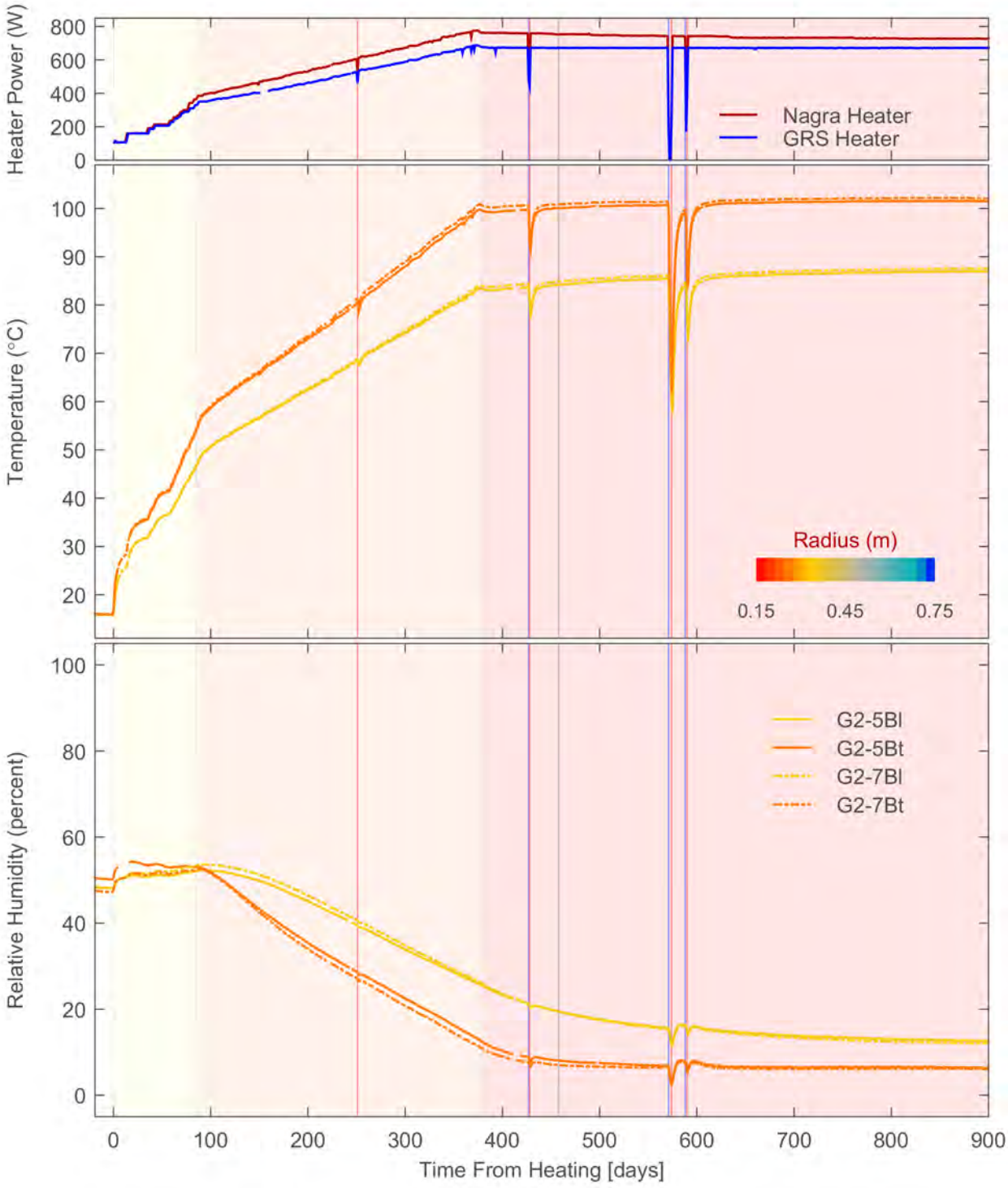

Figure A–10. Daily Average Measured Heater Power (Top), Temperature (Middle), and Relative Humidity (Bottom) in the Bentonite Block Pedestal at the G2 Cross Section [°F = (1.8 × T °C + 32), 1 m = 3.3 ft]

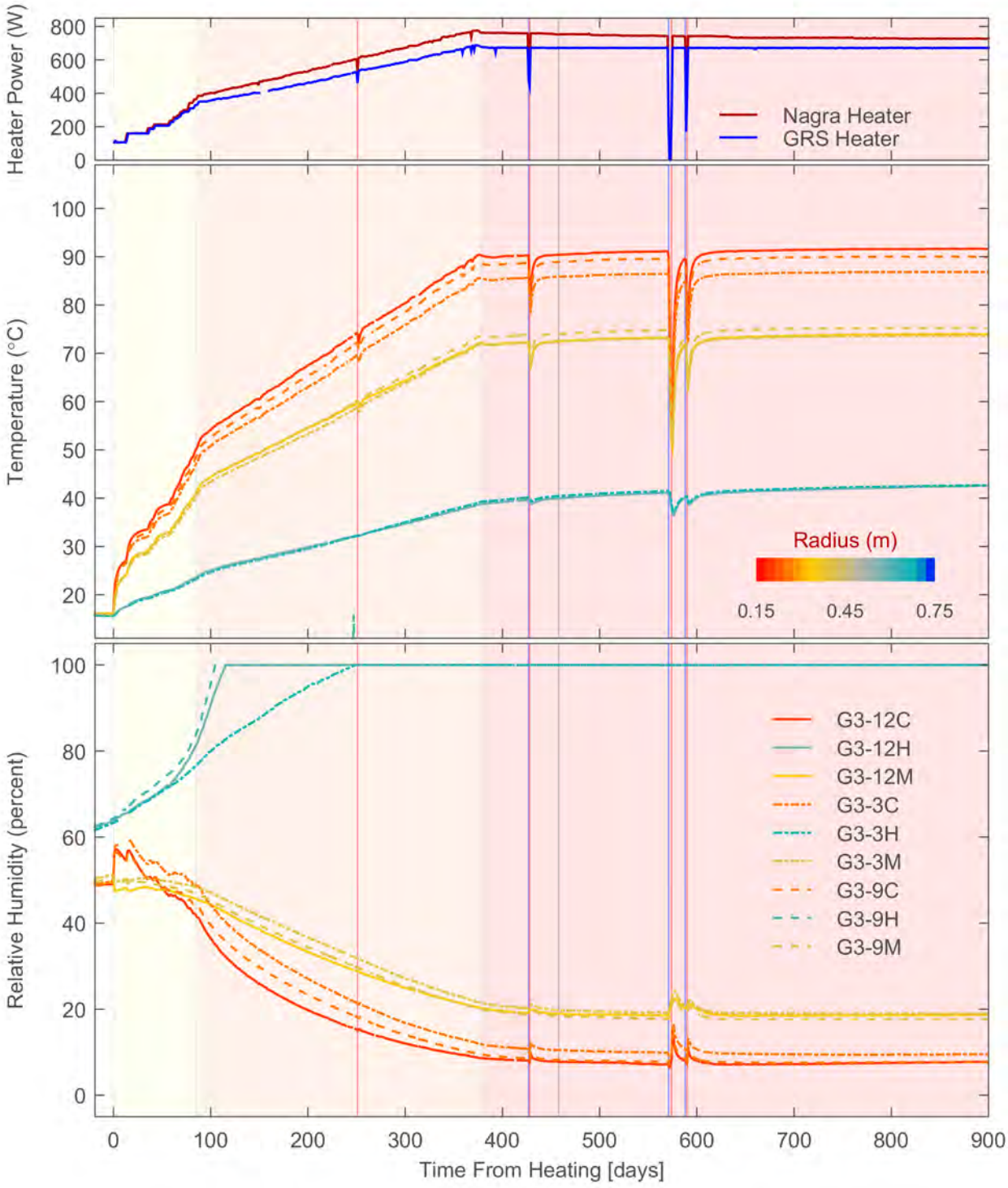

Figure A–11. Daily Average Measured Heater Power (Top), Temperature (Middle), and Relative Humidity (Bottom) in the Sand–Bentonite Buffer and Host Rock at the G3 Cross Section [°F = (1.8 × T °C + 32), 1 m = 3.3 ft]

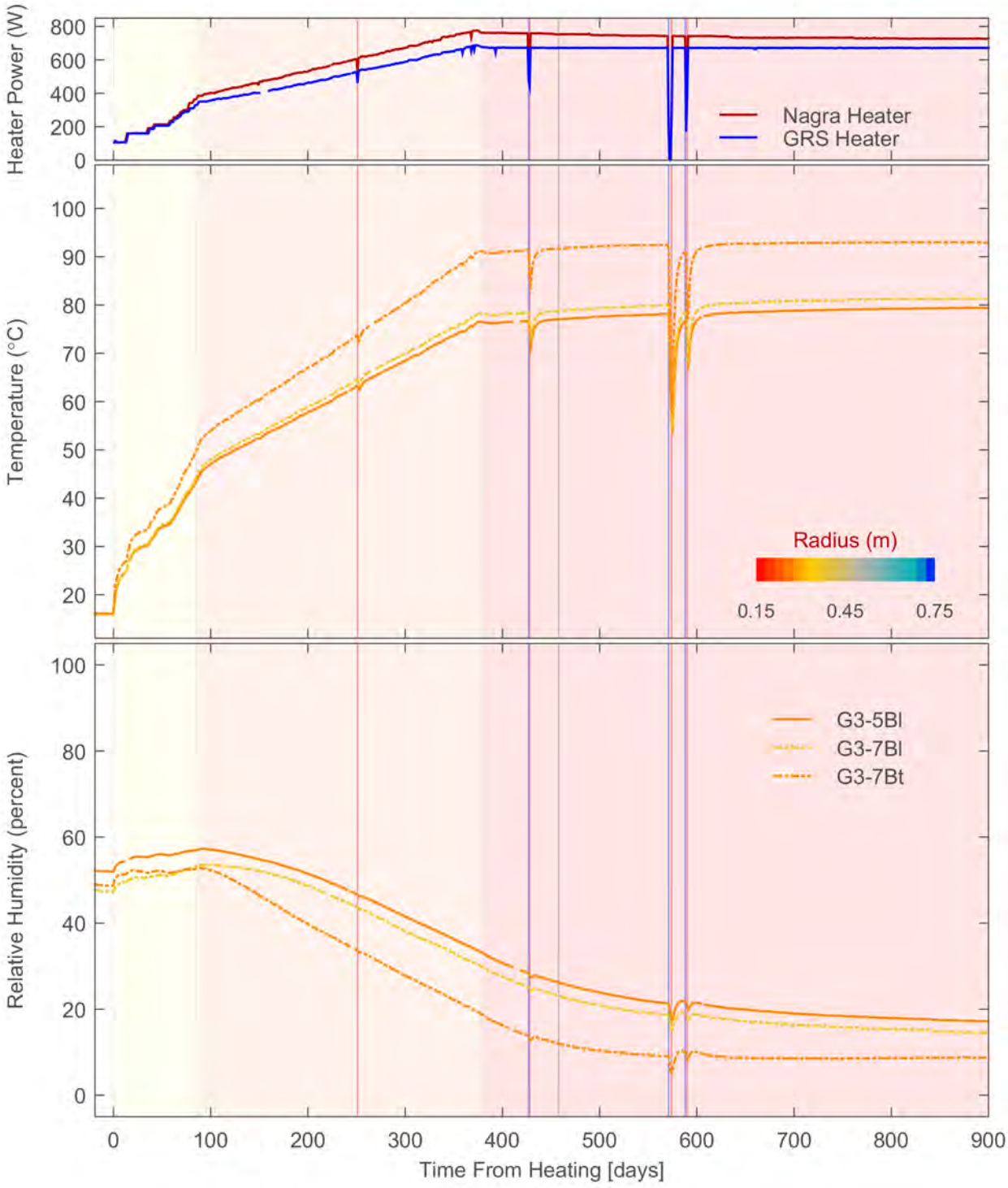

Figure A–12. Daily Average Measured Heater Power (Top), Temperature (Middle), and Relative Humidity (Bottom) in the Bentonite Block Pedestal at the G3 Cross Section. G3-5BI Appears to be Mislabeled in the Sensor Records and Probably Should be G3-5Bt. [°F = (1.8 × T °C + 32), 1 m = 3.3 ft]

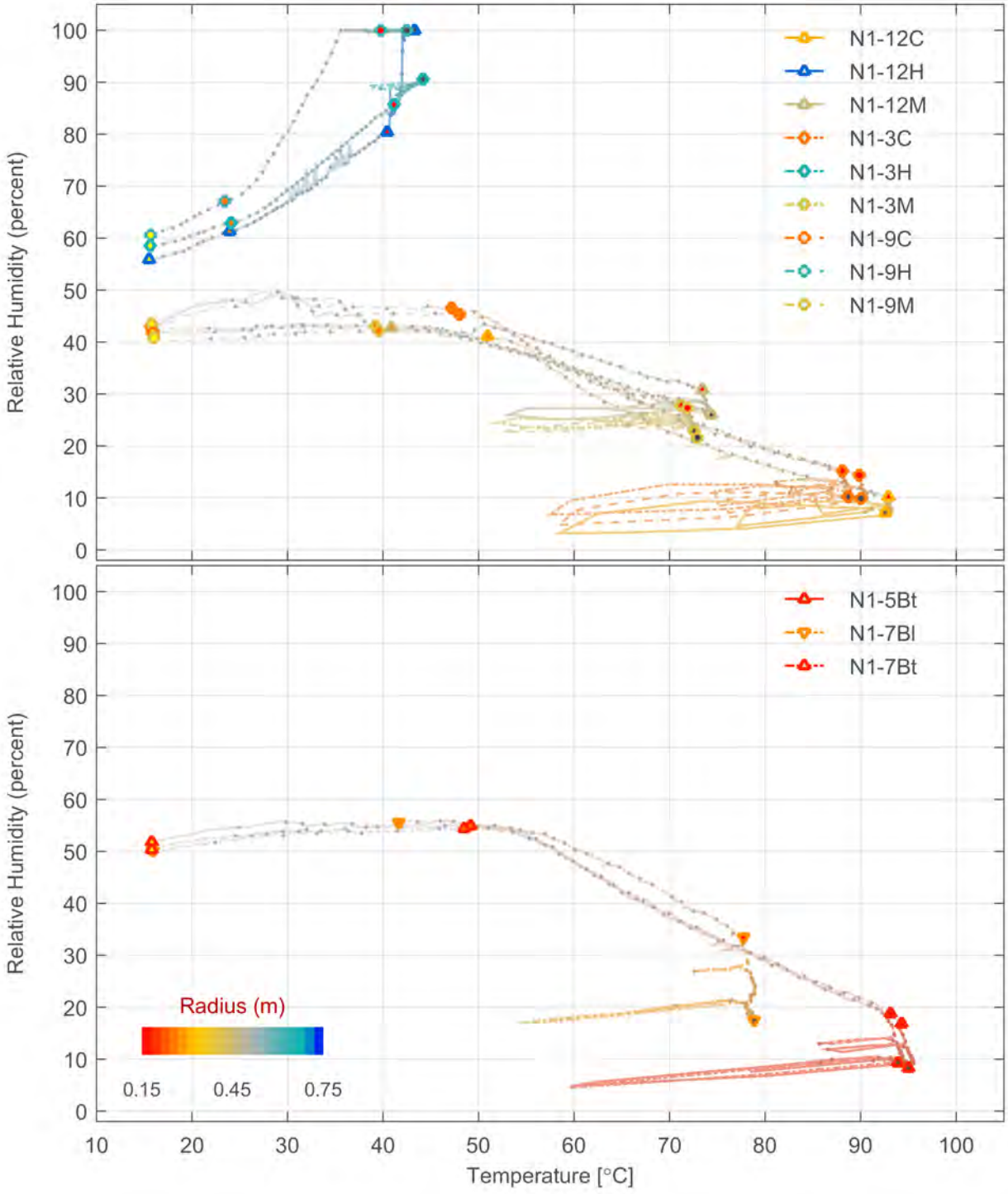

Figure A–13. Joint Response of Daily Average Measured Temperature and Relative Humidity in the Granular Bentonite Buffer and Host Rock (Top) and in the Bentonite Block Pedestal (Bottom) at the N1 Cross Section. Dots are Spaced 10 Days Apart. [°F = (1.8 × T °C + 32), 1 m = 3.3 ft]

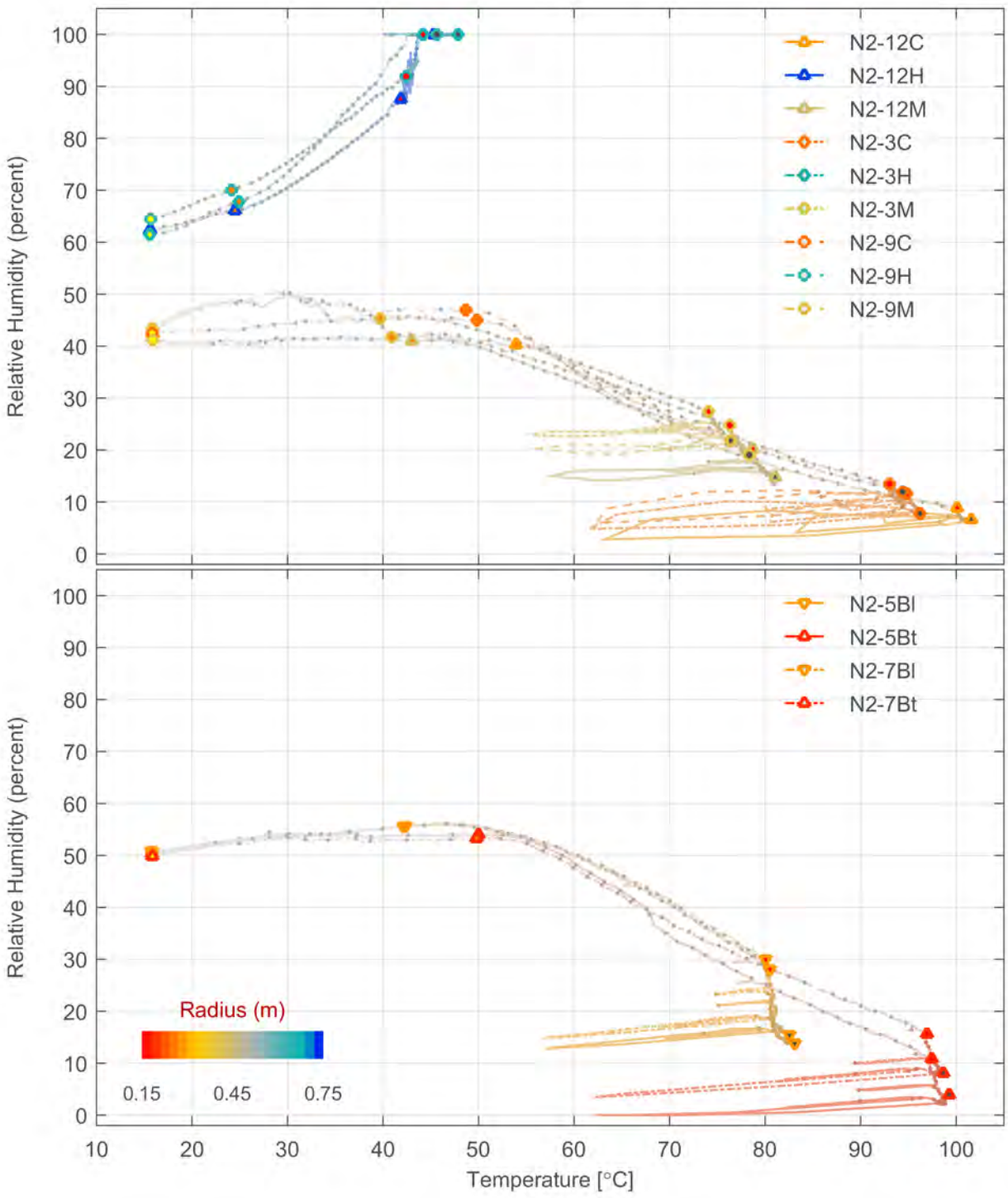

Figure A–14. Joint Response of Daily Average Measured Temperature and Relative Humidity in the Granular Bentonite Buffer and Host Rock (Top) and in the Bentonite Block Pedestal (Bottom) at the N2 Cross Section. Dots are Spaced 10 Days Apart. [°F = (1.8 × T °C + 32), 1 m = 3.3 ft]

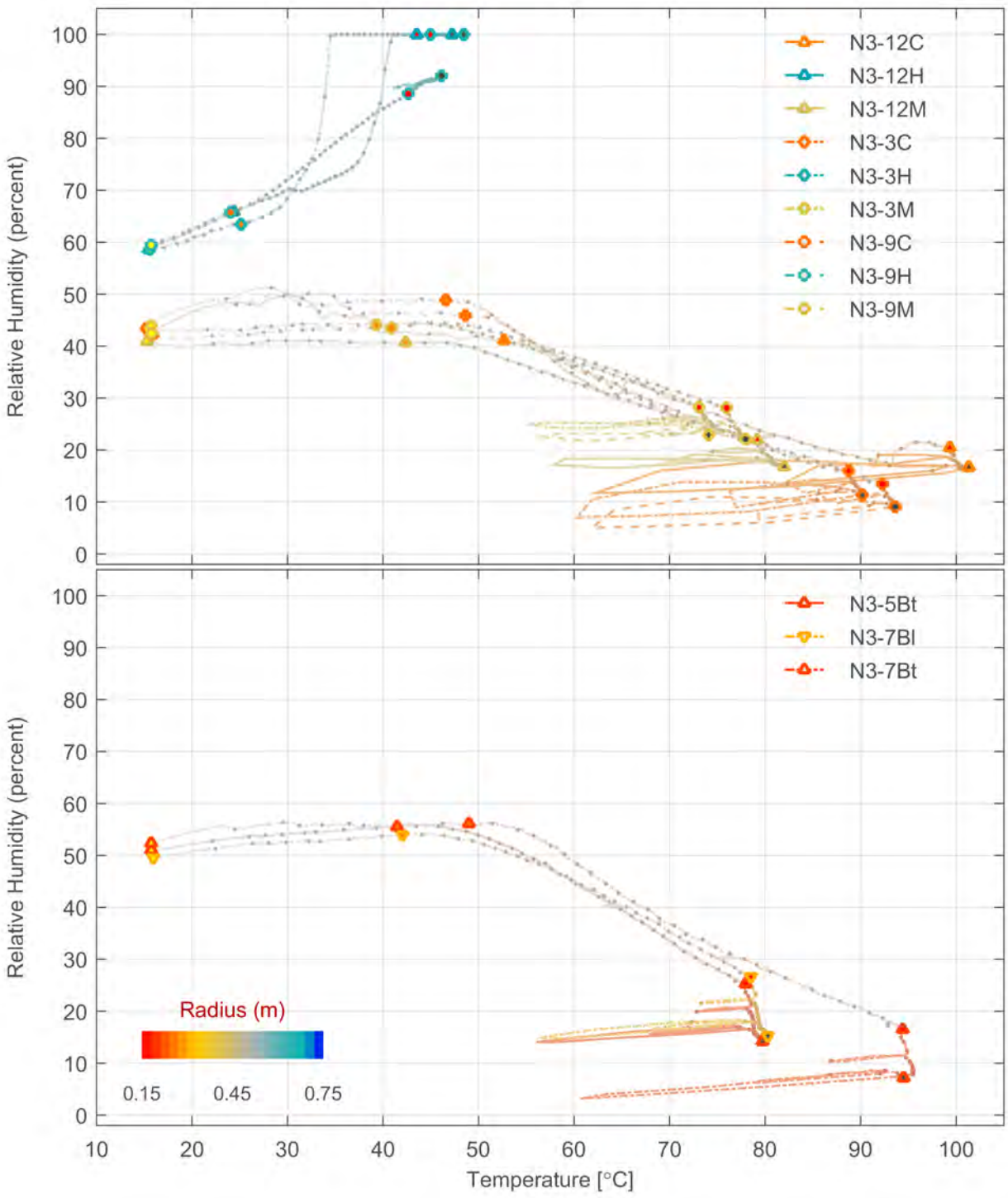

Figure A–15. Joint Response of Daily Average Measured Temperature and Relative Humidity in the Granular Bentonite Buffer and Host Rock (Top) and in the Bentonite Block Pedestal (Bottom) at the N3 Cross Section. Dots are Spaced 10 Days Apart. [°F = (1.8 × T °C + 32), 1 m = 3.3 ft]

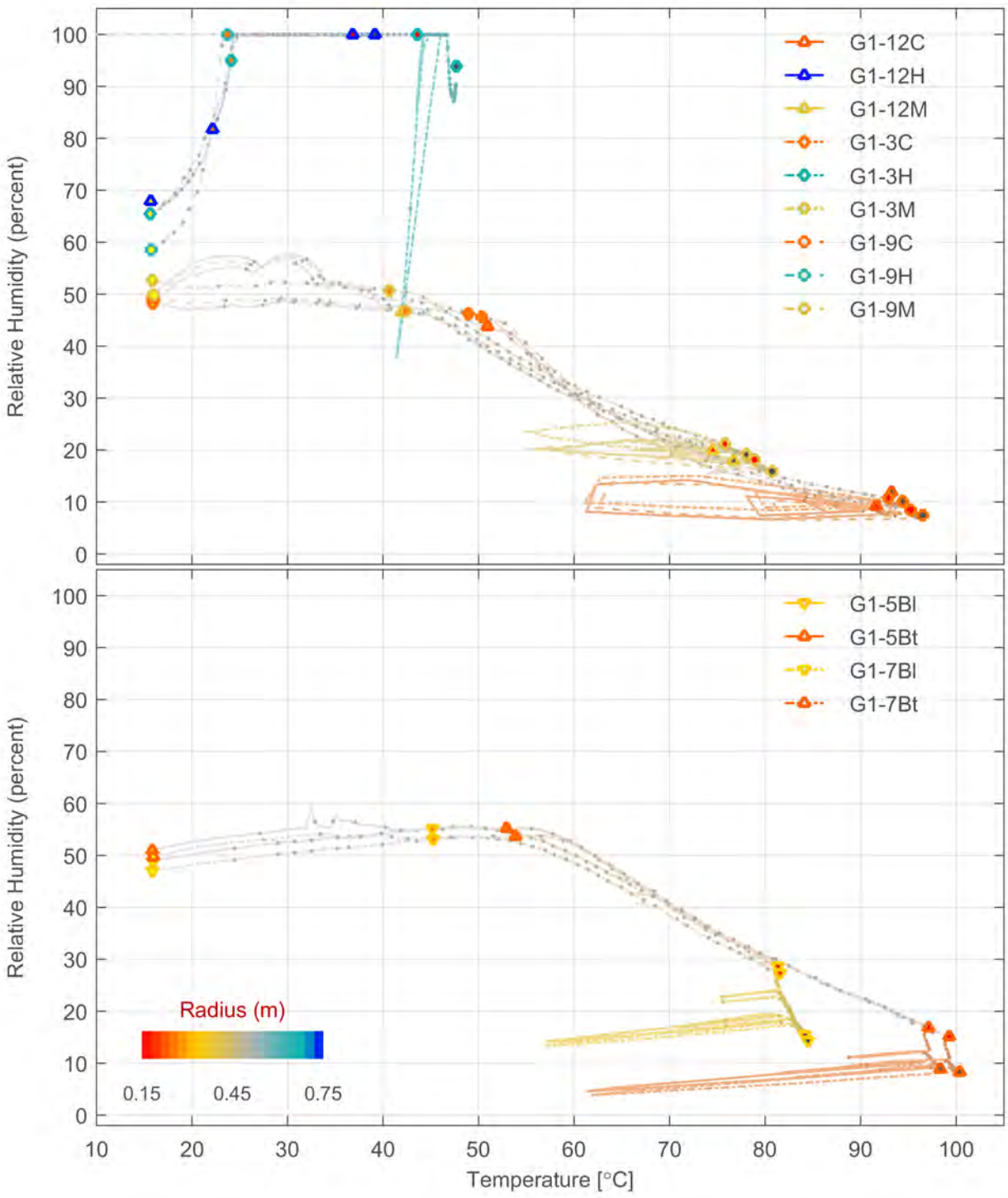

Figure A–16. Joint Response of Daily Average Measured Temperature and Relative Humidity in the Granular Bentonite Buffer and Host Rock (Top) and in the Bentonite Block Pedestal (Bottom) at the G1 Cross Section. Dots are Spaced 10 Days Apart. [°F = (1.8 × T °C + 32), 1 m = 3.3 ft]

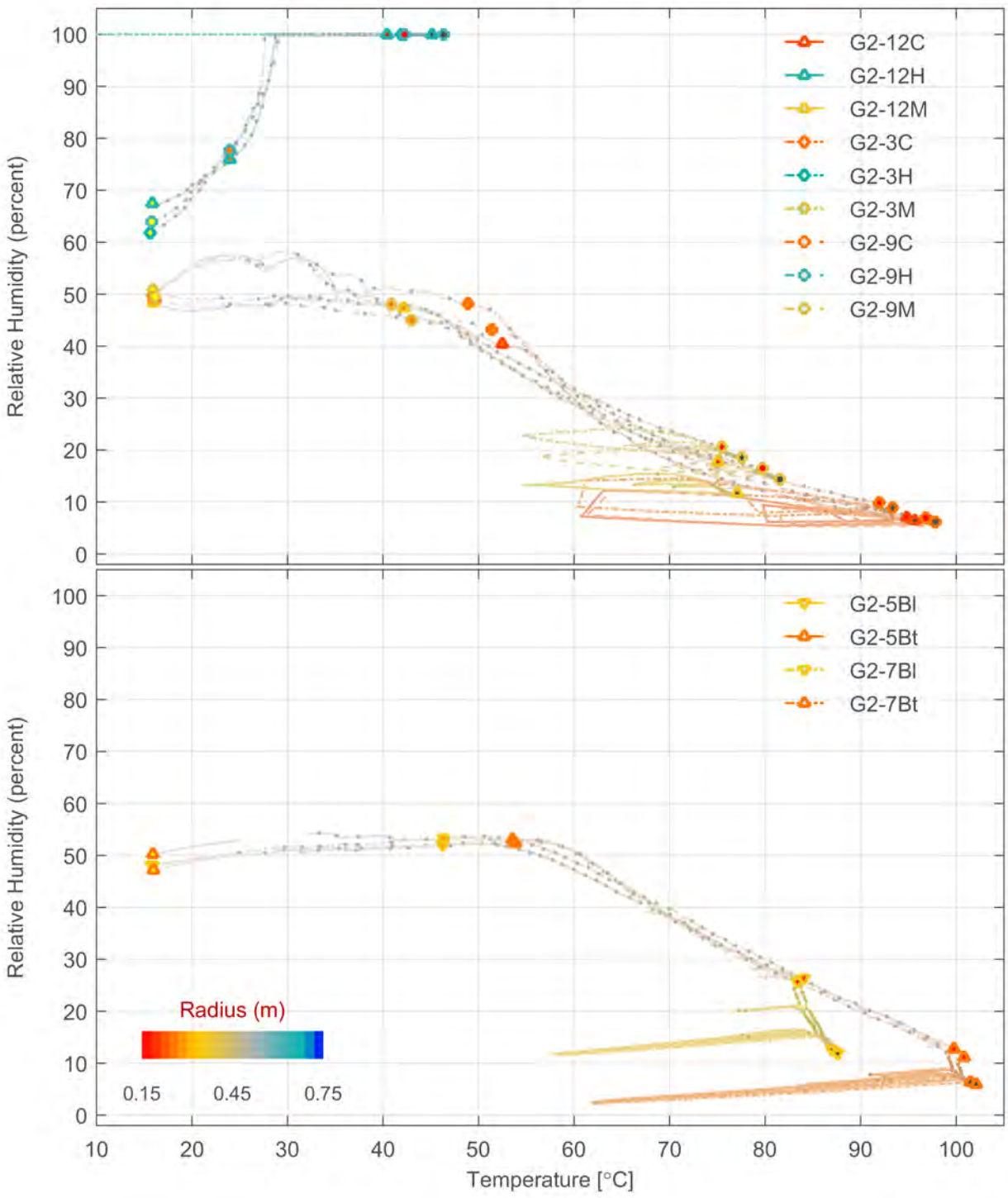

Figure A–17. Joint Response of Daily Average Measured Temperature and Relative Humidity in the Granular Bentonite Buffer and Host Rock (Top) and in the Bentonite Block Pedestal (Bottom) at the G2 Cross Section. Dots are Spaced 10 Days Apart. [°F = (1.8 × T °C + 32), 1 m = 3.3 ft]

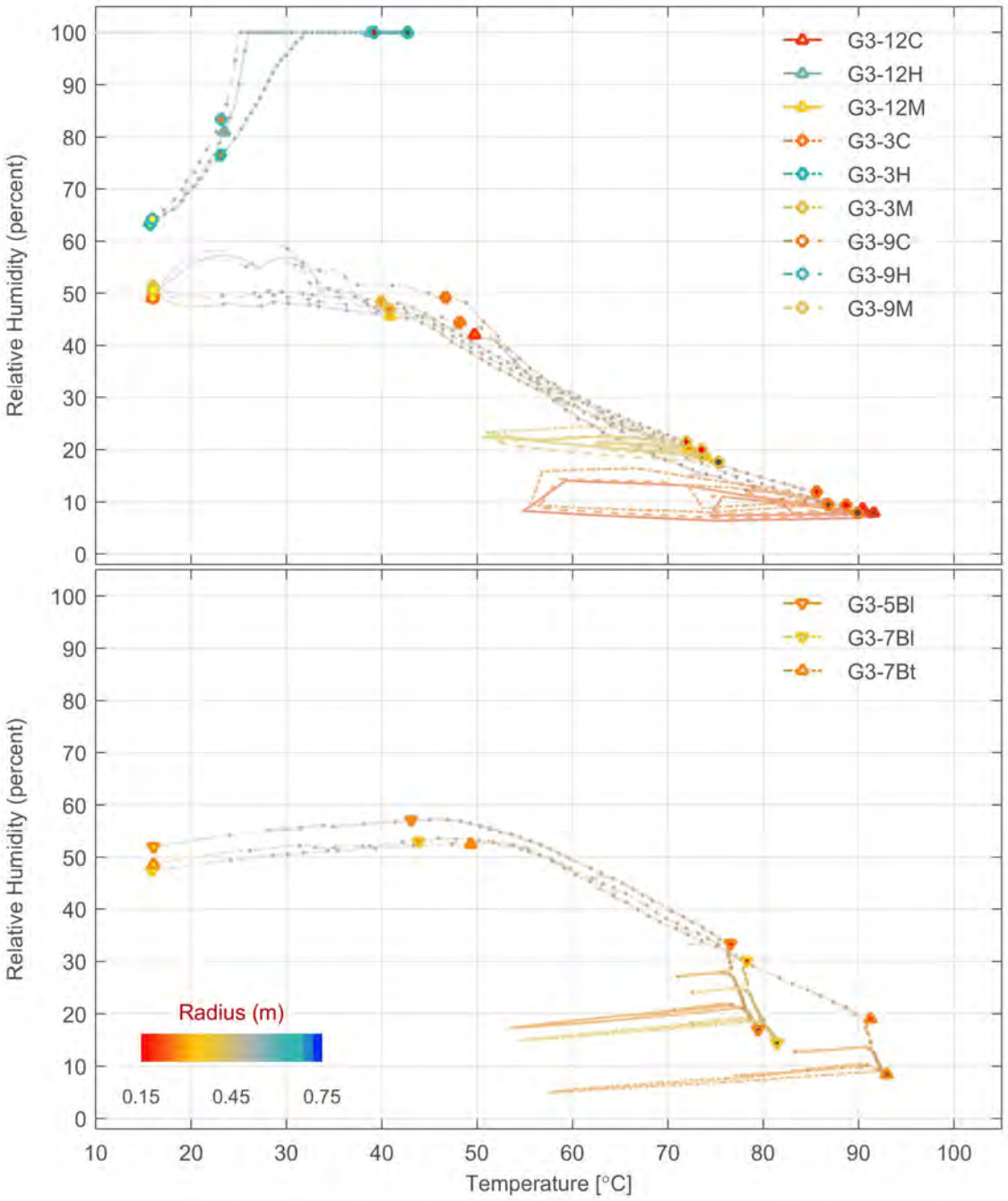

Figure A–18. Joint Response of Daily Average Measured Temperature and Relative Humidity in the Granular Bentonite Buffer and Host Rock (Top) and in the Bentonite Block Pedestal (Bottom) at the G3 Cross Section. Dots are Spaced 10 Days Apart. G3-5BI Appears to be Mislabeled in the Sensor Records and Probably Should be G3-5Bt. [°F = (1.8 × T °C + 32), 1 m = 3.3 ft]

APPENDIX B

LINER-TEMPERATURE SIMULATION RESULTS

Temperature Simulation Results

Figures B–1 through B–10 repeat Figures 5-1 through 5-10, except that the uncalibrated parameter set is used with a fixed liner temperature boundary condition.

Figures B–11 through B–20 repeat Figures 5-1 through 5-10, except that the calibrated parameter set is used with a fixed liner temperature boundary condition.

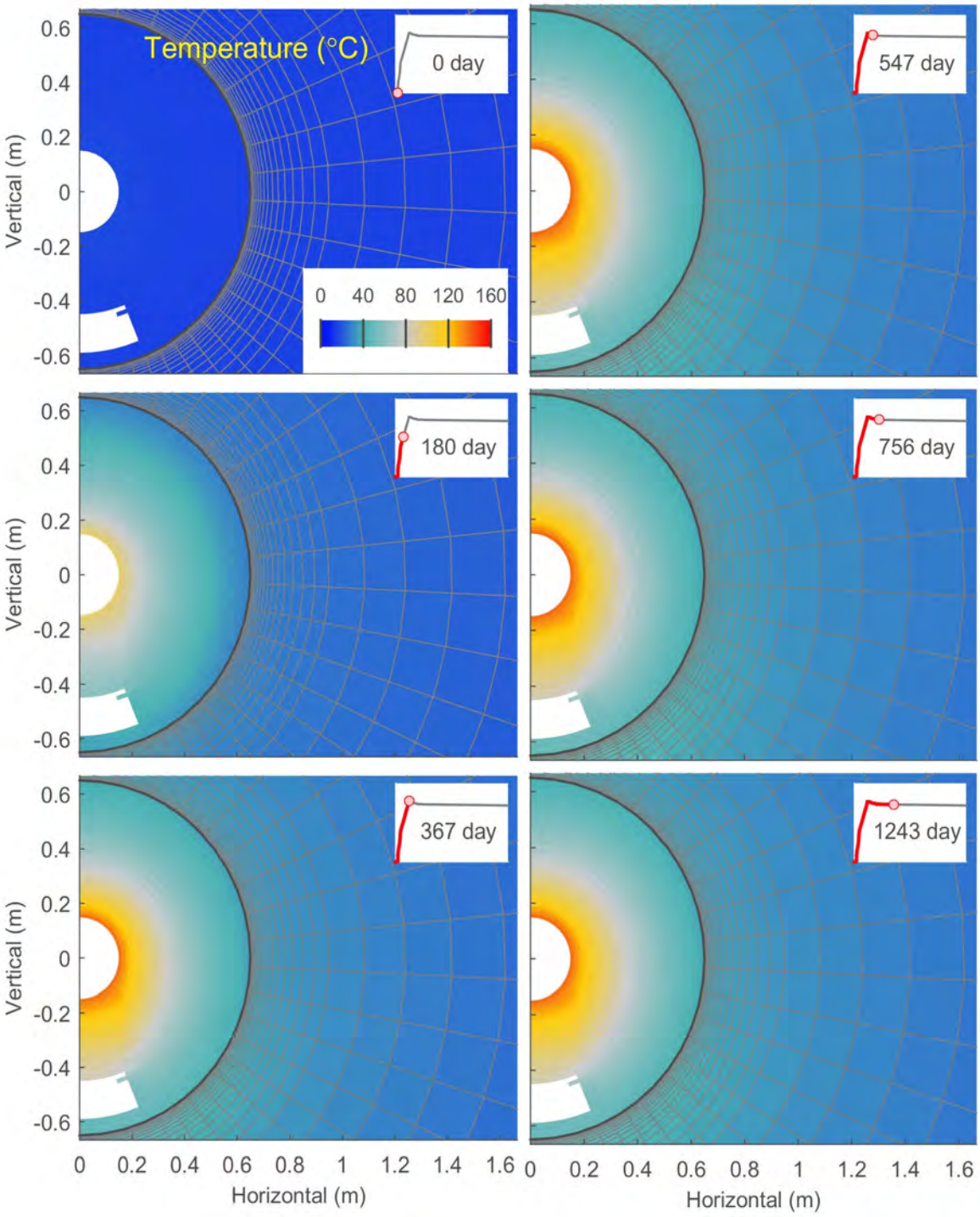

Figure B–1. Spatial Distribution of Calculated Temperature at Selected Time Instants After Start of Heating for the Uncalibrated Parameter Set With Specified Liner Temperature [°F = (1.8 × T °C + 32), 1 m = 3.3 ft]

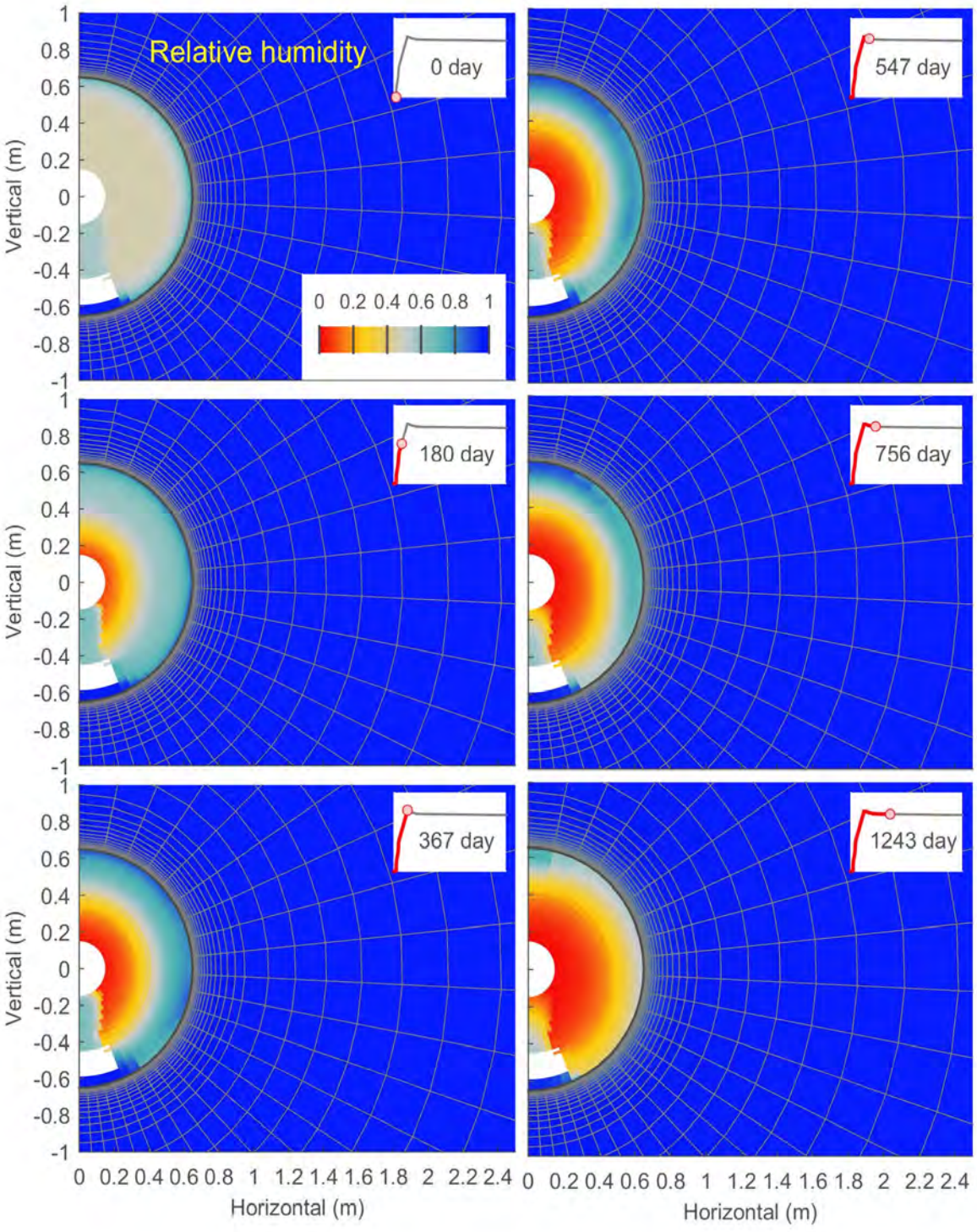

Figure B–2. Spatial Distribution of Calculated Relative Humidity at Selected Time Instants After Start of Heating for the Calibrated Parameter Set [1 m = 3.3 ft]

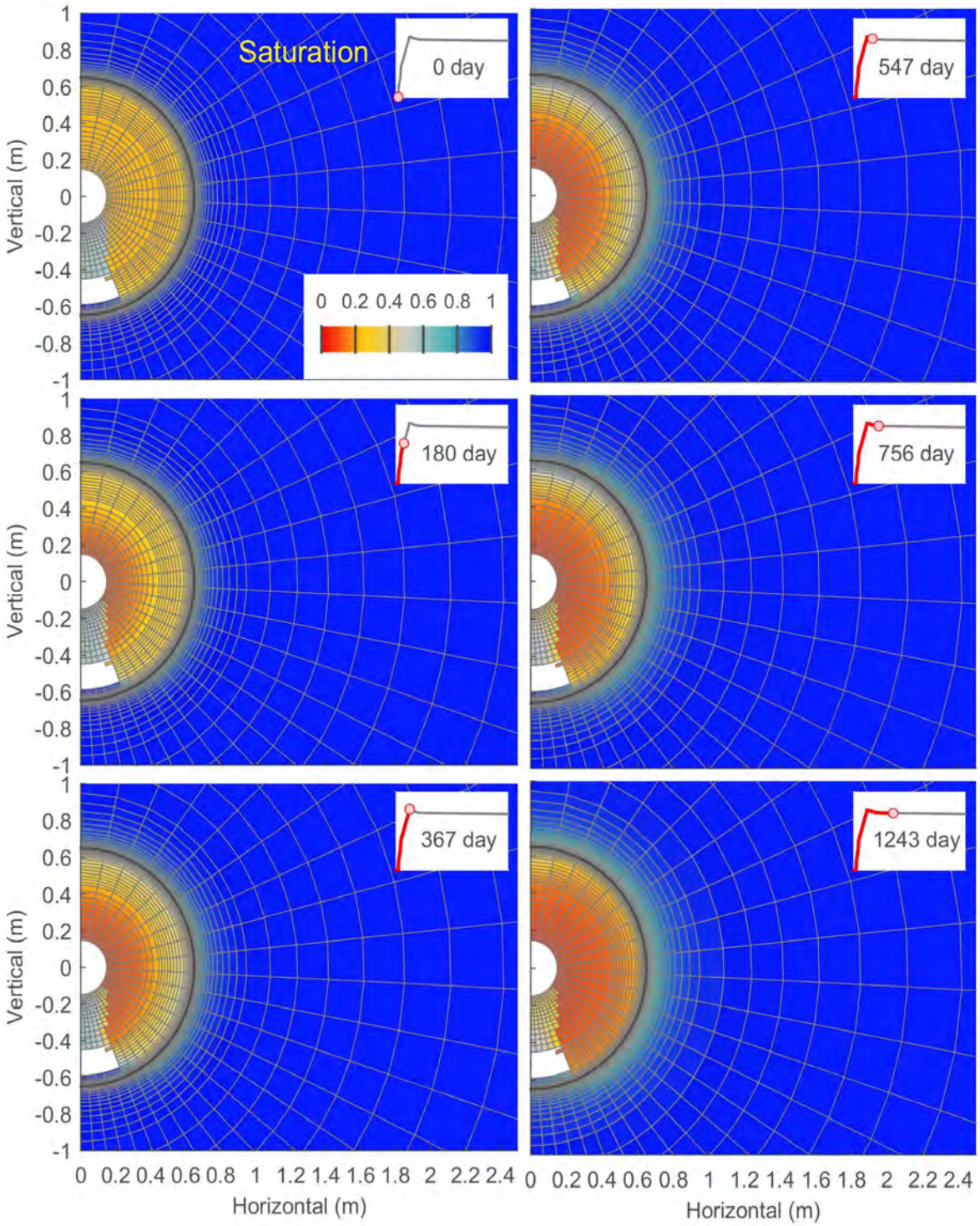

Figure B–3. Spatial Distribution of Calculated Liquid Saturation at Selected Time Instants After Start of Heating for the Uncalibrated Parameter Set With Specified Liner Temperature [1 m = 3.3 ft]

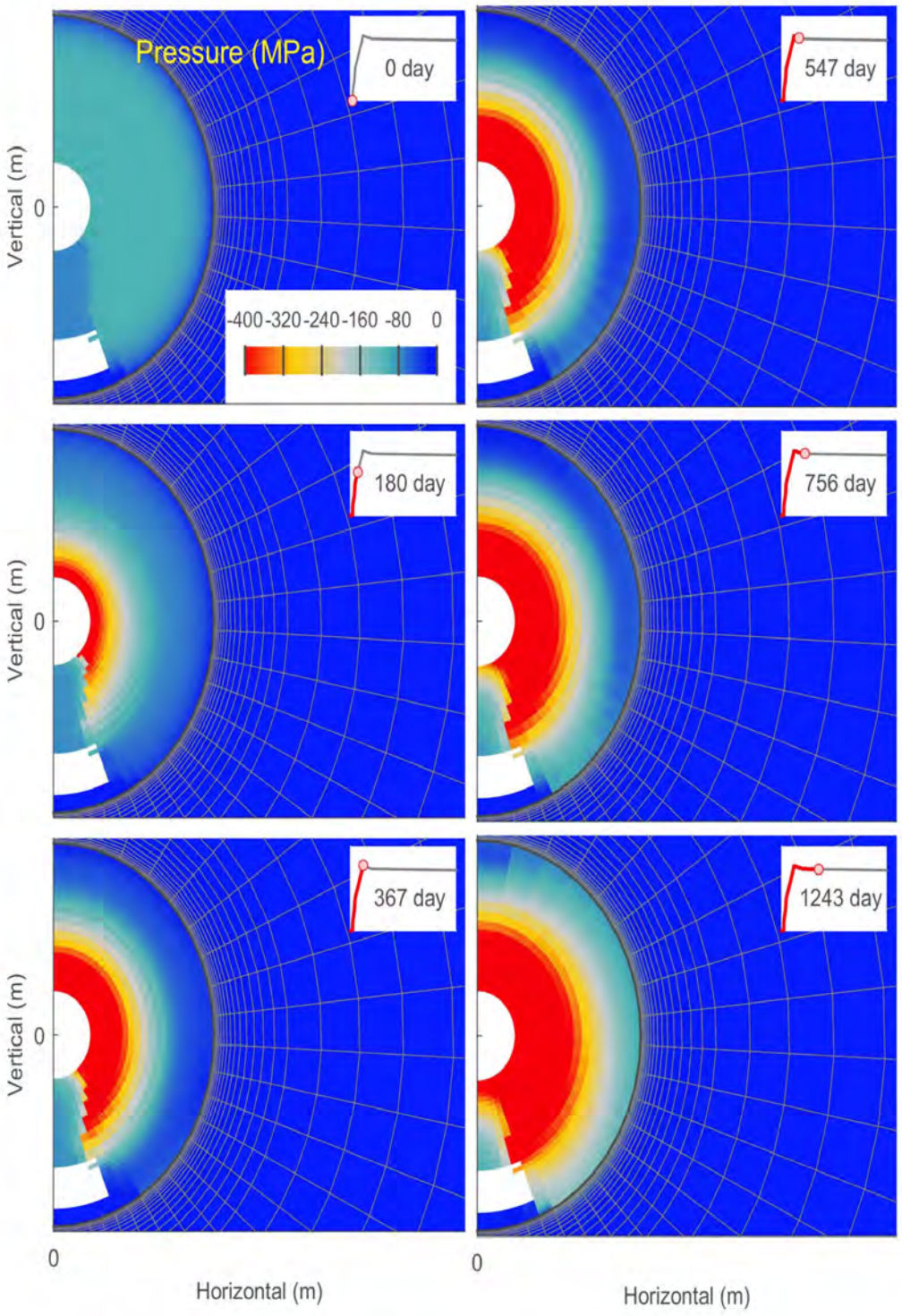

Figure B–4. Spatial Distribution of Calculated Liquid Pressure at Selected Time Instants After Start of Heating for the Uncalibrated Parameter Set With Specified Liner Temperature. Note That Liquid Pressure is Clipped. [1MPa = 145 psi, 1 m = 3.3 ft]

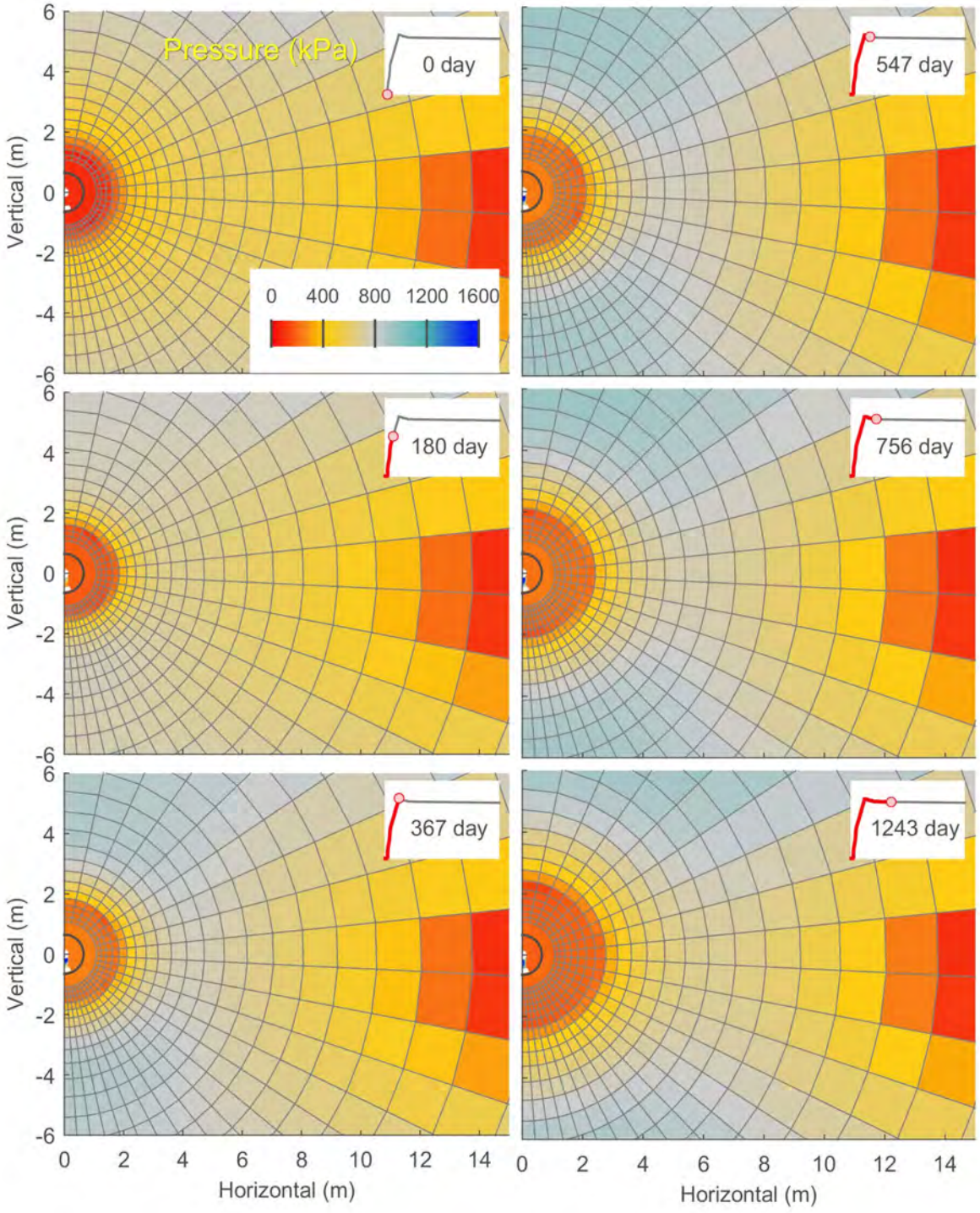

Figure B–5. Spatial Distribution of Calculated Gas Pressure at Selected Time Instants After Start of Heating for the Uncalibrated Parameter Set With Specified Liner Temperature. Note That xFlo Sets Gas Pressure to Liquid Pressure Where Fully Liquid Saturated. [1kPa = 0.145, 1 m = 3.3 ft]

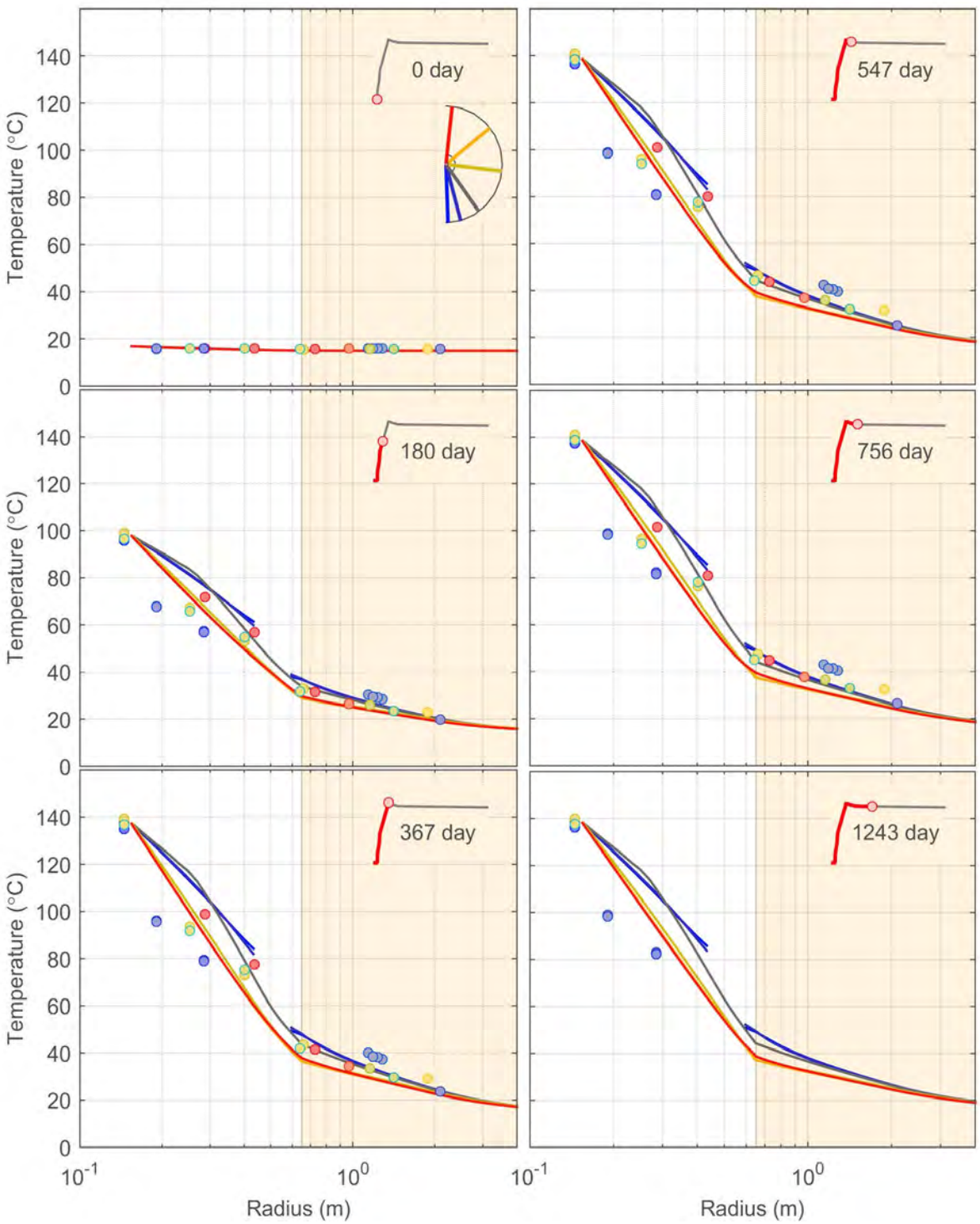

Figure B–6. Radial Profiles of Calculated and Measured Temperature at Selected Time Instants After Start of Heating for the Uncalibrated Parameter Set With Specified Liner Temperature [°F = (1.8 × T °C + 32), 1 m = 3.3 ft]

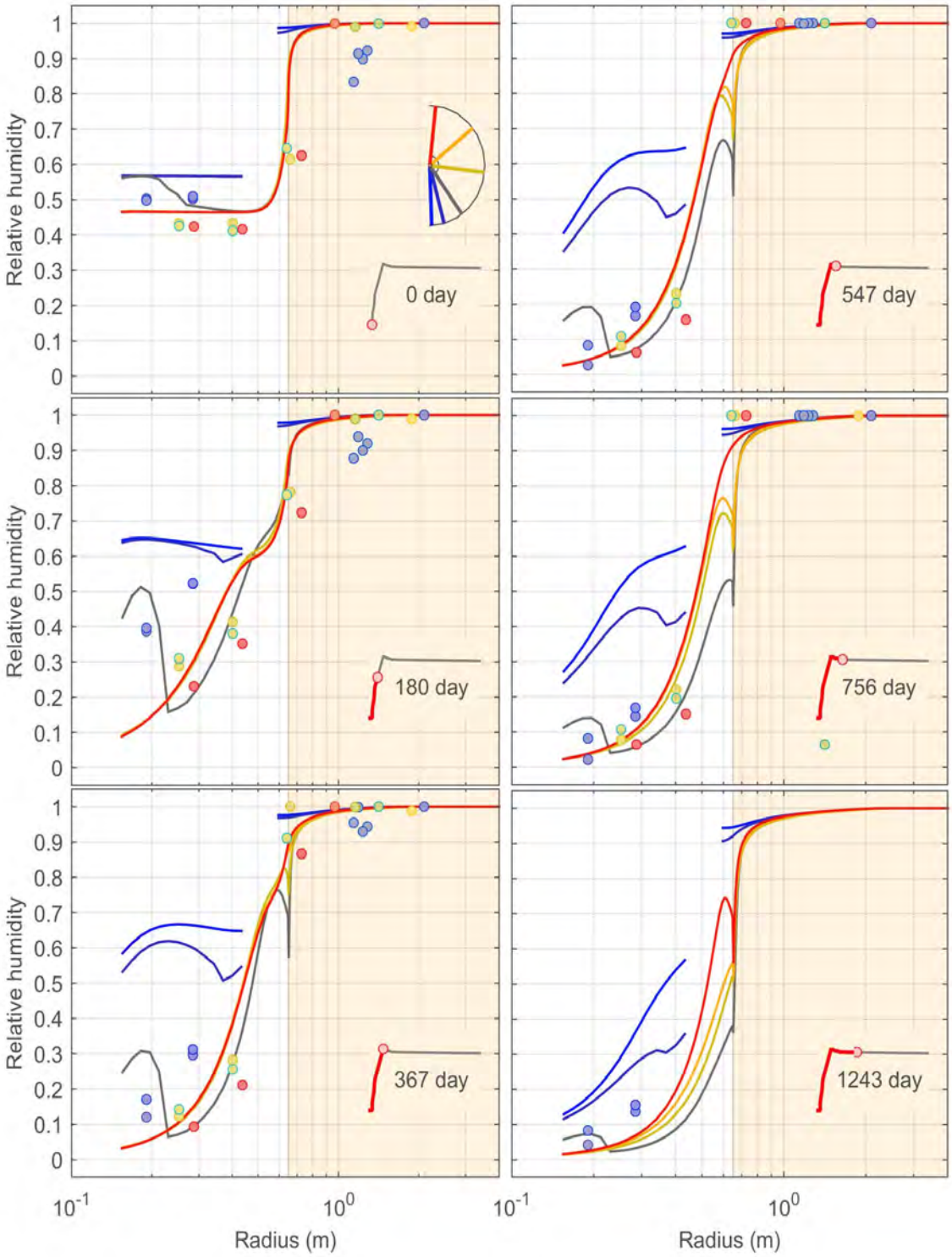

Figure B–7. Radial Profiles of Calculated and Measured Relative Humidity at Selected Time Instants After Start of Heating for the Uncalibrated Parameter Set With Specified Liner Temperature [1 m = 3.3 ft]

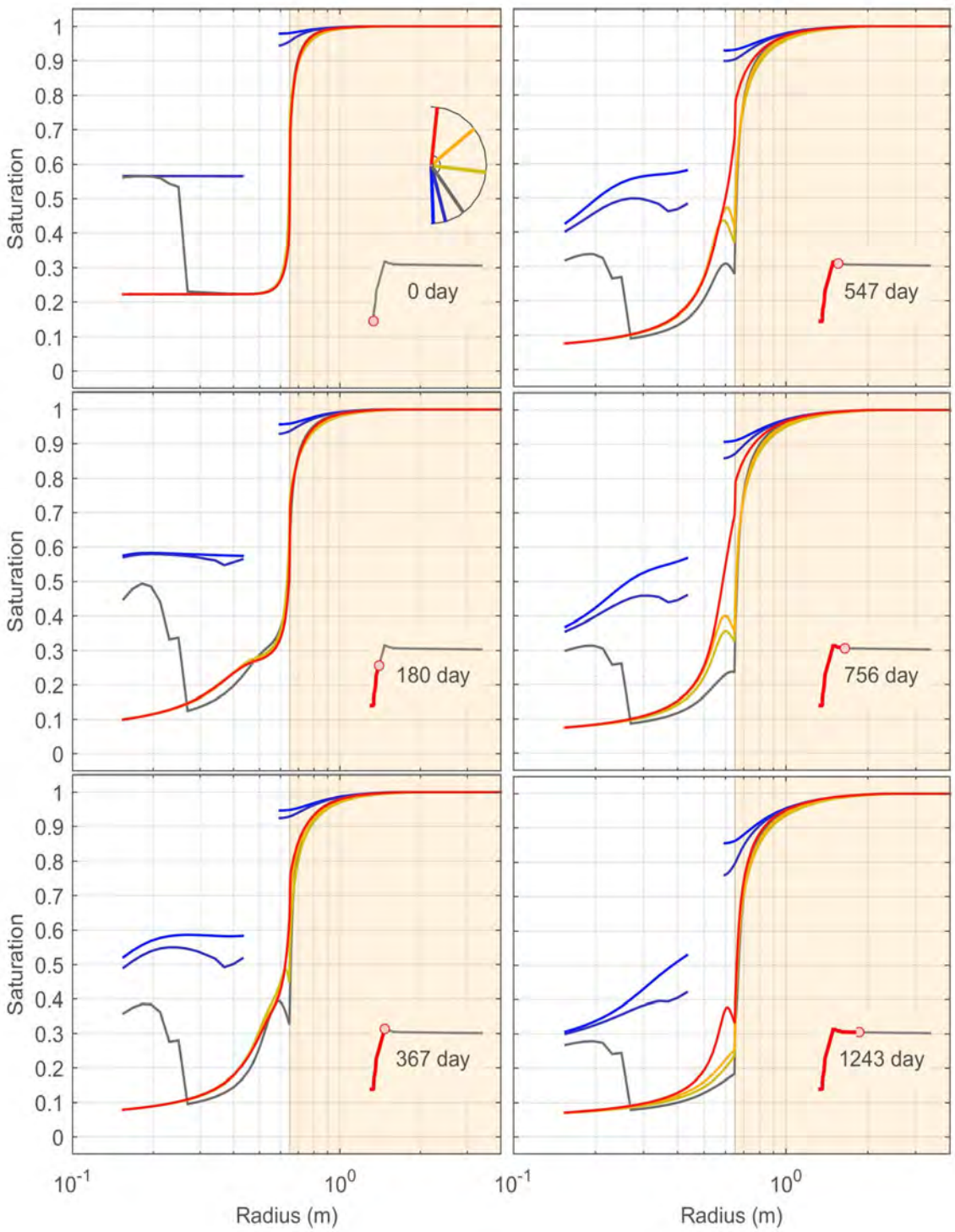

Figure B–8. Radial Profiles of Calculated Liquid Saturation at Selected Time Instants After Start of Heating for the Uncalibrated Parameter Set With Specified Liner Temperature [1 m = 3.3 ft]

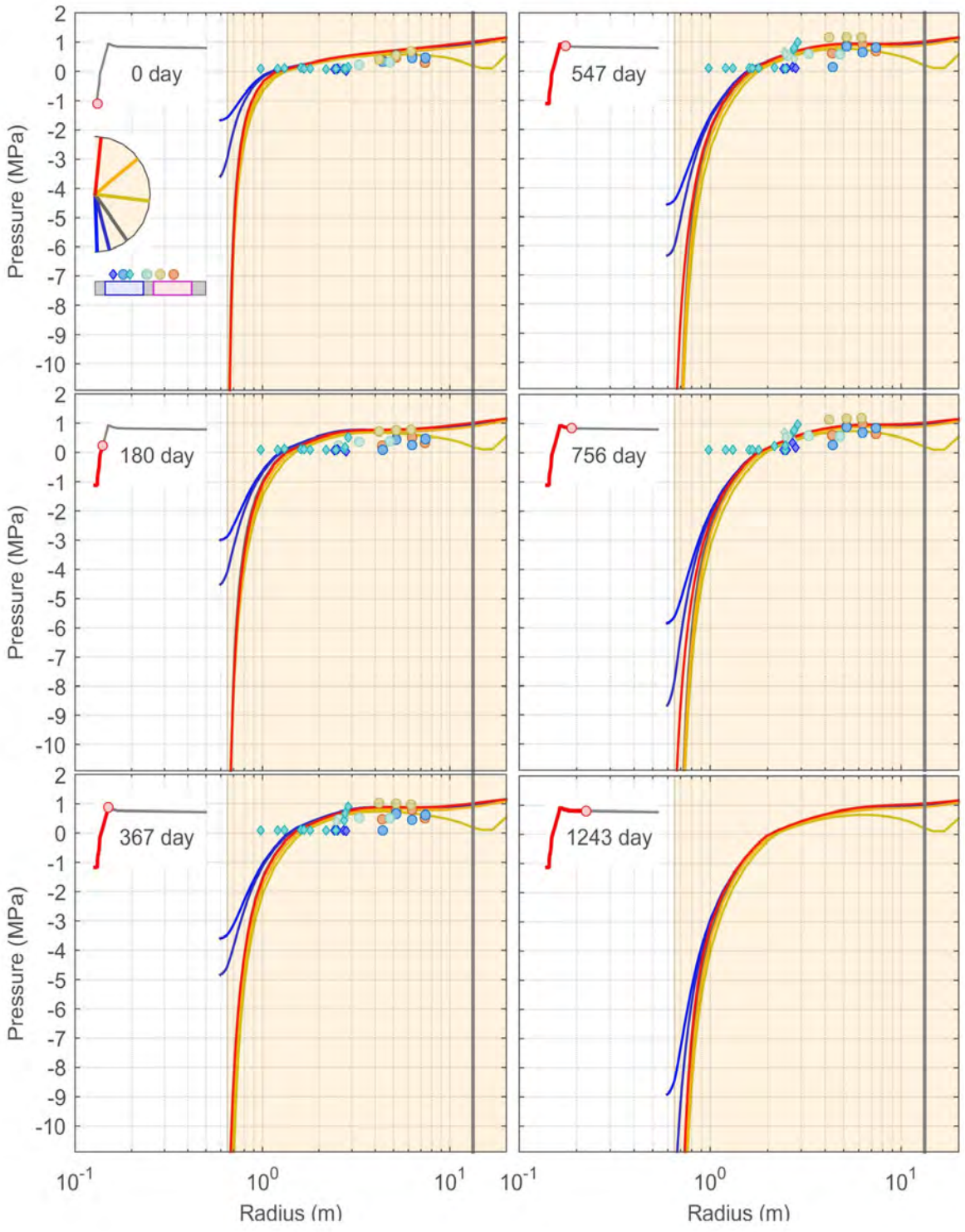

Figure B–9. Radial Profiles of Calculated and Measured Pore Pressure at Selected Time Instants After Start of Heating for the Uncalibrated Parameter Set With Specified Liner Temperature. Circles and Diamonds Indicate Pore Pressure in Gallery 98 and Microtunnel Boreholes, Respectively. BE-1, BVE-1, BVE-91, and BE-2 are Colored Blue, Cyan, Tan, and Orange, Respectively. [1MPa = 145 psi, 1 m = 3.3 ft]

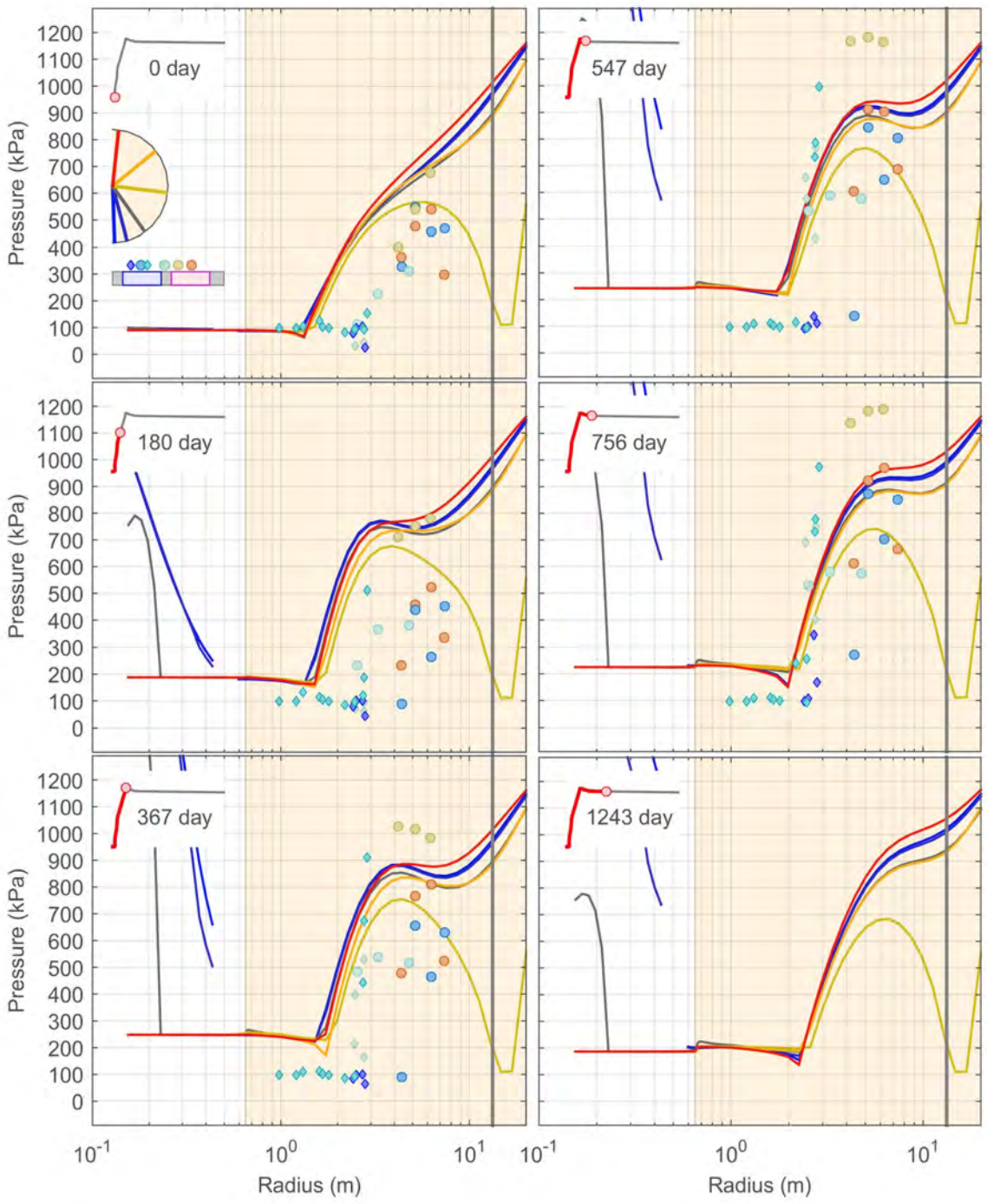

Figure B–10. Radial Profiles of Calculated Gas and Measured Pore Pressure at Selected Time Instants After Start of Heating for the Uncalibrated Parameter Set With Specified Liner Temperature. Circles and Diamonds Indicate Pore Pressure in Gallery 98 and Microtunnel Boreholes, Respectively. Note That xFlo Sets Gas Pressure to Liquid Pressure Where Fully Liquid Saturated. [1kPa = 0.145 psi, 1 m = 3.3 ft]

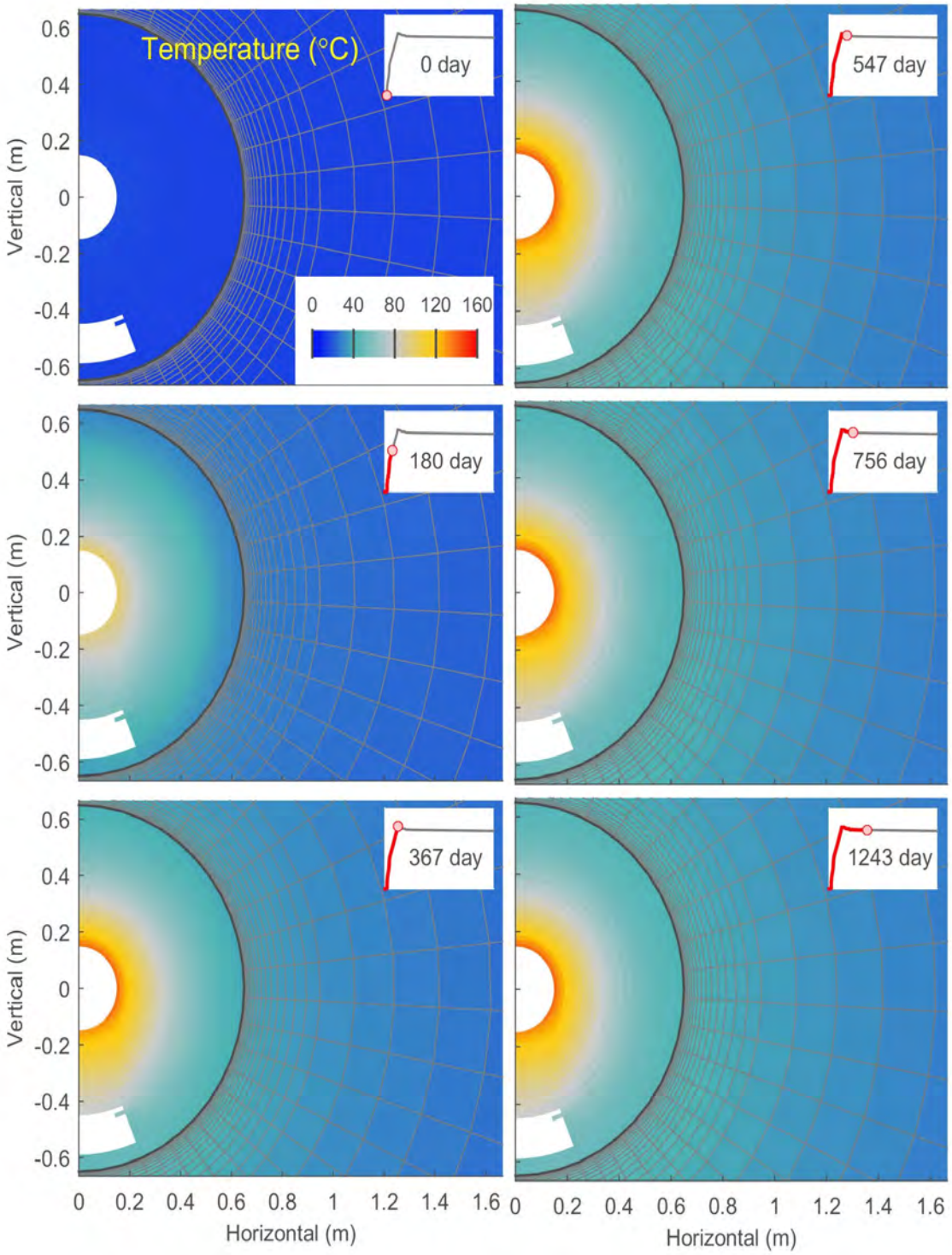

Figure B–11. Spatial Distribution of Calculated Temperature at Selected Time Instants After Start of Heating for the Calibrated Parameter Set With Specified Liner Temperature [°F = (1.8 × T °C + 32), 1 m = 3.3 ft]

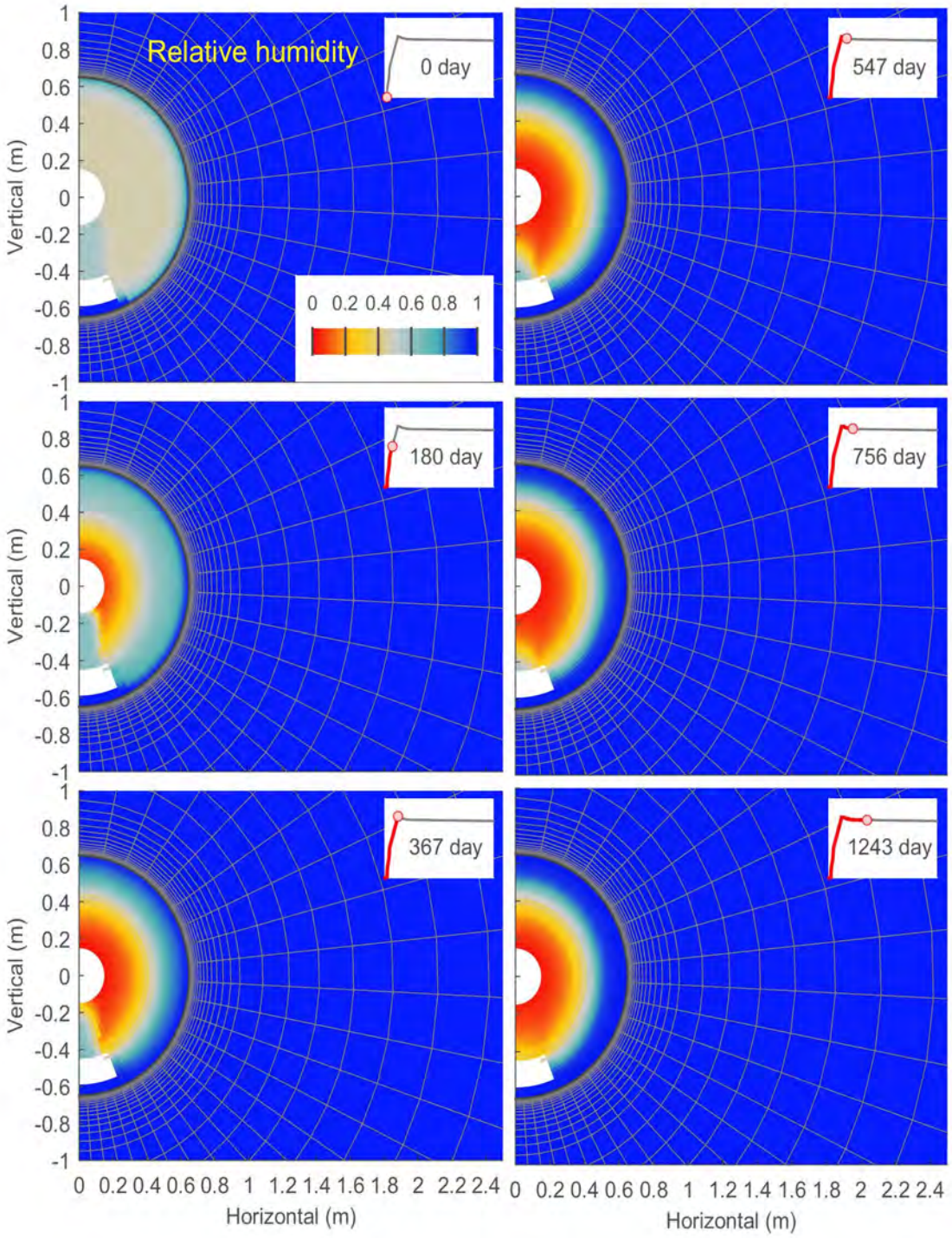

Figure B–12. Spatial Distribution of Calculated Relative Humidity at Selected Time Instants After Start of Heating for the Calibrated Parameter Set With Specified Liner Temperature [1 m = 3.3 ft]

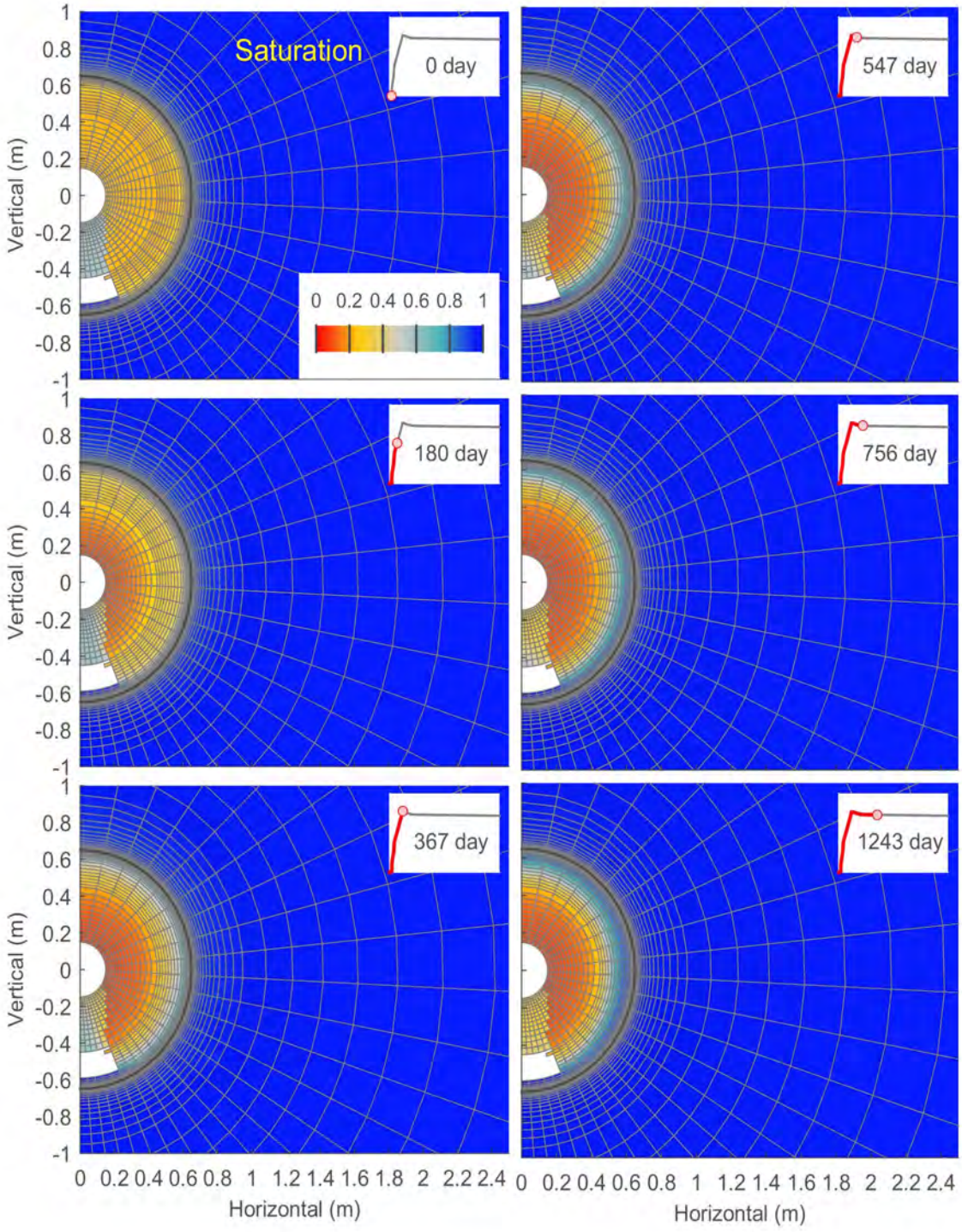

Figure B–13. Spatial Distribution of Calculated Liquid Saturation at Selected Time Instants After Start of Heating for the Calibrated Parameter Set With Specified Liner Temperature [1 m = 3.3 ft]

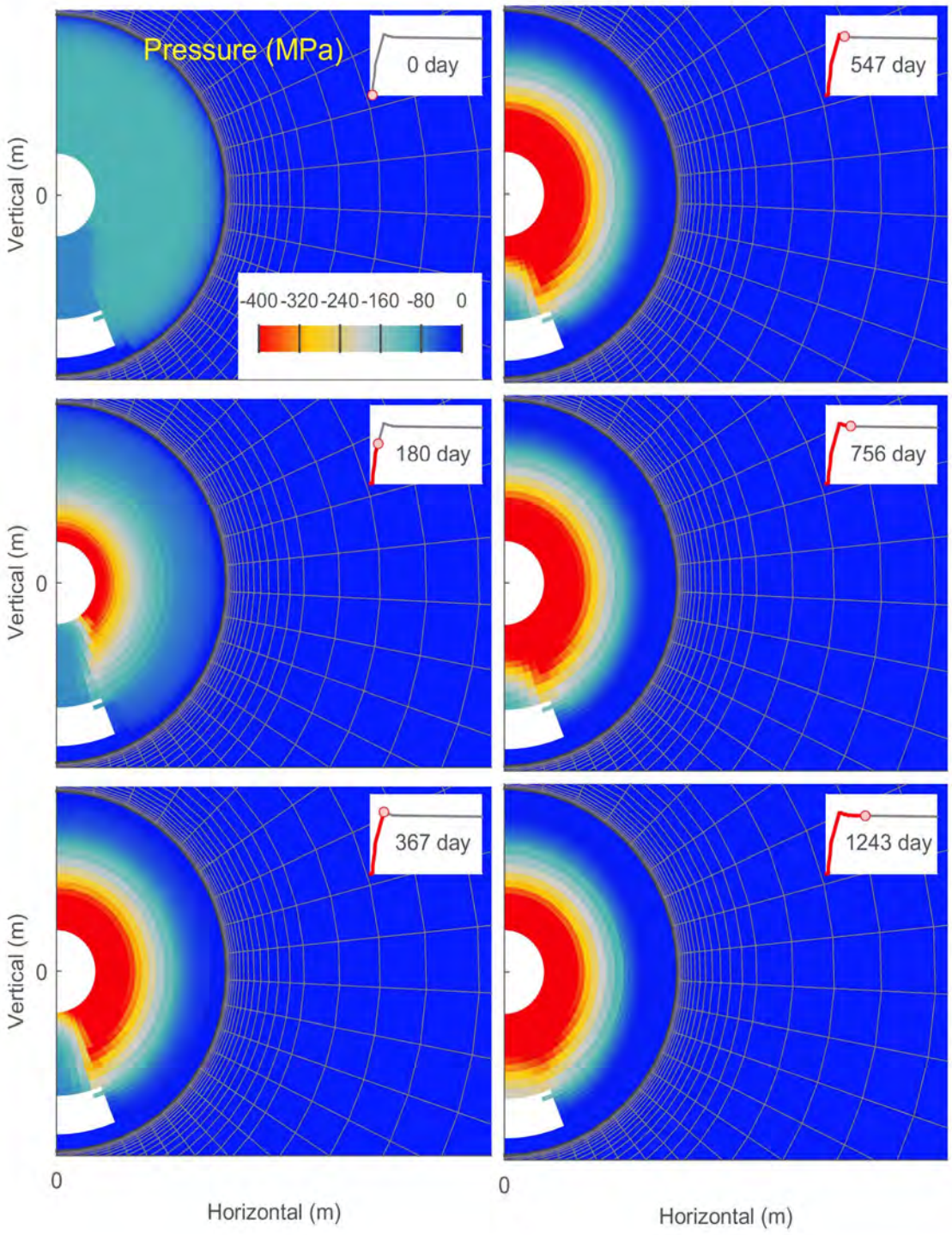

Figure B–14. Spatial Distribution of Calculated Liquid Pressure at Selected Time Instants After Start of Heating for the Calibrated Parameter Set With Specified Liner Temperature. Note That Liquid Pressure is Clipped. [1 MPa = 145 psi, 1 m = 3.3 ft]

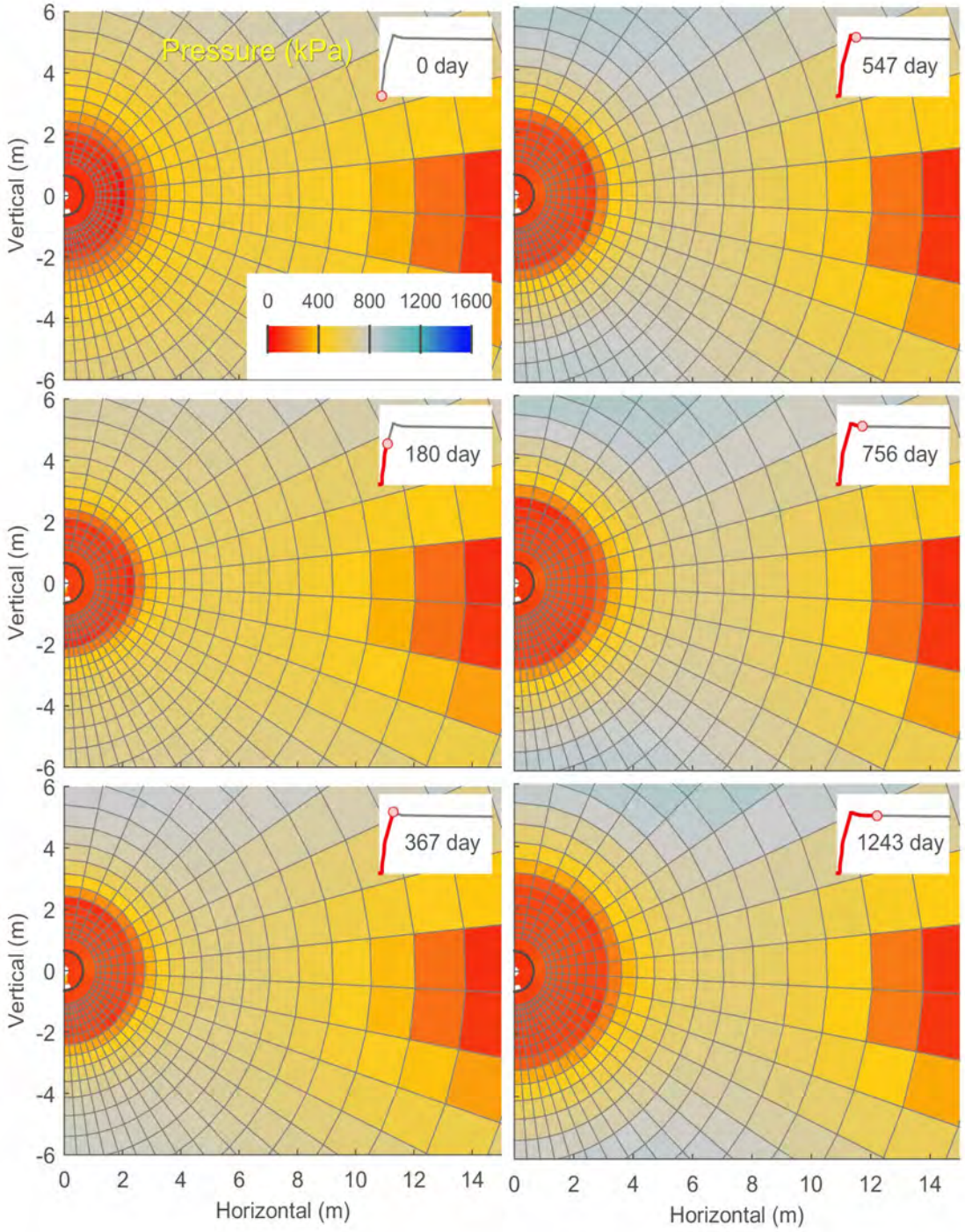

Figure B–15. Spatial Distribution of Calculated Gas Pressure at Selected Time Instants After Start of Heating for the Calibrated Parameter Set With Specified Liner Temperature. Note That xFlo Sets Gas Pressure to Liquid Pressure Where Fully Liquid Saturated. [1 kPa = 0.145 psi, 1 m = 3.3 ft]

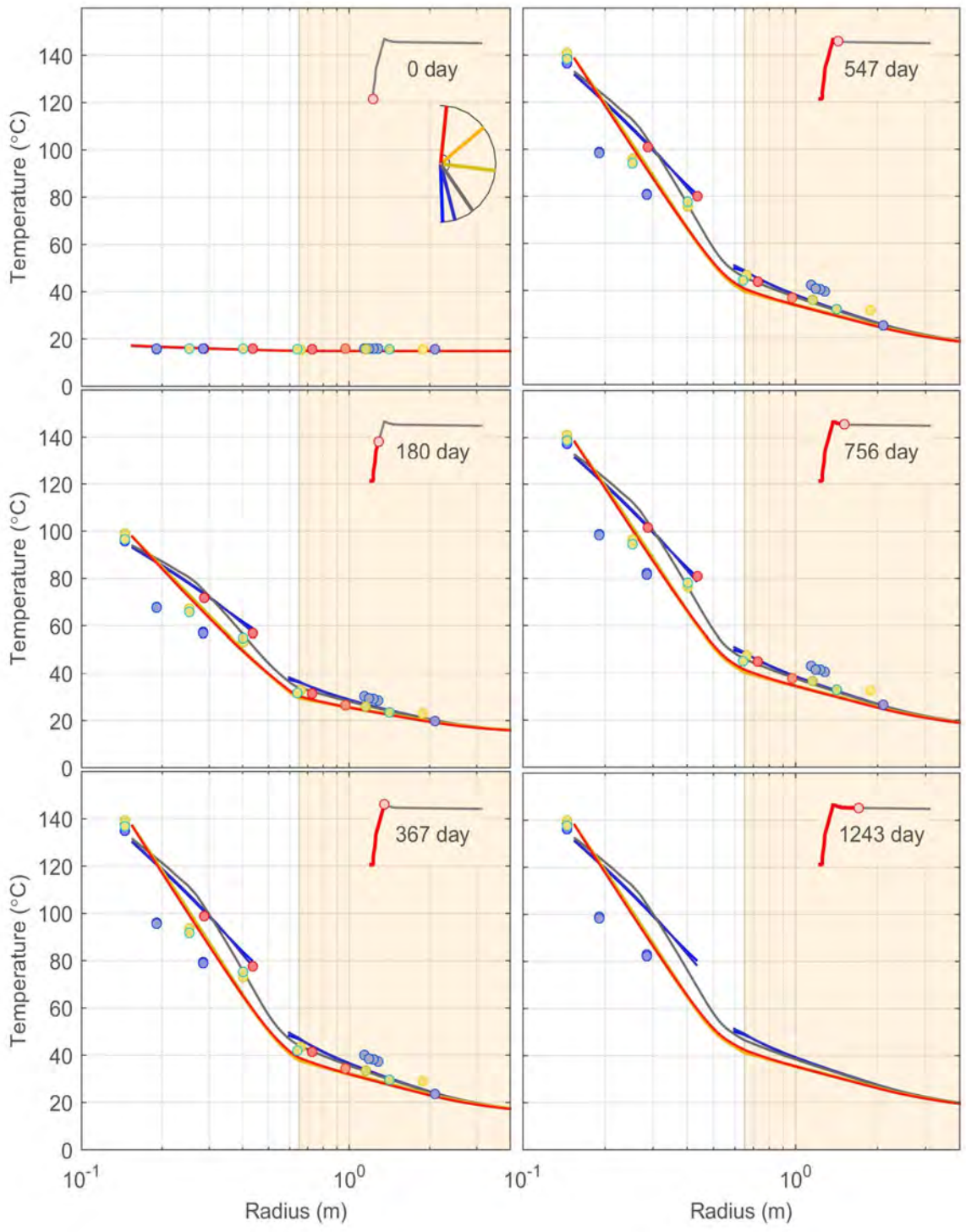

Figure B–16. Radial Profiles of Calculated and Measured Temperature at Selected Time Instants After Start of Heating for the Calibrated Parameter Set With Specified Liner Temperature [°F = (1.8 × T °C + 32), 1 m = 3.3 ft]

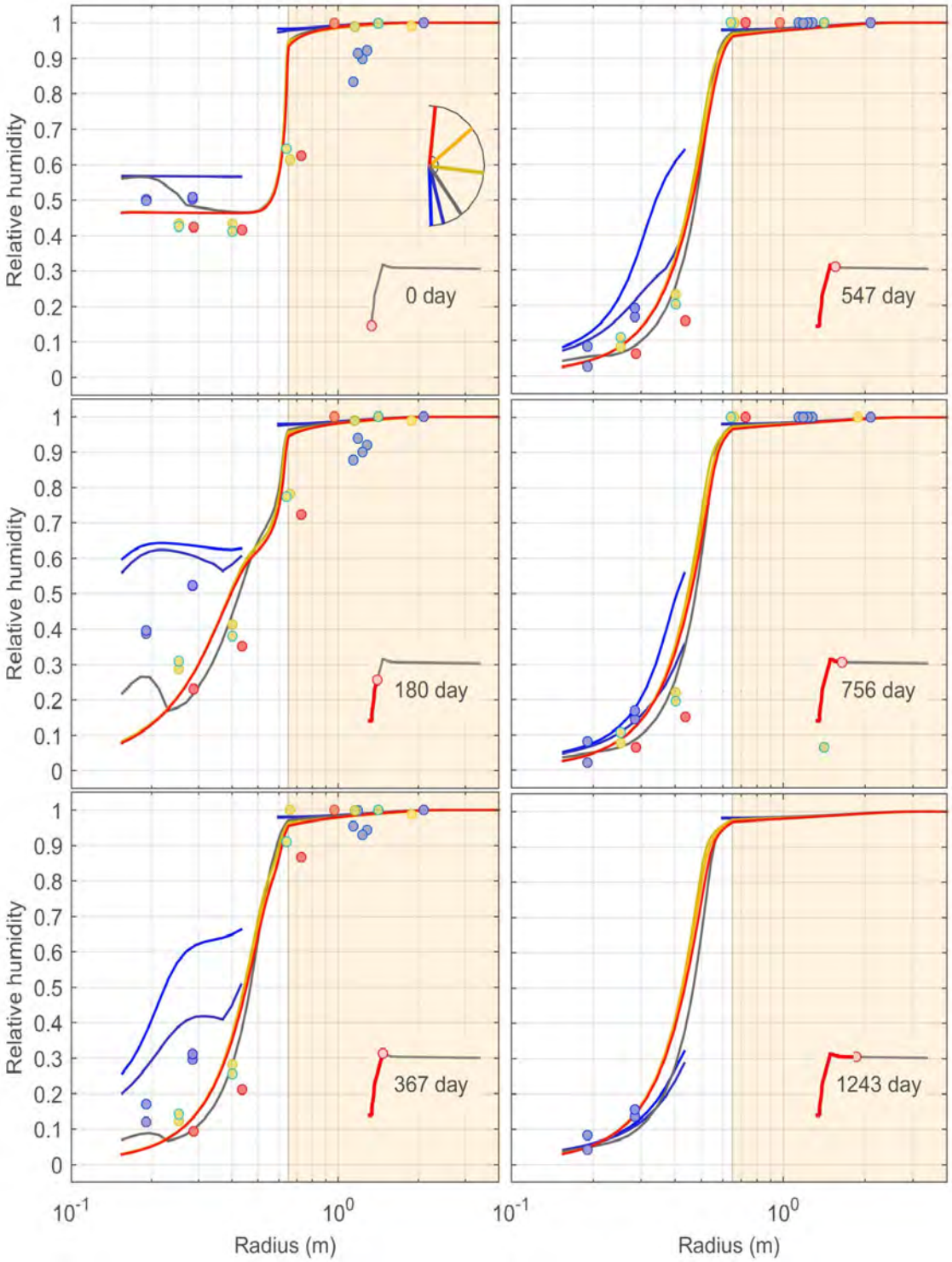

Figure B–17. Radial Profiles of Calculated and Measured Relative Humidity at Selected Time Instants After Start of Heating for the Calibrated Parameter Set With Specified Liner Temperature [1 m = 3.3 ft]

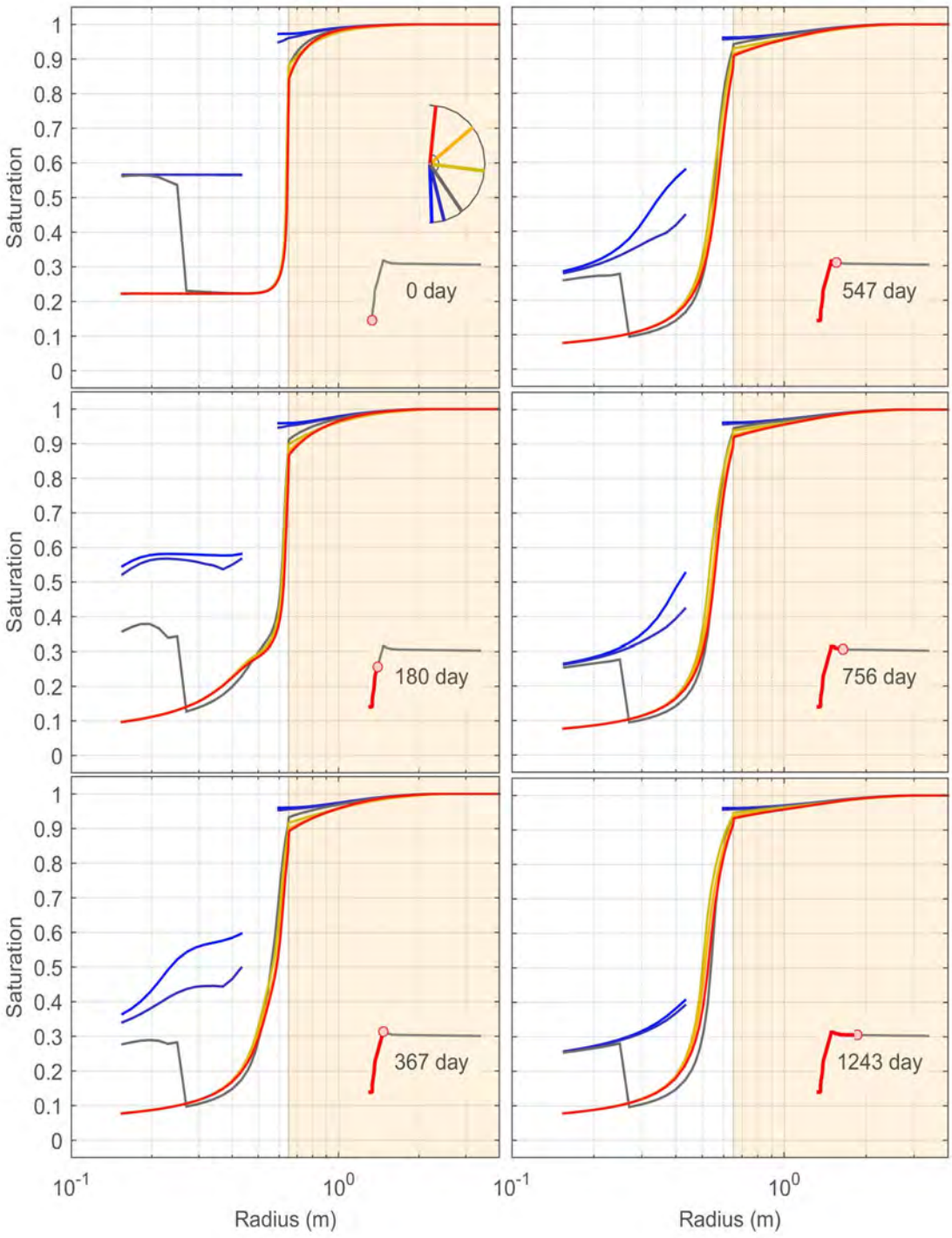

Figure B–18. Radial Profiles of Calculated Liquid Saturation at Selected Time Instants After Start of Heating for the Calibrated Parameter Set With Specified Liner Temperature [1 m = 3.3 ft]

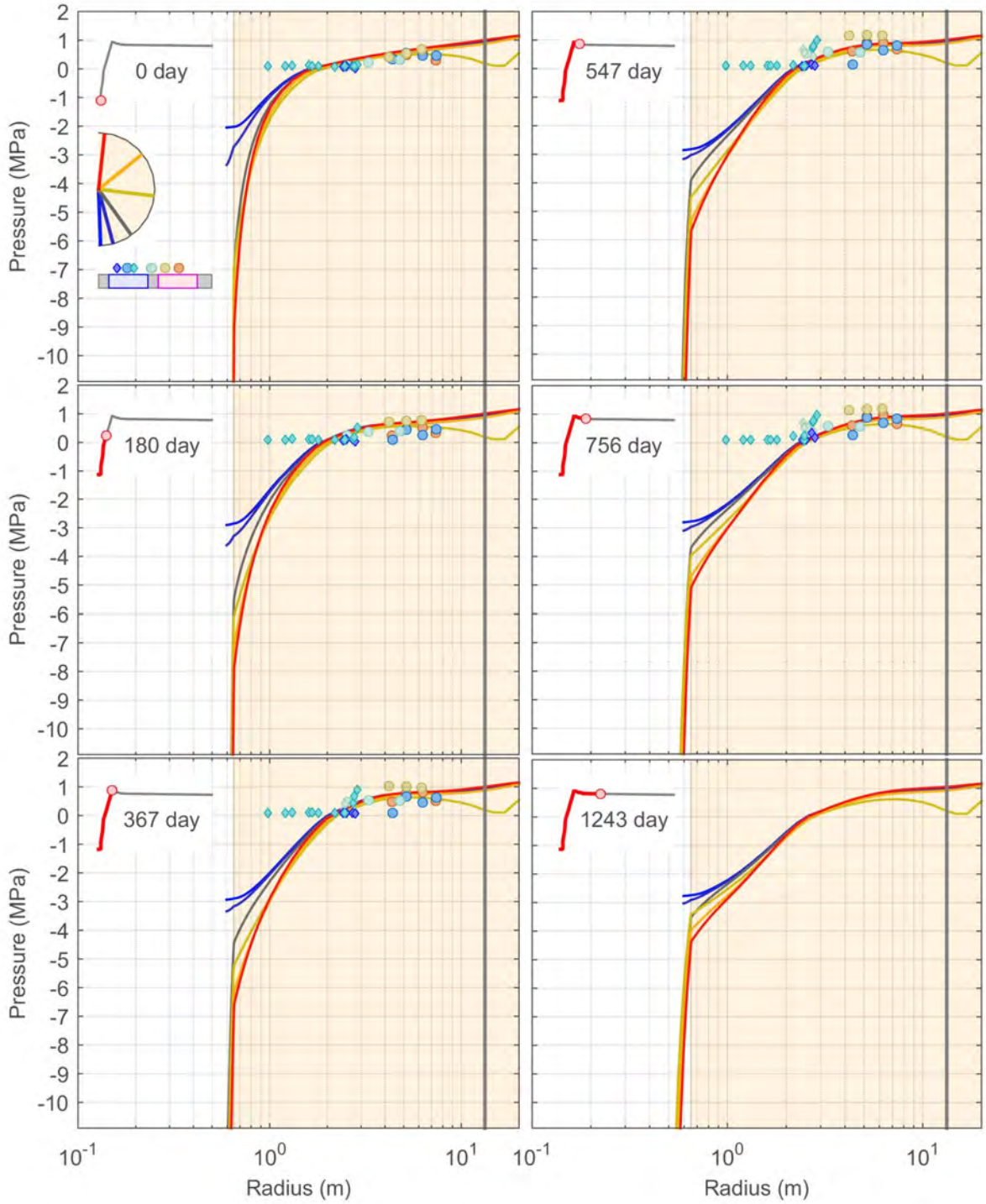

Figure B–19. Radial Profiles of Calculated and Measured Pore Pressure at Selected Time Instants After Start of Heating for the Calibrated Parameter Set With Specified Liner Temperature. Circles and Diamonds Indicate Pore Pressure in Gallery 98 and Microtunnel Boreholes, Respectively. BE-1, BVE-1, BVE-91, and BE-2 are Colored Blue, Cyan, Tan, and Orange, Respectively. [1 MPa = 145 psi, 1 m = 3.3 ft]

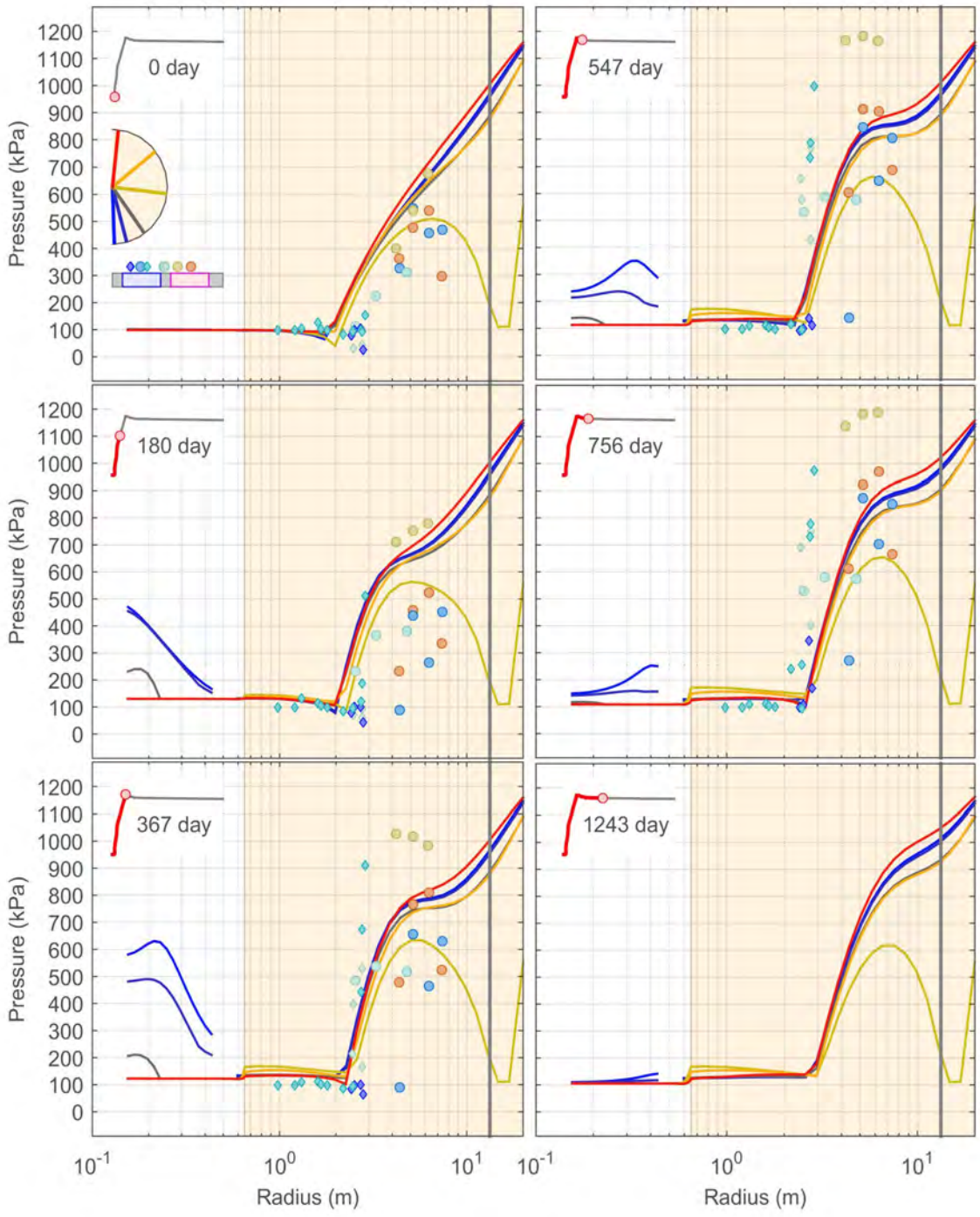

Figure B–20. Radial Profiles of Calculated Gas and Measured Pore Pressure at Selected Time Instants After Start of Heating for the Calibrated Parameter Set With Specified Liner Temperature. Circles and Diamonds Indicate Pore Pressure in Gallery 98 and Microtunnel Boreholes, Respectively. Note That xFlo Sets Gas Pressure to Liquid Pressure Where Fully Liquid Saturated. [1 kPa = 0.145 psi, 1 m = 3.3 ft]